Numerical study of shock waves propagation and attenuation in confined areas

Nassim Brahmi

Normandie Université

THÈSE

pour obtenir le diplôme de doctorat

Spécialité : Mécanique des fluides

Préparée au sein du Laboratoire CORIA, UMR 6614 CNRS.

Etude numérique de la propagation et l'atténuation des ondes de choc en milieux confinés

présentée par

Nassim BRAHMI

Thèse soutenue publiquement le 01 octobre 2020 devant le jury composé de		
Isabelle SOCHET	Professeur, INSA Centre Val de Loire, France	Rapporteur
Georges JOURDAN	Professeur, Université d'Aix-Marseille, France	Rapporteur
Arnab CHAUDHURI	Professeur, Université d'Oslo, Norvège	Examinateur
Sergey KUDRIAKOV	Docteur-Ingénieur, CEA Saclay, France	Examinateur
Arnaud BULTEL	Maitre de conférences-HDR, Université de Rouen Normandie, France	Examinateur
Bechara TAOUK	Professeur, INSA de Rouen Normandie, France	Examinateur
Abdellah HADJADJ	Professeur, INSA de Rouen Normandie, France	Directeur de Thèse

Thèse dirigée par Abdellah HADJADJ, laboratoire CORIA UMR-6614, France.

INSA INSTITUT NATIONAL DES SCIENCES APPLIQUÉES ROUEN NORMANDIE

591 ED PSIME

UMR 6614 CORIA COMPLEXE DE RECHERCHE INTERPROFESSIONNEL EN AEROTHERMOCHIMIE

Normandie Université

THESIS

for the degree of Doctor of Philosophy

Specialized in : Fluid Mechanics

From CORIA, UMR 6614 CNRS.

Numerical study of shock waves propagation and attenuation in confined areas

by

Nassim BRAHMI

Thesis defended publicly on the 1st October 2020 in fulfillment of the requirements from		
Isabelle SOCHET	Professor, INSA Centre Val de Loire, France	Reviewer
Georges JOURDAN	Professor, Aix-Marseille University, France	Reviewer
Arnab CHAUDHURI	Professor, Oslo University, Norway	Examiner
Sergey KUDRIAKOV	Docteur-Ingènieur, CEA Saclay, France	Examiner
Arnaud BULTEL	Associate professor, Rouen Normandy University, France	Examiner
Bechara TAOUK	Professor, INSA de Rouen Normandie, France	Examiner
Abdellah HADJADJ	Professor, INSA de Rouen Normandie, France	Supervisor

Under the supervision of Abdellah HADJADJ, CORIA CNRS, FRANCE.

INSA INSTITUT NATIONAL DES SCIENCES APPLIQUÉES ROUEN NORMANDIE

ED 591 PSIME

UMR 6614 CORIA COMPLEXE DE RECHERCHE INTERPROFESSIONNEL EN AEROTHERMOCHIMIE

Abstract

The propagation of shock waves involves complex interactions between waves and surrounding media, which gives rise to several phenomena such as reflection, diffraction, etc. To shed more light into the fundamental physics associated with these phenomena, high resolution numerical simulations were carried out. In particular, analysis of shock diffraction over double concave cylindrical wedges revealed that the transition angles, from regular to Mach reflection, increase with the Mach number, whereas they are found to be almost the same over the two concave surfaces for the transonic Mach regimes and relatively larger on the second surface for high ones showing that the flow is capable of retaining the memory of the past events over the entire process for the high Mach numbers. The analysis of the vorticity equation balance showed, for the first time, that the diffusion of the vorticity due to the viscous effects is quite important compared to the baroclinic term for low Mach numbers, while this trend is inverted for higher Mach numbers. The study also showed that the stretching of the vorticity due to the compressibility effects plays an important role in the vorticity production. On the basis of these numerical simulations, an approximate universal relation is proposed, allowing to predict the incident-shock trajectory and velocity as a function of the incident-shock Mach number, the radius of curvature of the geometry, and the gas properties. Afterward, the study of shock-waves propagation and their attenuation in channel flow having different heights and exhibiting a hollow circular cavities with different depths has been done. The results also showed the importance of reducing the height of the channel and changing the position of the reduced section in addition to the diffraction angle and the cavity depth for better shock-waves attenuation. A subtle arrangement of channel position/height and a cavity location/depth was found.

Keywords Shock waves, vorticity, attenuation, reflection and diffraction, numerical simulations, supersonic flows.

Résumé

La propagation des ondes de choc implique des interactions complexes entre ondes et milieux environnent, ce qui engendre plusieurs phénomènes tels que la réflexion, la diffraction, etc. Pour clarifier davantage la physique associée à ces phénomènes, des simulations numériques hautes résolutions ont été réalisées. En particulier l'analyse de la diffraction des ondes de choc sur deux surfaces concaves cylindriques a révélé que les angles de transition, d'une réflexion régulière à une réflexion de Mach, augmentent avec le nombre de Mach, alors qu'ils sont presque égaux sur les deux surfaces concaves pour les régimes de Mach transsoniques et relativement plus important sur la deuxième surface pour les nombres de Mach plus élevés. Ceci prouve que l'écoulement est en

mesure de conserver l'historique des événements passés sur l'ensemble du processus pour des nombres de Mach élevés. L'analyse de l'équation de transport de vorticité a montré, pour la premiére fois, que la diffusion de la vorticité dûe aux effets visqueux est assez importante par rapport au terme baroclinic pour les faibles nombres de Mach, alors que cette tendance est inversée pour les nombres de Mach les plus élevés. L'étude a également montré que le stretching de la vorticité dû aux effets de compressibilité joue un rôle important dans la production de vorticité. Á la base de ces simulations numériques, une relation universelle a été proposée, permettant de prédire la trajectoire et la vitesse de l'onde incidente en fonction du nombre de Mach incident, du rayon de courbure de la géométrie et des propriétés du gaz. Par la suite, l'étude de la propagation des ondes de choc et leur atténuation dans des conduites de différentes hauteurs et présentant des cavités circulaires creuses de différentes profondeurs a été effectuée. Les résultats ont montré l'importance de la réduction de la hauteur du canal et le changement de la position de la section réduite en plus de l'angle de diffraction et de la profondeur de la cavité pour une meilleure atténuation des ondes. Un arrangement optimal de la position/hauteur du canal et de l'emplacement/profondeur de la cavité a été trouvé.

Mots clés Ondes de choc, atténuation, réflexion et diffraction, vorticité, simulations numériques, écoulements supersoniques.

List of Publications

Peer-reviewed Journals

1. Soni, V., Chaudhuri, A., **Brahmi, N.**, Hadjadj, A. (2019). Turbulent structures of shock-wave diffraction over 90° convex corner. *Physics of Fluids*, **31(8)**. https://doi.org/10.1063/1.5113976

2. **Brahmi N.**, Hadjadj A., Soni V., Chaudhuri A. (2020). Analysis of shock-wave diffraction over double concave cylindrical wedges. Part I: Shock dynamics. *Acta Astronautica*, **172**, 134-139.

3. **Brahmi N.**, Hadjadj A., Soni V., Chaudhuri A. (2020). Analysis of shock-wave diffraction over double concave cylindrical wedges. Part II: Vorticity generation. *Acta Astronautica*, **172**, 140-150.

4. **Brahmi N.**, Hadjadj A. (2020). Achieving an optimal shock-wave mitigation inside open channels with cavities for weak shock waves: A computational study. *Theoretical and Applied Mechanics Letters, **10**, 354-365.*

5. **Brahmi N.**, Hadjadj A. (2020). Velocity scaling of a shock wave diffracting over double concave cylindrical surfaces. *submitted to Shock waves journal.*

International Conferences

1. **Brahmi N.**, Hadjadj A. (2019), High-resolution numerical simulations of shock-diffraction induced vorticity generation in cylindrical cavities, 32^{nd} *International Symposium on Shock Waves (ISSW32), Jul 2019, Singapore, Singapore.*

2. **Brahmi N.**, Soni V., Hadjadj A. (2018), Vorticity production in shock waves diffraction over double cylindrical wedges, 4^{th} *International Conference on Energy, Materials and Applied Energetics (ICEMAEP'2018), Apr 2018, Constantine, Algeria.*

Contents

Acknowledgements

First and foremost, I would like to express my gratitude towards my esteemed supervisor Prof. Abdellah HADJADJ for providing me the opportunity to work on this deeply interesting topic of shock waves and supersonic flows. His sense of direction and guidance kept me motivated throughout the course of my research work. He helped me learn the basic and advanced concepts related to shock waves. I would also like to massively thank him for his pushing support providing a good sense of direction to my research work. I am also grateful to the reviewers of my thesis namely, Prof. Isabelle SOCHET and Prof. Georges JOURDAN, and also the jury members Prof. Taouk BECHARA, Prof. Arnab CHAUDHURI, Prof. Sergey KUDRIAKOV and Dr. Arnauld BULTEL investing their valuable time in evaluating this manuscript.

I would like to acknowledge the access to HPC resources provided by the regional computing center of Normandy CRIANN (1998022). The funding resources provided by the Algerian Government is deeply appreciated.

Furthermore, I would also like to extend my thanks to Dr. Mostafa SAFDARI-SHADLOU and the former PhD/postdocs of our group i.e. Dr. Vineet SONI, Dr. Arthur PIQUET, for their precious support and fruitful discussions. Dr. SONI helped me a lot to familiarize the structure of our solver which definitely sped-up the progress of the work, so thanks a lot for always being there to help. I am thankful to my lab buddies Boubakr, Sushank, Margio with whom I started this journey of PhD. And, also Ms. Fatemeh and Mr. Celep who joined us later on.

Finally, I could not thank enough to my lovely parents; HACEN, and ZAKIA, to whom I want to say that if I arrived here today it is because of them and it is for them that I have done everything I have done. My wife; ASMAA, my son: ILYANE, my brother; SALIM and his wife; DIHIA and their son; YASTEN, my sister; KAMY and his husband; AKI and their children; ADAM and ALICE for bearing with me through the highs and lows of this journey. They are an endless source of motivation, encouragement, and support. They endured me throughout my life and also during this journey being my backbone, and made the things worthwhile. TO MY SUPERVISOR: BELEMRABET TOUFIK. TO MY FRIEND: COPCH: BELEKBIR LOTFI.

Glossary

Abbreviations and nomenclatures

Nomenclature

d'	Additional shock
E	Total energy per unit mass
e	Internal energy per unit mass
G	Grid
G_f	Fluid domain
G_s	Solid domain
I	Incident shock
I_p	Static-pressure impulse
I_{pd}	Dynamic-pressure impulse
L	Global refinement level
l	Local refinement level
ℓ	Error norm
$MaxL$	Maximal refinement level
$MinL$	Minimal refinement level
M_s	Incident-shock-Mach number
$\mathcal{P}$	Normalized overpressure
Pr	Prandtl number
p	Static pressure
$\mathcal{R}$	Universal gas constant
R	Concave radius
r	Reflected shock
S	Sutherland temperature
T	Temperature
t	Time
$\mathbf{v}$	Velocity vector

Greeks

Γ	Vorticity circulation
γ	Ratio of heat capacities
λ	Thermal conductivity
μ	Dynamic viscosity
ρ	Density
ω	Local vorticity
ω_1	Angle of the first wedge
ω_2	Angle of the second wedge
ω_c	Convection vorticity term
ω_t	Unsteady vorticity term
ϵ	Multiresolution tolerance
$\mathfrak{d}$	Wavelet/detail coefficient
Δx	Spatial grid spacing
Δt	Time step
θ_w^{tr}	InMR $\rightarrow$ TRR transition angle
θ_w	Initial wedge angle

Abbreviations

BAR	Baroclinic torque
BP	Boundary point
CAD	Computer aided design
CMR	Complex–Mach reflection
CPU	Central processing unit
DFV	Diffusion of vorticity due to viscosity
DiMR	Direct–Mach reflection
DMR	Double–Mach reflection
DMR^+	Positive double–Mach reflection
DMR^-	Negative double–Mach reflection
DNS	Direct numerical simulation
DS	Diffracted shock
DTP	Double–triple point
FG	Fine grid
GP	Ghost point

IB	Immersed boundary
InMR	Inverse–Mach reflection
IP	Image point
IR	Irregular reflection
KHI	Kelvin-Helmholtz instability
LES	Large eddy simulation
LS	Lambda shock
MS	Mach stem
MR	Mach reflection
MR	Multiresolution
NP	Neighbor point
PTMR	Pseudo-transitional-Mach reflection
PV	Primary vortex
RK	Runge–Kutta
RR	Regular reflection
SL	Slipstream
STL	Stereolithography
StMR	Stationary-Mach reflection
STP	Single–triple point
SMR	Single–Mach reflection
SLI	Shear-layer instabilities
SS	Secondary shocks
SV	Secondary vortex
TP	Triple point
TVD	Total variation diminishing
TRR	Transitioned–regular reflection
TMR	Transitional–Mach reflection
vNR	von Neumann reflection
VSC	Stretching of vorticity due to compressibility
VSG	Stretching/tilting of vorticity due to velocity gradients
VTE	Vorticity transport equation
WENO	Weighted essentially non–oscillatory

Résumé

1 Contenu de la thèse

La propagation des ondes de choc implique des interactions d'ondes complexes avec les structures en raison de plusieurs phénomènes mis en jeux tels que la réflexion, la diffraction, l'atténuation/l'amplification, la focalisation des chocs et l'interaction choc-turbulence. La compréhension de ces phénomènes est cruciale pour un large éventail d'applications d'ingénierie dans la biomédecine, la gestion des catastrophes, la détonation, l'exploitation minière, l'industrie de l'aviation et des transports et autres.

La nécessité d'une meilleure compréhension des différents phénomènes physiques présents lors de l'interaction d'une onde de choc avec des obstacles de géométries complexes a été établie. Une attention particulière a été portée à la propagation des ondes de choc dans les zones confinées, compte tenu des configurations complexes d'écoulement et d'onde de choc suite à la propagation d'une onde de choc plane à travers des conduits.

L'atténuation des ondes de choc est importante pour de nombreuses applications pratiques, telles que la propagation des ondes de souffle à travers les tunnels, les accidents industriels non intentionnels et la mécanique structurelle aérospatiale à grande vitesse. Dans certains scénarios, des changements brusques dans les sections de canaux peuvent fournir une solution d'atténuation économique et facile à mettre en œuvre. Les changements soudains dans les sections des tunnels permettent une protection passive des personnes et des structures sans recourir à une technologie intégrée coûteuse. Ces changements peuvent soit amplifier ou atténuer les effets des ondes de choc en fonction de leur configuration, de leur disposition et de la direction de l'onde de choc. Par conséquent, il est devenu d'un intérêt vital et d'actualité de comprendre les différents mécanismes conduisant à l'atténuation des ondes de choc.

Le travail suivant vise à mettre en évidence les configurations d'écoulements et d'onde de choc se propageant dans des zones confinées, en utilisant des simulations numériques directes (DNS) comme principal outil pour générer les données. Les données sont ensuite analysées dans le but d'éclairer quelques questions fondamentales, concernant l'effet de divers paramètres physiques sur les phénomènes liés à l'interaction des ondes de choc avec les structures. En particulier, nous visons à:

- Comprendre le mécanisme et le processus de production de vorticité et l'influence de différents paramètres physiques sur le taux de production de vorticité.

- Étudier l'implication de différents paramètres physiques dans la détermination des différentes configurations d'écoulement et d'ondes de choc résultant de la propagation d'ondes de choc à travers des zones confinées aux géométries complexes.

- Déterminer les différents paramètres physiques et géométriques conduisant à une atténuation optimale des ondes de choc dans les conduits.

2 Aperçu de la thèse

La vue d'ensemble de l'organisation par chapitre de la thèse est donnée ci-dessous :

Chapitre 2: Ce chapitre commence par la description des équations gouvernantes, y compris l'équation linéaire de transport, ainsi que les équations non linéaires d'Euler et de Navier-Stokes. De plus, la méthode multirésolution à valeur de point pour effectuer l'adaptabilité dynamique de l'espace est expliquée avec ses éléments pertinents. La méthode des frontières immergées (IB), qui facilite la réalisation de simulations sur des grilles non conformes, est également présentée. De plus, une technique d'infographie appelée lancer de rayons est élaborée, qui complète la méthode IB pour localiser tout modèle solide complexe dans les grilles cartésiennes.

Chapitre 3: Dans ce chapitre, la diffraction des ondes de choc sur des surfaces cylindriques à double concave a été étudiée numériquement à différents régimes d'écoulement en variant le nombre de Mach de l'onde de choc incidente de M_s = 1,6 (régime transsonique) à M_s = 4,5 (régime supersonique). L'objectif principal de cette étude est de mieux comprendre la dynamique de la structure des ondes de choc et les configurations d'ondes associées. En outre, une relation universelle approximative est dérivée, qui prédit la trajectoire de l'onde de choc transmise en fonction du nombre de Mach du choc incident dans la plage de 1,6 <M_s <4,5, pour un rapport de chaleur spécifique de 1,4 et un rayon de surface de 50 mm. Les résultats sont publiés dans: Acta Astronautica (Brahmi et al. 2020a).

Chapitre 4: En complément du chapitre précédent, ce chapitre traite l'aspect instationnaire des structures d'écoulement turbulent générées par la diffraction d'onde de choc sur des doubles surfaces cylindriques, avec un angle de diffraction initial de 75°. La production de vorticité est quantifiée pour différents nombres de Mach, allant des régimes transsoniques aux régimes supersoniques. Contrairement aux études précédentes où seule la production totale de vorticité est évaluée, ce chapitre offre plus d'informations sur le comportement spatio-temporel de la circulation en évaluant l'évolution de l'équilibre instantané de l'équation de vorticité. L'intensité du choc est également évaluée dans ce chapitre en calculant les impulsions de pression dynamique ainsi que statique et la surpression normalisée. Les résultats sont publiés dans: Acta Astronautica (Brahmi et al. 2020b).

Chapitre 5: Au chapitre 3, une relation universelle approximative est dérivée, qui prédit la trajectoire de l'onde de choc transmise en fonction du nombre de Mach du

choc incident pour un rapport thermique spécifique fixe de 1,4 (l'air comme gaz). Dans ce chapitre, la géométrie ainsi que le nombre de Mach de l'onde de choc sont maintenus constants tels que M_s = 1,6, tandis que le gaz est varié. Quatre gaz, avec des masses moléculaires différentes, des rapports thermiques spécifiques et des impédances acoustiques en plus de l'air, sont utilisés comme gaz de travail, à savoir, He, Ar, CO_2 et SF_6. La relation proposée au chapitre 3 a été généralisée à différents gaz ayant des rapports thermiques spécifiques différents. Les résultats sont soumis à: Shock waves Journal.

Chapitre 6: Ce chapitre consiste en une étude numérique de la propagation des ondes de choc et de leur atténuation dans un canal de différentes hauteurs et présentant des cavités circulaires creuses avec des profondeurs et des angles de diffraction différents à l'intérieur. Une attention particulière a été portée à l'atténuation des ondes de choc se propageant dans ce type de canal. Une configuration optimale avec la position/hauteur du canal et une profondeur de cavité menant à une atténuation efficace de la pression se trouve dans ce chapitre. Les résultats sont publiés dans: Theoretical and Applied Mechanics Letters Journal.

Chapitre 7: Le résumé des travaux de recherche entrepris ainsi que les remarques de conclusion et les perspectives de l'étude sont présentées dans ce chapitre.

3 Conclusions et perspectives

L'objectif principal de cette thèse est d'utiliser des simulations numériques à haute résolution pour clarifier davantage la physique des écoulements liés à la propagation et à l'atténuation des ondes de choc dans des milieux confinées. Un accent particulier est mis sur l'étude de différentes géométries complexes.
Les résultats de la présente étude peuvent être résumés comme suit :

3.1 Diffraction des ondes de choc sur des surfaces cylindriques doubles concaves

La diffraction des ondes de choc sur des surfaces cylindriques doubles concaves est d'abord étudiée à différents régimes d'écoulement en variant le nombre de Mach de l'onde de choc incidente de M_s = 1,6 (régime transsonique) à M_s = 4,5 (régime supersonique). La dynamique des ondes de choc est analysée profondément, l'évaluation de l'angle de transition, θ^{tr}, d'une réflexion régulière à une réflexion de Mach (RR → MR) a montré que θ^{tr} augmente avec le nombre de Mach. L'analyse a également révélé que θ^{tr} est presque le même sur les deux surfaces pour les nombres de Mach faibles, jusqu'à M_s = 2,5, et qu'il est relativement plus grand sur la deuxième surface pour les nombres de Mach élevés, M_s = 3,5 et 4,5. Le suivi de la trajectoire du

point triple a montré des comportements d'ondes de choc différents, en particulier au niveau de la seconde moitié de la seconde surface. En fonction du nombre de Mach de l'onde de choc, différentes configurations de choc sont observées:

- Pour $M_s \leq 2,5$: apparition d'une configuration simple point triple, dite STP (single triple point).

- Pour $M_s = 3,5$: après l'apparition du premier point triple, un second se forme, provoquant une transition des configurations STP vers DTP (transition STP → DTP).

- Pour $M_s = 4,5$: après la formation du premier et du deuxième points triples, les deux configurations se confondent et donnent naissance à nouveau à une configuration STP, conduisant à une transition STP → DTP → STP.

Une analyse plus approfondie concerne l'étude de la vorticité générée par la diffraction des ondes de choc sur des surfaces cylindriques doubles concaves. Il a été démontré que l'intensité des chocs augmente la production de la vorticité. La production de vorticité a été étudiée plus en détail en évaluant l'évolution de l'équation de transport de vorticité instantané. Il a été constaté que l'étirement du tourbillon dû à la compressibilité de l'écoulement joue un rôle important dans la dynamique de la vorticité. Les résultats montrent également que la diffusion de la vorticité dûe aux effets visqueux est assez importante par rapport au terme baroclinique pour les régimes à faibles nombres de Mach, $M_s \leq 2,5$, alors que cette tendance est inversée pour les régimes à nombres de Mach plus élevés, $M_s \geq 3,5$. À la connaissance de l'auteur, ce résultat n'a pas encore été rapporté. En termes d'intensité des chocs, l'effet de la première surface concave s'est avéré efficace pour diminuer suffisamment les impulsions de pression dynamique et statique. En termes de vitesse de choc, la décélération du choc s'est avérée augmenter avec le nombre de Mach de l'onde de choc. Des comparaisons quantitatives entre les résultats numériques pour différentes conditions initiales (intensités des ondes de choc, propriétés des gaz) sont effectuées pour trouver les paramètres physiques affectant la trajectoire et la vitesse du choc incident. Une relation universelle approximative est dérivée, qui prédit la trajectoire et la vitesse de l'onde de choc incidente en fonction du nombre de Mach de l'onde de choc incidente. La relation proposée a été testée dans la gamme Ms ($1,6 \leq M_s \leq 4,5$) et différents gaz, ayant différentes masses moléculaires, rapports thermiques spécifiques et impédances acoustiques, principalement: air, He, Ar, CO_2 et SF_6. En trouvant le temps sans dimension approprié, il était possible de montrer les données de différentes simulations avec différentes conditions initiales se regroupant en une seule courbe.

3.2 Propagation des ondes de choc à l'intérieur d'un canal à cavités cylindriques

Dans une seconde partie, la dynamique des écoulements instationnaires complexes à l'intérieur d'un canal avec des cavités cylindriques de différentes profondeurs et angles de diffraction est étudiée. Au fur et à mesure que le processus de diffraction évolue, les vortex des coins d'extrémité de la paroi se forment avec un enroulement de vortex qui sont convectés quasi-linéairement à l'écart de l'entrée de la cavité. Ces instabilités de coin se caractérisent par la formation d'un vortex primaire qui est suivi d'un vortex secondaire pour les cavités ayant un angle de diffraction $\theta_w \leq 90°$. Les mécanismes clés derrière l'apparition de cette instabilité secondaire proche de la paroi sont la vitesse d'avance suffisamment grande générée par la couche limite de la cavité. On constate que l'interaction de cette instabilité secondaire avec le vortex primaire dans la partie amont de la cavité est l'une des principales sources d'excitations et de transition possible vers la turbulence. Des configurations sans instabilités secondaires étaient également présentes, principalement pour des angles de diffraction supérieurs à 90°, où la vitesse d'advection n'est pas suffisante pour déstabiliser la couche limite de paroi. Les résultats mettent également en évidence l'effet des angles de diffraction sur l'évolution et la trajectoire du vortex principal dans lequel les instabilités secondaires jouent un rôle important. La production totale de vorticité a été quantifiée. L'effet des angles de diffraction sur la production de vorticité est étudié et s'avère négligeable au moins au stade antérieur du processus de diffraction. De plus, la contribution de l'onde de choc à la production de vorticité a été évaluée à l'aide d'un indicateur de choc basé sur le capteur Ducros, et la contribution s'est avérée négligeable (~ 10% de la vorticité total).

En termes d'atténuation des chocs, une meilleure atténuation des chocs est obtenue avec un angle de diffraction de $\theta_w = 90°$, où l'énergie totale de choc est réduite d'environ 38%. L'effet de la hauteur du tunnel sur l'atténuation des chocs pour deux angles de diffraction a été examiné. Une analyse minutieuse des structures d'écoulement a révélé qu'en plus de la variation de la hauteur du canal, la position de ces modifications joue un rôle important dans l'atténuation des chocs. Une disposition subtile de la position/hauteur du canal et de la profondeur de la cavité a été trouvée, conduisant à un facteur d'atténuation significatif d'environ 57% à la sortie du canal.
Pour $\theta_w = 60°$, une disposition arbitraire peut avoir des conséquences dramatiques sur l'amplification de l'onde de choc d'un facteur d'environ 30% en bout du canal, ce qui n'est pas souhaitable du point de vue de la sécurité et de la gestion de la prévention des risques.
En résumé, l'atténuation des ondes de choc dans un canal semi-ouvert avec une cavité à l'intérieur peut être associée aux mécanismes suivants:

- Diffraction des chocs sur la cavité qui se traduit par la formation d'un vortex à l'extrémité de la paroi, conduisant à une grande région dissipative responsable de la diminution de la pression derrière le choc.

- Apparition d'une réflexion de Mach inverse (InMR) due à la réflexion de choc qui se traduit par la formation d'une réflexion régulière transitoire (TRR) sur la cavité qui conduit à la formation des chocs supplémentaires.

- Apparition d'une réflexion de Mach Direct (DiMR) due à la réflexion du choc au coin supérieur droit de la cavité.

- Formation de multiples ondes transversales dues aux réflexions de choc des parois supérieure et inférieure du canal du fait de l'effet de confinement.

1

Introduction

Shock/blast wave propagation involves complex wave interactions with structures and surface boundaries owing to several phenomena such as shock reflection, shock diffraction, shock mitigation/amplification, shock focusing and shock-turbulence interaction. Understanding of these phenomena is crucial for a wide range of engineering applications in bio-medicine, disaster management, detonation, mining, aviation/transport industry and others. Knowledge of such complex dynamics is integral part of the design and optimization of devices for shock-wave lithotripsy, shock/blast-wave attenuation, suppression of tunnel sonic boom, etc.

1.1 Shock-wave reflection

The shock reflection phenomenon dates back to the 19th century. Ernest Mach (1878), who reported his discovery as early as 1878, was the first scientist to notice and record the shock waves reflection phenomenon with his pioneering work, where he discovered the regular and the Mach reflection structures. Intensive research of the shock wave reflection phenomena was re-initiated in the early 1940s by von Neumann (1963). Later, Smith (1945) and White (1951) discovered two new reflection structures, namely complex Mach reflection (CMR), known nowadays as transitional Mach reflection (TMR) and double Mach reflection (DMR). Intending to shed more light on the shock reflection phenomena, a sizable amount of work has been done (Heilig (1969), Ben-Dor & Glass (1979), Ben-Dor (1980), Ben-Dor et al. (1980), Itoh et al. (1981), Gvozdeva et al. (1982), Skews & Kleine (2007), Geva et al. (2013), Shadloo et al. (2014), Soni et al. (2017)).

There are many types of shock wave reflection, the type generated will depend on the flow conditions and the surface inclination. Reflections can broadly be broken down into two different categories: regular reflection (RR) and irregular reflection (IR). The RR wave configuration consists of two shock waves, the incident shock wave, I, and the

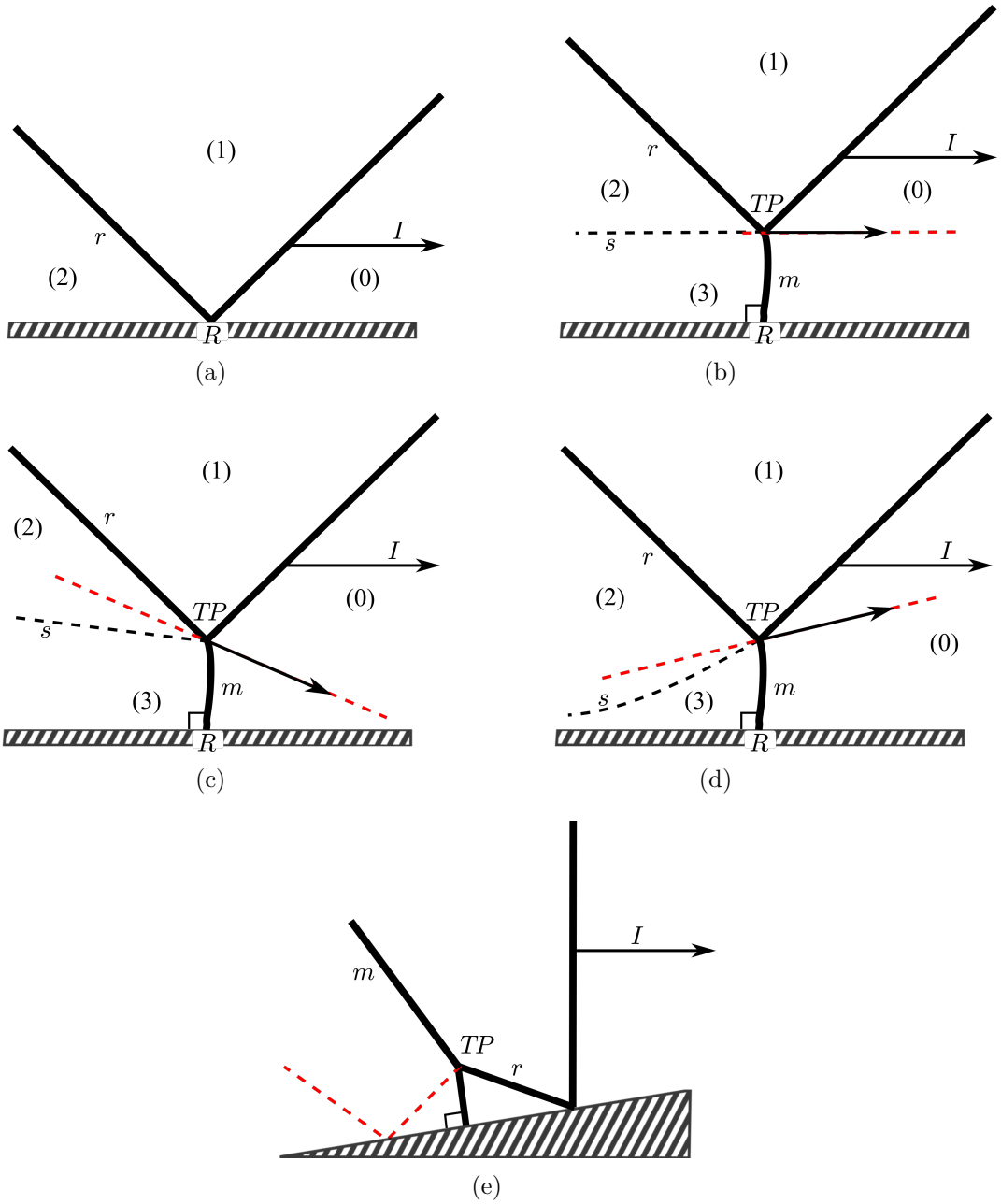

Figure 1.1: Schematic illustration of, (a): a regular reflection, (b): a stationary-Mach reflection, (c): an inverse-Mach reflection, (d): a direct-Mach reflection, (e): a transitioned regular reflection. I: incident shock, r: reflected shock, R: reflection point, m: Mach stem, TP: triple point, s: slipstream

reflected one, r, that meet at the reflection point, R, which is located on the reflecting surface. A schematic illustration of a RR is shown in Figure1.1(a). The IR can be divided, in general, into two categories: von Neumann reflection ,vNR, and Mach reflection, MR. The Mach reflection (MR) consists of three shock waves, the incident shock wave, I, and the reflected shock, r, the Mach stem, m, and the slipstream, s. These four discontinuities meet at a single point known as triple point, TP, which is located above the reflecting surface. Depending on the direction of propagation of the triple point, TP, with respect to the reflecting surface, three different types of MR configurations are possible:

- The MR is stationary, StMR, if the triple point moves parallel to the reflecting surface, schematic illustration of a StMR is shown in Figure1.1(b).

- The MR is inverse, InMR, if the triple point moves towards the reflecting surface, schematic illustration of an InMR is shown in Figure1.1(c).

- The MR is direct, DiMR, if the triple point moves away from the reflecting surface, schematic illustration of a DiMR is shown in Figure1.1(d).

Since the InMR is a MR in which the triple point moves towards the reflecting surface, it terminates as soon as its triple point collides with the reflecting surface. The termination of the InMR leads to the formation of a new wave configuration. This configuration consists of a RR followed by a MR. A schematic illustration of this wave configuration is shown in Figure1.1(e). Since this configuration is formed following a transition from an InMR, and since its main structure is a RR, it is called transitioned regular reflection, TRR.

The 13 possible shock wave reflection configurations are presented in the Ben-Dor diagram in Figure 1.2, with: IR: irregular reflection; RR: regular reflection; vNR/VR/GR: von Neumann, Vasilev, Guderley reflections, respectively; MR: Mach reflection; StMR: stationary-Mach reflection; InMR: Inverse-Mach reflection; InMR: Inverse-Mach reflection; TRR: transitioned regular reflection; DiMR: direct-Mach reflection; SMR: single-Mach reflection; DMR: double-Mach reflection; PTMR: pseudo-transitional-Mach reflection; TMR: transitional-Mach reflection; DMR^{+}; positive double-Mach reflection; DMR^{-}: negative double-Mach reflection; TerDMR: terminal double-Mach reflection.

The transition from regular to non-regular reflection has been studied by many authors. Von Neumann theoretically became interested in this subject as early as 1943 (von Neumann 1943*a*,*b*). In their review, Bazhenova et al. (1984) considered transitions between one type of reflection and another. They proposed three types of transitions namely, transition from single to complex Mach reflection, transition from complex Mach reflection to double Mach reflection and transition from regular to Mach reflection for weak

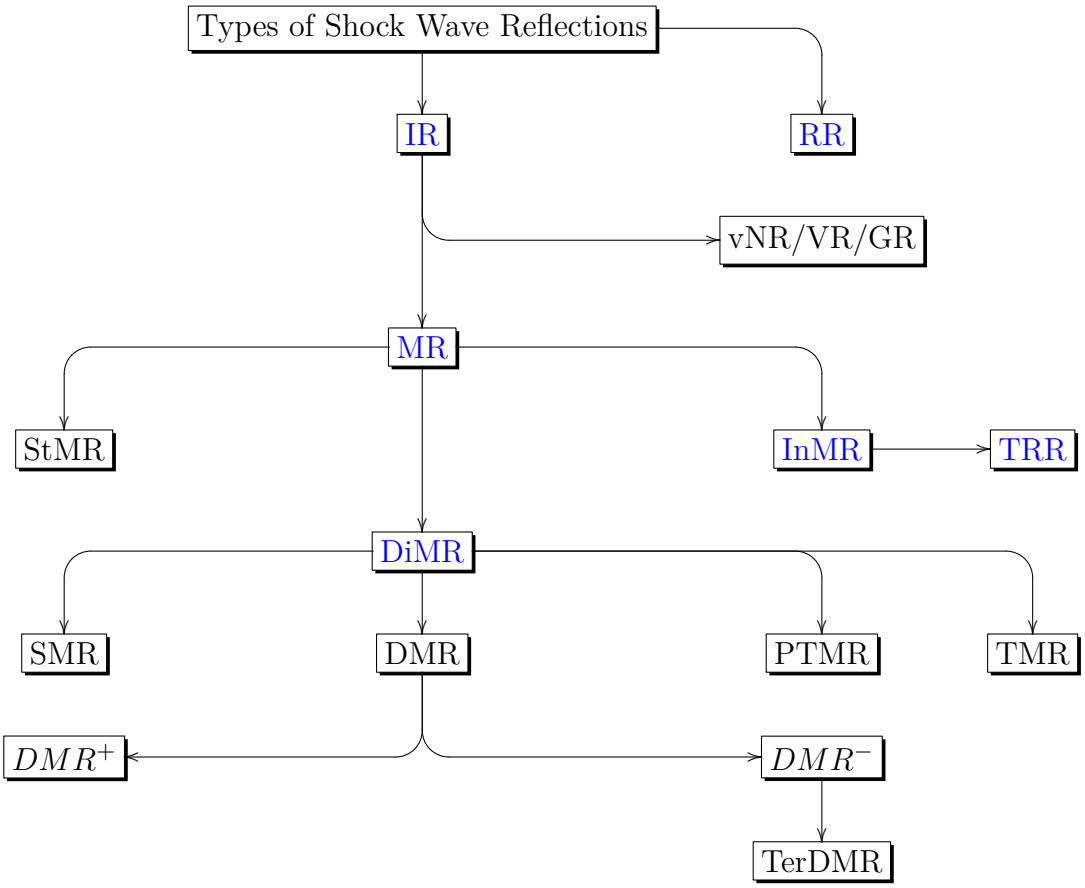

Figure 1.2: Diagram of the 13 possible shock reflections, Ben-Dor (2007)

and strong shock waves. Ben-dor used shock polars to explain the various proposed RR $\rightleftharpoons$ IR transition criteria, namely, detachment criterion, mechanical-equilibrium criterion, sonic criterion and length-scale criterion. It should be noted here that von Neumann initiated most of these criteria already in the early 1940s Ben-Dor (2007). In a recent study, Soni et al. (2017) investigated the shock-wave reflections over double-concave cylindrical surfaces. In this study, for the first time, a single-TP→double-TP→single-TP→double-TP transition has been observed on the same reflector. Moreover, for the same wedge reflector, the flow features exhibit strong differences in shock-wave reflection patterns over the first and the second reflectors. In addition, contrary to past studies where SMR→TMR→DMR transition process has been observed, an SMR→DMR→TMR transition process is observed in their study for the first time.

1.2 Shock-wave diffraction

A common phenomenon that is encountered by a shock wave is diffraction process. This occurs when a shock wave traverse over a convex curved wall. The shape, strength and

the orientation of the planar shock change with time as a result of the disturbances propagated by a change in wall geometry. Diffraction of planar shock waves has been treated analytically by Whitham (1957), Whitham (1959) in the method now famously known as Geometrical Shock Dynamics (GSD). This method was compared to experimental shock wave profiles by Skews (1967*b*), who found that the theory under predicted weak shock wave propagation and over predicted that of strong shock waves. The Mach number of diffracting weak shock waves were predicted to quickly vanish to $M_s = 1$ whereas, in reality, this takes significantly longer to occur. As the shape of a diffracted shock wave is interesting in its own right, several researches have been conducted to complete Witham's work, Rosciszewski (1960), Oshima et al. (1965*a*). etc. This point is discussed in Section 1.6.

The diffraction of a normal shock wave motivates the compression of the gas particles adjacent to the shock. This compression process is unsteady with region of flow perturbation behind the diffracted shock. Within this region the flow separates from the wall surface due to the presence of adverse pressure gradient. Shear layer evolved from the separating region with other flow features. Understanding of the complex flow features behind a diffracted shock wave plays a very important role in the design of supersonic flow devices such as blast wave attenuator, exhaust nozzles of an internal combustion engine, gas transmission line, supersonic jet engines, selection of optimum profile for missiles, etc.

The shock diffraction over sharp geometries had significant interest by researchers. An overview of unsteady shock wave interactions is given in the excellent review by Bazhenova et al. (1984). This review covers shock wave interactions with concave and convex corners as well as with curved surfaces, shock wave diffraction at a curved convex surface and wave systems arising from shock diffraction at a convex corner. Modifications to Whitham's theory for the calculation of the shape of diffracting waves are also proposed. The pioneering work on the perturbed region behind a diffracting shock wave over sharp geometries was conducted by Skews (1967*a*), in which he showed experimentally the flow features present behind a diffracting shock wave. In this work he showed how complex flow features varied with differing corner angle and Mach number. The research highlighted that past a critical corner angle of $\theta > 75°$, the flow features are largely independent of corner angle for a given incident shock speed. Past this value of $\theta > 75°$ the flow becomes dependent only on incident shock Mach number. Many researchers have investigated the flow generated by a shock wave diffracting around a 90° corner. Notable experimental works were carried out by Skews (Skews (1967*b*), Skews (1967*a*), Skews et al. (2012)), Bazhenova et al. (1973), Sun & Takayama (1997).

Baird & Stollery (1987) visualized vortices emitted from the exit of a circular cross

sectional shock tube and found that the resulting vortex ring moved at nearly constant speed. Broadbent & Moore (1987), testing a similar flow, showed that the jet driving the vortex ring was subjected to an adverse pressure gradient. Brouillette et al. (1995) further determined the threshold of the secondary shock wave formation behind a shock wave moving out of a circular cross-section shock tube. The threshold value of incident shock strength was $M_s = 1.34$ in air. Hillier produced his well-known numerical work on shock wave diffraction around a sharp corner Hillier (1991). In this work he discussed the applicability of an Euler simulation to shock diffraction around a 90° sharp corner. He states that sharp-edged separation (i.e. separation from sharp edge where attached flow would create completely non-physical gradients in the flow) can be captured and resolved well by the Euler equations. To the author's knowledge, Hillier's work was the first to show what has now become known as the vortex shock. Sun & Takayama (1997) showed very similar wave structures to Hillier. In their study they were interested to the formation of a secondary shock wave behind the shock wave diffracting at convex corner. As in Brouillette et al. (1995), the threshold incident-shock-wave Mach number at which a secondary shock wave appears is found to be $M_s = 1.32$ at an 81° corner and $M_s = 1.33$ at a 120° corner. According to them, these secondary shock waves are formed because of the existence of a locally supersonic flow behind the diffracting shock wave. Behind the diffracting shock wave, the subsonic flow is accelerated and eventually becomes locally supersonic. A simple unsteady flow analysis revealed that for gases with specific heats ratio $\gamma = 1.4$ the threshold shock-wave Mach number was $M_s = 1.346$. Kleine et al. (2016) investigated the flow field behind a diffracting shock for a small shock Mach number range of $1.33 < M_s < 1.37$. In this study they concluded that there are, indeed, embedded local supersonic areas in the flow field where the fluid returns to a subsonic flow without being decelerated by a shock wave, hence going through an isentropic supersonic-to-subsonic transition. Good agreement is found when comparing the threshold for these processes with the analytical prediction made by Sun & Takayama (1997). Their results confirmed that for $M_s = 1.33$ the flow is on the verge of establishing these supersonic pockets while for $M_s = 1.37$ the local flow Mach number can be as high as 1.06, without any optical evidence for a shock wave. The results are therefore interpreted as illustrating the theoretically possible but rarely observed isentropic deceleration of a supersonic flow to subsonic levels. In a recent numerical study, Chaudhuri & Jacobs (2017) analyzed shock wave diffraction over a convex sharp splitter geometry. Their Simulations capture the essential wave diffraction, transverse wave interaction with the deforming and growing primary vortex, and weaker secondary vortices arising from the Kelvin-Helmholtz instability. The analysis reveals the mechanism of unwinding of vortices and its link with the divergence of the Lamb vector. In the same study, the authors revisited the shock

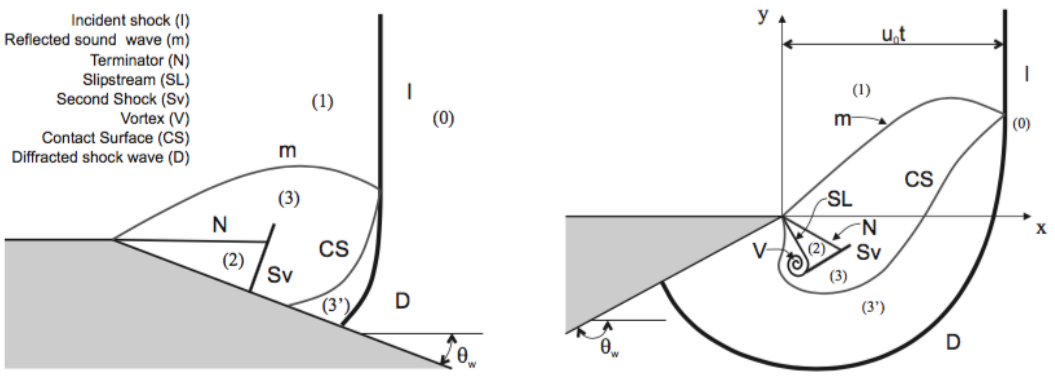

Figure 1.3: Features of shock diffraction pattern over a corner: (a) small angles and (b) large angles. From Skews (1967*a*).

diffraction over 90° convex corner and addressed some intricate features of resolving the viscous and turbulent flow features. The main issues related to the 2D numerical predictions of this flow dynamics are to address the experimentally observed (i) secondary viscous vortex associated with the wall shock interaction with the boundary layer and (ii) the shear layer behavior, so, they suggested that 3D DNS or LES study is required to substantiate the existence of smaller scales and shear layer instabilities. Accordingly Soni et al. (2019) have conducted a very powerful and interesting 3D large eddy simulation (LES) of the turbulent structures and long-time flow dynamics of shock diffraction over 90° convex corner. The study, performed with 3.3×10^9 mesh points, captures the 3D turbulent scales, embedded shocks/shocklets within the main vortex and the shear layer behavior and boundary layer interactions in the viscous vortex region. The spatio-temporal growth of the shear layer is strongly influenced by the lambda shock as well as by the counterclockwise rotating viscous vortex near the diffraction corner. It was also shown that the lambda-shock- shear-layer interaction at the upper side of the shear layer is more intense than that of the interaction of the contact surface at the bottom side of the shear layer. It was also noted that the foot of the lambda shock more effectively perturbs the shear layer and increases its growth. This aspect is clearly resolved in their LES study. The shape and large-scale structures of the turbulent envelop at the wall viscous vortex region is also satisfactorily predicted by the LES.

Figure 1.3(a) represents the shock diffraction pattern for a convex corner for angles (θ_w) lower than 45°. The shock diffraction takes place by a series of expansion waves N. The flow turns parallel to the wall. Therefore, the slipstream and vortex are almost absent up to angles of 45°. The increase of the Mach number leads to the formation of a secondary shock, Sv. This is due to the difference between the accelerated flow in the expansion wave and the flow behind the diffracted shock, D. When the convex corner is

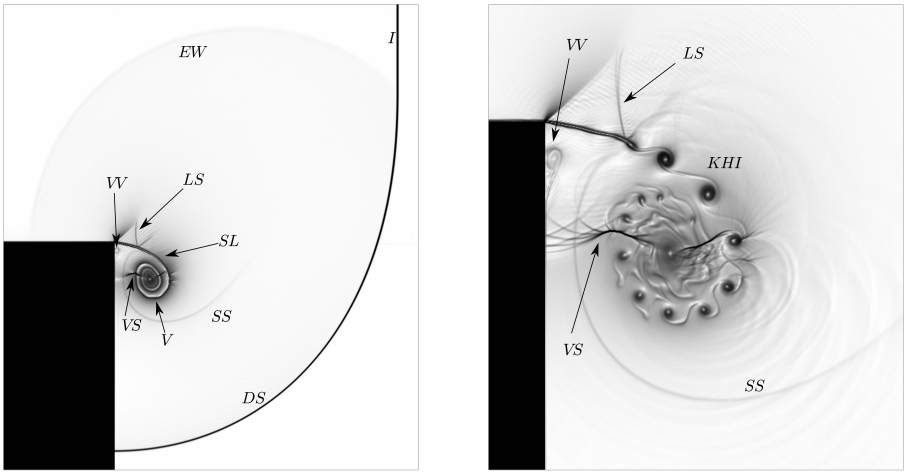

(a) (b)

Figure 1.4: 2D shock diffraction over 90° corner: numerical schlieren images at (a) $t = 48$ μs and (b) $t = 104$ μs using $M_s = 1.5$, I: incident shock wave, EW: expansion wave, VV: viscous-vortex, LS: lambda-shock, SL: shear layer, VS: vortex shocks, V: vortex, SS: slipstream, DS: diffracted shock, KHI: Kelvin-Helmholtz instability. By Soni et al. (2017).

greater than 45°, Figure 1.3(b), the flow behind the diffracted shock wave turns through a smaller angle than that of the convex wall which leads to the appearance of a slipstream. The slipstream, SL, separates the region of expanding flow from the region almost at rest. The vortex, V, is produced by the roll-up of the slipstream Skews (1967*a*). The position of the slipstream, tail of the Prandtl-Meyer fan, N, and the velocities of the contact surface and the second shock are almost independent of corner angle for angles greater than 75°. The shape of the diffracted shock curve, D, is not a single curve. The diffracted shock portion attached to the wall is perpendicular to it and tangential to the tangent to the diffracted shock wave. This portion of the diffracted shock is referred to as the wall shock. Independent of the corner angle, the diffracted shock wave forms an envelope around the flow. However, the wall shock is not part of this envelope.

An example of shock diffraction around a 90° corner is shown in Figure 1.4. As the shock propagates along the wall, it encounters a sudden expansion which causes the flow to separate at the corner. This leads to complex flow features. Some of these flow structures are highlighted in Figures 1.4(a), 1.4(b), where a slipstream, SS, is emanating from the junction of the incident shock, I, the diffracted shock, DS, and the expansion wave, EW. The flow separation leads to the generation of a highly sheared layer, SL, which rolls up to form a large vortex, V. The latter consists of a pair of vortex shocks, VS, and the flow above the shear layer becomes supersonic, allowing a lambda-shock, LS, system to form. As a result of the inviscid-viscous interaction, the viscous-vortex, VV, is also observed at the corner beneath, SL, Soni et al. (2017). In contrast to the findings

of Tseng & Yang (2006), as the flow evolves, the SL becomes unstable and breaks down into small vortices that are mainly driven by the Kelvin-Helmholtz instability, KHI, as found by Skews et al. (2012).

1.2.1 Vorticity generation in shock-wave diffraction

The formation and the evolution of the vortex rings produced by a shock diffraction are also one of the phenomena that has been studied in the past Howard & Matthews (1956), Skews (1967*a*), Gnani et al. (2014). Sun & Takayama (2003*a*) used Euler and Navier-Stokes solvers to investigate the secondary vortex generation in shock diffraction. Both solvers detected the small vortices formed along the slip-stream. Although the past studies provided qualitative descriptions of the flow structures in the shock diffraction and vortices generation, no quantitative measurement of the vorticity production has been performed. Consequently, Sun & Takayama (2003*b*) numerically quantified, using an Euler solver, the vorticity production in shock diffraction over convex corner. Their results indicated that, for a given gas, the vorticity production is dependent only on the incident-shock Mach number and the diffracting angle. Their data also showed that the slipstream represents a large amount of the total vorticity and it can be the more dominating factor in producing vorticity in compressible flows than baroclinic effects. Moreover, Sun and Takayama used only an Euler simulation in their study, Tseng & Yang (2006) used both the Euler and the laminar Navier-Stokes solvers to investigate the vorticity production and the subsequent reflected shock/main-vortex-core interaction during the shock-wave diffraction. Different circulation production rates are observed between the Euler and Navier-Stokes solutions as a result of the boundary layer and the secondary vortex contribution in vorticity production. It was found that the shock reflection influences the rate of vorticity production that depends on the incident shock strength and the diffracting angle. Abate & Shyy (2002) studied the dynamics of shock diffraction using the vorticity transport equation. They discussed the link between high strain rates resulting from the expansion corner to the solenoidal dissipation rates and the stress rates to the dilatational dissipation rates of turbulent kinetic energies. The baroclinic torque enhances the vorticity generation in such interactions. The viscous effects and small-scale turbulent dissipations are important for longtime evolution of a primary vortex and smaller vortices generated from the Kelvin-Helmholtz instability and their interactions with shocks and shocklets. Reeves & Skews (2012) have investigated both numerically and experimentally the unsteady aspects of three-dimensional shock-wave diffraction phenomena. They found that the trends of circulation production correlated quite well with those obtained from the two-dimensional diffraction case. Furthermore, they showed that the rate of vorticity production tends to be constant once the incident shock wave had

fully diffracted over the surface edge. Recently, Chaudhuri & Jacobs (2017) performed a numerical study with a new detailed analysis of shock-wave diffraction over a sharp splitter plate. The shock dynamics and the evolution of the flow topology were studied using the probability density functions of various parameters in addition to the enstrophy transport equation and the invariants of the velocity gradient tensor. Their analysis reveals the mechanism of unwinding of vortices and its link with the divergence of the Lamb vector. Soni et al. (2019) numerically investigated the turbulent structures of shock diffraction over 90° convex corner. The analysis of the budget terms of the mean vorticity transport equation reveals that the stretching of vorticity due to compressibility and stretching of vorticity due to velocity gradients play an important role compared to diffusion of vorticity due to viscosity as well as the baroclinic term. In a recent study, Zhu et al. (2020) analyzed the SF_6 bubble evolution in shock-accelerated flow with a transverse density gradient. Their analysis showed that impingement by incident and reflected shocks induces additional vorticity in the bubble region and promote increased bubble volumes. The increased bubble volumes could weaken the average vorticity. Upon increasing the incident shock Mach number, the vorticity was strengthened. They further analyzed the vorticity kinetics equation of the two-dimensional compressible fluid. This analysis reveals that the absolute value of each transport term increases when the incident shock intensity is enhanced. They showed that the influence of the viscosity term on the vorticity evolution is nearly negligible. Conversely, the compression term has a greater influence on vorticity evolution in the SF6 bubble region than the baroclinic term.

1.2.1.1 Vortex strength in shock-wave diffraction

The strength of a vortex, in a domain S enclosed by contour L, can be represented by circulation, Γ, which is the summation of vorticity ω in the domain,

$$\Gamma = \int_s \omega \, ds = \int_L u \, dl \tag{1.1}$$

The integral contour or path, L, is taken along the boundary that exactly encloses the perturbed region behind a diffracting shock wave. In a practical evaluation, the integral is calculated along the boundary of the whole computational domain to avoid the ambiguity in determining the perturbed region in the numerical results. Since unperturbed flow regions are uniform, their contribution to the integral is zero only if the inlet is parallel to the incident shock front and there is no wave reflection from outside boundaries. A better quantity to characterize the vorticity production in shock production is the ratio of circulation to time, Γ/t, which is referred to as the rate of circulation production. The rate of circulation production is related to the incident shock-Mach number M_s, the

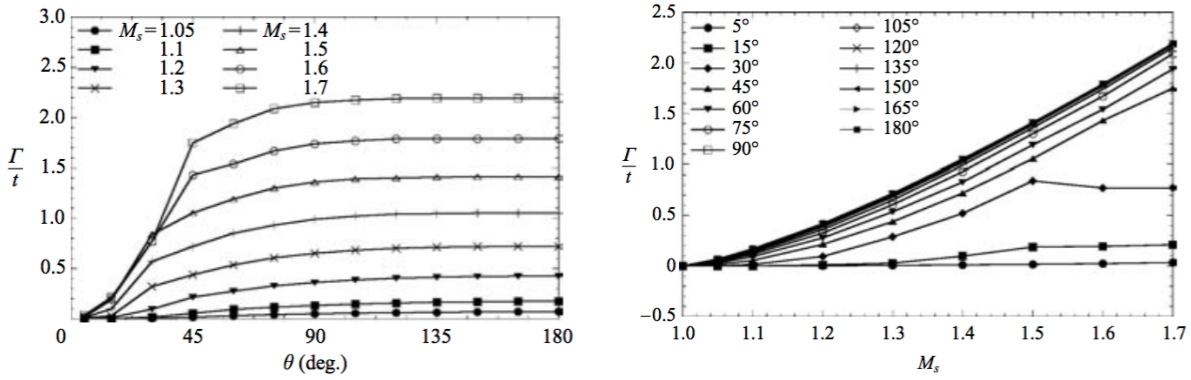

(a) (b)

Figure 1.5: (a): Effect of wall angle on the rate of circulation production, (b): Effect of incident shock strength on the rate of circulation production. By Sun & Takayama (2003*b*).

diffraction angle and the gas properties. For a given gas, the ratio Γ/t can be uniquely determined as a function of shock wave strength and wall angle as:

$$\frac{\Gamma}{t} = f(M_s, \theta) \tag{1.2}$$

where θ is the wall angle. Sun & Takayama (2003*b*) investigated the effect of both shock wave strength and wall angle on the rate of circulation production. The obtained results are shown in Figure1.5. Note that all the data of circulation production presented by Sun and Takayama are dimensionless values. Since the rate has the dimension of the square of the velocity, one may obtain dimensional data by multiplying the dimensionless value with the square of the characteristic velocity,

$$\frac{\Gamma'}{t'} = \mathcal{R} \times T_0 \frac{\Gamma}{t} \tag{1.3}$$

where $\mathcal{R}$ is the universal gas constant divided by the molecular weight of air, and T_0 is the temperature in front of the incident shock.

1.2.1.2 The effect of wall angle on vorticity generation

It is seen from Figure1.5(a) that the rate of vorticity shedding always increases with the wall angle for a given shock Mach number. The vorticity production increases sharply near a wall angle of 30°. For instance, the vorticity increases by approximately four times when the wall angle changes from 15° to 45° for $M_s = 1.5$. However, for wall angles over 90°, the vorticity production hardly changes, and all curves tend to approach their corresponding constant values. Sun & Takayama (2003*b*).

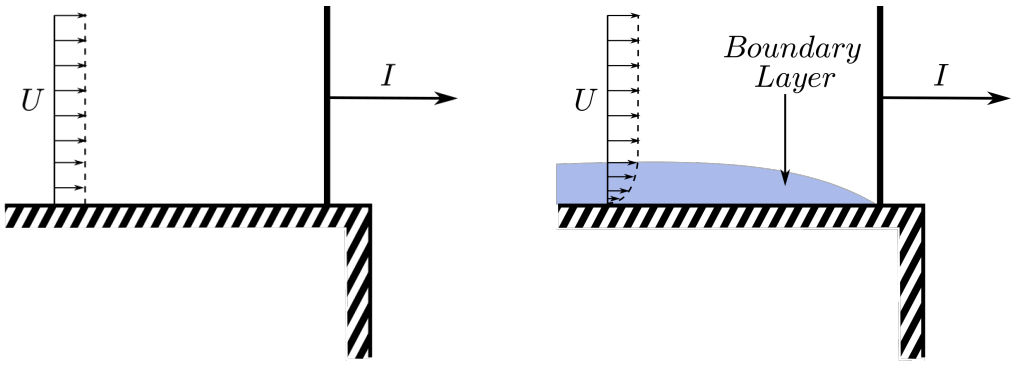

(a) Ideal case (b) Real case

Figure 1.6: Schematic representation of a shock propagation, (a): Ideal case (without boundary layer), (b): Real case (with boundary layer).

1.2.1.3 The effect of incident shock strength on vorticity generation

The effect of shock strength on the rate of vorticity production is investigated by changing incident shock Mach number M_s. The results are presented in Figure1.5(b), the rate basically increases with shock strength, and it increases much faster for wall angles greater than 45°. For wall angles over 90°, the vorticity production hardly changes, and all curves tend to approach their corresponding constant values. Sun & Takayama (2003*b*).

1.2.1.4 The effect of the boundary layer on vorticity generation

Tseng & Yang (2006) compared the circulation production results predicted by the Euler solver with those obtained from the Navier-Stokes solver for the case of incident shocks with Mach numbers of $M_s = 1.5$ and 2.5 diffracting around a 90° convex corner. The results are shown in Figure 1.7. In the Navier-Stokes solutions, the rate of circulation production increases linearly as a result of the boundary layer that developed before the arrival of the incident shock wave at the corner (as shown in Figure 1.6). The boundary layer that developed at the solid wall and the secondary vortex originating at the diffraction corner cause the circulation production predicted by the Navier-Stokes solver to be greater than that obtained using the Euler solver. Tseng & Yang (2006).

1.3 Shock-wave propagation and diffraction over cavities

The interaction of shock waves with complex rigid boundaries has been the subject of many investigations during the past decades. The shock-wave interaction with cavities is truly non-stationary and possesses no similarity throughout its duration. Such in-

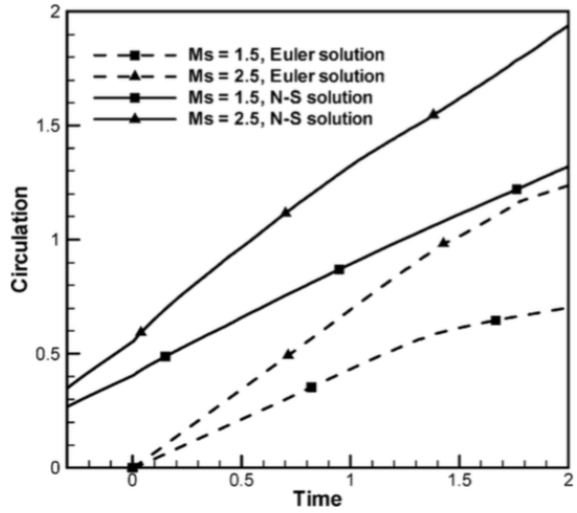

Figure 1.7: Comparison of circulation production results obtained using Euler and Navier-Stokes solvers for $M_s = 1.5$ and 2.5 and $\theta = 90°$. By Tseng & Yang (2006).

teractions involve all of the phenomena cited above, diffraction, reflection, etc. Several attempts were made to study such flows, for example Gvozdeva et al. (1988) and Bazhenova et al. (1990). In these investigations the flow field was studied experimentally, using interferometric flow visualization technique. In addition, an attempt was made to predict the post-shock flow pressure using the two-dimensional Whitham approximation. Igra et al. (1996) studied experimentally and numerically the interaction of a planar shock wave with a square cavity. They showed that the flow which started as a self-similar one turned quickly into a really time-dependent flow in which no self-similarity existed. According to them the flow developed inside and around the cavity depended on the strength of the incident shock wave. In air, for $M_s < 2$ the post shock flow is subsonic and the flow expansion into the cavity is via a vortex. For $M_s > 2$ the post-shock flow is supersonic and the flow expansion into the cavity is through a centered expansion wave. The interactions between the various waves reflected from the cavity walls, and between them and the vortex or the centered expansion wave, produced a complex unsteady flow in which no self-similar structure could be observed. Heilig (1975) conducted experimental investigations of shock wave propagation in a rectangular, two-dimensional branched duct as well as in a configuration where the process was three-dimensional as the branched duct had a circular cross section. Results from the 2D case appear in Igra et al. (1998) and simulations of the 3D case appear in Igra & Igra (2012). In Igra et al. (1998) only shadowgraph pictures were taken showing the wave pattern inside the branched duct, and in Igra & Igra (2012) only static pressures were recorded at various locations along the branched pipe walls, but no pressure records were made at the end wall of the branched segment. Wang et al. (2001) studied the interaction between a planar shock wave and

a square cavity filled with dusty gas, the loading ratios were taken equal to 1 and 5, and particle diameters were taken equal to 1, 10 and 50 μm. The results show that the diffraction patterns in the cavity were decisively attenuated by the dust suspension, particularly for the higher loading ratio. The particle size has a pronounced effect on the flow and wave pattern developed inside the cavity. They found that the presence of solid particles inside the cavity brings about significant changes in the cavity flow relative to a similar pure gas case. The speed of diffracted and reflected shock waves decreases as the dust mass loading ratio increases, or the dust particle diameter decreases. However, no observable changes are found for the flow above the cavity, and the passing shock wave is almost unaffected by the mass loading ratio of the gas-particle suspension inside the cavity. In the same context Igra & Igra (2016*a*) investigated numerically the case when an incident shock wave propagates in a duct with a square cavity filled with different gases mainly, helium, argon, air, or SF_6, whereas the rest of the duct contained only air. Their study reveals that although the presence of different gases inside the cavity has significant effect on the flow-field evolved inside the cavity, it has negligible effect on the prevailing pressure downstream of the cavity. Biamino et al. (2014) conducted an experimental and numerical investigation examining the option of using branched duct geometry for shock wave attenuation. The study reveals that the length of the branched duct has a strong influence on the resulting flow. In a short branched segment, strong pressure fluctuations are unavoidable. For longer pipes, a well-established shock wave propagates downstream leaving behind it a fairly uniform high pressure zone.

An example of shock wave, at $M_s = 1.3$, interaction with a square cavity, presented by Igra et al. (1996), is shown in Figure1.8. The sequence of Figures 1.8(a) to 1.8(h) shows the evolution of the various waves which resulted from the interaction of the incident shock wave S_1, with the square cavity. The first stage of the interaction process is shown in Figure 1.8(a) where the incident shock wave S_1, starts diffracting over the cavity upper-left corner, forming a vortex behind it. With advancing in time, S_1 propagates toward the cavity exit and its bottom, while the vortex grows in size and remains close to the cavity upper-left corner as shown in Figure 1.8(b). In Figure 1.8(c), the incident shock wave, S_1, hits the cavity upper-right corner and splits into a transmitted, S_1, and a reflected, Sr_1, shock waves. The vortex grows in size and its centre slowly moves away from the cavity upper-left corner. In Figure1.8(d) the descending part of S_1 has reached the cavity bottom and is reflected upward as Sr_2. S_1' is the part of S_1 which is still moving toward the cavity lower-right corner. The reflected shock wave Sr_1 is also visible. As time progresses, S_1', approaches the cavity lower-right corner and therefore its size decreases while Sr_2 and Sr_1 become larger and weaker (the stronger the shock wave is, the darker it appears in the photograph). Figure 1.8(e) shows an exceptional situation.

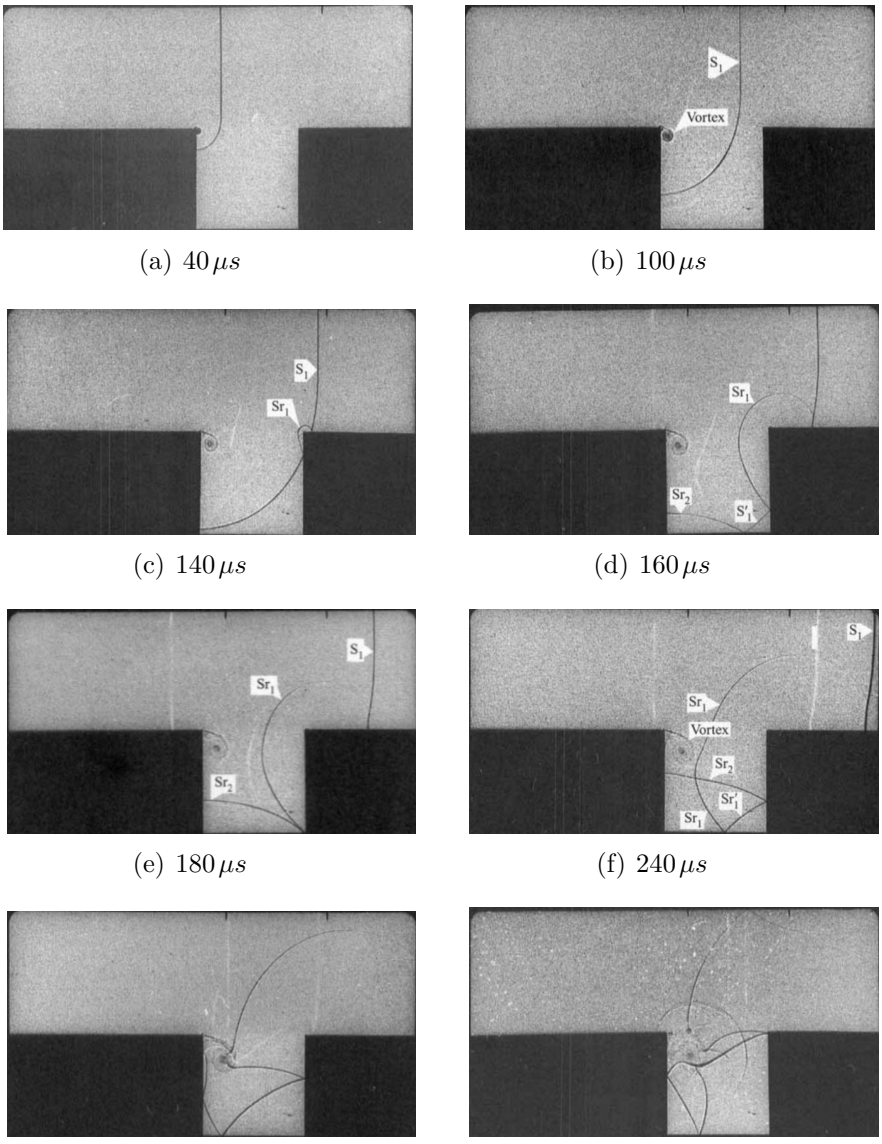

(a) $40\,\mu s$ (b) $100\,\mu s$

(c) $140\,\mu s$ (d) $160\,\mu s$

(e) $180\,\mu s$ (f) $240\,\mu s$

(g) $280\,\mu s$ (h) $340\,\mu s$

Figure 1.8: Wave pattern during the interaction of a planar shock wave of $M_s = 1.3$ with a square cavity. By Igra et al. (1996).

This shadowgraph was taken at the exact moment when S_1' hits the cavity lower-right corner, displaying a meeting between Sr_1 and Sr_2 at this corner. Sr_1 grows in size and its upper part, that starting from S_1 immediately behind the end of the Mach stem, gets still weaker. The vortex is growing up and continues its movement away from the cavity upper-left corner. At $t = 240$ μs, Figure 1.8(f), three shock waves are present within the cavity and their continued interactions with each other, with the cavity walls and with the vortex, are exhibited in the following shadowgraphs. Such multiple interactions lead to many reflections and distortions of the participating waves. The beginning of the complex collision/reflection process which takes place inside the cavity is shown in Figure 1.8(g). As the process evolves, the flow and wave configuration inside the cavity become more and more complex as can be seen from the shadowgraph shown in Figure 1.8(h), a large amount of shock waves of various strengths is shown. The wave pattern is a result of multiple interactions among the waves and between the waves and the cavity walls, and also between waves and the vortex. Igra et al. (1996). The expanding flow evolves into a complicated system of distorted and splitted shocks with separated regions and vortices formation.

Note that the wave pattern and the flow behavior in such interactions depend on numerous parameters mainly; the incident shock wave Mach number, the diffraction angle and the shape of the cavity. Igra et al. (1996) observed a different wave pattern and flow behavior when the incident shock wave Mach number is raised to a level that results in a supersonic flow behind it, in their case they used $M_s = 2.032$. Since the post-shock flow is sonic, instead of a vortex near the cavity upper-left corner (which characterized the flow expansion for $M_s = 1.3$), they observed an expansion wave centered at the corner. They also noticed the generation of a secondary, upstream-facing, shock wave. This secondary shock wave is generated in order to match between the high-pressure zone which exists behind the incident shock wave and the low pressure behind the expansion wave centered at the cavity upper left corner.

1.4 Shock-wave mitigation

Research on shock wave mitigation is closely related to the development of effective protection and disaster control, and it is motivated by the catastrophic damage that may be caused by shock waves. Overall, the approaches to attenuate a shock wave can be divided into three categories, in terms of mechanism, which are attenuating the shock wave by i) breaking the incident shock wave into multiple shocks with different arrival times, ii) dissipating energy through viscosity, and iii) transferring kinetic energy of the shock-induced flow to the potential energy of a solid or a liquid barrier.

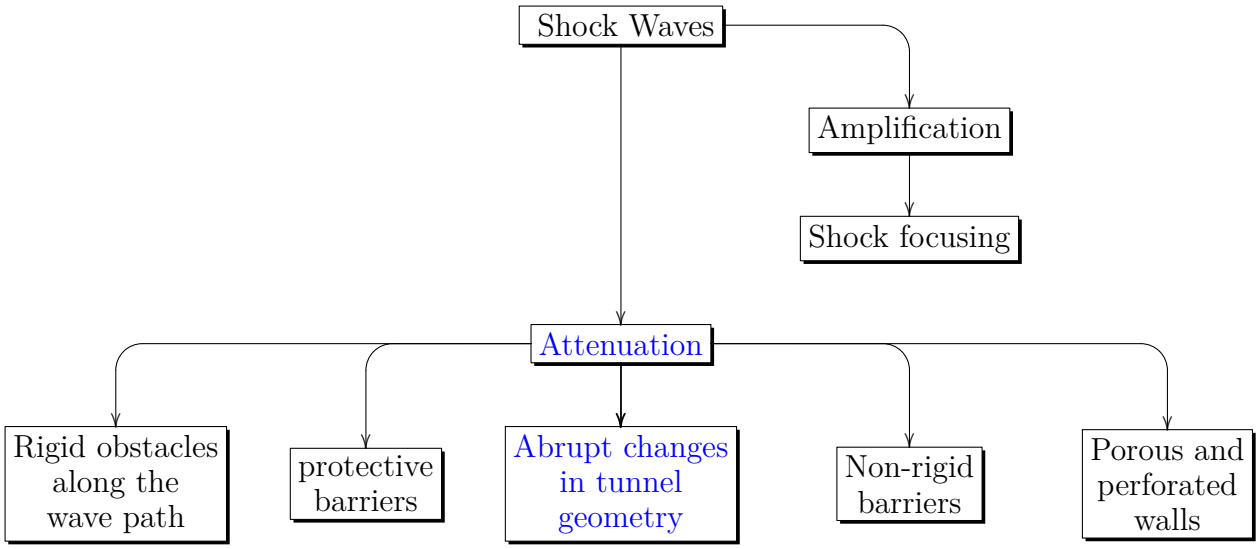

Figure 1.9: Diagram of the shock-wave mitigation and amplification.

The literature shows various approaches to attenuate shock-waves, e.g., foams, porous materials, granular filters, metallic grids, perforated plates/walls, rigid barriers, branched/bend duct, duct with rough walls, etc. Some of the most used methods to attenuate shock waves are shown in Figure 1.9, these methods are summarized in Table 1.1 with illustrations and some references.

Shock attenuation methods	References	Illustrations
Abrupt changes in tunnel geometry	- Igra et al. (2001) - Chaudhuri (2019) - Marty et al. (2019) - Kim et al. (2004) - Igra & Igra (2016*a*) - Chester (1953) - Chisnell (1955) - Whitham (1958) - Igra et al. (2001) - Nettleton (1973) - Igra et al. (1998)	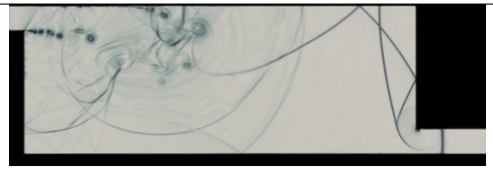 Figure 1.10: Numerical schlieren pictures, Chaudhuri (2019). 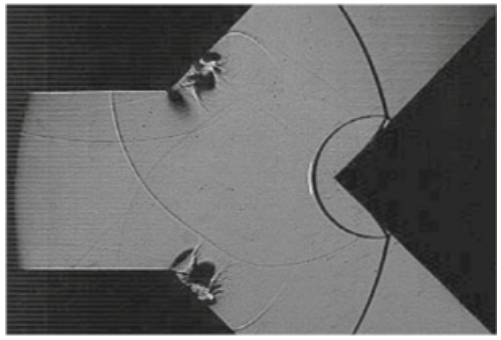 Figure 1.11: Schlieren photographs, Marty et al. (2019). 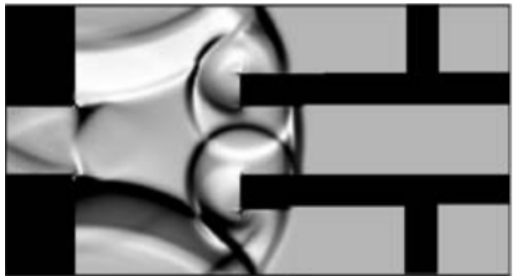 Figure 1.12: Numerical schlieren pictures, Kim et al. (2004). 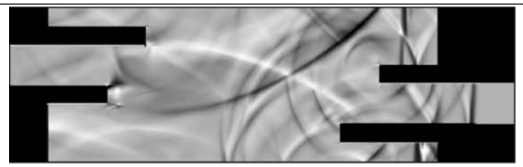 Figure 1.13: Numerical schlieren pictures, Kim et al. (2004). 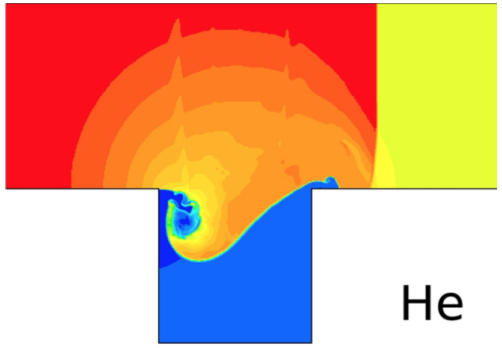 Figure 1.14: Density variation in cavity filled with Helium, He, Igra & Igra (2016*a*). 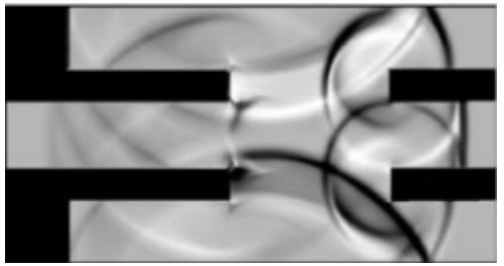 Figure 1.15: Numerical schlieren pictures, Kim et al. (2004).

<table>
<tr><th>Shock attenuation methods</th><th>References</th><th>Illustrations</th></tr>
<tr><td>Rigid obstacles along the wave path</td><td>- Wan & Eliasson (2015)
- Berger et al. (2010)
- Igra & Igra (2016b)
- Chaudhuri et al. (2013)
- Skews et al. (1998)
- Chaudhuri et al. (2012)
- Dosanjh (1956)</td><td> 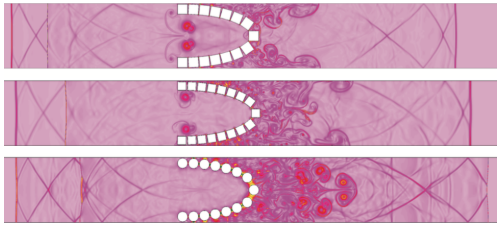
Figure 1.16: Numerical schlieren pictures, Wan & Eliasson (2015).
 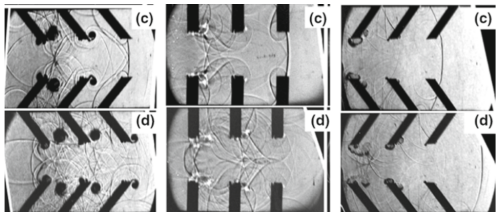

Figure 1.17: Schlieren photographs, Berger et al. (2010).
 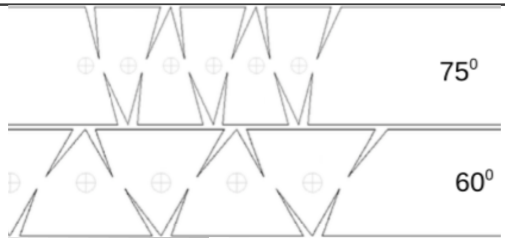

Figure 1.18: Geometry of barriers used in Igra & Igra (2016b).
 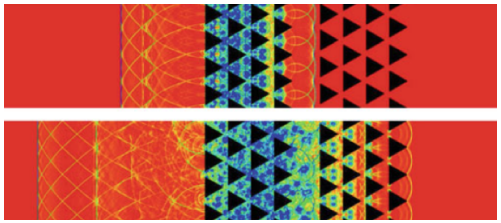
Figure 1.19: Numerical schlieren pictures, Chaudhuri et al. (2013).</td></tr>
<tr><td>Non-rigid barriers</td><td>- Wan et al. (2019)
- Hadjadj & Sadot (2013)
- Chauvin et al. (2011)
- Jourdan et al. (2010)
- Yasuhara et al. (2006)
- Igra & Takayama (2003)</td><td> 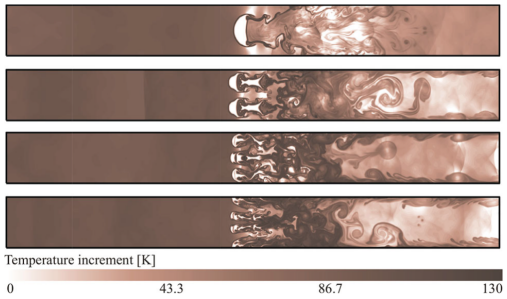

Figure 1.20: Interaction of blast wave with water cylinders, Wan et al. (2019).
 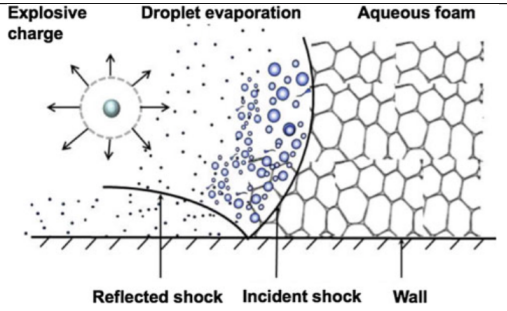

Figure 1.21: Shock/aqueous foam interaction, Hadjadj & Sadot (2013).</td></tr>
</table>

Shock attenuation methods	References	Illustrations
Porous and perforated walls	- Mortazawy et al. (2019) - Gongora-Orozco et al. (2009) - Gongora-Orozco (2010) - Skews (2005) - Szwumoski (1971) - Takayama et al. (1995) - Sasoh et al. (1994) - Igra et al. (2001) - Sasoh et al. (1998) - Abe et al. (2003) - Jiang et al. (2014)	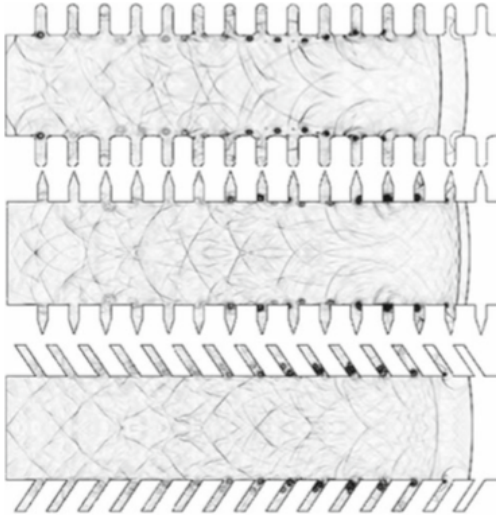 Figure 1.22: Numerical schlieren pictures, Mortazawy et al. (2019). 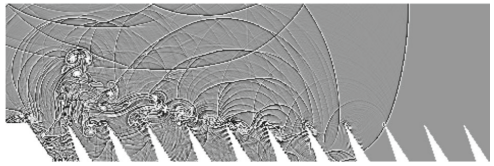 Figure 1.23: Numerical shadowgrams, Jiang et al. (2014). 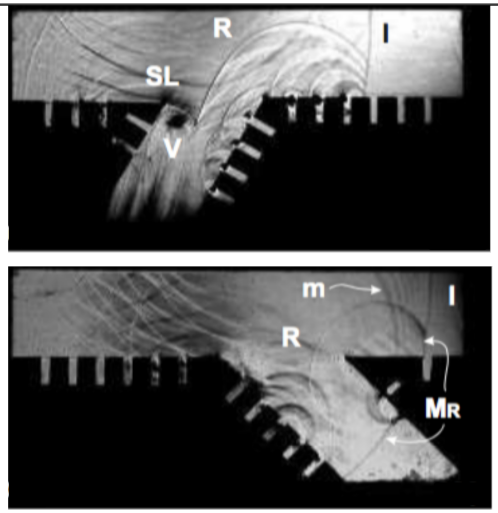 Figure 1.24: Schlieren photographs, Gongora-Orozco (2010). 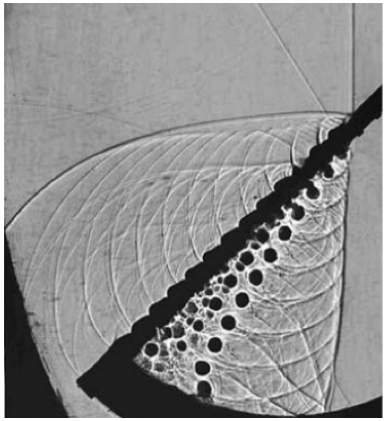 Figure 1.25: Shadow images, Skews (2005).

Shock attenuation methods	References	Illustrations
Protective barriers	- Sochet et al. (2017) - Sebastien (2013) - Jiang et al. (2014) - Allain (1994) - Borgers (2010) - Sochet et al. (2013) - Zhou & Hao (2008)	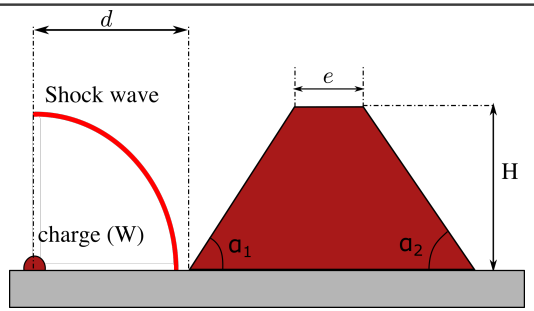 Figure 1.26: Schematic diagram of a protection barrier, Sochet et al. (2017). 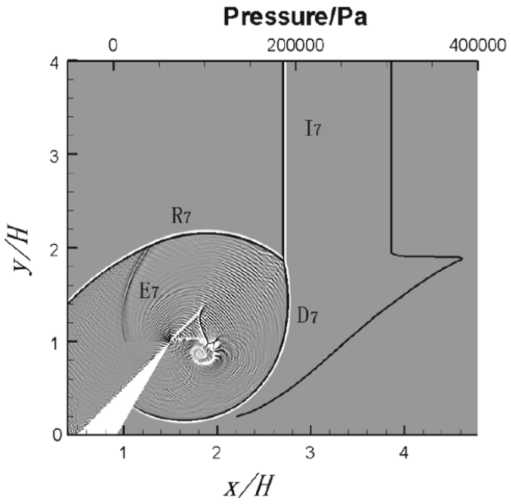 Figure 1.27: Numerical shadowgrams, Jiang et al. (2014). 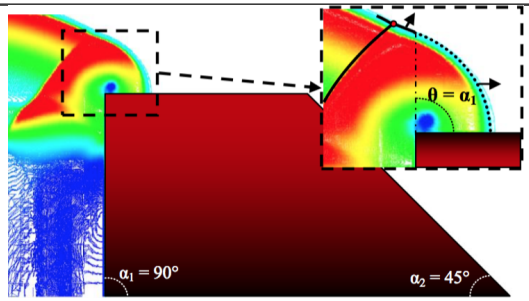 Figure 1.28: Shock wave interaction with a protection barrier, Sebastien (2013). 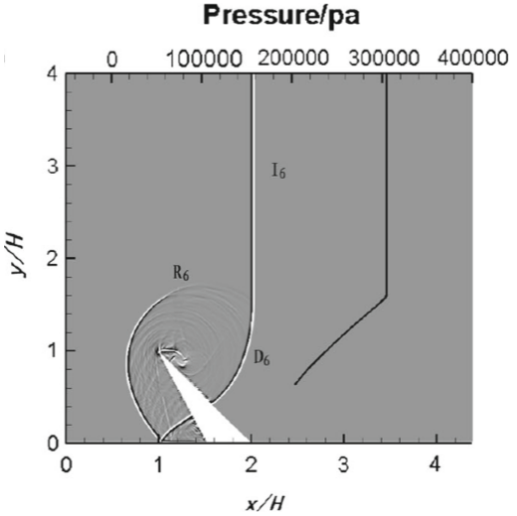 Figure 1.29: Numerical shadowgrams, Jiang et al. (2014).

Table 1.1: Shock-waves attenuation methods

1.4.1 Shock-wave attenuation in ducts

Research on shock wave mitigation in channels has been a topic of much attention in the shock wave community. Many approaches are adopted to attenuate shock wave in channels, among them: the use of obstacles of various geometries arranged in different patterns, branched/bend duct, perforated plates/walls, duct with rough walls, foams, etc.

Different factors are taken into consideration when choosing a geometry for shock attenuation. One important factor which determines (or limits) the geometry for shock wave attenuation in a confined area is the application. As high pressure jumps lead to shock wave generation in various scenarios of industrial, daily and extreme conditions; the geometry or process which causes these pressure jumps might be unavoidable. A useful example of this is the barriers on tunnels where a high-speed train is traveling. In this example, the most viable solution is to alter the inner walls of the tunnel, or attach a damping geometry on the front of the moving train (Sasoh et al. (1994) Takayama et al. (1995)). Several studies on shock attenuation have been carried out for different geometries and Mach numbers. Porosity is a key factor for shock attenuation in channels. When barriers are introduced as shock absorbers, the blockage ratio of the flow, the geometry of the elements, and position of the barrier are taken into account to achieve maximum shock attenuation. In the case of junctions or bends, the angle, length, number of junctions (deflections of the flow), and expansion chambers, if there are any, play an important role in pressure damping.

1.4.1.1 Shock-wave attenuation through abrupt changes in the geometry

When a planar shock wave propagates in a uniform-cross-section duct, it slowly attenuates due to momentum and energy loses via friction and heat transfer. A much faster decay in the shock wave strength and shape (pressure signature) is observed when it propagates into a branched duct. In this case the main mechanism responsible for reducing the shock wave strength, in addition to its diffraction over the bend corner, is multiple shock wave reflections initiated by the bending, Igra et al. (2001). The propagation of a planar shock wave and its subsequent interactions with the duct walls, result in a highly non-stationary two-dimensional flow. Among many examples where this type of interaction occurs, we are usually interested in quickly reducing the intensity (impulse) of the propagating shock, or blast wave. It is therefore not surprising that numerous studies regarding ways to attenuate propagating shock or blast waves in a complex ducts having area changes have been published in the past decades e.g., Chester (1953), Chisnell (1955), Whitham (1958) etc.

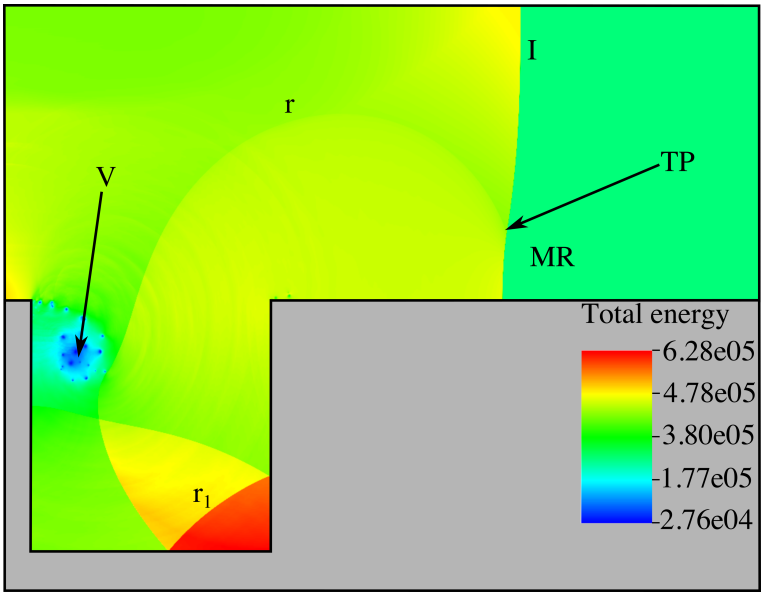

Figure 1.30: Total energy contours in a square cavity with $M_s = 1.5$ at $t = 348\,\mu s$, I: incident shock wave, MR: Mach reflection, TP: triple point, r: reflected shock from MR, V: vortex, r_1: reflected shock from the lower right cavity corner, current study.

Nettleton (1973) experimentally investigated the effect of the angle of divergence, the magnitude of the area ratio, and the specific-heat ratio of the gas on the shock attenuation in a two-dimensional area expansion. Igra et al. (1996) carried out a numerical and experimental study of the interaction between a planar shock wave and a square cavity. High peak pressures were experienced by the cavity wall on which a head-on collision with the incident shock wave takes place in the lower right cavity corner. The lowest peak pressures were found on the cavity wall along which the incident shock wave diffraction took place. The study was expanded later on by Igra et al. (1998). In this study the configuration of the cavity was replaced by a tube with a 90° branch. In the experiments carried out, they observed that the planar shock-wave diffracted when the first bend was encountered. The shock wave splitted into the main and branched tube forming a cylindrical (two-dimensional) shock wave on both branches. The interaction with the wall gave way to a complex reflection, where Mach reflections could be observed. The pressure history presented several peak pressures as the reflected wave returned to the branched duct. The shock wave transmitted down the 90° branch is weaker than the one propagating along the original direction. Therefore, if one looks for protection from the high pressure generated behind the incident shock wave, the best place to be is in the 90° branching tunnel, preferably near its left wall. The worst place would be in proximity to the branching segment right corner (as shown in Figure 1.30). In a later study carried out by Igra et al. (2001), the configuration was modified as a double bent duct. Four different models where studied which considered the smoothness of the wall

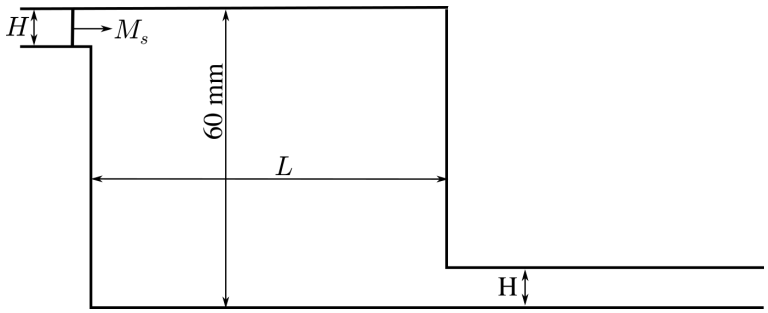

Figure 1.31: Schematic descriptions of the double bent duct used by Igra et al. (2001) and Chaudhuri (2019).

and the change of volume inside the duct. The incorporation of roughness to the tube was simulated by including small cavities to the walls of the duct. The double bent geometry proved effective for attenuating the transmitted shock wave. Furthermore, they found a critical value, L/H, for which effective wave attenuation is obtained, where L and H are the corresponding length (straight section) and height of the duct (see Figure 1.31), which in this case was found to be L/H = 4, for incident shock wave Mach number of 1.35. Chaudhuri (2019) numerically investigated the planar shock-wave propagation through a double-bend duct having L/H = 16, and the shock-wave Mach numbers were chosen similar to those presented in the experimental work of Igra et al. (2001) as $M_s = 1.3466$ and 1.53. The normalized pressure signals (P/P_1, where P_1 is the pressure of the stagnant state) at the bottom wall of the double-bend duct were analyzed in order to highlight the attenuation aspect of the flow configuration. The value of P/P_1 predicted from his simulations near the exit section of the domain was found to be about 1.5 for $M_s = 1.3466$ and 1.8 for $M_s = 1.53$. The author further estimated the overpressure (defined as $\Pi = \frac{P-P_1}{P_2-P_1}$) at the duct exit, the results yield $\Pi \approx 0.53$ for $M_s = 1.3466$ and 0.551 for $M_s = 1.53$. The results showed the effectiveness of the double-bend duct in shock-wave mitigation.

Marty et al. (2019) investigated the propagation of a planar shock wave through a channel splitted into two symmetric secondary channels, for three different shock wave Mach numbers ranging from about 1.1 to 1.7. A parametric numerical study was carried out where the angular displacement of the two channels that define the bifurcation was changed from 90°, 45°, 20°, and 0°. It was shown that the pressure prevailing behind the reflected shock wave from the end wall of the Y-shaped duct is less than half of what exists behind a reflected shock wave from a similar straight duct under the same initial conditions. Therefore, such duct geometry is a suitable proposal for significantly reducing the potential danger of a traveling shock/blast wave in tunnels. Moreover, they also pointed out that the expansion ratio of the cross-sectional area is a preponderant

parameter in attenuating the strength of a shock wave compared to the duct geometry.

1.4.1.2 Shock-wave attenuation using porous and perforated walls

Szwumoski (1971) explained the shock attenuation process with porous and perforated walls. When a shock wave passes through a porous or perforated wall, the mass flow through the perforated wall subsequently induces a loss of momentum and energy fluxes and thereby decreases shock wave strength. Additionally, the porous wall affects the energy distribution that slows down the formation of secondary shocks.

The work of Szwumoski (1971) was one of the earliest studies using perforated walls. His study reveals the importance of the length of the perforated surface. It was reported that the shock Mach number, M_s, changes with distance and the perforation coefficient of the walls. For a finite perforated length, the shock Mach number increases when the shock travels along the unperforated length (after the perforated surface). This is contrary to the infinite case where shock Mach number decreased as it moves downstream along the perforated surface.

The production and suppression of sonic boom on high-speed trains entering tunnels has inspired research on weak shock attenuation in this area. Takayama et al. (1995) used the same scaled train tunnel simulator constructed by Sasoh et al. (1994). In their study, they directed their attention to add porosity to the tunnel walls in order to suppress or attenuate the sonic boom. The walls were partially or completely covered with aluminum plates. The porous wall effectively reduced the pressure peaks; however, this reduction depends on the area and length covered by the porous surface. The velocity of the scaled train speed simulated was 75 m/s which corresponds to $M_s = 1.009$.

A discussion of shocks reflecting from perforated plates was carried out by Ben-Dor (2007). A more recent study of regular reflection on perforated plates has been conducted by Skews (2005). In this work, the perforation ratio, the wedge angle, and the thickness of the plate were varied in order to assess the effects of gap guidance and shock Mach numbers. Both the pressure difference and the stagnation pressure loss across the plate are evaluated. It is found that over the range tested the plate thickness has a minimal effect. On the other hand, Igra et al. (2001), in a double-bend duct, studied the smoothness of the wall inside the duct. The incorporation of roughness to the tube was simulated by including small cavities to the walls of the duct. Furthermore, Igra et al. (2001) found a critical value for which effective wave attenuation is obtained. The roughness in the duct wall reduced the pressure jumps across the transmitted shock wave. The effects of the flow field using two types of baffle plates, solid and rigid porous plates, were also studied by Abe et al. (2003). The height of the baffle plates was either 30 mm or 50 mm. The reflection and diffraction of shock waves over porous material generated a series of

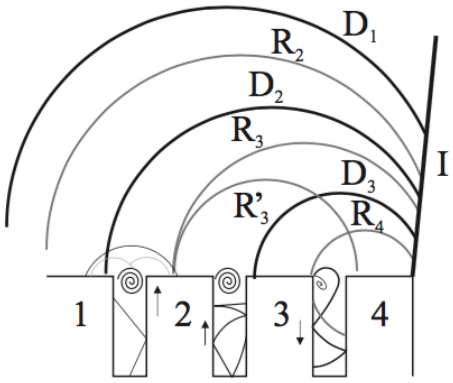

Figure 1.32: Schematic of behavior of transmitted waves inside grooves. Gongora-Orozco (2010).

weak compression and expansion waves, which later on interacted with the incident shock wave, causing the loss of momentum thereby leading to attenuation of the transmitted shock wave.

Mortazawy et al. (2019) conducted experimental investigations and numerical simulations of normal shock waves of different strengths propagating inside ducts with roughness. The roughness is added in the form of grooves. The experimental and numerical findings suggest that effective attenuation of shocks propagating in ducts can be achieved when roughness in the form of grooves is incorporated. As expected, double-sided grooved walls are more effective than single-sided grooves in terms of reducing the shock front speed, hence the strength, and the pressure jump across it. Numerical simulations indicated that the effect of the groove shape is also significant in shock attenuation.

Schematic of behavior of transmitted waves inside grooves is presented in Figure 1.32. The diffracted, D, and reflected, R, waves are indicated with the corresponding groove number which produces them after the incident shock wave encounter. In groove 3, the diffracted shock wave is propagating downward and R_4 is reflecting of the right corner producing R'_3. In the second groove the transmitted shock waves are traveling upwards, and becoming normal to the side walls of the groove. By the third groove, the transmitted shock wave has exited the groove forming a cylindrical compression wave growing radially Gongora-Orozco (2010).

1.4.1.3 Shock-wave attenuation by introducing rigid obstacles along the wave path

The simplest way of obtaining attenuation of a shock/blast wave propagating inside a straight duct is by introducing rigid obstacles in the shock wave path. Effects on shock wave attenuation by obstacles have been investigated by numerous research groups and

among the first to publish results was Dosanjh (1956). Dosanjh performed shock tube experiments with grids inserted in the path of the shock wave to study the reflected and transmitted shock waves, using both shadowgraph visualizations and hot-wire anemometry. Various grids were used for a range of Mach numbers, and choking effects by obstacles in supersonic flow were explained.

The use of wedges to dissipate the energy and momentum of a flow is studied using numerical analysis by Skews et al. (1998). The barrier geometry used is based on the fact that flow resistance, and reflected shock strength, are less for a triangular body with the body positioned with its apex facing upstream than when the base faces the flow as depicted in Figure 1.33(a). At the first instance when the shock wave enters the array, multiple weak reflections are produced by the encounter. The wedge arrangement traps the transmitted shock wave. The wave exits the array of wedges, strong internal reflections are produced. The following parameters were taken into account in the arrangement of the wedges. First is the angle of incidence of the wedge: 10°, 20° and 30° angles, secondly the size of the triangle arrangement in the duck blockage. The distance between each row of elements is varied; and finally, the influence of staggering the elements was taken into account. Two incident shock Mach numbers are studied $M_s = 1.5$ and 3. The reflected shock wave with Mach number $M_s = 3$ moves slowly upstream because of the supersonic flow behind it, the speed of the shock will decelerate forming a stable stationary shock further upstream. When the horizontal distance between the wedges is shortened a reduction of 8% on the shock strength is achieved for $M_s = 3$. The time for the reflected shock wave to expand and strengthen at its edges is minimized in this case, leading to the weakening of the shock. The effect of volume of the channel on shock wave attenuation has been investigated. By increasing the volume ratio from 5:4 to 2:3 they observed a significant reduction in the amount of disturbances egressing with the transmitted shock wave. It was stated that the optimum design of the trap by wedges is by combining the reduction and transmission characteristics of the following parameters: angle of incidence of the wedges (10°, 20° and 30°), area ratio of the duct and distance between maze section.

Abe & Takayama (2001) studied the attenuation of a shock wave with $M_s = 1.2$ in a two and three-dimensional flow. The corresponding geometries for the two- and three-dimensional flows were 20 by 60 mm cylinders and 22 mm diameter spheres. The spheres were arranged in a staggered equilateral formation. The blockage ratio of the test section with this arrangement is 54% and 63% with the cylinder configuration. The array of spheres shows a better attenuation of pressure history than that for the cylinders. This study concluded that expansion waves formed by the interaction of waves with the sphere, overtake the transmitted wave more efficiently than with the two-dimensional cylinder array, even though the blockage ratio is higher in the case of the cylinder.

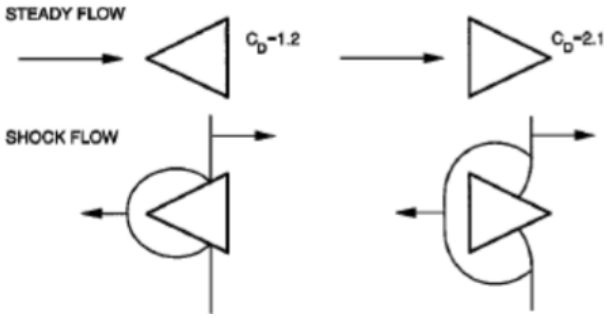

(a) Flow around a triangular bar

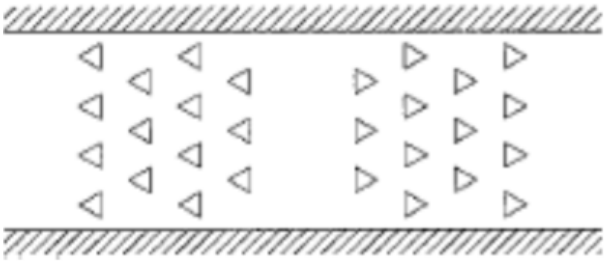

(b) Maze of triangular rods in the path of a shock wave

Figure 1.33: Array of triangular geometries for shock wave trapping used by By Skews et al. (1998)

Chaudhuri et al. (2012) and Chaudhuri et al. (2013) provided a detailed numerical study of shock wave propagation through different arrays of solid obstacles and its degree of attenuation. Obstacles of cylindrical, square and triangular shape were placed inside a shock tube using array-matrix arrangements in both non-staggered and staggered columns. After the shock propagates through the obstacle arrays, time-averaged pressures and velocities behind a wide range of array combinations were compared with each other. The results showed that backward-facing triangular obstacles placed in a staggered array pattern were the most efficient method among the ones investigated to attenuate the incident shock.

In Chaudhuri et al. (2012), a comprehensive analysis of the interaction of the moving shock through an array of cylinder matrix is then conducted by varying the number of cylinders in the matrix block while keeping the same opening passage. The relaxation length between two adjacent columns of cylinders is kept identical to study uniquely the effect of surface-to-volume ratio of the obstacle matrix. The two cases adopted in this study are shown in Figure 1.34. Their study showed that the pressure attenuation is marginally higher for case 1. The computed shock speed in the presence of obstacles was compared with the incident-shock speed. Because of the presence of the array of cylinders, the transmitted incident shock wave experiences retardation and they observed little or no differences in terms of shock-speed reduction between the two test cases. Their study

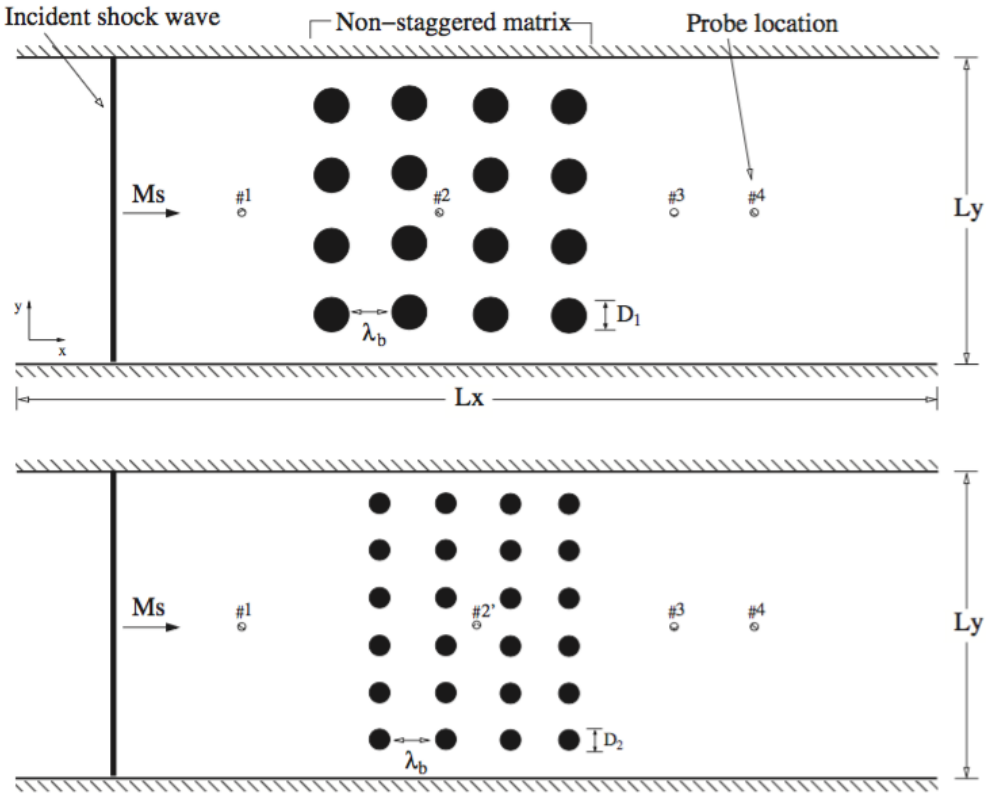

Figure 1.34: Schematic representation of arrangement of obstacles for case 1 (top) and case 2 (bottom), with $M_s = 1.4$, $L_x = 400\ mm$, $L_y = 46.7\ mm$, $D_1 = 4\ mm$, $D_2 = 2.67\ mm$, and $\lambda_b = 6\ mm$. Chaudhuri et al. (2012).

reveals that although the average-pressure attenuation is less pronounced for case 2, the shock speed is more or less equivalent for both cases. The effect of surface-to-volume of the obstacle matrix is mainly manifested in terms of later stage evolution of the flow field farther downstream to the obstacle matrix, and the influence of different geometrical shapes on shock-wave attenuation is very small for higher percentage of open passage.

In Chaudhuri et al. (2013), shock-wave interaction with matrices of different geometrical obstacles and its attenuation are numerically analyzed. Based on the previous study, Chaudhuri et al. (2012), comparison among the different geometrical shapes of obstacles was carried out for low percentage of open passage ($\epsilon = 0.25$, where ϵ is defined as the ratio of the available flow area to the total cross-sectional area). In total seven cases were used and are depicted in Figure 1.35.

From their study Chaudhuri et al. (2013) have drawn important conclusions. At low ϵ of the barrier configuration, the obstacles geometry influences the shock mitigation, among the non-staggered formulations, approximately 13% of reduction in the transmitted shock velocity is achieved with reverse triangular prism matrix arrangement, C_4. It was also shown that the staggered formulations of obstacles favor shock-wave attenuation. Their results also reveals that the most effective configurations, in terms of shock

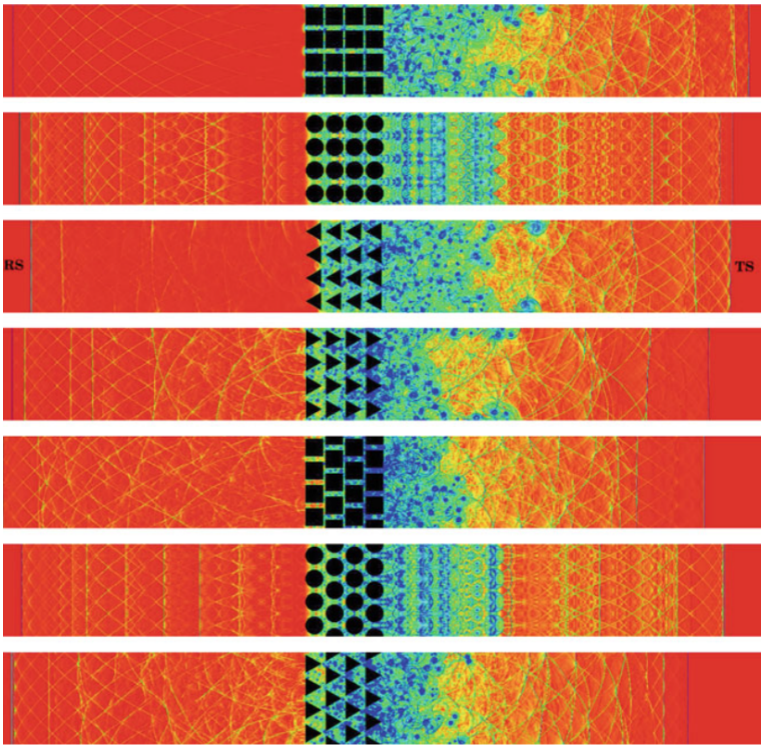

Figure 1.35: Numerical schlieren for the different test cases used by Chaudhuri et al. (2013), TS: transmitted shock, RS: reflected shock, C_1, C_2, C_3, C_4, C_{1S}, C_{2S}, C_{4S}, from top to bottom.

attenuation, is the reverse triangular prism, with staggered arrangement, C_{4S}, with about 21% reduction in the transmitted shock velocity and highest pressure mitigation.

Wan & Eliasson (2015) were inspired by the study of Chaudhuri et al. (2013) to present numerical simulations using a different obstacle pattern. Instead of using a matrix of obstacles, an arrangement of square or cylindrical obstacles placed along a logarithmic spiral curve was investigated. The results showed that a logarithmic spiral can be used to attenuate a planar incident shock wave. The results indicated also that the logarithmic spiral decreases the pressure and delays the shock velocity downstream of the obstacles for certain ranges of Mach numbers. Additionally, the reflected shock is effectively delayed but the pressure ratio remains relatively high. Therefore, when the reflected shock is fully developed, much later than the time span shown in the presented simulations, it may catch up with the reflected shocks in the other simulated cases. It might still be a viable solution to use a logarithmic spiral compared to matrix arrangements, since viscosity will act on the flow, and the longer the shock wave is delayed, the more it will dissipate Wan & Eliasson (2015).

1.4.1.4 Shock-wave mitigation using non-rigid barriers

Water has the potential to be successfully used to attenuate shock waves for several reasons. Water is relatively easy to obtain and environmentally friendly. It has a large heat capacity, where a large amount of heat could be absorbed by water when mitigating the blast wave. On the other hand, taking account of the environment inside an underground mining structure, solid barriers are hard to install in the narrow channels and may block the lifesaving path during an explosion if collapsed. In comparison, a large bulk of water will be broken into small droplets when impacted by a shock wave, but it will not block the channel due to its fluidic properties. Water can be used in different forms, such as mists, sprays and bulk, to mitigate shock and blast waves Kailasanath et al. (2002).

Chauvin et al. (2011) compared the pressure changes caused by the propagation of a planar shock wave in a gas, gas with solid obstacles and gas with liquid obstacles. The three cases are schematically summarized in Figure 1.36. In the homogeneous gaseous medium, across a shock, there is always an extremely rapid, abrupt and almost discontinuous increase in the shock wave characteristics found to be quasi-identical at any point of the flow (at S_1 and S_2) as represented in Figure 1.36(a). When an incident shock wave (Isw) interacts with solid particles medium, the pressure traces obtained upstream (S_1) and downstream (S_2) of the interaction show, respectively, a reflected shock wave (Rsw) that goes back upstream and a refracted shock through the solid particle medium leading to a weaker transmitted shock wave (Tsw) which propagates downstream with an overpressure peak which decreases as the shock advances as shown in Figure 1.36(b). The most complicated case is depicted in Figure 1.36(c), in the case of a liquid droplet medium, the two-phase shock wave scheme is modified. It does not consist of a shock directly followed by a relaxation zone in which the velocities of the two phases relax to the mixture velocity and the pressure rises directly to a maximum. Here, the shock is followed by rarefaction waves and by a pressure build-up leading to the same equilibrium state. This tendency can be attributed to the process of atomization of droplets generally divided in the literature into two stages Chauvin et al. (2011). According to Guildenbecher et al. (2009), during the first stage, the droplets deform, increasing the exchange surface between gas and droplets. In the second stage, the deformed droplets are broken into smaller ones. The diminution of the mean diameter increases the exchange surface between the gas phase and the dispersed phase. Moreover, the momentum and heat exchanges between the two phases increase with the surface area of the water medium leading to a diminution of the velocity, pressure, and temperature of the carrier gas. Therefore, the fragmentation process, which induces an increase in the exchange surface, leads to a diminution of the pressure and gas velocity due to momentum exchanges until the stabilization of the global exchange surface area. When the droplets reach a stable

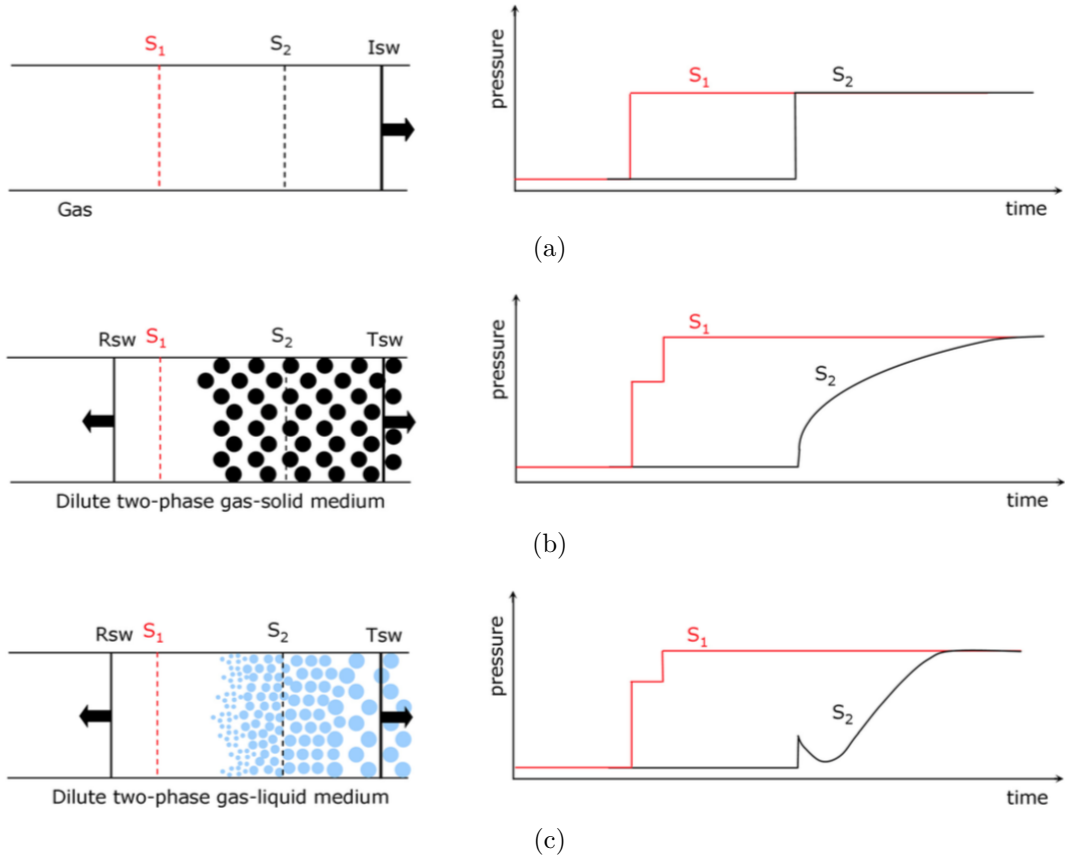

Figure 1.36: Schematic diagrams illustrating the propagation of a planar shock wave in a gas (a), in a dilute two-phase solid-gas mixture (b) and in a dilute two-phase liquid-gas mixture (c), associated with the pressure traces recorded upstream (S_1) and downstream (S_2) of the interaction. Isw, Tsw, and Rsw represent the incident, the transmitted shock wave in the two-phase mixture, and the shock wave reflected off the cloud front respectively. By Chauvin et al. (2011).

state, the classic behavior of the interaction between a shock wave and a solid medium takes place: the velocity and temperature relaxation processes continue resulting in a pressure rise to reach the equilibrium value. Finally, as the atomization of the droplets generates rarefaction waves following the shock wave, these waves may catch up with the shock wave reducing the pressure induced inside and after the water cloud Chauvin et al. (2011).

Several investigations have shown that water spray under certain circumstances can reduce explosion effects considerably. The most important studies that were performed in this respect are the studies performed by Acton et al. (1990), Bjerkelvedt & Bjarkhaug (1991), Thomas & Brenton (1993), Catlin et al. (1993), Wingerden et al. (1995) etc.

Jourdan et al. (2010) experimentally investigated the mitigation of shockwave passing through a cloud of water droplets. Experiments were conducted using a vertical shock tube and water droplets were carefully controlled to be 120, 250 and 500 μm in diameter. The attenuation of the shock was characterized by reducing the peak pressure after

passing through the water cloud. Results showed that the attenuation is negligible for droplets of 120 μm, while droplets of 500 μm significantly reduced the peak pressure behind the transmitted shock by 65%. Chauvin et al. (2011) conducted similar experiments using different heights of water droplets clouds while the droplet diameter was fixed. It has been shown that the major factor of shock wave mitigation is the exchange surface area of droplet atomization, which is defined as the effective area of the droplets crossed by the shock wave at a given location, non-dimensionalized by the cross-section of the shock tube. Cylindrical water obstacles have also been studied experimentally by Igra & Takayama (2003). Water cylinders were placed in a tandem configuration and results were presented in terms of acceleration terms and drag coefficients. The tandem configuration was also compared to that of a single water cylinder and results showed that the single water cylinder behaved virtually the same as the front cylinder in the tandem case. The rear cylinder experienced less displacement, less acceleration and had a lower drag coefficient compared to the front cylinder. Recently Wan et al. (2019) have studied the possibility of attenuating shock waves by using a water spray obstacles. The transfer of kinetic energy from the shock-induced flow to the water cylinders has been quantified and it was found that the transfer rate of kinetic energy, in the early stage, from the shock-induced flow to the water cylinders, increases as the cylinders number is increased. According to their study, water drops have the potential to efficiently attenuate shock waves given the important amount of heat that could be absorbed by water when mitigating the blast wave. In their study, shock attenuation effects of the water spray have been compared to solid obstacles devices using the same geometrical setup. Results showed that water like cylinders have a better capability to absorb the shock energy compared to solid obstacles of the same blockage area.

1.4.2 Shock-wave mitigation using protective barriers

Protective barriers are widely used for attenuating shock waves. The presence of a protection barrier ensures the easy protection of buildings and people against the heating effects of an explosion and the projection of fragments. However, protection from the effects of overpressure is not guaranteed simply by the presence of a physical protection barrier of unspecified form. Indeed, the interaction of a shock wave with a structure is difficult to predict and depends on many parameters.

Sebastien (2013) summarized the precedent works of Allain (1994) and Borgers (2010) in which they proposed different configurations shown in Figure 1.37. Allain (1994) comprised barriers with two inclined slopes of 45° without a flat crest and using a height of $H = 1.5\ m$ "Merlon N°1" in Figure 1.37(a). These tests demonstrated that a barrier, according to its geometry and form factors, can lead to various flow modes. The pro-

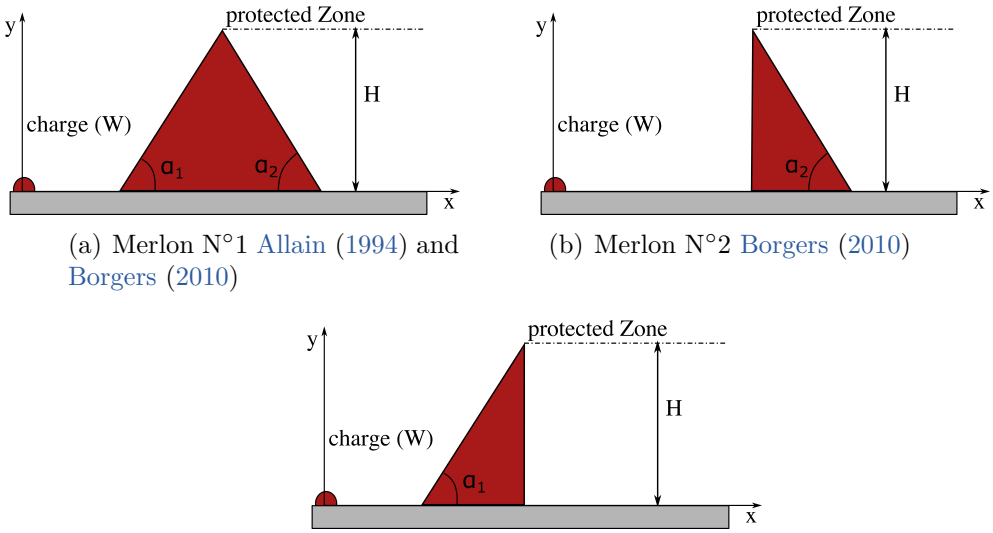

(a) Merlon N°1 Allain (1994) and Borgers (2010)

(b) Merlon N°2 Borgers (2010)

(c) Merlon N°3 Borgers (2010)

Figure 1.37: Schematic diagrams illustrating the configurations studied by Allain (1994) and Borgers (2010). schema reproduced from Sebastien (2013).

tective barrier considered in this case accentuated the positive overpressure of the shock wave and thus did not show a protective effect. These results have been confirmed by the simulations of Borgers (2010), who noted that the relaxation on the rear face of a Mach stem results from reflection on the front face or from an incident wave (for a regular reflection) for certain configurations. This can lead to an accentuation of the reflection of the shock wave on the ground downstream of the obstacle (according to the nature of the wave and the angle of inclination of the wall). The experimental work of Allain and the numerical studies of Borgers have obtained different findings for this type of structure without a thickness at the top and with one or two 45° slopes. These studies have shown that the reflection on the upstream side (facing the explosion), regular or Mach reflection, is followed by rarefaction waves, the reflection is continued on the downstream face (rear), which accelerates the front and the reflection on the ground, thus increasing the pressure. The evolution of the pressure throughout the propagation of the shock wave does not obey a linear function in terms of the distance from the centre of the explosive charge. Therefore, the protective effects of the barrier are dependent on its geometry (e.g., length and thickness at the top corners of the upstream and downstream sides). Recently Sochet et al. (2017) studied the influence of the protective barriers geometry on the propagation of shock waves. They designed the barriers geometrical configurations and dimensions in such a way to analyze several physical phenomena (reflection, relaxation and recombination of shock waves) as well as the protective effect of protective barriers according to their geometry. Their study reveals that the ideal protective barrier is a parallelepiped with significant height and thickness. According to them the optimal

dimensioning of a protective barrier thus depends on the available resources and dimensions of the configuration of interest (position of the zone to be protected with respect to the blast load).

Figure 1.38(b) shows the phenomenon of blast wave recombination behind the barrier. This phenomenon, generally, occurs for small barrier (small length), where the waves from the side faces are combined with that from the top, leading to the formation of a Mach stem and an increase in pressure downstream of the barrier. All of these studies converge on the same conclusion, a protective barrier is only effective under certain conditions and according to predefined parameters, mainly: charge mass (W), height of barrier (H), thickness at crest of obstacle (e), angle of inclination of the barrier faces (α) and distance between centre of charge and the front face (d) as shown in Figure 1.38(a).

A detailed review of different suggestions proposed for shock/blast attenuation discussed above is given in the interesting review of Igra et al. (2013). The Various methods suggested for achieving shock/blast attenuation included introduction of abrupt geometrical changes (in the flow direction or transverse to the flow cross-section) in the conduit through which the shock/blast wave propagates, adding roughness to the conduit walls, introducing small solid particles (dust) or liquid droplets to the gaseous phase. Other options are introduction of rigid obstacles (barriers) having different shapes and orientations along the considered wave path. The choice of a suitable option for a specific case depends on both, the considered flow field geometry and the availability of mechanism/resources needed for introducing the needed obstacles, i.e., dust/droplets or rigid barrier(s) to the protected site Igra et al. (2013).

1.5 Shock-wave focusing

A shock wave the shape of which is concave to the direction of its propagation can converge to a focal region. The focusing of shock waves produces localized high pressures and temperature in the focal region, and the shock emerges from the focus with the front geometry fundamentally changed. Understanding the mechanisms of focusing is critical because converging fronts occur frequently, for example when passing through nonuniform media or reflecting from curved surfaces. The high pressures localized near the focus may be beneficial, as in shock wave lithotripsy, or detrimental, as in superbooms from supersonic aircraft. The change in shock geometry downstream of the focus has significant implications for shock stability, sonic boom propagation. Examples of application of shock wave focusing include extracorporeal shock wave lithotripsy (ESWL). In this treatment for kidney stone disease, weak converging shock waves are generated in water outside the patient's body and shaped to focus on the stone. In the focal region, the shock pressure

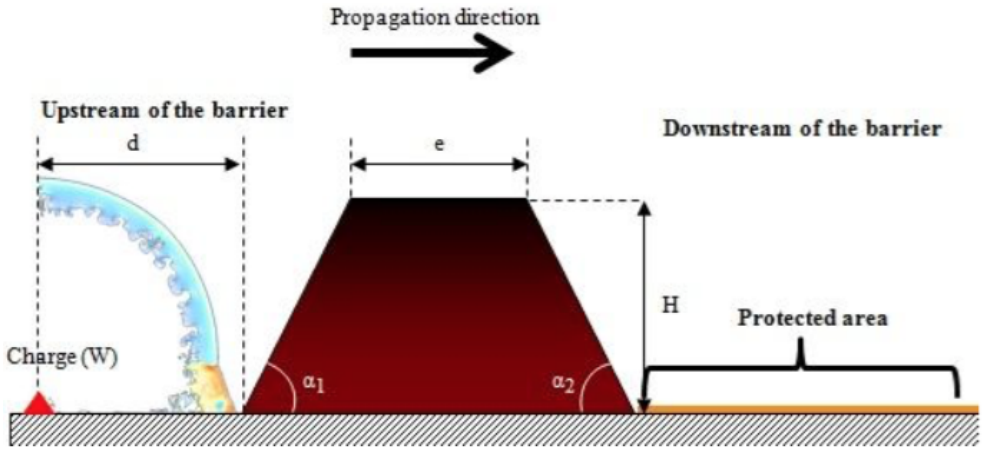

(a)

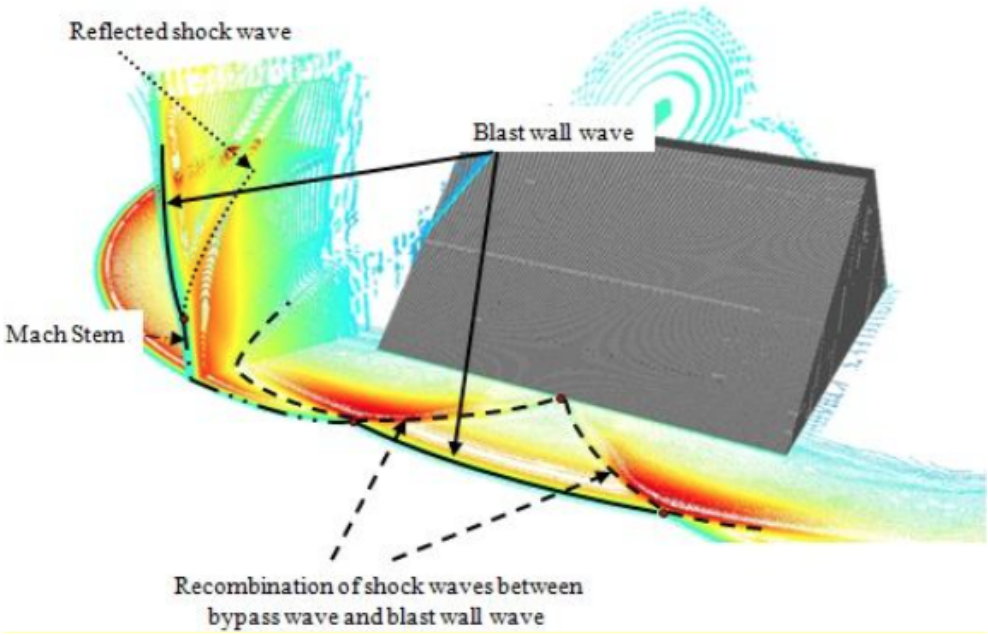

(b)

Figure 1.38: (a): Schematic diagram of a protection barrier, W: charge mass, d: distance between centre of charge and the front face (m), e: thickness at crest of obstacle (m), H: height of barrier (m), α_1: angle of inclination of front face, α_2: angle of inclination of rear face, (b): blast wave recombination behind the barrier. By Sochet et al. (2013)

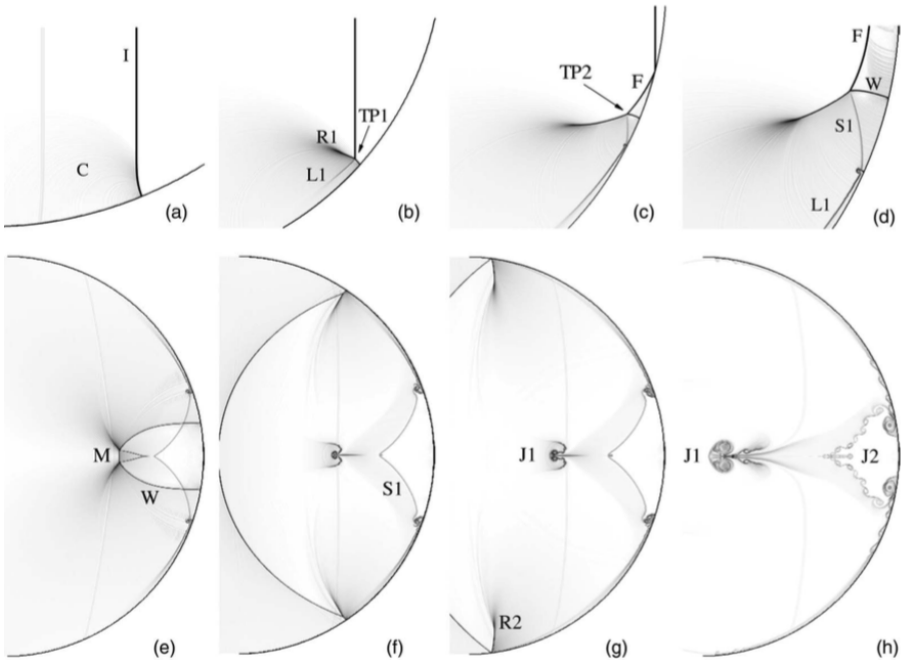

Figure 1.39: Numerical schlieren pictures for $M_s = 1.35$ at different time instants. C: compressive acoustic waves, I: incident shock, R1: primary reflected shock, L1: primary slipstream, TP1 and TP2: first and second triple points, F: new reflected shock, S1: secondary slipstream, W: shock at the wall, M: main reflected shock, J1 and J2: primary and secondary jets. By Shadloo et al. (2014).

increases to about 20 MPa, sufficiently strong to fragment the stone. Another example consists to use the localized high pressures and temperature in the focal region to initiate detonations and self-ignition in transport and power systems, such as liquid propellant rocket engines and diesel engines.

The reflection of a planar shock over a concave surface has attracted the interest of many researchers during the past few years because this type of reflection yields a truly complex and unsteady flow. Guderley (1942) was the first to derive the self similar solution for symmetrically converging cylindrical and spherical shock waves and showed that the pressure at the center of convergence becomes infinite. The study of Guderley is followed later by Perry & Kantrowitz (1951) who produced the first schlieren images of the focusing process. Intending to shed more light on the shock focusing phenomena, a large amount of work has been done using different reflector profiles such as, a log-spiral duct by Inoue et al. (1995), a cavity with symmetrically placed plane walls by Bond et al. (2009) and symmetrical cavities with curved walls, by Sturtevant & Kulkarny (1976), Izumi et al. (1994), MacLucas et al. (2020). etc. The shock focusing was successfully applied to disintegration of kidney stones, known as extracorporeal shock wave lithotripsy (ESWL), by Russel (1986) and Sturtevant (1989). The phenomenon of self-ignition and deflagration initiation under focusing conditions has been widely studied. Borisov et al.

(1988) showed that the application of the curved end-wall instead of the planar wall gives rise to a significant decrease of the intensity of the shock wave that causes self-ignition. Chan et al. (1989) revealed that the realization of deflagration and detonation modes of ignition in the highly sensitive oxygen-hydrogen mixture depends on incident-shock Mach number. Gelfand et al. (2000) used different focusing elements shapes in order to investigate their effects on the flame fronts configurations.

Numerical schlieren pictures, presented by Shadloo et al. (2014), highlighting the shock focusing process from a cylindrical concave surface is shown in Figure 1.39.

1.6 Modeling of shock-wave propagation

The problem of determining the motion of shock waves has received considerable attention over the last several decades. The development of simplified models, able to estimate the position, shape, and strength of a shock, is of prime importance in several domains such as the pyrotechnics industry, explosion hazards, or noise annoyance among others. The ideal method should deal with the interaction of shock waves with complex obstacles and provide an accurate estimate of the overpressure peak in a reduced computation time. Among the models applicable to sustained shock waves, we can cite the Geometrical Shock Dynamics and Kinematics models.

1.6.1 Geometrical Shock Dynamics model of Whitham

In 1957, Whitham published a hyperbolic model called geometrical shock dynamics (GSD) (Whitham 1957, 1959) able to estimate at a moderate cost, but with reasonable accuracy, the propagation of a shock interacting with geometrical elements. This model consists in on the decomposition of the shock front into elementary ray tubes of radius, of elementary section, A, evolving at the local speed, M. Assuming small changes in the ray tube and neglecting the influence of the post-shock flow on the shock, a simple relation linking the local curvature and velocity of the front, known as the A–M rule, is obtained. The successive positions of the shock are given by a set of curves α = cst, shown as full lines in Figure 1.40. The orthogonal trajectories of this set of curves, called rays, are represented by curves β = cst and are drawn as dashed lines. The coordinate α and the arrival time of the front, t, are related by $\alpha = c_0 t$ for a single pass front. Since c_0 is constant, α is also called a pseudo-time for the sake of simplicity. Geometrical relations in the local coordinates of the shock, (α, β), are straightforward (Whitham 1957):

$$\frac{\partial \theta}{\partial \beta} - \frac{1}{M}\frac{\partial A}{\partial \alpha} = 0 \tag{1.4}$$

$$\frac{\partial\theta}{\partial\alpha}+\frac{1}{A}\frac{\partial M}{\partial\beta}=0 \tag{1.5}$$

where θ is the direct angle between the (Ox) axis and rays. Two neighboring rays delimit a ray tube of cross-sectional area A. It is worth noticing that, since A measures the distance between rays, the curvilinear abscissa along the shock, s, is determined by the differential relation: ds = Adβ. By considering a ray tube as a channel with rigid walls, a simple law linking A to M closes the system. This relation, called the A-M rule, is obtained from the 1D Euler system with varying cross section Ridoux et al. (2019):

$$\frac{1}{A}\frac{dA}{d\alpha}+\frac{M\lambda(M)}{M^2-1}\frac{dM}{d\alpha}+h(M)Q=0 \tag{1.6}$$

where,

$$\lambda(M)=\left(1+\frac{2}{\gamma+1}\frac{1-\mu^2}{\mu}\right)\left(1+2\mu+\frac{1}{M^2}\right),\ h(M)=\frac{\gamma+1}{2}\frac{\mu(\mu-1)}{M^2-1}$$

and μ is the post-shock Mach number. The term Q contains all the post-shock flow terms. Whitham chose to neglect this term under the assumption of the smallness of post-shock effects. The resulting equation:

$$\frac{1}{A}\frac{dA}{d\alpha}+\frac{M\lambda(M)}{M^2-1}\frac{dM}{d\alpha}=0 \tag{1.7}$$

Finally, the GSD model is composed of the geometrical system (1.4, 1.5) and the A-M relation 1.7.

Although developed for strong shocks, many studies showed that the Whitham model gives fairly good results even for weak shocks. It has been investigated for different problems, in the past, for cases of converging flows (Schwendeman & Whitham 1987, Schwendeman 2002), propagation through non-uniform media Catherasoo & SturteVant (1983) and for outdoor propagation Besset & Blanc (1994). Nevertheless, the model suffers from a limitation for the problem of shock diffraction over a convex wall. Skews (1967*b*) found that the theory under predicted weak shock wave propagation and over predicted that of strong shock waves. The Mach number of diffracting weak shock waves were predicted to quickly vanish to $M_s = 1$ whereas, in reality, this takes significantly longer to occur. For sufficiently weak shocks, no solution of the GSD model exists up to the wall above a given deflection angle. While the experimental studies of Skews (1967*b*) showed that the diffracted shock front should still exist at the wall, even for weak shocks and at large deflection angles.

Some modifications of GSD were proposed. Best (1991) proposed an extension to post-shock flow, T. V. Bazhenova & Zhilin (1979) proposed another treatment of the

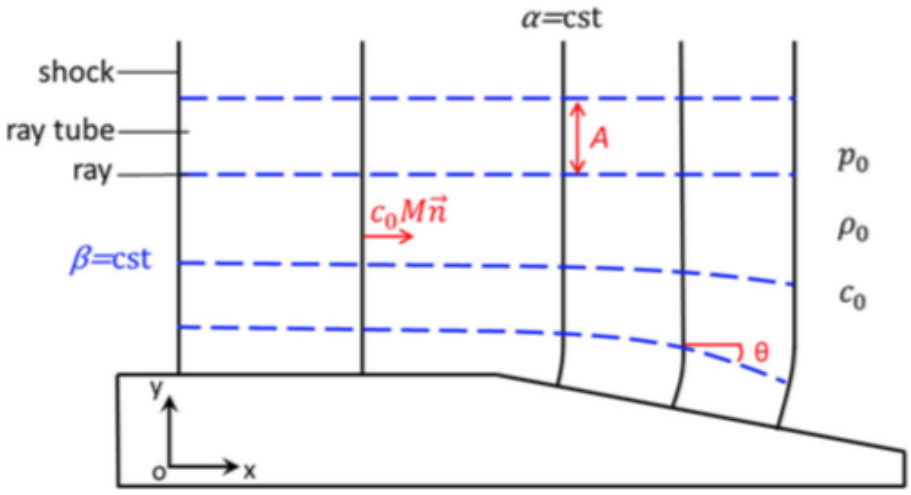

Figure 1.40: 2D shock wave propagation in the geometrical shock dynamics theory. The solid black lines are the successive shock positions and correspond to α coordinates. The dashed blue lines are the rays and correspond to β coordinates. θ is the direct angle between the (Ox) axis and rays. Rays delimit ray tubes of area A. By Ridoux et al. (2019).

wall conditions. The proposed modifications are able to recover the inflection point experimentally observed for strong shocks, but do not remove the limitation.

1.6.2 Kinematic model

Another simplified model for shock front propagation is the kinematic model. The kinematic model was initially expressed by Wright (1976) in 1974 for a perfect gas. As is the case with GSD, it describes only the leading shock front. It consists in assimilating the shock wave to a singular surface. This mathematical point of view makes it possible to define compatibility relations at the level of the front, and to give an intrinsic description to the movement of the surface. This model is based on a combination of the 3D Euler equations applied in the vicinity of the shock and the Rankine-Hugoniot relations at the front. This allows the model to take into account the cross-flow at the shock, and no assumption on the shock strength is necessary, which is a desirable property. The model was studied in detail for an ideal gas by Sharma & Radha (1995) in 1994, and extended to the case of real gases by Pandey & Sharma (2009) in 2009. The analysis of this model is however limited to essentially theoretical considerations.

As the shock is considered as a singular surface moving with its normal velocity Un. The shock position, x_s, is then defined by

$$\frac{dx_s}{dt} = c_0 Mn \tag{1.8}$$

The equation for the Mach number variation is given by:

$$\frac{dM}{dt} = -c_0 \frac{M^2-1}{\lambda_K(M)} \left(\nabla \cdot n + f_K(M) \frac{(\partial_n P)}{P_0} \right) \tag{1.9}$$

where $\nabla \cdot n$ is the local curvature of the front and:

$$f_K(M) = \frac{(\gamma+1)^2}{2\gamma(2\gamma M^2 + 1 - \gamma)}$$

The term $(\partial_n P) = (n \cdot \nabla P)$ contains the post-shock flow effect. For the kinematic model, the λ function reads,

$$\lambda_K(M) = \frac{(\gamma+1)\left(2(2\gamma-1)M^4 + (\gamma+5)M^2 + 1 - \gamma\right)}{(2\gamma M^2 + 1 - \gamma)(2 + (\gamma-1)M^2)}$$

After some calculations we get:

$$\frac{dn}{dt} = -\nabla U + n(n \cdot \nabla U) = -c_0 \nabla^S M. \tag{1.10}$$

Under the hypothesis that the post-shock flow influence over the shock $(n \cdot \nabla P)$ is known, the kinematic model is thus composed of equations 1.8, 1.9, and 1.10.

1.6.3 Taking into account transverse flow in Whitham's A-M rule

Oshima et al. (1965*b*), Oshima (1965) proposed a generalized theory of GSD which includes shear effects. The correction of the A-M relation suggests a kind of interaction between ray tubes which transposes into a transverse variation along the shock curve. The study of this extension is limited to only a linearized solution which shows some improvement in the solution. Indeed, the correction increases the wall Mach number, which, in the range from $M_0 = 1.5$ to 2.8, is in better agreement with experiment. Nevertheless, the modified A-M relation is complex to solve in general and there is no indication that the limitation is removed. Furthermore, the transverse terms will modify the behavior of the model for compressive waves (concave corner), which may lower the quality of the model. Ridoux et al. (2019).

Ridoux (2017), Ridoux et al. (2019) proposed modifications of the GSD and Kinematic models in order to remove their limitations for expansive shocks. This modification consists in *adhoc* modeling of a transverse flow along the shock in the A-M relation. This new closure is fitted against experimental observations, which ensures, by construction, a correct behavior for expansive shocks. In the compressive zones, in particular at the level of the shock-shocks, the A-M classic relation is applied. These models systematically lead

to the formation of a Mach stem, even for a weak shock for which the reflection would be theoretically regular. This results in a significant overestimation of the intensity of the shock wave when reflecting a weak shock. According to Ridoux (2017) this limitation can be removed by introducing a diffusion term in the A-M relation, for example, a term which would be all the more active since the shock would be weak. Another perspective would be to treat the boundary condition of the impact on the wall of the obstacle differently.

1.7 Scope of the present work

Based on the above discussion of the existing literature, the need for a better understanding of the different physical phenomena present during the interaction of a shock wave with obstacles of complex geometries was established. Special attention was paid to the propagation of shock waves in confined areas, given the complex flow and shock-wave patterns following an initially planar shock wave propagating through ducts.

Attenuation of shock waves is of importance for many practical applications, such as blast wave propagation through tunnels, unintentional industrial accidents, and high-speed aerospace structural mechanics. In some scenarios, abrupt changes in channels sections may provide a cost-effective and easy-to-implement attenuation solution. Sudden changes in tunnels sections allow for passive protection of people and structures without the need for expensive integrated technology. These changes can either amplify or attenuate the shock wave effects depending on their configuration, arrangement and the shock wave direction. Therefore, it has become of vital, topical interest to understand the different mechanisms leading to shock mitigation.

The following work intends to highlight the flow and the shock-wave patterns propagating in confined areas, using Direct-Numerical simulations as the primary tool to generate the data. The data are then analyzed with the intention of shedding some light on some scarce fundamental questions, concerning the impacts of various physical parameters on the phenomena. In particular we aim to:

1. Understand the mechanism and the process of vorticity production and the influence of different physical parameters on the rate of vorticity production.

2. Investigating the implications of different physical parameters in determining different flow and shock-wave patterns resulting from the propagation of shock waves through confined areas with complex geometries.

3. Determine the different physical and geometrical parameters leading to an optimal attenuation of shock waves in channels.

1.8 Outline of the dissertation

The chapterwise organizational overview of the thesis is given below:

Chapter 2: This chapter starts with the description of the governing equations including the linear equation of transport, as well as the nonlinear Euler and Navier-Stokes equations. In addition, the point-value multiresolution method to perform dynamic space adaptivity is explained together with its relevant elements. The immersed boundary (IB) method, which facilitates to conduct simulations over non-conforming grids is also presented. Moreover, a computer graphic technique called ray tracing is elaborated, which complements the IB method to localize any complex solid model in the Cartesian grids.

Chapter 3: In this chapter, Shock-wave diffraction over double concave cylindrical surfaces has been numerically investigated at different flow regimes by varying the incident-shock-wave Mach number from $M_s = 1.6$ (transonic) to $M_s = 4.5$ (super- sonic regime). The main objective of this study is to better understand the dynamics of shock-wave structure and the associated wave configurations. In addition, an approximate universal relation is derived, which predicts the transmitted-shock-wave trajectory as a function of the incident-shock Mach number in the range of $1.6 < M_s < 4.5$, for specific heat ratio of 1.4 and concave surface radius of 50 mm. The results are published in: *Acta Astronautica* (Brahmi et al. 2020*a*).

Chapter 4: As a complement to the previous chapter, this chapter deals with the unsteady aspect of turbulent flow structures generated by a shock-wave diffraction over double cylindrical wedges, with initial diffracting angle of 75°. The vorticity production is quantified for different incident-shock-Mach numbers, ranging from transonic to supersonic regimes. Unlike previous studies where only the total vorticity production is evaluated, this chapter offers more insights into the spatio-temporal behavior of the circulation by evaluating the evolution of the instantaneous vorticity equation balance. The shock strength is also evaluated in this chapter by computing the dynamic as well as the static pressure impulses and the normalized overpressure. The results are published in: *Acta Astronautica* (Brahmi et al. 2020*b*).

Chapter 5: In Chapter 3, an approximate universal relation is derived, which predicts the transmitted-shock-wave trajectory as a function of the incident-shock Mach number for a fixed specific heat ratio of 1.4 (air as working gas). In this chapter the geometry as well as the shock-wave Mach number are kept constant such as $M_s = 1.6$, while the working gas is changed. Four gases ,with different molecular weights, specific heat ratios,

and acoustic impedances in addition to the air, are used as working gases, namely, He, Ar, CO_2 and SF_6. The relation proposed in Chapter 3 has been generalized to different working gas having different specific heat ratios. The results are submitted to: *Shock waves Journal*.

Chapter 6: This chapter deals with a numerical study of shock-waves propagation and their attenuation in channel flow having different heights and exhibiting a hollow circular cavities with different depths and diffraction angles inside. Specific attention was paid to the mitigation of the shock waves propagating in this kind of channel. An optimal configuration with channel position/height and a cavity depth leading to an efficient pressure attenuation is found in this chapter. The results are published in: *Theoretical and Applied Mechanics Letters*.

Chapter 7: The summary of the research work undertaken along with the concluding remarks and the perspectives of the study are given in this chapter.

2

Governing equations and numerical methods

Highlights

- Fully compressible Navier–Stokes equations in their conservative form are presented.
- The point–value multiresolution numerical method is described with the essential details that include the tree structure, multiresolution representation, etc.
- Inviscid and viscous fluxes are computed using a fifth-order weighted essentially non-oscillatory (WENO5) scheme and a fourth-order central difference formula, respectively.
- Time advancement is ensured using a third-order Runge-Kutta method (RK3).

Abstract This chapter presents the governing equations and the core numerical methods used throughout the thesis. The point–value multiresolution method is described with the essential details that include the tree structure, multiresolution representation, thresholding, etc. The semi–adaptive multiresolution technique empowers the solver to capture small flow details by dynamically adjusting the mesh resolution. Additionally, the immersed boundary in the form of ghost–cell method together with the ray tracing technique are given facilitating the study of flow around complex obstacles.

2.1 Governing equations

2.1.1 Advection scalar equation

The advection equation (LeVeque 1992) is one of the simplest forms of partial differential equations (PDE) describing the advection of a scalar quantity into the medium. It is given by

$$\frac{\partial u}{\partial t} + \mathbf{v} \cdot \nabla u = 0 \tag{2.1}$$

where u is a given quantity and $\mathbf{v}$ is the velocity vector.

2.1.2 Euler equations

The compressible Euler equations for multi-dimensional compressible inviscid flows can be written in conservative form as

$$\frac{\partial \mathbf{U}}{\partial t} + \nabla \cdot \mathbf{F}(\mathbf{U}) = 0 \tag{2.2}$$

where $\mathbf{U}$ is the conservative variable vector and $\mathbf{F}(\mathbf{U})$ is the inviscid flux, given by

$$\mathbf{U} = [\rho, \rho\mathbf{v}, \rho E]^T \tag{2.3}$$

$$\mathbf{F}(\mathbf{U}) = [\rho\mathbf{v}, \rho\mathbf{v} \otimes \mathbf{v} + p\mathbf{I}, \mathbf{v}(\rho E + p)]^T \tag{2.4}$$

where ρ, $\mathbf{v}$, p and E are the density, velocity vector, pressure and total energy per unit of mass, respectively. The equation of state for ideal gas closes the system according to:

$$p = (\gamma - 1)\rho\left(E - \frac{\mathbf{v}^2}{2}\right) \tag{2.5}$$

with the specific heat ratio $\gamma = 1.4$ for air.

2.1.3 Navier–Stokes equations

The Navier–Stokes equations can be obtained by adding the viscous terms to the Euler equations as

$$\frac{\partial \mathbf{U}}{\partial t} + \nabla \cdot \mathbf{F}_I(\mathbf{U}) = \nabla \cdot \mathbf{F}_V(\mathbf{U}) \tag{2.6}$$

where $\mathbf{U}$ is the conservative variable vector and $\mathbf{F}_I(\mathbf{U})$ and $\mathbf{F}_V(\mathbf{U})$ are the inviscid and viscous flux tensors, respectively, given by

$$\mathbf{U} = [\rho, \rho\mathbf{v}, \rho E]^T \tag{2.7}$$

$$\mathbf{F}_I(\mathbf{U}) = [\rho\mathbf{v}, \rho\mathbf{v} \otimes \mathbf{v} + p\mathbf{I}, \mathbf{v}(\rho E + p)]^T \tag{2.8}$$

$$\mathbf{F}_V(\mathbf{U}) = [\mathbf{0}, \tau, \tau\mathbf{v} + \lambda\nabla T]^T \tag{2.9}$$

where ρ, $\mathbf{v}$, p, T, λ and E are the density, velocity vector, pressure, temperature, thermal conductivity and total energy per unit of mass, respectively. The viscous stress tensor is defined by

$$\tau = \mu \left[\nabla \otimes \mathbf{v} + (\nabla \otimes \mathbf{v})^T - \frac{2}{3}(\nabla \cdot \mathbf{v})\mathbf{I} \right] \tag{2.10}$$

μ denotes the dynamic viscosity, and follows the Sutherland's law as

$$\mu = \mu_{ref} \left(\frac{T}{T_{ref}} \right)^{3/2} \frac{T_{ref} + S}{T + S} \tag{2.11}$$

here, μ_{ref} and T_{ref} are the reference viscosity and temperature, and S is the Sutherland temperature. The equation of state for ideal gas closes the system as

$$p = (\gamma - 1)\rho \left(E - \frac{\mathbf{v}^2}{2} \right) \tag{2.12}$$

with the specific heat ratio $\gamma = 1.4$ for air.

The inviscid and viscous flux computations are performed using a classical fifth–order WENO and a fourth–order compact central differencing schemes, respectively along with the Roe scheme for flux splitting. While explicit third–order TVD Runge–Kutta (RK3) scheme is employed for time advancement. The details of these numerical schemes are presented in Appendix A.

2.2 Multiresolution method

The idea of multiresolution analysis was first presented by Mallat (1989), and further extended to point-value and cell-average representation of data by Harten (1993, 1995).

A brief description about the general theory of wavelet and the multiresolution analysis can be found in Appendix B.1.

The basic element of the multiresolution analysis is to represent the data on the finer grid as data on the coarser grid, plus a series of differences at different levels of the grid. These differences are smaller in regions of smooth solution, and higher otherwise.

2.2.1 Tree structure

In this part, the graded tree structure of the point–value multiresolution is explained along with its relevant terminology:

- A tree structure, as the name suggests, has a root, a body and leaves. The connectivity between the root and the leaves is ensured via the body.
- The *root* is the basis of the tree, which corresponds to the layer 0. And, it has 2^d points, where d denotes the dimension of the problem.
- The *nodes* are the points of the tree structure, which connect the leaves to the root. In other words, all the points enclosed by the leaves are considered as nodes.
- The *leaves* are the top points above which there exist no nodes. These are the only points where the fluxes are calculated.
- The whole tree structure consists of layers of points lying on top of each other. There are $\left(2^l+1\right)^d$ points in a grid of level l.
- The grids at any level of a one dimensional domain can be written as

$$G_l = \{x_{l,i} \quad | i = 0, 1, 2, \ldots, 2^l\} \tag{2.13}$$

Here, for convenient notations, a specific analogy is used to distinguish some characteristics of the tree structure and the operations performed during the grid adaptation. They are explained below:

- The point at the beginning and the points at the end of the arrows are called *parent* and *children* points, respectively. As illustrated by the tree structure, presented in Figure. 2.1, the arrows represent the link between the lower and the upper level points, which can be identified as a parent-child relationship.
- As it can be seen in 2.2.2 that the *even* points of the grid are ignored while performing the adaptation. Hence, this peculiarity makes the whole algorithm faster to some extent, as only the *odd* points are taken into account.

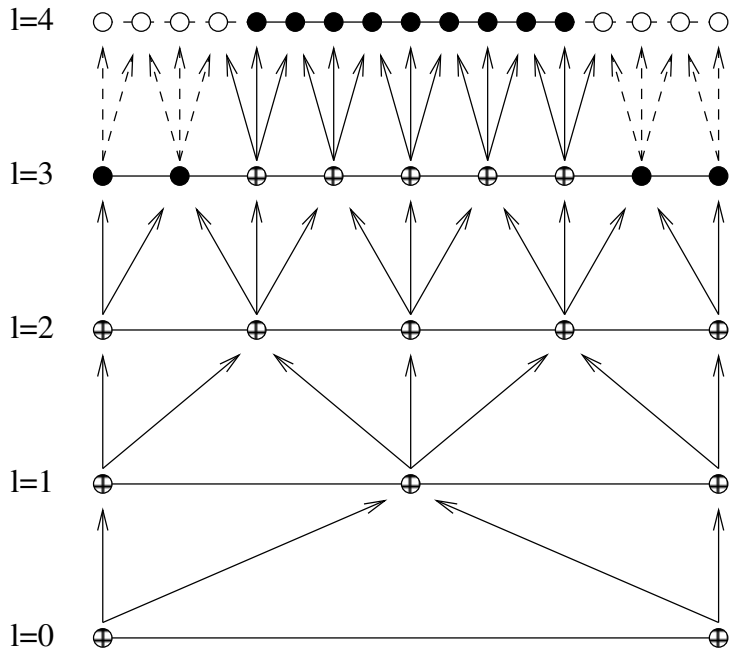

Figure 2.1: Schematic diagram of a 1D tree structure with leaves (•), nodes (⊕) and empty points (∘).

- The parent point with odd index has therefore 2^d children points with odd indices during the grid adaptation operation.
- If a child on the level l with odd index has its *detail* higher than a prescribed tolerance, a *split* operation is performed, creating thereby 2^d children (leaf) points and marking the concerned point as a parent (node) point.
- Inversely, if all children points on the level $(l+1)$ with odd indices have their *details* lower than the prescribed tolerance, the *combine* operation is performed removing all concerned children points and marking their parent point on level (l) as a child (leaf) point.
- The *uncle* points are the neighboring points of the parent point.

The grid adaptation is carried out by performing different operations in between at each time step. The following points explain the facts of the tree structure along with some requirements that must be achieved to keep the tree structure graded:

- A coarser level grid can be obtained by removing the points with odd indices from the finest grid and vice versa.
- The new points are always created or removed in the set of 2^d (odd indexed) points.
- One level of security must always be added while executing the combine operation. In other words, if parent and children points have smaller details than the tolerance,

only the children points are removed at a time.

- The tree must be maintained perfectly graded. Hence, each leaf point must have its uncle points as either nodes or leaves.

Since the tree structure changes dynamically depending on the solution, the fluxes are computed only on the leaves in order to speedup the simulations. The neighbors of the leaves *i.e.* node and empty points are physically present in the memory; and they are taken into account as a part of the WENO stencils. The solution is updated at the empty as well as at the node points by the means of prediction and/or projection operators at every Runge–Kutta iteration. Hence, no special treatment is required for the flux computations in the multiresolution method. In other words, the number of operations required in the WENO scheme for the fine grid (FG) computations are almost the same as in the multiresolution method. However, since the spatial distribution of the grid points is very dense in the case of fine grid simulations, they need significantly more time to compute the fluxes across the computational domain.

2.2.2 Multiresolution representation

The point–value multiresolution method is described in detail in what follows. Its extension to two– and three–dimensional cases is made using a tensor-product approach. The corresponding coefficients are given in Appendix B.2.

The method consists of using two operators, named projection and prediction acting as a carrier, to move the data in the tree structure from finer to coarser grids and vice versa. The *projection* operator is used to estimate the point-values of a function from the level $l+1$ to l:

$$P_{l+1\to l} : U_{l+1} \mapsto U_l \tag{2.14}$$

where U_l is the ensemble of the point data u on level l.

In the case of point–value multiresolution, this operator is always exact and unique. Furthermore, as given in subsection 2.2.1, the coarser grids are formed by simply removing the odd points from the finer level of grids. This operator is simply a decimation of the values from the finer grid, *i.e.*

$$P_{l+1\to l} : u_{l,i} = u_{l+1,2i} \tag{2.15}$$

Inversely, the *prediction* operator maps the point-values from level l to level $l+1$.

$$P_{l\to l+1} : U_l \mapsto \hat{U}_{l+1} \tag{2.16}$$

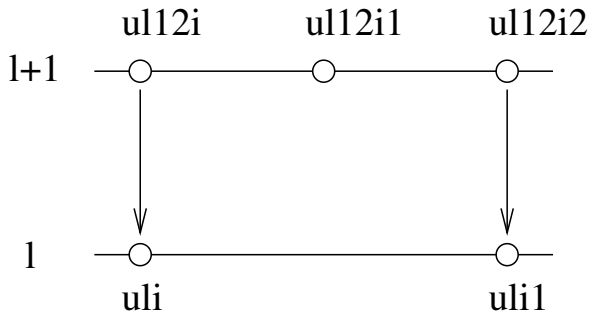

Figure 2.2: Schematic representation of the projection operator.

The prediction operator is neither exact nor unique, and it interpolates the values from the coarser grid to the finer one. However, the key requirements of the prediction operator are: i) it has to be local, and ii) consistent with the projection *i.e.* $P_{l+1\to l} \circ P_{l\to l+1} = Id$, where Id denotes the identity operator. In other words, the prediction operator must give back the original value when projecting the predicted values. For the even values, it returns the same quantity. The odd values can be obtained using a polynomial interpolation of degree $(r-1)$ from the coarser grid, as suggested by Harten (1995).

$$\begin{aligned} \hat{u}_{l+1,2i+1} &= I(U_l; l+1, 2i+1) \\ &= \textstyle\sum_{n=1}^{s} \phi_n (u_{l,i-n+1} + u_{l,i+n}) \quad (\textit{odd index}) \\ \hat{u}_{l+1,2i} &= u_{l,i} \qquad\qquad\qquad\qquad\quad (\textit{even index}) \end{aligned} \tag{2.17}$$

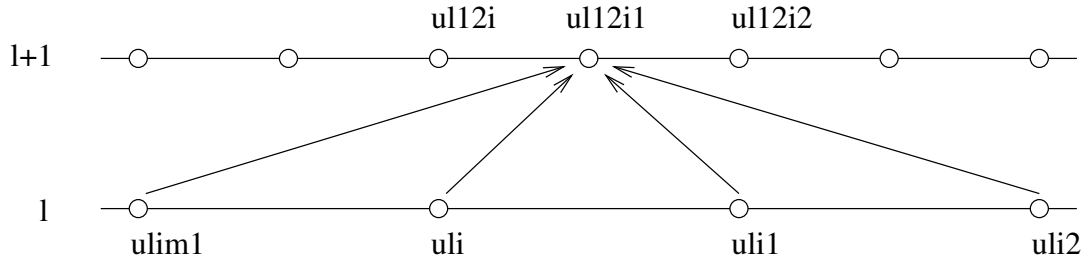

Figure 2.3: Schematic diagram illustrating the relationship between a child and its parents and uncles in the prediction operator.

Here, the order r of the multiresolution is associated with the number of uncles s required for the interpolation by the relation $r = 2s$. The corresponding coefficients of different degrees of interpolation are shown below:

$$\begin{cases} r=2 \;\Rightarrow\; \phi_1 = 1/2 \\ r=4 \;\Rightarrow\; \phi_1 = 9/16, \quad \phi_2 = -1/16 \\ r=6 \;\Rightarrow\; \phi_1 = 150/256, \quad \phi_2 = -25/256, \quad \phi_3 = 3/256 \end{cases} \tag{2.18}$$

For our computations, we have used $r = 4$. Since the ghost points are added on each level

of the tree, the polynomial interpolations of the prediction operator are not required to be modified near the boundaries of the domain.

The difference between the exact values and the predicted ones is called the *detail*, which can be written as

$$\mathfrak{d}_{l,i} = u_{l,i} - \hat{u}_{l,i} \tag{2.19}$$

Let us note that the details at even points become zero, since the projection and prediction are just a copy from the finer and coarser grid, respectively. Hence, only the odd points are relevant for the computation of details. Therefore, from equations (2.17) and (2.19), one can write

$$\begin{aligned} u_{l+1,2i} &= u_{l,i} \\ u_{l+1,2i+1} &= \hat{u}_{l+1,2i+1} + \mathfrak{d}_{l+1,2i+1} \end{aligned} \tag{2.20}$$

Here, as per the theory of wavelet, it is possible to observe that the knowledge of $(U_{l-1}, \mathfrak{D}_l)$ is equivalent to the knowledge of U_l, which can be written as

$$U_l \leftrightarrow (\mathfrak{D}_l, U_{l-1}) \tag{2.21}$$

Applying this operation recursively on L levels of grids, one gets the point–value multiresolution transform of U_L (Harten 1995):

$$\mathbf{M} : U_L \mapsto (\mathfrak{D}_L, \mathfrak{D}_{L-1}, \ldots, \mathfrak{D}_1, U_0) \tag{2.22}$$

The point-value multiresolution method is a smart way of representing the data, since the detail coefficients are the errors of prediction, which tend to zero when the solution is regular.

The thresholding operation consists of removing points in smooth regions. Given a global tolerance ϵ, a tolerance for each grid ϵ_l is defined, and checked against the detail $\mathfrak{d}_{l,i}$

$$|\mathfrak{d}_{l,i}| < \epsilon_l \tag{2.23}$$

If the relation (2.23) is satisfied, the local data are considered as smooth and can be removed. The term ϵ_l in the equation writes (Harten 1995, Cohen et al. 2003):

$$\epsilon_l = 2^{d(l-L)}\epsilon \tag{2.24}$$

where d is the space dimension and L denotes the highest level. In this work, the thresholding operation is performed using ℓ_1 error of the conservative variables.

Finally, the entire multiresolution methodology is briefly presented hereafter in algo-

rithm 1.

Algorithm 1 Multiresolution algorithm

procedure INITIALIZE
    initialize MR parameters, *e.g.*, minimum *(MinL)* and maximum *(MaxL)* grid level, tolerance (ϵ)
    for each leaf on $MaxL$ **do**
        set values of u
    for each point between $MaxL$ to $MinL$ **do**
        if node point **then**
            perform projection operator to set values of u
        else if boundary point **then**
            initialize boundary conditions
procedure COMPUTATION
    for $n = 1,\ N_{iterations}$ **do**
        for each grid point of *odd* index **do**
            compute details on parent points $\mathfrak{d}_p$ and on children points $\mathfrak{d}_c$
            if $\mathfrak{d}_p < \epsilon_l$ and $\mathfrak{d}_c < \epsilon_l$ **then**
                perform combine operation
            else if any $\mathfrak{d}_c > \epsilon_l$ **then**
                perform split operation
            if any leaf has a node uncle **then**
                perform split (property of graded tree)
        compute Δt
        compute time evolution (Runge-Kutta 3 - WENO5)
        update grid:
            use projection operator
            compute values of u on each non-leaf point
            compute boundary conditions
procedure OUTPUT
    save data
    release memory

2.3 Direct forcing technique – Immersed boundary method

The direct forcing technique is one of the methods developed to study the flow around an obstacle or a group of obstacles embedded in the Cartesian grids. This method extends the usability of the solver using a simple Cartesian grid, since it does not need to have conforming grids near the obstacle. The immersed boundary (IB) method term was introduced by the pioneering work of Peskin (1972) who performed the cardiac mechanics and the associated blood flow on the Cartesian grids imposing the immersed boundary on

the flow. Since then, numerous research has been carried out proposing new modifications and refinements for different flow physics (Fadlun et al. 2000, Iaccarino & Verzicco 2003, Tseng & Ferziger 2003, Dadone & Grossman 2004, Gao et al. 2007, Ghias et al. 2007, Kang et al. 2009, Chaudhuri et al. 2011, Schneider 2015). Extensive discussion can be found in the review paper of Mittal & Iaccarino (2005). The underlying principle of this method relies on reconstructing the boundary conditions at the interface between the fluid and solid, where the fluid and the solid are the points embedded in the Cartesian grids. Out of all variations of the IB method, the one implemented in this work is called the direct forcing technique based on the ghost cell method.

The first step towards the implementation of IB is to define the grid points lying inside the solid domain. Based on these points, the ghost points (GP) are flagged, which are the nearest points to the fluid inside the solid. The image points (IP) are the mirrored points of the GPs in the fluid, such that these points are normal to the physical interface, and have the same distance from the interface as the GPs. The essential idea behind IB technique is to interpolate the flow properties at IPs from their neighboring points (NP), and reflect them to the GPs, whereby the fluid–solid interface is maintained.

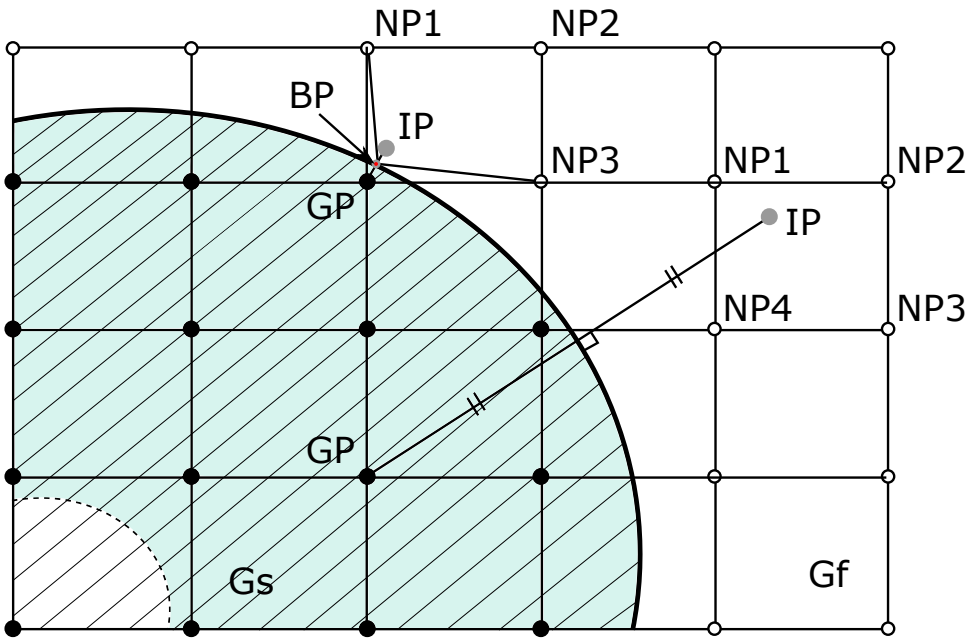

Figure 2.4: Schematic depicting the immersed boundary and the associated terms, whereby (●) and (○) points highlight the solid and fluid points, respectively, and (●) represents the image point; the hatched region highlights the actual solid, while the colored region shows the depth of GP layer.

Figure. 2.4 clarifies the various points and domains schematically. As it can be seen, the two sets of points enclosed by the fluid and solid domains are flagged with the mask as,

$$\begin{aligned} G_s &= \{mask_{i,j} = 1 \quad | \; i \in [0, N_x], j \in [0, N_y]\} \\ G_f &= \{mask_{i,j} = 0 \quad | \; i \in [0, N_x], j \in [0, N_y]\} \end{aligned} \tag{2.25}$$

The number of GPs created depends on the length of the stencils required by the numerical scheme, which in the current work is 6 points, thereby the GPs are created up to the depth of 3 points from G_f inside G_s, as shown by the colored part in Figure. 2.4. Each GP has its reflected point in G_f called IP, such that the mid point between GP and IP lies on the fluid–solid interface represented as boundary point (BP). The interpolation technique at the IPs is crucial in determining the quality and reliability of the solution near the wall. For the current method, the solution at IPs are reconstructed using a bi–linear/tri–linear interpolation from NPs. For a flow variable Q, it can thus be approximated as,

$$Q(x, y) = C_1 xy + C_2 x + C_3 y + C_4 \tag{2.26}$$

where C_1, C_2, C_3 and C_4 are the weighting coefficients of the four NPs. These weighting coefficients can be computed by inverting the Vandermonde matrix,

$$\begin{bmatrix} C_1 \\ C_2 \\ C_3 \\ C_4 \end{bmatrix} = \begin{bmatrix} x_1 y_1 & x_1 & y_1 & 1 \\ x_2 y_2 & x_2 & y_2 & 1 \\ x_3 y_3 & x_3 & y_3 & 1 \\ x_4 y_4 & x_4 & y_4 & 1 \end{bmatrix}^{-1} \begin{bmatrix} Q_1 \\ Q_2 \\ Q_3 \\ Q_4 \end{bmatrix} \tag{2.27}$$

In this case, all NPs are found to be inside the fluid. However, it is quite often to encounter one or more NPs to be in the solid domain (see Figure. 2.4), for which the flow properties at the BP can be realized as,

$$Q_B(x, y) = C_1 x_B y_B + C_2 x_B + C_3 y_B + C_4 \tag{2.28}$$

Since the velocity at the wall is zero for the no–slip condition, the velocity components in such case can be found by modifying the weighting coefficient of the Vandermonde matrix as,

$$\begin{bmatrix} C_1 \\ C_2 \\ C_3 \\ C_4 \end{bmatrix} = \begin{bmatrix} x_1 y_1 & x_1 & y_1 & 1 \\ x_2 y_2 & x_2 & y_2 & 1 \\ x_3 y_3 & x_3 & y_3 & 1 \\ x_B y_B & x_B & y_B & 1 \end{bmatrix}^{-1} \begin{bmatrix} Q_1 \\ Q_2 \\ Q_3 \\ Q_4 = 0 \end{bmatrix} \tag{2.29}$$

The no–slip condition applied to the pressure makes it to vary with zero pressure gradient across the wall in the normal direction, hence using the gradient at wall becomes,

$$\frac{\partial Q}{\partial n} = C_1(y_B n_x + x_B n_y) + C_2 n_x + C_3 n_y = 0 \tag{2.30}$$

which translates to the Vandermonde matrix as,

$$\begin{bmatrix} C_1 \\ C_2 \\ C_3 \\ C_4 \end{bmatrix} = \begin{bmatrix} x_1 y_1 & x_1 & y_1 & 1 \\ x_2 y_2 & x_2 & y_2 & 1 \\ x_3 y_3 & x_3 & y_3 & 1 \\ y_B n_x + x_B n_y & n_x & n_y & 0 \end{bmatrix}^{-1} \begin{bmatrix} Q_1 \\ Q_2 \\ Q_3 \\ Q_4 = 0 \end{bmatrix} \tag{2.31}$$

This can be easily extended to three dimensional problems in the similar way, whereby the matrix would become of the size of 8×8.

2.4 Ray tracing

Ray tracing technique is a powerful method of rendering a very high quality photo–realistic images in the computer graphics. The readers are advised to refer to the book of O'Rourke (1998) for exhaustive details about the ray tracing. The principle of this technique is adapted to define the mask function required in the use of IB method. As a result, the ray tracing technique enhances the versatility of the flow solver to accommodate the complex solid obstacles efficiently.

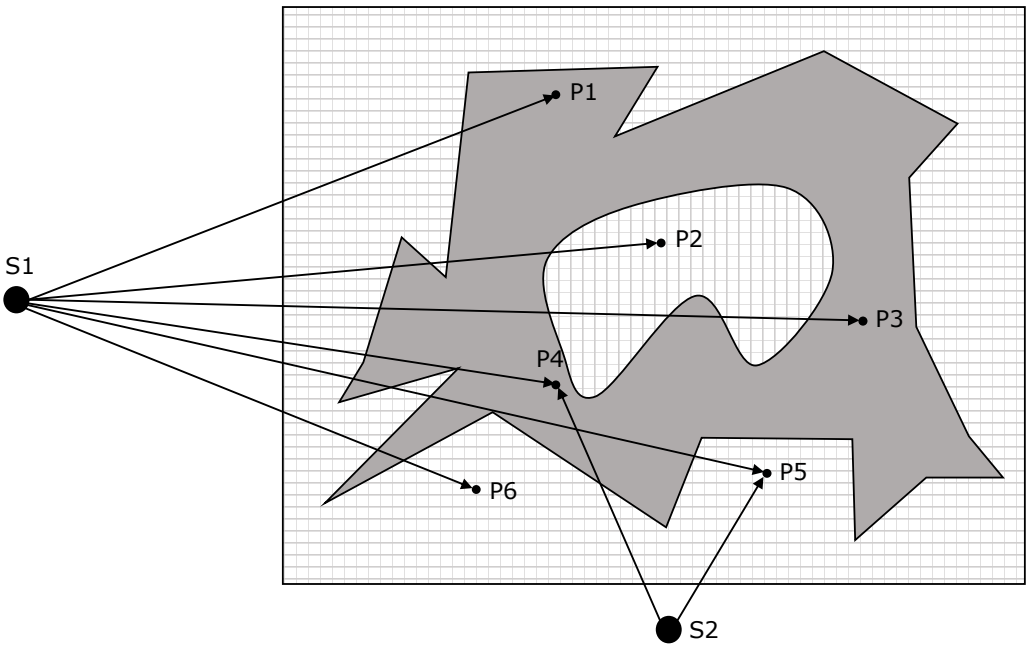

Figure 2.5: Schematic representation of the ray tracing method.

The basic essence of this method is to superimpose the solid over the grid, and cast the rays from a far away location to the grid points and to verify the number of intersections

they make with the solid. This idea makes the technique very flexible, since it enables the use of any modeling tool, such as AutoCAD, FreeCAD, CATIA, etc., to generate the complex geometric models of the solid easily. The computational geometry is decomposed into triangular mesh elements; and are exported in the format of STereoLithography (STL) from the modeling tool. The STL format includes the vertices and the surface normals of each mesh element, which are essential to perform the ray tracing operation.

The ray tracing operation is illustrated schematically in Figure. 2.5, where P_n and S_n denote the query points and source points, respectively. The method comprises some simple algebraic manipulations to define the mask function, and it can be summarized as in the pseudo–code 2.

Algorithm 2 Ray tracing algorithm

```
for each grid point P in G_{i,j} do
    define line, l, passing through P and source S
    count = 0
    for each element, e, in stl file do
        compute intersection point, P_I, of l and a plane containing e
        if P_I lies inside e then
            count = count + 1
    if count is odd number then
        mask_{i,j} = 1
    else
        mask_{i,j} = 0
```

However, there are some precautions to be taken while performing the ray tracing. Having the triangular mesh elements exported from a modeling tool, it is not uncommon to find a few missing elements, or having some duplicated facets, or misplaced vertices. Therefore, it is absolutely necessary to use a conditioning tool, such as MeshLab, to get rid of these inconsistencies, and to obtain a watertight mesh to achieve reliable results. Moreover, in certain cases, the rays from the source to the grid point could possibly intersect with either an edge or a corner of the mesh element. In such scenarios, it is imperative to use a secondary source of ray to confirm the intersection (see P_4, P_5 and S_2 in Figure. 2.5).

The results (mask function) of the ray tracing code for various complex geometries are highlighted in Figure. 2.6. Here, the mask function is visualized by small spheres corresponding to the solid points embedded in the Cartesian grids. As can be seen, even for a very complex mesh, the ray tracing method exhibits excellent performance.

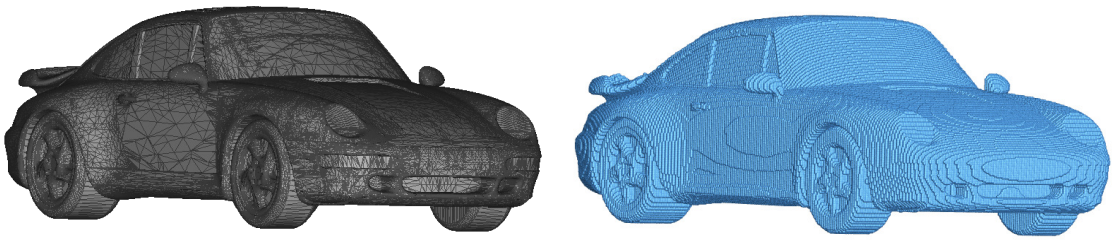

Figure 2.6: Ray tracing: CAD stl mesh *(left)* of a car having 148046 elements, and its corresponding ray tracing *(right)* result.

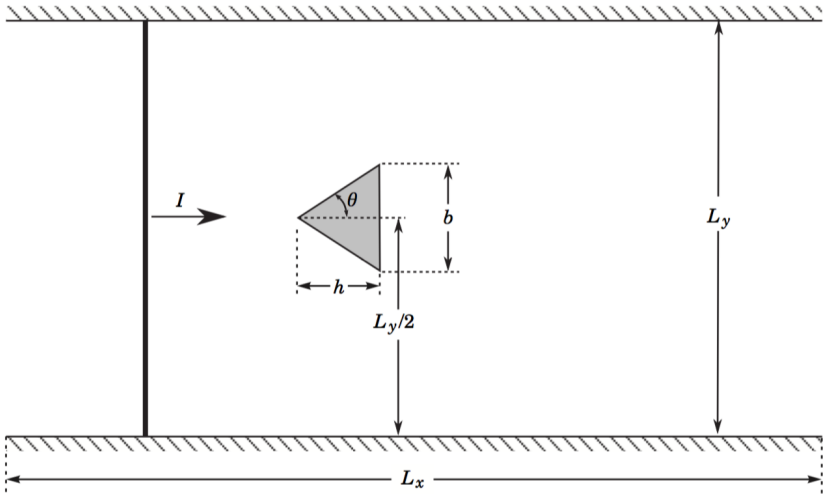

Figure 2.7: 2D shock prism interaction: problem set–up, $M_s = 1.3$, $L_x = 150\ mm$, $L_y = 100$, $mm\ \theta = 30°$, $b = 11\ mm$. By (Soni 2016).

2.5 Validation

The solver has been previously used and validated for simulating quite complex flow scenarios such as the shock/obstacles interactions (Soni et al. 2017, 2019, Shadloo et al. 2014, Soni et al. 2017, Soni 2016). The multiresolution code is developed, validated and used by (Soni 2016, Soni et al. 2017, 2019). Validation tests are given by (Soni 2016), using the classical test cases, where a planar shock–wave is propagated towards a stationary obstacle. The results are compared with the experimental and numerical data available in the literature.

2.5.1 2D shock prism interaction

The problem setup of this test case is shown in Figure 2.7 as used by Schardin (1957). The multiresolution tolerance and the grid resolution are set by varying them until a satisfactory comparison with the experimental schlieren and the triple point trajectories have been obtained.

The shock–reflection phenomenon over the prism can be considered as the pseudo–

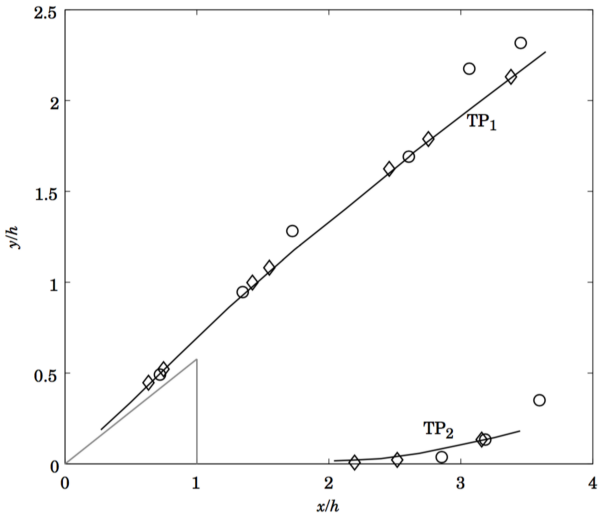

Figure 2.8: 2D shock prism interaction: triple point trajectory of the MR solution is compared with the previously reported experimental and numerical data, – Multiresolution, ◇ Num. data (Chang & Chang 2000), ◯ Exp. data (Chang & Chang 2000). By (Soni 2016).

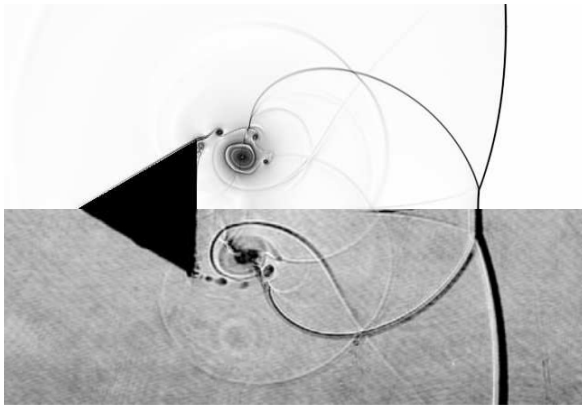

Figure 2.9: 2D shock prism interaction: schlieren images are compared of the MR method *(upper)* using analytical geometry with the experimental one *(bottom)* at $t = 138\mu s$. By (Soni 2016).

steady flow, since the prism has a constant angle of incidence along its surface, which results in the linear trajectory of TP over the reflector. The TP trajectories obtained with MR method are compared with the experimental and numerical data in Figure 2.8. As can be seen, a good agreement is found to exist for both TP_1 and TP_2.

Figure 2.9 highlights the numerical schlieren (upper half) compared with the experimental (lower half) one, and a very good level of flow details are found to be preserved conforming to the experimental result. (Soni 2016).

3

Analysis of shock-wave diffraction over double concave cylindrical wedges. Part I: Shock dynamics.

Published in: *Acta Astronautica journal*

Highlights

- Dynamics of shock diffraction over double concave surface is studied.
- The transition angle is found to be larger on the second surface for high Mach numbers.
- The flow is seen to be able to retain the past events history for high Mach numbers.
- A new scaling law for shock-velocity propagation is proposed.

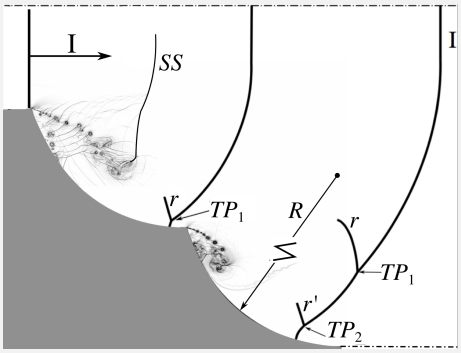

Schematic representation of a double-concave cylindrical surfaces. I: incident shock, SS: secondary shock, r, r': reflected shock on the first and the second cylinder respectively, R: cylinder surfaces radius, TP: triple point.

Acta Astronautica 172 (2020) 134–139

Contents lists available at ScienceDirect

Acta Astronautica

journal homepage: www.elsevier.com/locate/actaastro

Research paper

Analysis of shock-wave diffraction over double concave cylindrical wedges. Part I: Shock dynamics

N. Brahmi[a,*], A. Hadjadj[a], V. Soni[a], A. Chaudhuri[b]

[a] Normandie University, INSA of Rouen, CNRS, CORIA, 76000 Rouen, France
[b] Department of Civil Engineering and Energy Technology, OsloMet – Oslo Metropolitan University, Pilestredet 35, PB 4, St. Olavs Plass, 0130, Oslo, Norway

ARTICLE INFO

Keywords:
Shock diffraction
Shock waves
Shock reflection
Numerical simulation

ABSTRACT

Shock-wave diffraction over double concave cylindrical surfaces has been numerically investigated at different flow regimes by varying the incident-shock-wave Mach number from $M_s = 1.6$ (transonic) to $M_s = 4.5$ (supersonic regime). The purpose of this study is to better understand the dynamics of shock-wave structure and the associated wave configurations. A mesh-independent solution is obtained and the flow is assessed through different physical quantities (transition angles, triple points trajectories, wall-pressure and skin-friction distributions, velocity and shock location). It is found that the transition angles, from regular to Mach reflection, increase with the Mach number. This phenomenon remains almost the same over both concave surfaces for weak Mach numbers (up to $M_s = 2.5$) and becomes relatively larger on the second surface for high Mach numbers. In terms of shock dynamics, it is found that by increasing the incident incident-shock-wave Mach number to $M_s = 4.5$, unlike the first reflector, the transition from a single-triple-point (STP) wave configuration to a double-triple-point (DTP) wave configuration and back occurred on the second reflector, indicating that the flow is capable of retaining the memory of the past events over the entire process. For the shock velocity, the velocity deficit is found to be increasing with increase in M_s. A best fitting scaling law is derived, to ensure a universal decay of the shock velocity depending on the flow parameters.

1. Introduction

The interaction of shock-waves with rigid boundaries has been the subject of many investigations, since shock-wave diffraction occurs and takes place in the majority of important applications today, such as design of inflow/outflow valves in an internal combustion engine and aerospace propulsion systems. In order to understand the different phenomena resulting from these interactions such as shock-diffraction, shock-reflection, shock-focusing, shock-attenuation and the different flow structures generated by the passage of the shock-wave, several studies have been conducted (Whitham (1956) [1], Whitham (1957) [2], Whitham (1958) [3], Bird (1958) [4], Bazhenova (1978) [5], Henderson (1980) [6], Hilier (1991) [7], Sivier et al. (1992) [8], Skews et al. (2011) [9]). . Two types of shock-reflection configuration namely RR (regular reflection involving two shock waves configuration) and MR (Mach reflection involving three shock waves configuration) were first introduced by the pioneering experimental work of Ernest Mach (1878). However, no significant progress was made until the eminent work of von Neumann in the 1940s. Since then, a considerable amount of work has been carried out in order to better understand the phenomena of shock-waves reflection (Bryson and Gross [10]; Henderson and Lozzi [11]; Krassovskaya and Berezkina [12]; Soni et al. [13]; Chernyshov and Tolpegin [14]). Berezkina et al. were interested in the diffraction of shock waves by cylindrical surfaces. In a first study [23], they studied diffraction of a two-shock configuration by a convex cylindrical surface with the diffraction angle varying continuously, as opposed to [23], where the process, starting at small angles of diffraction, develops at ever-increasing angles, diffraction in [24] starts at a large angle, which progressively decreases. This distinction causes a substantial difference in the formation and development of the structures within the perturbed flow-field. Gvozdeva et al. [15] have found a new pattern of the triple-shock configuration with a negative angle of shock reflection, which is formed in a steady supersonic flow within the range of Mach numbers exceeding 3.0 and specific heat ratios below 1.4. Recently, Smirnov et al. ([16,17]) have investigated mixture ignition and detonation onset in RAM engines due to focusing of a shock wave reflected inside a cone in order to change the mode of flame propagation from slow combustion to detonation. Soni et al. [13] have conducted numerical simulations in order to understand the different wave configurations associated with the shock-wave reflection over

* Corresponding author.
E-mail address: nassim.brahmi@insa-rouen.fr (N. Brahmi).

https://doi.org/10.1016/j.actaastro.2020.01.025
Received 18 February 2019; Received in revised form 31 July 2019; Accepted 17 January 2020
Available online 31 January 2020

double-concave cylindrical reflectors. The double-concave cylinder configuration is different than that presented in Ref. [13] in terms of the orientation and entrance of the shock wave.

In this work, a parametric study is performed to determine the influence of the incident shock strength on shock-wave diffracting mechanism. We use the Navier-Stokes solver to quantify the shock strength, the dynamics of shock-waves and the different wave configurations in shock-wave diffraction over double-concave cylindrical surfaces. Furthermore, different grid resolutions are used to investigate the grid size effect on the results. The paper is organized as follows. Section 2 introduces the numerical methodology used in this study. Section 3 is devoted to introduce the problem set-up and different conditions used in this study. Section 4 is dedicated to discussing the results obtained in this study. In §4.1, the effect of shock strength on transition angle from regular to Mach reflection and triple point trajectories is investigated. The effect of shock strength on shock position and velocity is discussed in §4.2.

2. Governing equations and numerics

2.1. Governing equations

The numerical solution is obtained by solving compressible Navier-Stokes equations for an ideal gas

$$\partial_t \rho + div(\rho \mathbf{v}) = 0 \tag{1}$$

$$\partial_t (\rho \mathbf{v}) + div(\rho \mathbf{v} \otimes \mathbf{v}) + \nabla p = \nabla \tau \tag{2}$$

$$\partial_t (\rho E) + div(\rho E \mathbf{v}) + div(\rho \mathbf{v}) = \nabla(\tau \mathbf{v} + \lambda \nabla T) \tag{3}$$

$$p = (\gamma - 1)\rho e,\ E = \frac{1}{2}\left|\mathbf{v}\right|^2 + e \tag{4}$$

$$\tau = \mu\left[\nabla \otimes \mathbf{v} + (\nabla \otimes \mathbf{v})^T - \frac{2}{3}(\nabla \cdot \mathbf{v})\mathbf{I}\right] \tag{5}$$

where t stands for the time, ρ, $\mathbf{v}$, p, E, T, λ, μ, e are the density, velocity, pressure, total energy, temperature, thermal conductivity, dynamic viscosity and internal energy. The working gas is air with $\gamma = 1.4$ and Prandtl number $Pr = 0.72$. The fluid viscosity follows Sutherland's law.

To simulate the flow field, we used an in-house parallel compressible solver equipped with the adaptive multi-resolution method [18–20]. The code uses an immersed-boundary method (IBM) to handle fluid-solid interaction problems [21]. The solid body is embedded in a Cartesian grid tracked using a ray-tracing technique. Inviscid and viscous fluxes were computed using a fifth-order weighted essentially non-oscillatory (WENO 5) scheme and a fourth-order central difference formula, respectively, while the time was advanced using a third-order Runge-Kutta method [22]. The time step is computed as:

$$\Delta t = \frac{CFL}{max(\Delta t_x, \Delta t_y)} \tag{6}$$

and

$$\Delta t_x = max\left(\frac{|u| + c}{\Delta x}, \frac{2}{\Delta x^2}\frac{\mu}{\rho.\ Pr}\right) \tag{7}$$

The computations are performed with a CFL number of 0.7, which gives $\Delta t \approx 10^{-8} s$.

3. Problem set-up

Numerical simulations were conducted to understand the dynamics of shock-wave undergoing a double-concave cylindrical surfaces, a schematic representation of the solid is given in Fig. 1. As for the computational specifications, the boundary conditions were set to inlet and outlet at the left (with $\bar{h}$) and the right (with $\bar{H}$) (see Fig. 1), of the computational domain, respectively, while the top boundary and the bottom-right part of the domain are treated as symmetry plane, and the solid surface is considered with a no-slip boundary condition. In all the simulations, the geometric parameters such; $R_1 = R_2 = R = 50\ mm$ and $\omega_1 = \omega_2 = 75°$ were kept constant, the incident Mach number was varied in the range of $1.6 \leq M_s \leq 4.5$. Initially, the shock is located at $x = 5\ mm$ for all Mach numbers. Rankine-Hugoniot relations are used to set the initial conditions for left (shocked state) and right (stagnant state) states associated with the chosen M_s. Air is considered as working fluid and the initial stagnant state is assigned with temperature $T = 300K$ and pressure $p = 101.\ 3kPa$, and the flow is initialized as uniform flow. A grid dependency study is performed to determine the effect of numerics on the results. Grid convergence studies were carried out by using different levels of grid refinement. Five different meshes were used for Mach number $M_s = 1.6$. Table 1 summarizes the relevant parameters for grid sensitivity analysis.

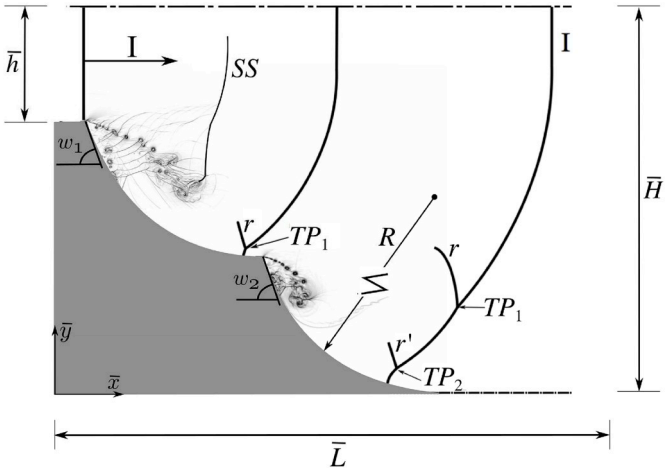

Fig. 1. Schematic representation of a double-concave cylindrical surfaces. *I*: incident shock, *SS*: secondary shock, *r*: reflected shock on the first cylinder, *r'*: reflected shock on the second cylinder, *R*: cylinder surfaces radius, *TP*: triple point, $\bar{h} = 0.32R$, $\bar{H} = 1.8R$, $\bar{L} = 3.4R$, $\bar{x} = x/R$, $\bar{y} = y/R$.

4. Results and discussion

All length scales are normalized by the concave radius $R_1 = R_2 = R = 50\ mm$ and the dimensionless time is defined as $\bar{t} = t.\ a_1/R$ where a_1 is the speed of sound of the gas initially at rest. Fig. 1 shows a planar shock-wave (*I*) with a Mach number of M_s propagating downstream and diffracting around a corner with a diffracting angle $\omega_1 = \omega_2 = 75°$. When the shock wave arrives on the edge of the first concave, the diffraction process starts. As the diffraction process evolves, the end-wall corner vortices are formed with a rolling-up of eddies that are convected away from the cavity entrance. These corner instabilities are characterized by the formation of a primary vortex that is followed by a secondary one. The key mechanism behind the appearance of this secondary near-wall instability are a large enough advection velocity generated by the cavity boundary layer. It is found that the interaction of this secondary instability with the primary vortex

Table 1
Different grid resolution used, for shock-wave Mach number $M_s = 1.6$ (MP: million points).

Grid	$\Delta x_{min}\ (\mu m)$	$\Delta y_{min}\ (\mu m)$	number of points (MP)
$\mathscr{G}_0$	95	88	1.83
$\mathscr{G}_1$	60	50	5.04
$\mathscr{G}_2$	40	40	8.84
$\mathscr{G}_3$	30	29	17.3
$\mathscr{G}_4$	20	21	33.55

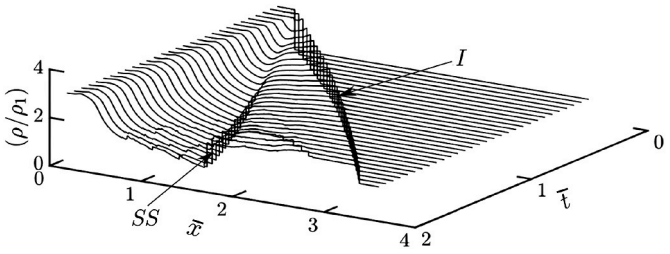

Fig. 2. Evolution of density ratio along $\bar{y} \approx 1.58$ for $M_s = 2.0$, with $\bar{t} = ta_1/R$.

Table 2
Transition angles, from regular to Mach reflection (RR → MR), over the two concave surfaces for different grid resolution for $M_s = 1.6$.

	θ_1^{tr}	θ_2^{tr}
$\mathscr{G}_0$	9. 6°	9. 7°
$\mathscr{G}_1$	10. 7°	10. 8°
$\mathscr{G}_2$	11. 8°	11. 8°
$\mathscr{G}_3$	12. 7°	12. 6°
$\mathscr{G}_4$	12. 7°	12. 6°

core in the upstream part of the cavity is one of the main sources of excitations and possible transition to turbulence and appearance of secondary shocks (*SS*). When the conditions are gathered (the angle between the incident shock wave and the surface of the first concave and the Mach number), reflection of the shock wave takes place and we can see appearance of reflected shocks (*r* for the first concave, *r′* for the second concave) and triple points (TP_1 for the first concave, TP_2 for the second concave), the details of shock reflection are discussed on section 4.1.

Fig. 2 shows density ratio evolution along the axis $\bar{y} \approx 1.58$ for $M_s = 2$, in the space-time diagram. Because of the area increase, the flow and the shock-wave undergo an expansion, the propagation of the incident or primary shock-wave (*I*) in the medium at rest can be clearly observed. Eventually, a left-running (with respect to the fluid) secondary shock-wave (*SS*) appears and is carried to the right because of the supersonic carrier flow.

4.1. Transition angle from regular to Mach reflection

In this section, we present the mesh sensitivity analysis with respect to the transition angle for Regular to Mach reflection (RR → MR). Table 2 shows that the transition angle is the same in both surfaces for all the cases, and it begins to be independent of grid resolution from $\mathscr{G}_3$. Where θ_1^{tr} and θ_2^{tr} are respectively the transition angles in the first and second concave surfaces. Fig. 3 represents non-dimensional wall pressure and skin friction distribution for different grid resolution for

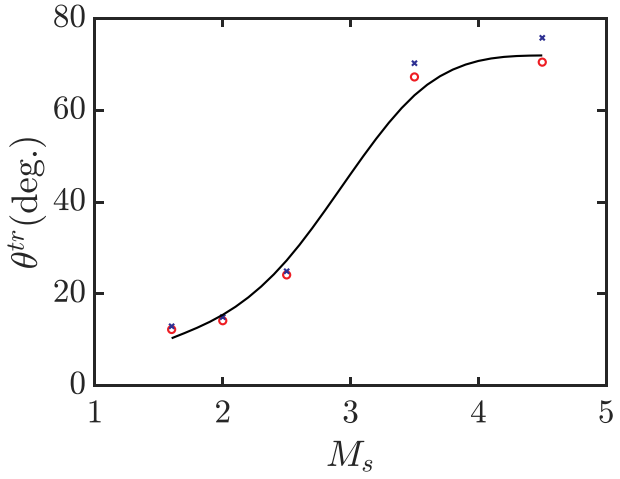

Fig. 4. Transition angles from regular to Mach reflection (RR → MR), over: ◦ the first concave surface; × the second concave surface; - fitting curve, *vs*. Incident-shock-wave Mach numbers.

$M_s = 1.6$. It can be seen that the two parameters start to be mesh independent from $\mathscr{G}_3$. Based on these observations a mesh resolution of $\mathscr{G}_4$ is used for the rest of the study.

Fig. 4 shows the RR → MR transition angles, θ^{tr}, over the first and the second concave surfaces. As it can be seen, θ^{tr} increases for larger shock-wave Mach numbers M_s. It is also interesting to note that θ^{tr} is almost the same for both surfaces, except for $M_s = 3.5$ and 4.5 in which θ^{tr} is relatively larger on the second surface (approximately 7% for $M_s = 4.5$ and 4% for $M_s = 3.5$). Soni et al. in their study [13] found θ^{tr} to be larger on the second cylindrical reflector (for Mach numbers up to $M_s = 2.5$) and they noted that this behavior can be perceived as resulting from the fact that the flow regions behind the Mach stems are subsonic, hence the information can be communicated through them.

In order to track the triple points, the ℓ^2- norm of the pressure gradient is computed, which translates to the analytical formula for the two-dimensional case at the *n*th time step as;

$$TP^n = \sqrt{\left(\frac{\partial p}{\partial x}\right)_n^2 + \left(\frac{\partial p}{\partial y}\right)_n^2} \tag{8}$$

Applying max (TP^n, TP^{n-1}) for each time step would give the entire trajectories of the triple points[13]. Figs. 5 and 6 show the shock reflection process on the second concave, for the Mach numbers: 3.5 and 4.5 respectively . In Figs. 5(a) and 6(a) we can see the presence of a single triple point (TP_2), this configuration is known as a STP (single triple point) configuration. A little further a second triple point is formed (TP_3 in Fig. 5(b) and 6(b)). This makes a transition from a

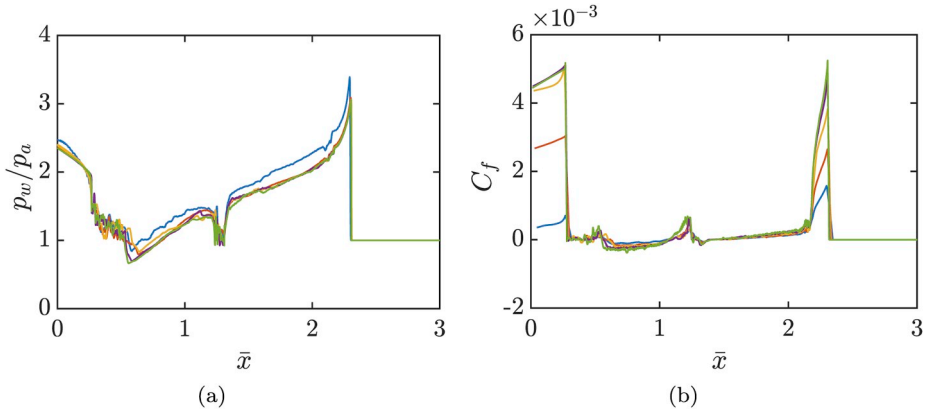

Fig. 3. (a): Non-dimensional wall-pressure distribution, (b): skin friction distribution at t = 294 μs for different grid resolutions at $M_s = 1.6$ ($\mathscr{G}_0$, $\mathscr{G}_1$, $\mathscr{G}_2$, $\mathscr{G}_3$, $\mathscr{G}_4$).

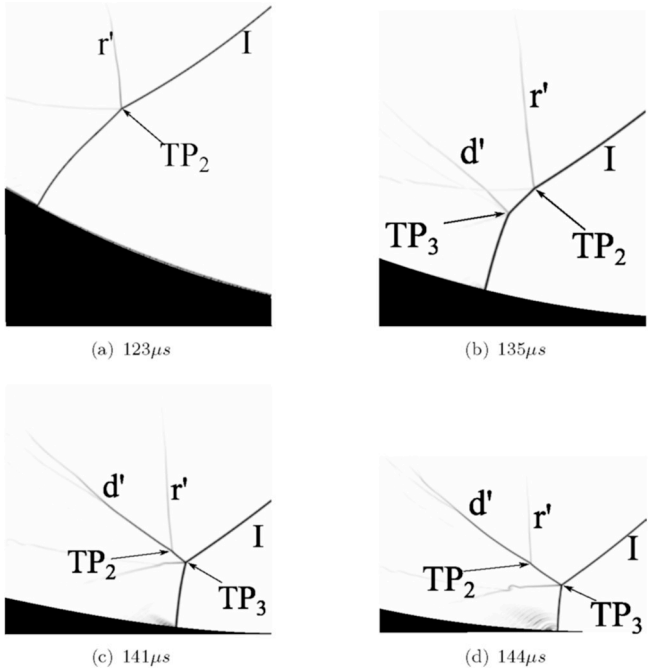

Fig. 5. Numerical schlieren pictures for $M_s = 3.5$ for the second concave surface, at different instant. r' and d': reflected and additional shocks created on the second concave surface, respectively, I: incident shock, TP: triple point.

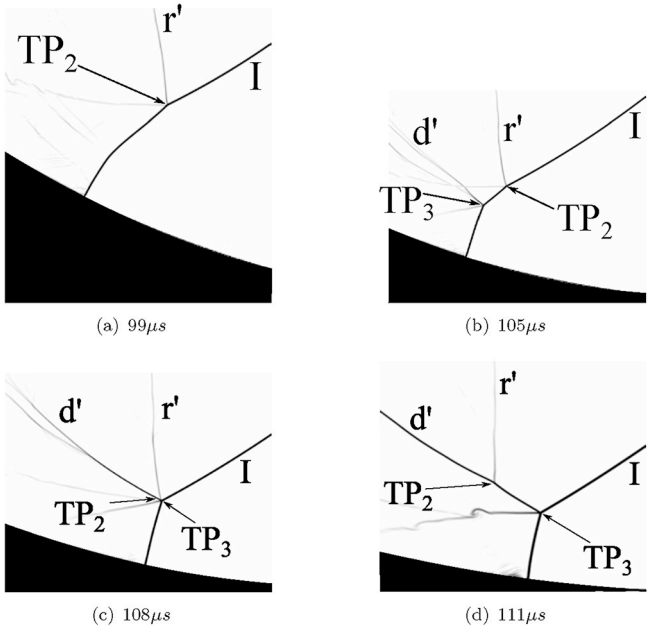

Fig. 6. Numerical schlieren pictures for $M_s = 4.5$ for the second concave surface at different instant. For legend, see caption of Fig. 5.

single-TP configuration to a double-TP configuration (STP → DTP transition) . Fig. 7 depicts the Triple Points trajectories obtained for the five shock-wave Mach numbers used in this study $M_s = 1.6$; $M_s = 2.5$; $M_s = 3.5$ and $M_s = 4.5$ (result for $M_s = 2.0$ is not shown as it is almost identical to that of $M_s = 2.5$). For the first surface and for the relatively low shock-wave Mach number ($M_s = 1.6$; 2.5) (Fig. 7(a) and (b)), a Mach reflection at the end of the surface is observed with a weak reflected shock-wave. For the higher mach numbers ($M_s = 3.5$; 4.5) (Fig. 7(c) and (d)) we observe a regular reflection (RR) just at the beginning of the surface, a little further on, a transition to a Mach reflection (MR) (RR → MR) takes place to give rise to a Mach reflection with stronger reflected shock-waves. For the second surface there is a change in behavior for the two shock-wave Mach numbers; $M_s = 3.5$ and 4.5 while for the shock-wave Mach numbers; $M_s = 1.6$, 2.0 and 2.5 the behavior of the shock-wave remains the same as that of the first surface. For the shock-wave Mach number $M_s = 1.6$, 2.0 and 2.5, we notice the apparition of a Mach reflection (MR) at the end of the surface. By increasing the shock-wave Mach number to 3.5 and 4.5, (Fig. 7(c) and (d)) the behavior is completely different. At the beginning of the second surface, we notice the appearance of a regular reflection (RR) followed by a transition to a Mach reflection (MR) (RR → MR), characterized by the formation of a triple point (it is a STP configuration). Further, at the end of the surface, we notice the appearance of a second triple point (which is a DTP configuration) appearing in this case. This makes a transition from a STP to a DTP configuration. For $M_s = 4.5$ and as the shock-wave moves further up, the two triple points merge together to give birth to a single-TP configuration again. So, we have STP → DTP → STP configuration. Another point to note is that the Mach stem associated with TP_3 for the $M_s = 4.5$ is more substantial than the one seen for $M_s = 3.5$.

4.2. Shock-wave propagation and its attenuation

Here we present the possible influence of grid resolution on the shock front position and velocity by using different meshes. We compared the values of $\bar{x}_s$ and W_s/W_s^i (where W_s is the velocity of the incident shock and W_s^i is the initial velocity of the incident shock) obtained by using five different refinements, and found their difference to be negligible (see Fig. 8(a) and (b) respectively). This indicates that the obtained solution is mesh independent. Fig. 8(a) shows the time evolution of the transmitted shock wave. After an initial linear evolution, the evolution of the transmitted shock wave becomes non-linear the velocity of the transmitted shock wave decreased as can be seen in Fig. 8(b), where, in the beginning before reaching the corner, the transmitted shock-wave moves with a constant velocity (equal to the initial velocity (W_s^i), the value given by the shock-tube theory (black line in Fig. 8(b), $W_s/W_s^i = 1$)). Once the shock-wave reaches the corner of the double concave, its velocity starts to decrease due to the deceleration of the transmitted shock-wave.

We will now discuss the evolution (speed and position) of the shock wave propagating within the double concave surfaces, by changing the incident shock-wave Mach number M_s and using the mesh resolution $\mathscr{G}_4$. Fig. 9(a) illustrates the evolution of the incident shock wave location ($\overline{x_s}$) as a function of dimensionless time ($\bar{t}$). By differentiating x_s with respect to t, one can easily obtain the dimensionless velocity (W_s/W_s^i) of the shock (Fig. 9(b)), for all shock-waves strength, the speed of the incident shock wave starts with a constant value (equal to the initial velocity) ($W_s/W_s^i = 1$), and decreases steadily in time. Furthermore, its rate of change is at first very large, but becomes smaller as it propagates through the double concave surfaces, and as we can see in Fig. 9(b), the speed of the incident shock wave starts to decrease earlier for stronger shock waves (highest shock-waves Mach numbers) and this result is expected because the shock waves with high shock-wave Mach numbers reach the corner of the double concave first, and the velocity deficit is increasing with the shock-wave Mach number.

The shock trajectory and velocity are plotted using dimensionless coordinates. By finding the appropriate dimensionless time, it was possible to show the data from different simulations with different Mach numbers collapse into a single curve. From the data analysis, the following relationship is found:

$$\tilde{t} = \frac{W_s^i}{R}\phi(\gamma, M_s)\, t \tag{9}$$

The scaling function $\phi(\gamma, M_s)$ is defined as:

$$\phi(\gamma, M_s) = (M_s + 1)\, ln(M_s + 1)^{1/\gamma} - \frac{\gamma - 1}{\gamma}(M_s^2 - 1) \tag{10}$$

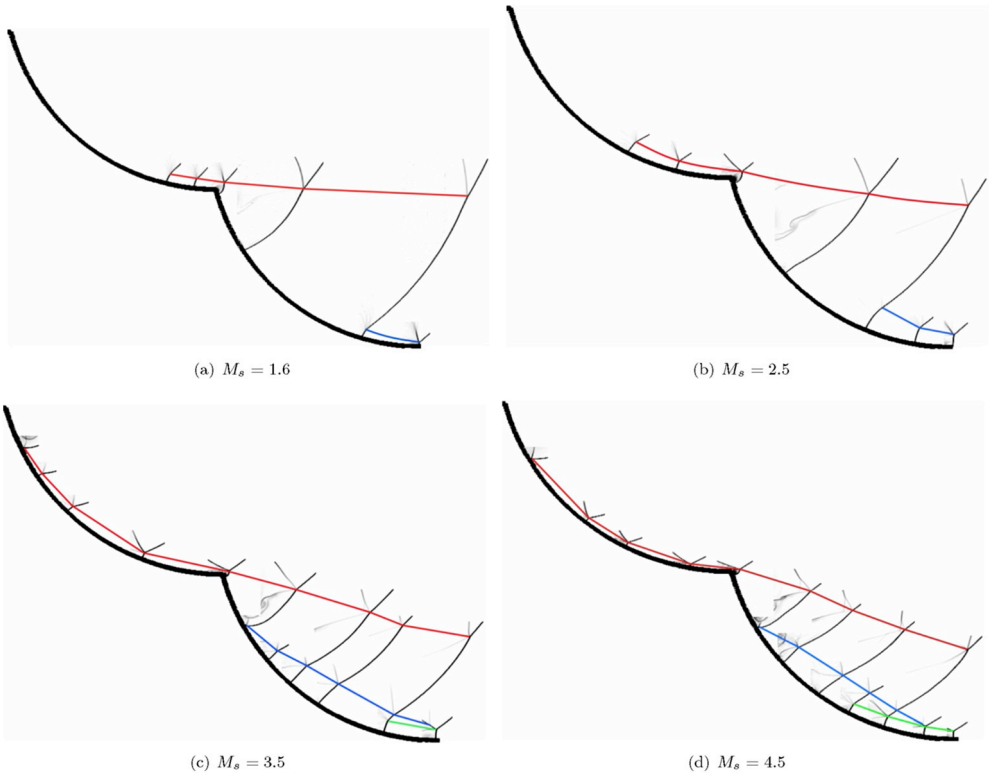

Fig. 7. Trajectories of the triple points for different shock-wave Mach numbers: (a): $M_s = 1.6$; (b): $M_s = 2.5$; (c): $M_s = 3.5$; (d): $M_s = 4.5$; (—: TP_1; —: TP_2; —: TP_3).

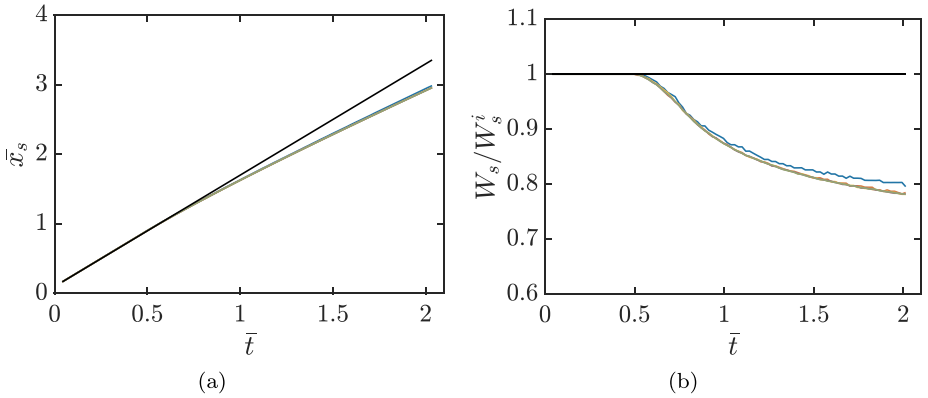

Fig. 8. Non-dimensional; (a); shock position and (b); shock velocity for different mesh resolutions; (— $\mathcal{G}_0$, — $\mathcal{G}_1$, — $\mathcal{G}_2$, — $\mathcal{G}_3$, — $\mathcal{G}_4$, — shock position and velocity given by the piston theory).

By applying this normalization (Equation (9)), all results (shock position, shock velocity for different Mach numbers) collapse together into single curve and the results are presented in Fig. 9(c) and (d) respectively.

5. Summary

In this paper, shock-waves diffraction over double-cylindrical wedges (the centre of the first concave surface is at higher y-cordinate than the second one) have been investigated. Numerical simulations were carried out to study the dynamics of shock wave with regards to the incident-shock-wave Mach number. Different grid resolutions were used to investigate the grid size effect on the numerical solutions and it was found that the quantities studied (transition angle, pressure and skin friction distributions at the wall, shock position and velocity) are mesh independent from certain resolution ($\Delta x_{min} = 20\mu m$, $\Delta y_{min} = 21\mu m$). The transition angle increases with Mach number, and was found to be almost the same over the two concave surfaces for weak Mach numbers (up to $M_s = 2.5$) and to be relatively larger on the second surface for high Mach numbers (approximately 7% for $M_s = 4.5$, 4% for $M_s = 3.5$), the behavior of the shock wave is completely different for $M_s = 4.5$, at the end of the second concave surface we have a STP→DTP→STP configuration, indicating that the flow was capable of retaining the memory of the past events over the entire process for high Mach numbers. In terms of shock's velocity, the velocity deficit was found to be increasing with Mach number. The shock position and shock velocity are proportional to the shock initial velocity reduced by a scaling function that depending on the incident shock-wave Mach number, the heat capacity ratio and the concave surface radius. The proposed scaling was tested in the range of M_s ($1.6 < M_s < 4.5$), for heat ratio of 1.4 and concave surface radius of $50mm$.

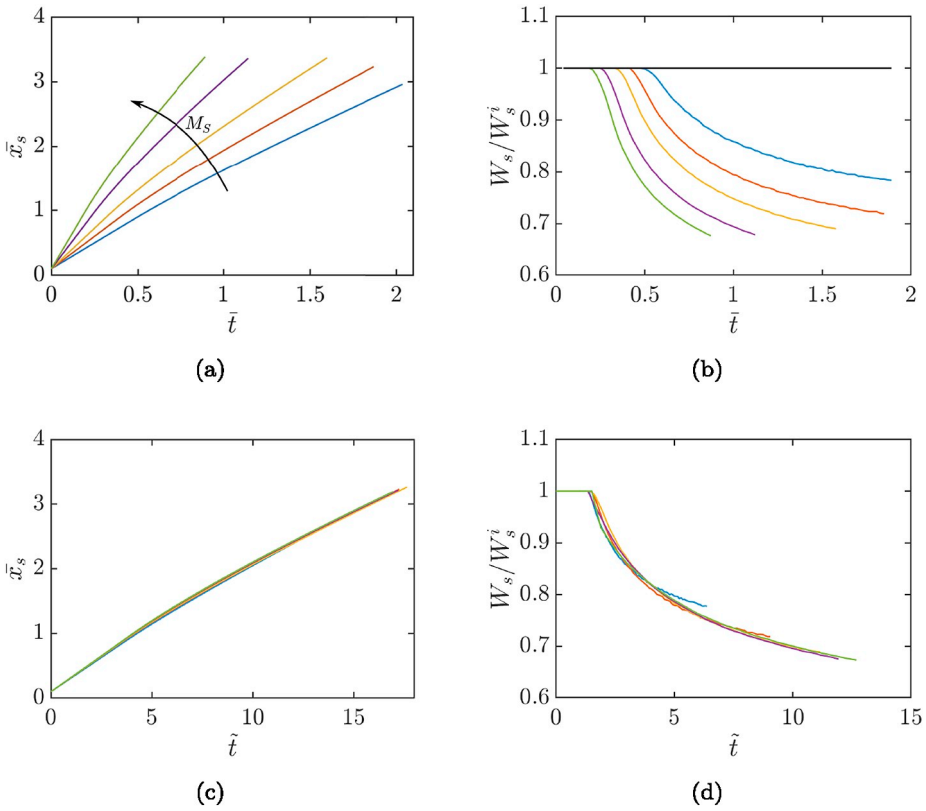

Fig. 9. Normalized; (a): shock-wave position; (b): shock-wave velocity; (c): Normalized shock-wave position *vs*. normalized time and (d): normalized shock-wave velocity *vs*. normalized time, for different shock-wave Mach numbers ($M_s = 1.6$, $M_s = 2.0$, $M_s = 2.5$, $M_s = 3.5$, $M_s = 4.5$, shock velocity given by the piston theory).

Acknowledgments

N. Brahmi gratefully acknowledges support from the Algerian Government through a PHD Fellowship. Computational facilities from 'Centre Régional Informatique et d'Applications Numériques de Normandie (CRIANN)', Rouen, France under allocation 1998022, are acknowledged.

References

[1] G.B. Whitham, On the propagation of weak shock waves, J. Fluid Mech. 1 (3) (1956) 290–318.
[2] G.B. Whitham, A new approach to problems of shock dynamics part i two-dimensional problems, J. Fluid Mech. 2 (1957) 145–171.
[3] G.B. Whitham, On the propagation of shock waves through regions of non-uniform area or flow, J. Fluid Mech. 4 (1958) 337–360.
[4] G.A. Bird, The effect of wall shape on the degree of reinforcement of a shock wave moving into a converging channel, J. Fluid Mech. 5 (1959) 60–66.
[5] T.V. Bazhenova, L.G. Gvosdeva, Y.V. Zhilin, Change in the shape of the diffracting shock wave at a convex corner, Acta Astronaut. 6 (1951) (1979) 401–412.
[6] L.F. Henderson, On the whitham theory of shock-wave diffraction at concave corners, J. Fluid Mech. 99 (4) (1980) 801–811.
[7] R. Hillier, Computation of shock wave diffraction at a ninety degrees convex edge, Shock Waves 1 (2) (1991) 89–98.
[8] S. Sivier, E. Loth, J. Baum, R. Löhner, Vorticity produced by shock wave diffraction, Shock Waves 2 (1) (1992) 31–41.
[9] B. Skews, A. Blitterswijk, Shock wave reflection off coupled surfaces, Shock Waves 21 (6) (2011) 491.
[10] A.E. Bryson, R.W.F. Gross, Diffraction of strong shocks by cones, cylinders, and spheres, J. Fluid Mech. 10 (1) (1961) 1–16.
[11] L.F. Henderson, A. Lozzi, Experiments on transition of mach reflexion, J. Fluid Mech. 68 (1) (1975) 139–155.
[12] I.V. Krassovskaya, M.K. Berezkina, Mechanism of formation of reflection configurations over concave surfaces, Shock Waves 27 (3) (2017) 431–439.
[13] V. Soni, A. Hadjadj, A. Chaudhuri, G. Ben-Dor, Shock-wave reflections over double-concave cylindrical reflectors, J. Fluid Mech. 813 (2017) 70–84.
[14] M.V. Chernyshov, O.A. Tolpegin, Optimal regular reflection of oblique shocks, Acta Astronaut. (2019) 1–7, https://doi.org/10.1016/j.actaastro.2019.01.015.
[15] L. Gvozdeva, M. Silnikov, S. Gavrenkov, Triple shock configurations with negative angle of reflection, Acta Astronaut. 116 (2015) 36–42.
[16] N.N. Smirnov, O.G. Penyazkov, K.L. Sevrouk, V.F. Nikitin, L.I. Stamov, Onset of detonation in hydrogen-air mixtures due to shock wave reflection inside a combustion chamber, Acta Astronaut. 149 (2018) 77–92.
[17] N.N. Smirnov, O.G. Penyazkov, K.L. Sevrouk, V.F. Nikitin, L. Stamov, V. Tyurenkova, Detonation onset following shock wave focusing, Acta Astronaut. 135 (2017) 114–130.
[18] V. Soni, Parallel Adaptive Multiscale Numerical Methods for Complex Compressible Flows, PHD Thesis, INSA Rouen, FRANCE, 2016.
[19] V. Soni, A. Hadjadj, O. Roussel, On the use of adaptive multiresolution method with time-varying tolerance for compressible fluid flows, Shock Waves (2017) 1–14.
[20] V. Soni, A. Hadjadj, O. Roussel, G. Moebs, Parallel multi-core and multi-processor methods on point-value multiresolution algorithms for hyperbolic conservation laws, J. Parallel Distr. Comput. 123 (2019) 192–203.
[21] A. Chaudhuri, A. Hadjadj, A. Chinnayya, On the use of immersed boundary methods for shock/obstacle interactions, J. Comput. Phys. 230 (5) (2011) 1731–1748.
[22] A. Chaudhuri, A. Hadjadj, A. Chinnayya, S. Palerm, Numerical study of compressible mixing layers using high-order WENO schemes, J. Sci. Comput. 47 (2) (2011) 170–197.
[23] M. Berezkina, I.V. Krasovskaya, D.Kh. Ofengeim, Diffraction of a Two-Shock Configuration by a Convex Cylindrical Surface, Technical Physics 51 (2006) 827–833.
[24] M. Berezkina, I.V. Krasovskaya, D.Kh. Ofengeim, Diffraction of a Two-Shock Configuration by a Concave Cylindrical Surface. Technical Physics 52 (2007) 1271–1280.

4

Analysis of shock-wave diffraction over double cylindrical wedges. Part II: Vorticity generation

Published in: *Acta Astronautica journal*

Highlights

- Vorticity generation in shock diffraction process is investigated numerically.
- The stretching of vorticity due to flow compressibility dominates the vorticity dynamics.
- The effect of the first concave surface is investigated in terms of shock attenuation.

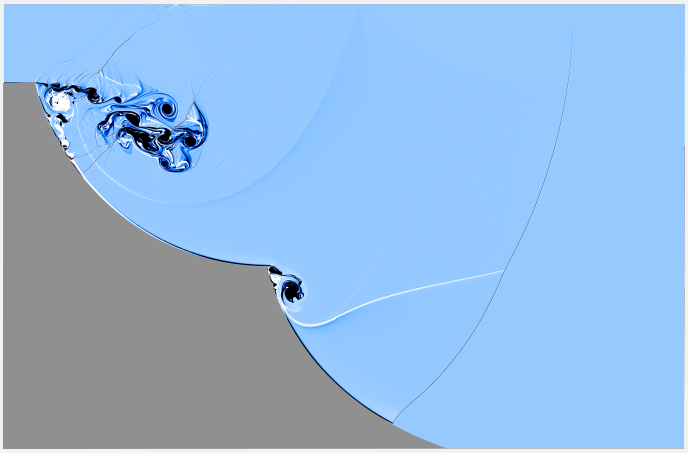

Numerical shleiren picture of a shock wave undergoing a double cylindrical wedges.

Acta Astronautica 172 (2020) 140–150

Contents lists available at ScienceDirect

Acta Astronautica

journal homepage: www.elsevier.com/locate/actaastro

Research paper

Analysis of shock-wave diffraction over double cylindrical wedges. Part II: Vorticity generation

N. Brahmi[a,*], A. Hadjadj[a], V. Soni[a], A. Chaudhuri[b]

[a] Normandie University, INSA of Rouen, CNRS, CORIA, 76000, Rouen, France
[b] Department of Civil Engineering and Energy Technology, OsloMet – Oslo Metropolitan University, Pilestredet 35, PB 4, St. Olavs Plass, 0130, Oslo, Norway

ARTICLE INFO

Keywords:
Shock wave
Shock diffraction
Vorticity
Vorticity transport
Numerical simulation

ABSTRACT

The unsteady aspect of turbulent flow structures generated by a shock-wave diffraction over double cylindrical wedges, with initial diffracting angle of 75°, are numerically investigated by means of two-dimensional high-fidelity numerical simulation. Different incident-shock-Mach numbers, ranging from transonic to supersonic regimes, are considered. Unlike previous studies where only the total vorticity production is evaluated, the current paper offers more insights into the spatio-temporal behavior of the circulation by evaluating the evolution of the instantaneous vorticity equation balance. The results show, for the first time, that the diffusion of the vorticity due to the viscous effects is quite important compared to the baroclinic term for low Mach numbers regimes, while this trend is inverted for higher Mach numbers regimes. It is also found that the stretching of the vorticity due to the compressibility effects plays an important role in the vorticity production. In terms of pressure impulses, the effect of the first concave surface on the shock strength has been quantified at both earlier and final stages of the shock diffraction process. Unlike the overpressure, the static and the dynamic pressure impulses are shown to be significantly reduced at the end of the first concave surface.

1. Introduction

The unsteady evolution of vortex rings produced by a shock diffraction undergoing a sudden expansion area is one of the most fascinating phenomenon in high-speed flows. This process was observed many decades ago [1–3], with different levels of qualitative description [4] and numerical modelling [5–7]. For instance, Skews [1] have discussed the behavior of disturbances produced in the perturbed region caused by the passage of a shock wave, whose Mach number varies from 1.0 to 5.0, through a convex corner. The experimental results of this study have shown that the velocities of the contact surface and the secondary shock become independent of the corner angles greater than 75°. Sun and Takayama [5] have evaluated numerically the vorticity production in a shock-wave diffraction problem over convex corners, with angles varied from 5° to 180°. The authors proposed an analytical model to evaluate the total vorticity production generated by the slipstream. They found that the rate of vorticity production is always increasing with the corner angle and the shock strength. They also reported that the slipstream is at the origin of the total vorticity generation and it can be the more dominating factor in producing vorticity in compressible flows in comparison to baroclinic effects. In another study, Sun and Takayama [8] have investigated the formation of secondary shock waves behind the incident shock wave. Accordingly, the threshold shock-wave Mach number was found to be $M_s = 1.346$ for a gas with $\gamma = 1.4$, when neglecting viscous effects on the formation of this secondary shock waves.

Quinn and Kontis [9] have investigated a shock-wave diffraction around a 172° corner at $M_s = 1.46$ using both numerical simulations and experimental visualizations. Their numerical study showed that although the evolution of the shear layer was obtained for very fine mesh, some very fine flow structures were under predicted. Cai et al. [10] have investigated the effect of back-pressure on the shock train location and its structure in a straight isolator. It is shown that the structure of the shock train largely depends on the relative Mach number and is very sensitive to it. Concerning the average back-pressure, it has a great influence on the location of the shock train in the oscillating region, while its amplitude has a noticeable effect on the size of this oscillating region. Reeves and Skews [11] have investigated both numerically and experimentally the unsteady aspects of three-dimensional shock-wave diffraction phenomena. They found that the trends of circulation production correlated quite well with those obtained from the two-dimensional diffraction case. Furthermore, they showed that the rate of vorticity production tends to be constant once the incident shock wave had fully diffracted over the surface edge. Finally, the shape of the

* Corresponding author.
E-mail address: nassim.brahmi@insa-rouen.fr (N. Brahmi).

https://doi.org/10.1016/j.actaastro.2020.02.017
Received 28 January 2020; Received in revised form 7 February 2020; Accepted 9 February 2020
Available online 18 February 2020

Nomenclature

E	total energy per unit mass
e	internal energy per unit mass
I_p	static-pressure impulse
I_{pd}	dynamic-pressure impulse
M_s	incident-shock-Mach number
$\mathscr{P}$	normalized overpressure
Pr	Prandtl number
p	static pressure
$\mathscr{R}$	universal gas constant
R	concave radius
T	temperature
t	time
$\mathbf{v}$	velocity vector

Greeks

Γ	vorticity circulation
γ	heat capacity ratio
λ	thermal conductivity
μ	dynamic viscosity
ρ	density
ω	local vorticity
ω_1	angle of the first wedge
ω_2	angle of the second wedge
ω_c	convection vorticity term
ω_t	unsteady vorticity term

Abbreviations

BAR	baroclinic torque
DFV	diffusion of vorticity due to viscosity
IBM	immersed-boundary method
I	incident shock wave
LS	lambda shock
PV	primary vortex
r	reflected shock wave
SLI	shear-layer instabilities
SS	secondary shocks
SV	secondary vortex
VSC	stretching of vorticity due to compressibility
VSG	stretching/tilting of vorticity due to velocity gradients
VTE	vorticity transport equation
WENO	weighted essentially non-oscillatory

diffracting edge appeared to have no significant impact on the results.

Abate and Shyy [12] studied the dynamics of shock-wave diffraction using the vorticity transport equation. They discussed the link between high-strain rates resulting from the expansion corner to the solenoidal dissipation rates and the stress rates to the dilatational dissipation rates of turbulent kinetic energies. The baroclinic torque enhances the vorticity generation in such interaction. Their study indicates that both viscous effects and small-scale turbulent dissipation are important for the evolution of the primary vortex as well as the small vortices generated by the Kelvin-Helmholtz instability. Zhao et al. [13] have investigated the shock wave focusing process with shock-turbulence interaction in a parabolic cavity with various intensity of shock and vortex strength. Their numerical results show that the net dilatational vorticity is the most dominant part in vorticity transport, followed by the baroclinic vorticity and the viscous vorticity generation.

Gnani et al. [4] have used experimental schlieren photography to qualitatively evaluate the development of a shock-wave diffraction around sharp and curved splitters. Recently, Chaudhuri and Jacobs [7] performed numerical analysis of shock-wave diffraction over a sharp splitter plate. The objective was to address a detailed analysis of the flow evolution using the probability density functions of various enstrophy equation parameters as well as the invariants of the velocity gradient tensor. Their study reveals the mechanism of unwinding of vortices and its link with the divergence of the Lamb vector.

Additionally, Tseng and Yang [6] investigated numerically shock-wave diffraction around a convex corner by solving both Euler and Navier-Stokes equations. The vorticity production formed during the shock-wave diffraction and the subsequent interaction between the reflected shock and the main vortex core have been analyzed. Different circulation production rates are observed between Euler and Navier-Stokes solutions as a result of the vorticity contribution from the boundary layer and the secondary vortex. It was also found that the reflection influences the rate of vorticity production, which is found to be dependent on the strength of the incident shock wave and the diffracting angle.

Chaudhuri et al. [14] used an immersed boundary (IB) method to study the interaction of the moving shock through an array of cylinder matrix. Their analysis confirmed earlier findings of Sun and Takayama [5], where the baroclinic production of the vorticity is found to be feeble. Recently, Soni et al. [15] have conducted numerical investigations of shock-wave reflection over double-concave cylindrical reflectors, where new shock reflection topologies were found.

The aim of the present study is to further analyze the evolution of the instantaneous vorticity production and the flow structure in shock diffraction problem.

2. Governing equations and numerics

The compressible Navier-Stokes equations for an ideal gas are given by:

$$\partial_t \rho + div(\rho\, \mathbf{v}) = 0 \tag{1}$$

$$\partial_t (\rho\, \mathbf{v}) + div(\rho\, \mathbf{v} \otimes \mathbf{v}) + \nabla p = \nabla \tau \tag{2}$$

$$\partial_t (\rho\, E) + div(\rho\, E\, \mathbf{v}) + div(\rho\, \mathbf{v}) = \nabla(\tau\, \mathbf{v} + \lambda \nabla T) \tag{3}$$

$$p = (\gamma - 1)\rho\, e, \qquad E = \frac{1}{2}\left|\mathbf{v}\right|^2 + e \tag{4}$$

$$\tau = \mu\left[\nabla \otimes \mathbf{v} + (\nabla \otimes \mathbf{v})^T - \frac{2}{3}(\nabla \cdot \mathbf{v})\mathbf{I}\right] \tag{5}$$

where t stands for the time, ρ, $\mathbf{v}$, p, E, T, λ, μ, e are the density, velocity vector, pressure, total energy per unit mass, temperature, thermal conductivity, dynamic viscosity and internal energy, respectively. The working gas is air with $\gamma = 1.4$ and Prandtl number $Pr = 0.72$. The fluid viscosity follows Sutherland's law.

To simulate the flow field, we used an *in-house* compressible parallel solver equipped with adaptive multi-resolution method [16,17] for mesh refinement. The code uses an immersed-boundary method (IBM)

Table 1
Different grid resolutions used for a given incident shock-wave Mach number of $M_s = 1.6$ (MP: million points).

Grid	$\Delta x_{min}\,(\mu m)$	$\Delta y_{min}\,(\mu m)$	number of points (MP)
$\mathscr{G}_0$	95	88	1.83
$\mathscr{G}_1$	60	50	5.04
$\mathscr{G}_2$	40	40	8.84
$\mathscr{G}_3$	30	29	17.3
$\mathscr{G}_4$	20	21	33.55

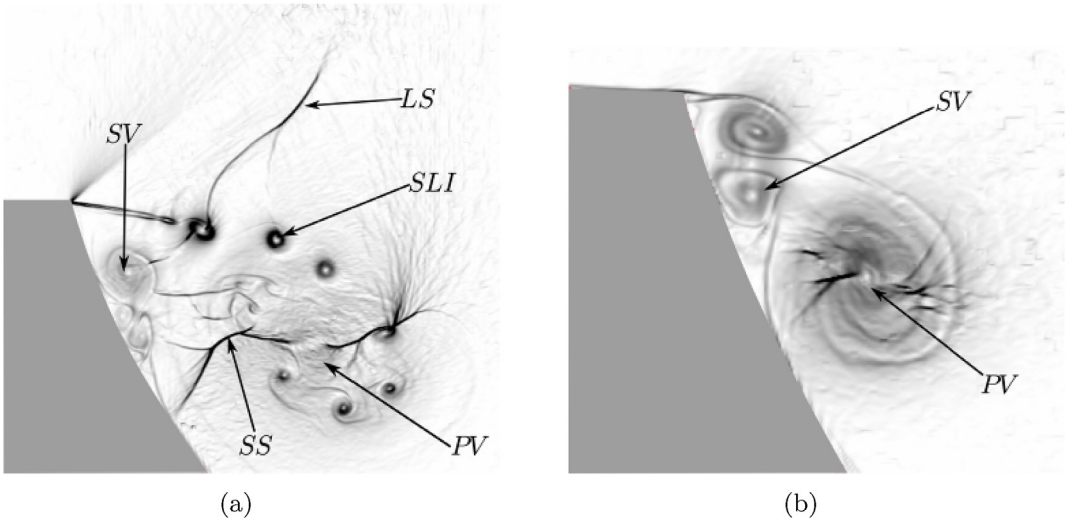

Fig. 1. Numerical schlieren pictures for $M_s = 1.6$ (a): first concave at $t = 184\ \mu s$ (b): second concave at $t = 292\ \mu s$. PV: Primary vortex, SV: Secondary vortex, LS: Lambda shock, SLI: Shear layer instabilities, SS: secondary shock (shocklets).

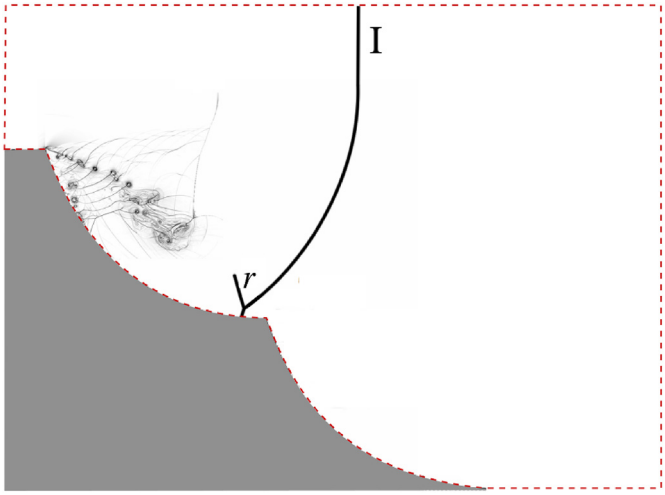

Fig. 2. Schematic representation of double concave surfaces, – – – integral path L, I: incident shock wave, *r*: reflected shock wave.

to handle fluid-solid interaction problems [14,18]. The solid body is embedded into a Cartesian grid and tracked using a ray-tracing technique. Inviscid and viscous fluxes are computed using a fifth-order weighted essentially non-oscillatory (WENO 5) scheme and a fourth-order central difference formula, respectively, while the time is advanced using a third-order Runge-Kutta method [19].

3. Problem set-up

As in Brahmi et al. [20], a two-dimensional problem of shock diffraction over double concave geometry, with constant radius of $R = 50\ mm$ and wedge angles $\omega_1 = \omega_2 = 75°$, is considered. As for the computational specifications, the boundary conditions were set to inlet and outlet at the left and the right sides of the computational domain, respectively, while the top and the bottom-right boundaries are considered as symmetry planes. On the solid surface, no-slip boundary conditions are applied. The incident-shock-Mach number was varied from 1.6 to 4.5. For all those Mach numbers, the shock is initially located 5 *mm* ahead of the first concave surface corner. Rankine-Hugoniot relations are used to fix the initial conditions for both left (shocked gas) and right (stagnant flow) states at a given M_s. Air is considered as a working fluid and the initial stagnant flow is assigned with temperature $T_0 = 300\ K$ and pressure $p_0 = 101.3\ kPa$. Given the sensitivity of the phenomena to the grid resolution, a grid dependency study is conducted in order to determine the grid resolution effect on the results. Five different meshes were used for $M_s = 1.6$, as summarized in Table 1.

4. Results and discussion

Fig. 1(a) and (b) show the flow structures behind the diffracting shock wave for the first and the second concave surfaces, respectively. Shortly after the penetration of the shock into the cavity, the expanding flow evolves into a complicated system of distorted and secondary shocks with separated regions and vortices formation. As shown in Fig. 1, an end-wall corner vortex (PV) is formed at $M_s = 1.6$ with a rolling-up of eddies that are convected away from the concave entrance as the diffraction process evolves. In addition to this important primary vortex, a secondary instability (SV) appears along the surface wall. The Reynolds number, based on the shocked flow properties (density, speed of sound, viscosity in the upstream of the shock and the radius of curvature *R*), is of the order of 10^6.

4.1. Vorticity production

In order to investigate the dynamics of the shear-layer formation, the vorticity production is first analyzed in term of total circulation Γ as:

$$\Gamma = \int_s \omega\, ds = \int_L u\, dl \tag{6}$$

where the integral contour (path L) is taken along the boundary so that to enclose the perturbed region behind the shock wave. The integral contour is depicted in Fig. 2 by a dashed red line. For better characterization of the vorticity production in shock-wave diffraction, the ratio of circulation to time, Γ/t, is used. The rate of circulation production is related to the incident shock-Mach number M_s, the diffraction angle and the gas properties. For a given gas and diffraction angle, the ratio Γ/t can be uniquely determined as a function of M_s [5] as:

$$\frac{\Gamma}{t} = f(M_s) \tag{7}$$

In this paper, the calculation of the circulation is directly obtained from the summation of the vorticity over each individual surface area. In general, the calculation of the circulation is performed only in the perturbed region behind the shock. However, in this study the total amount of circulation is calculated over the entire computational

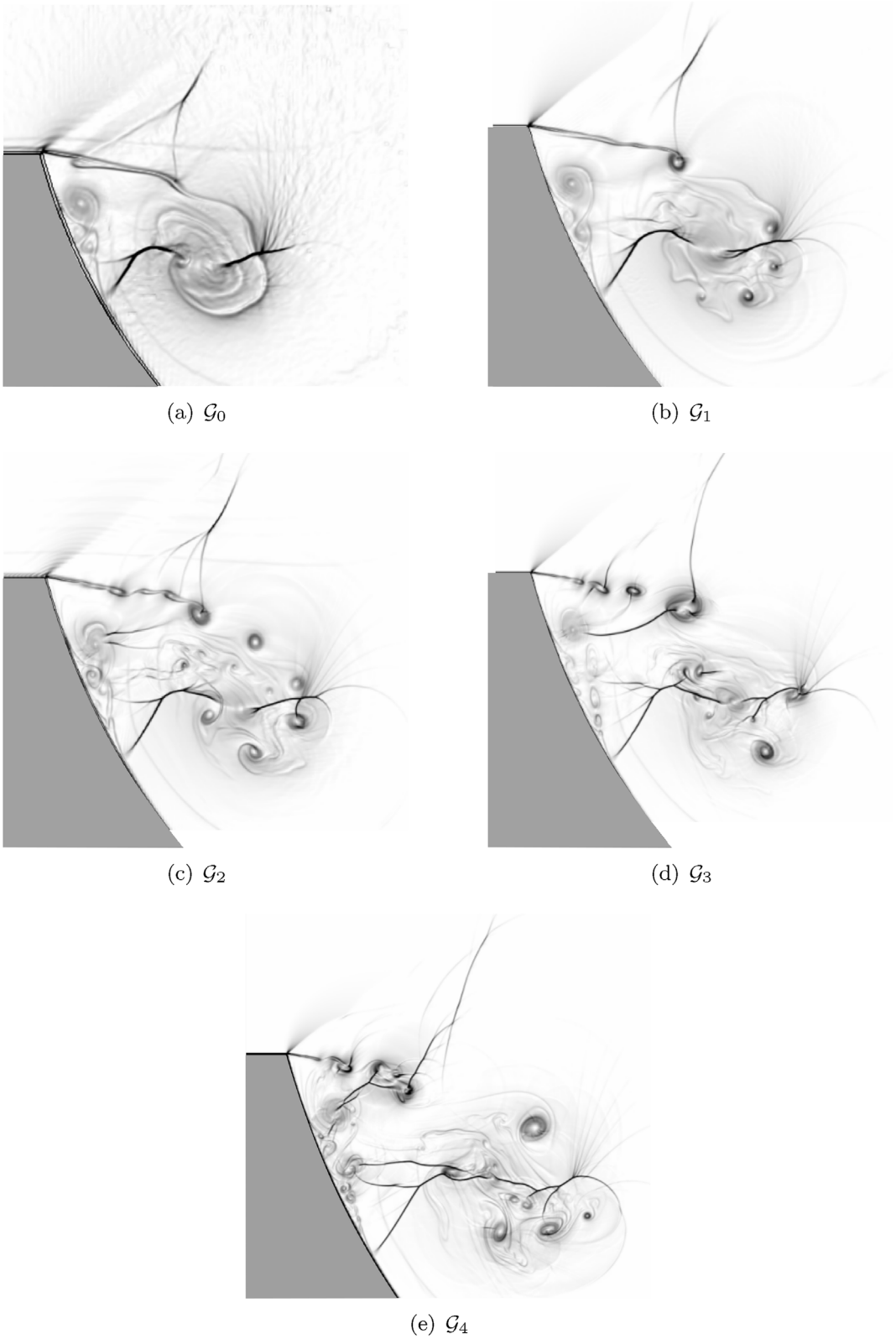

Fig. 3. Numerical schlieren pictures for different grid resolutions at $t = 150\,\mu s$ with $M_s = 1.6$.

domain since the unperturbed flow regions (uniform flow) provides almost no contribution to the circulation.

As it can be seen in Fig. 3, the flow topology of the primary vortex changes with the mesh resolution, the global variation of the vorticity production (Γ) and its rate (Γ/t) are insensitive to the grid resolution (see Fig. 4(a) and (b)). Indeed, the circulation Γ increases linearly in time regardless of the grid resolution. The results for the rate of vorticity production (Γ/t) are scaled by the product $\mathscr{R} \times T_0$, where $\mathscr{R}$ is the universal gas constant divided by the molecular weight of air taken as, $\mathscr{R} = 287\ J.\ Kg^{-1}.\ K^{-1}$ and T_0 is the temperature in front of the incident shock ($T_0 = 300\ K$). Since the rate has the dimension of the square of the velocity ($m^2 s^{-2}$), one may obtain dimensional results by multiplying the

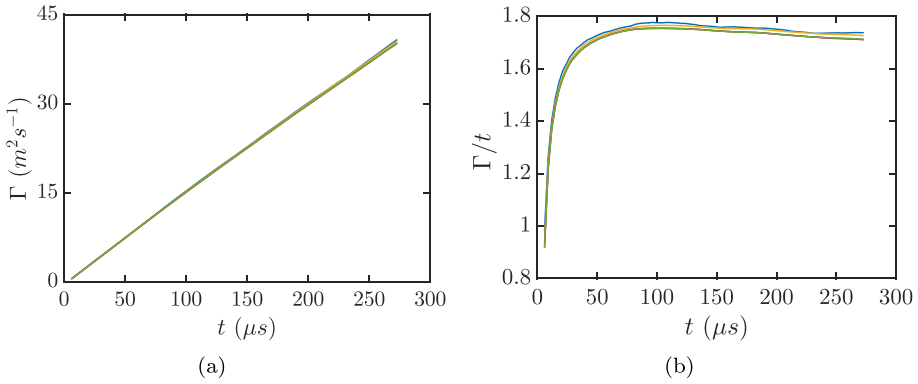

Fig. 4. Time history of (a): circulation (b): rate of circulation production for $M_s = 1.6$ and different mesh resolutions (– $\mathscr{G}_0$, – $\mathscr{G}_1$, – $\mathscr{G}_2$, – $\mathscr{G}_3$, – $\mathscr{G}_4$).

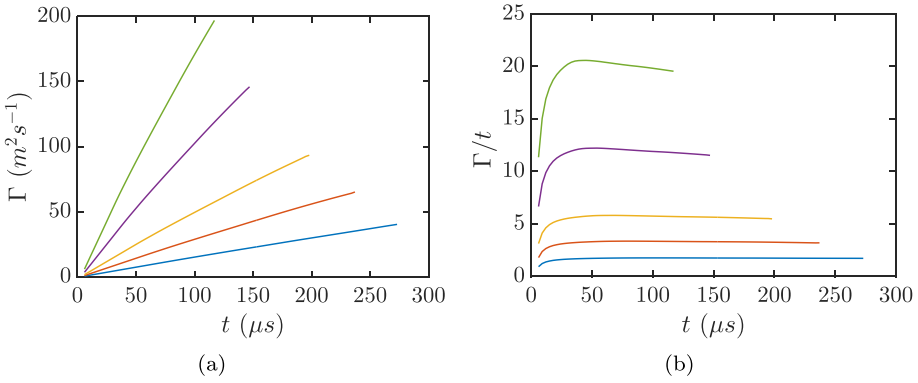

Fig. 5. Time history of (a): circulation (b): rate of circulation production for different incident-shock-Mach numbers (– $M_s = 1.6$, – $M_s = 2.0$, – $M_s = 2.5$, – $M_s = 3.5$, – $M_s = 4.5$).

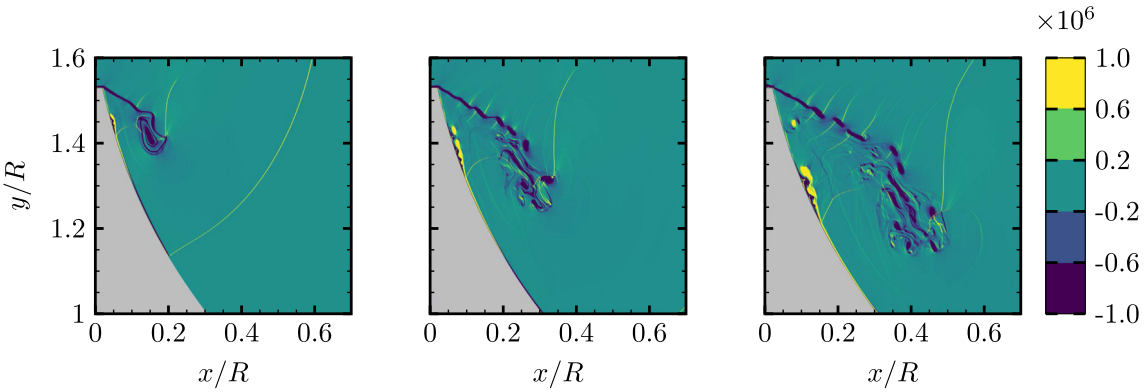

Fig. 6. Vorticity maps for $M_s = 2.0$. Column-wise (left-to-right): $t = 48\ \mu s$, $78\ \mu s$ and $108\ \mu s$.

dimensionless values by $\mathscr{R} \times T_0$,

$$\frac{\Gamma'}{t'} = \mathscr{R} \times T_0 \frac{\Gamma}{t} \tag{8}$$

Note that all the results of the rate of vorticity production, Γ/t, presented in this paper are dimensionless values.

The effect of shock strength on the vorticity production is investigated by changing M_s using the grid $\mathscr{G}_4$. The results are shown in Fig. 5(a) and (b). Basically both quantities increase with M_s. In other words, the strength of the main vortex increases at higher values of Mach number, and increases much faster for stronger shock waves as reported by Sun and Takayama [5]. The vorticity production occurs before the diffraction of the incident shock wave (at $t = 12\ \mu s$ for $M_s = 2.0$) as a result of the boundary-layer formation on the solid wall. This demonstrates the role played by viscous effects in forming the shock-wave diffraction structure as mentioned by Tseng and Yang [6].

Fig. 5(b) shows the rate of the circulation production. The five curves reach different constant values of 1.78, 3.79, 5.72, 11.42 and 18.73 for $M_s = 1.6$, 2.0, 2.5, 3.5 and 4.5, respectively. Similar trends were observed by Sun and Takayama [5] with constant values known as invariants of Euler equations in shock-wave diffraction.

Fig. 6 represents vorticity maps at different instants ($t = 48\ \mu s$, $78\ \mu s$ and $108\ \mu s$) for $M_s = 2.0$. As it can be seen, the main vortex and the highly disturbed shear layer split when interacting with the secondary shock waves. This results in a generation of fine scale turbulent eddies. Note that the production of vorticity is mainly concentrated in this turbulent region compared to the compression zone.

4.2. Vorticity transport equation

The vorticity transport equation provides further details on the mechanism of the vortex dynamics, it can be written as follows:

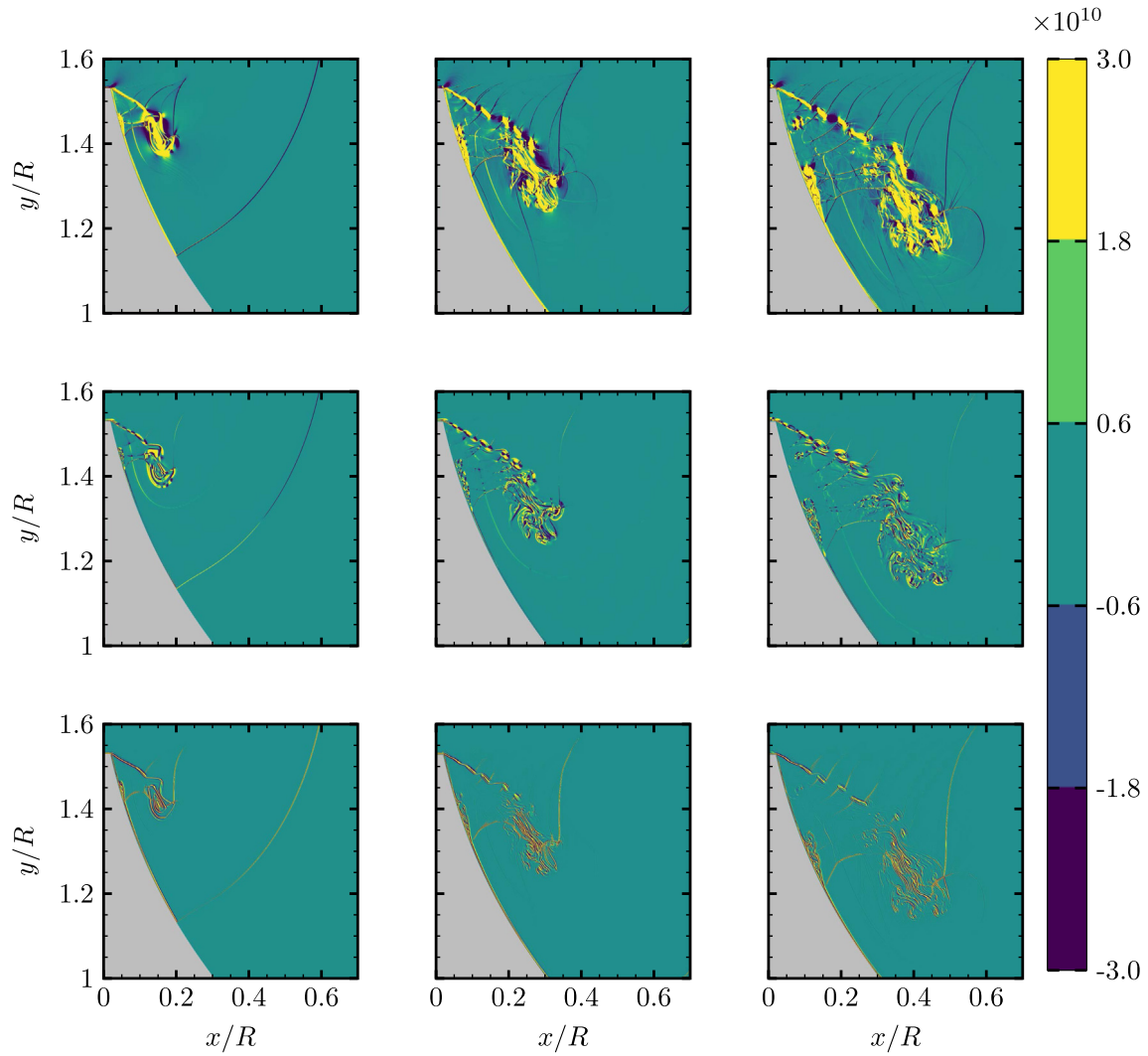

Fig. 7. Color maps of vorticity terms for $M_s = 2.0$. Row-wise (top-to-bottom): stretching of the vorticity due to flow compressibility (VSC), baroclinic (BAR) and diffusion of vorticity due to the viscous effects (DFV) terms. Column-wise (left-to-right): $t = 48\,\mu s$, $78\,\mu s$ and $108\,\mu s$.

$$\frac{D\omega}{Dt} = \underbrace{(\omega\cdot\nabla)u}_{\text{VSG}} - \underbrace{\omega(\nabla\cdot u)}_{\text{VSC}} + \underbrace{\frac{1}{\rho^2}(\nabla\rho\times\nabla p)}_{\text{BAR}} + \underbrace{\nabla\times\left(\frac{\nabla\cdot\tau}{\rho}\right)}_{\text{DFV}} \tag{9}$$

where the left-hand side represents the material derivative expressed as the sum of unsteady, ω_t, and convection, ω_c, terms. Here, $\omega_t = \partial\omega/\partial t$ and $\omega_c = U(\partial\omega/\partial x) + V(\partial\omega/\partial y)$.

The first term in the right-hand side of Eq. (9) represents the stretching or tilting of vorticity due to the flow velocity gradients, a term that is null in two-dimensional cases. The second term expresses the stretching of vorticity due to flow compressibility. The third contribution represents the baroclinic term, which accounts for the changes in the vorticity due to the intersection of density and pressure surfaces. The last term represents the diffusion of vorticity due to the viscous effects.

The different expressions appearing in the right-hand side of Eq. (9) are shown in Fig. 7 (in Row-wise) at different time intervals for $M_s = 2.0$. As one can see, the stretching of the vorticity due to flow compressibility (VSC) has the most dominant contribution. Based on the VSC contour, it is clear that there exist locally stretched structures in the core region of the vortex due to compressibility effect arising from local regions of compression/expansion. Additionally the results show the existence of evolving large scale vortices which interact with the different shock patterns present in the flow and finally split into small-scale vortices.

Fig. 8 shows the temporal evolution of the vorticity transport equation (VTE) terms. The stretching of vorticity due to flow compressibility (VSC) is almost constant over time independently of M_s, while its magnitude increases with Mach number. This contribution represents the effects of expansion on the vorticity field and plays a major role in the vorticity dynamics. The baroclinic term (BAR) is responsible of the generation of vorticity from unequal acceleration as a result of nonaligned density and pressure gradients. The lighter density fluid is faster accelerated than the high density one, which result in a shear-layer formation, that contributes to the generation of vorticity. The diffusion of vorticity due to the viscous effects (DFV) is essentially enhancing the viscous diffusion process on the vorticity distribution. As a result of viscosity, the vorticity tends to spread out spatially. Note that the diffusion of vorticity due to viscous effects (DFV) is quite important compared to the baroclinic term (BAR) for $M_s \leq 2.5$, while this trends is inverted for $Ms \geq 3.5$. As for the VSC term, the unsteady term, ω_t, which describes the rate of change in vorticity due to flow unsteadiness, is found to be constant in time regardless of M_s. For the convection term, ω_c, we also notice that it is almost constant in time for all shock-wave Mach numbers, and its magnitude increases at higher values of M_s. This term represents the change of vorticity of the moving fluid particles due to the motion of the fluid particle as it moves from one point to another.

Fig. 9 represents contours plots of ω_c for $M_s = 2.0$ at different

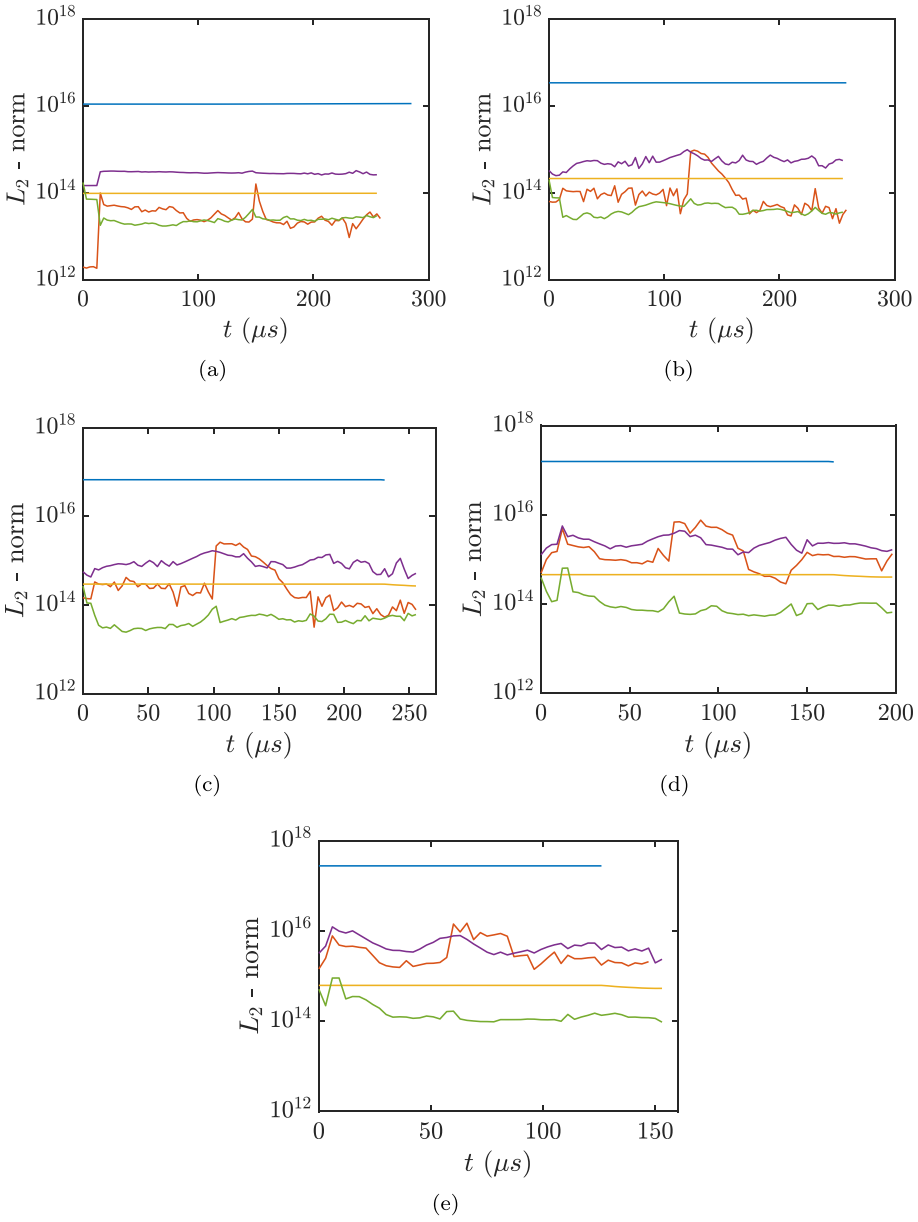

Fig. 8. Time history of normalized vorticity transport equation terms for (a): $M_s = 1.6$; (b): $M_s = 2.0$; (c): $M_s = 2.5$; (d): $M_s = 3.5$ and (e): $M_s = 4.5$ (¯: stretching of the vorticity due to flow compressibility (VSC) term, ¯: baroclinic (BAR) term, ¯: diffusion of vorticity due to the viscous effects (DFV) term, ¯: convection term (ω_c), ¯: unsteady term (ω_t)).

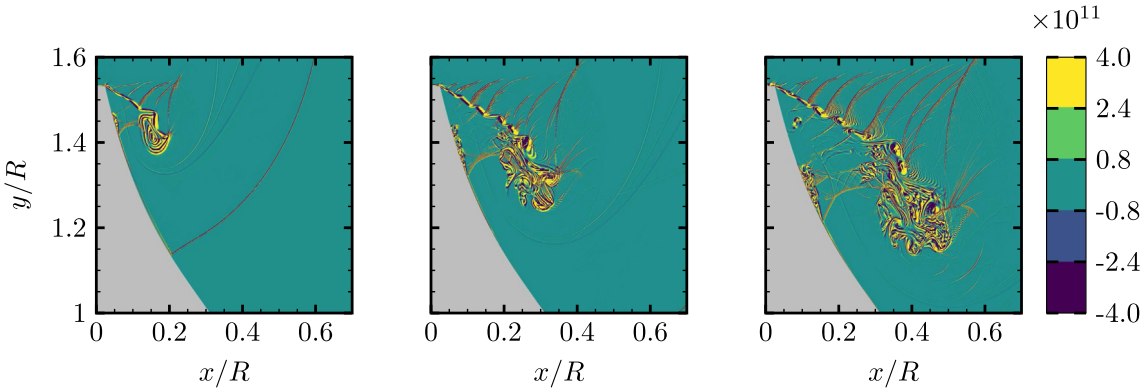

Fig. 9. Color maps showing the convection term of vorticity (ω_c) for $M_s = 2.0$. Column-wise (left-to-right): $t = 48\ \mu s$, $78\ \mu s$ and $108\ \mu s$.

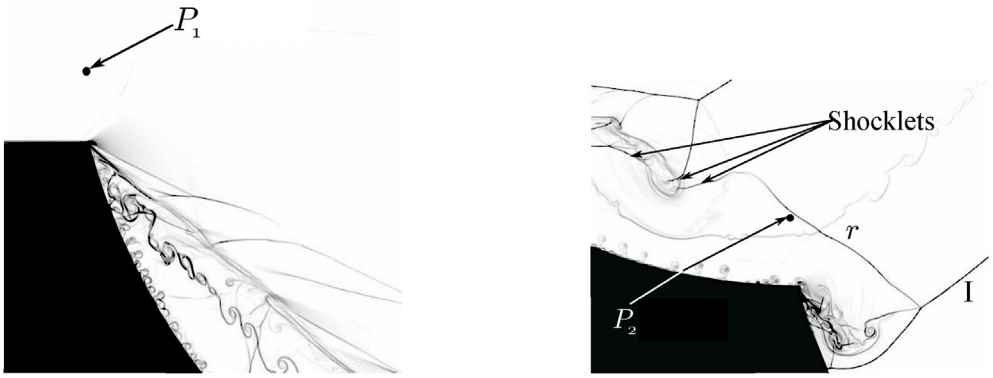

Fig. 10. Numerical schlieren pictures for $M_s = 4.5$ at $t = 69\ \mu s$: (a) beginning of the first concave surface; (b) beginning of the second concave surface; I: incident shock wave; r: reflected shock wave, P_1 and P_2 are two probes locations.

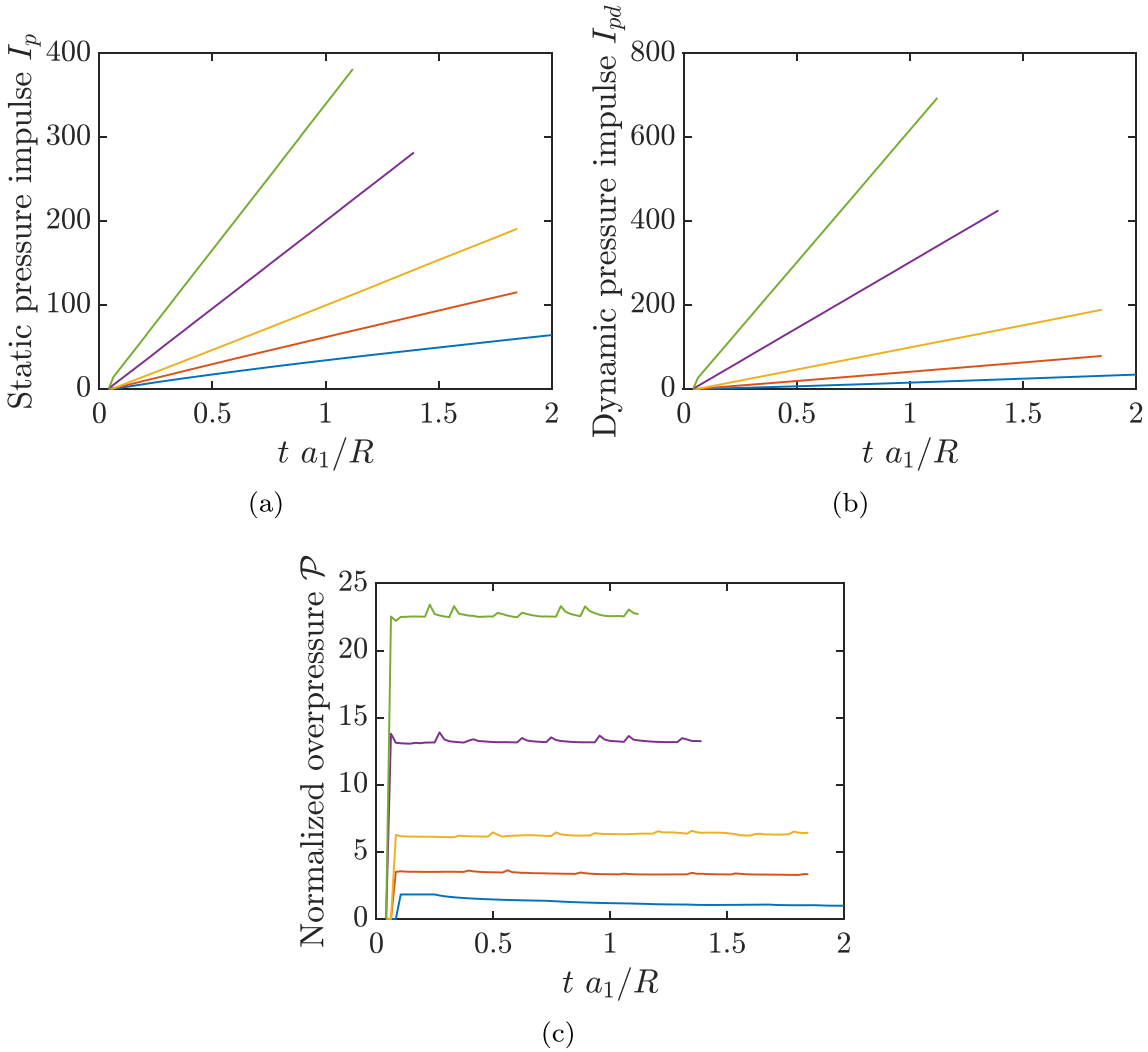

Fig. 11. Time history of (a): static pressure impulse, I_P (b): dynamic pressure impulse, I_{Pd} and (c): normalized overpressure $\mathscr{P}$, for different M_s at P_1 (– $M_s = 1.6$, – $M_s = 2.0$, – $M_s = 2.5$, – $M_s = 3.5$, – $M_s = 4.5$).

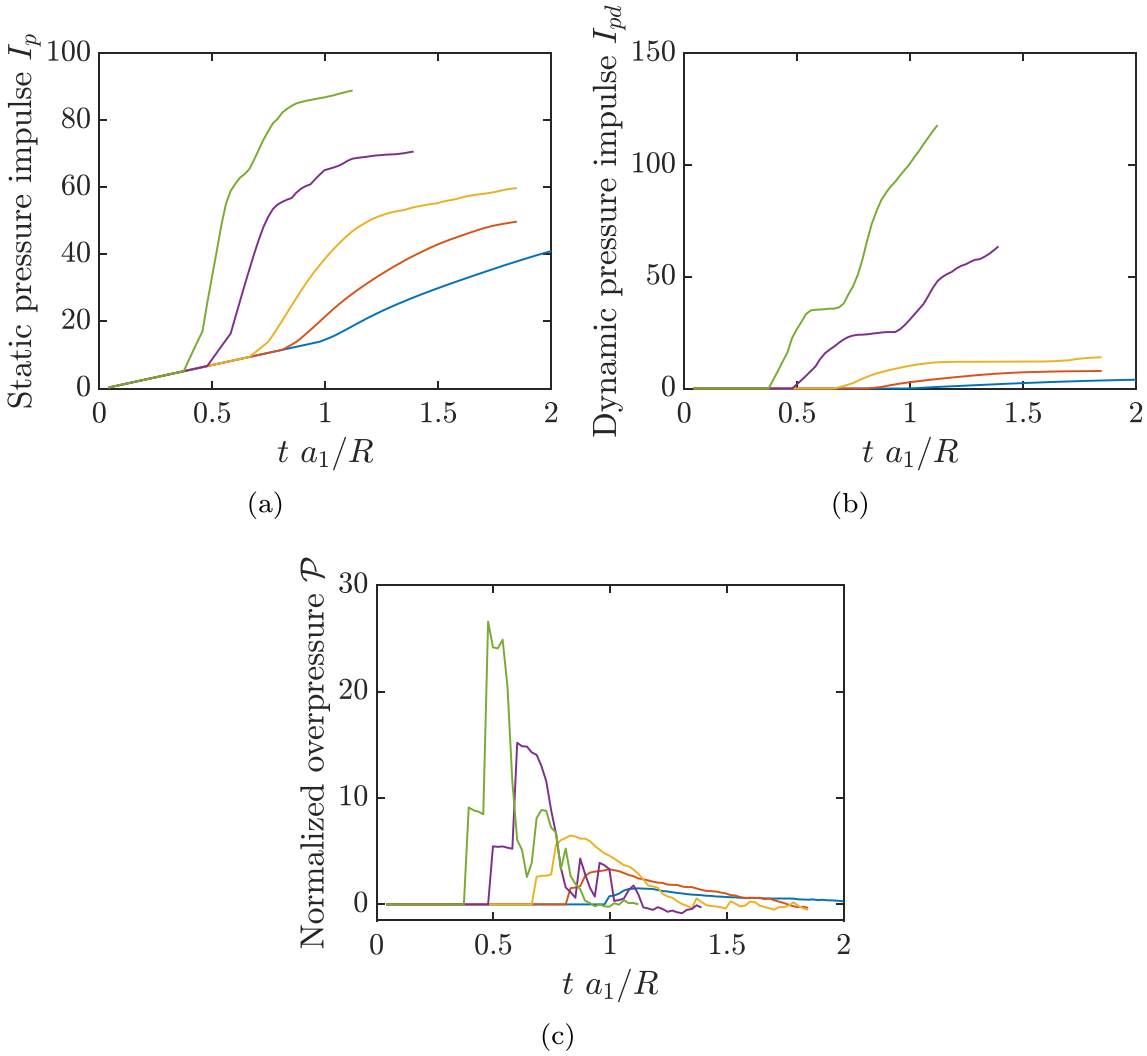

Fig. 12. Time history of (a): static pressure impulse, I_P (b): dynamic pressure impulse, I_{Pd} and (c): normalized overpressure $\mathscr{P}$, for different M_s at P_2 (– $M_s = 1.6$, – $M_s = 2.0$, – $M_s = 2.5$, – $M_s = 3.5$, – $M_s = 4.5$).

instants. As we can see, this term is mainly concentrated in the turbulent region as well as in the shear layer and in the near wall-region.

4.3. Static and dynamic pressure impulses and normalized overpressure

The effect of M_s on shock strength was investigated by computing the static and the dynamic pressure impulses along with the normalized overpressure, all defined as:

$$I_p = \int_{t_0}^{t_f} p\, dt \tag{10}$$

$$I_{pd} = \int_{t_0}^{t_f} \frac{1}{2}\rho\, \mathbf{v}^2\, dt \tag{11}$$

$$\mathscr{P} = (p - p_0)/p_0 \tag{12}$$

where p_0 is the static pressure of gas at rest, p, ρ and $\mathbf{v}$ are the local static pressure, density and velocity vector in the shocked region (t_0 and t_f being the initial and the final times). These quantities are calculated at two different space locations as shown in Fig. 10, with $P_1(x_1^*, y_1^*)$ corresponding to the beginning of the first concave surface, $x_1^* = x_1/R = 0.26$ and $y_1^* = y_1/R = 1.6$ and $P_2(x_2^*, y_2^*)$ corresponding to the beginning of the second concave surface, $x_2^* = x_2/R = 1.22$ and $y_2^* = y_2/R = 0.86$. The results are presented in Figs. 11 and 12, for P_1 and P_2, respectively.

At the upstream location, P_1, both static and dynamic pressure impulses are linearly increasing with time for all M_s. The passage of the incident wave is characterized by a sudden jump in these last two quantities (more visible for $M_s = 4.5$ as seen in Fig. 11(a) and (b)). This linear increase is due to the fact that P_1 is located at the inlet where no perturbation exists behind the shock wave. Concerning the normalized overpressure, one can see in Fig. 11(c) a sudden jump caused by the passage of the incident shock. Afterwards, it remains constant, except for $M_s = 1.6$, where it starts to decrease gradually as the shock propagates over the double concave surfaces.

At the downstream location, P_2, the flow behavior is completely different. The static pressure impulse is suddenly increased due to the passage of the shock. At this early stage of the diffraction process, the increasing rate is important. However, after the shock wave leads off the end of the geometry, it decreases giving almost constant value (see Fig. 12(a)). For the dynamic pressure impulse, we observe a sudden increase induced by the passage of the shock, after this it remains constant for a certain elapsed time until the arrival of the reflected shock and formation of the shocklets which generate a second increase due to the gas acceleration. Note that this behavior is more visible for $M_s = 4.5$ and $M_s = 3.5$ (see Fig. 12(b)). The arrival of the incident shock wave causes a sudden increase of the normalized overpressure (Fig. 12(c)). Afterwards, it remains almost constant until the reflected wave (r in Fig. 10(b)) arrives and causes a second increase. Once the reflected shock passed, the expanded gas gets driven away and causes a

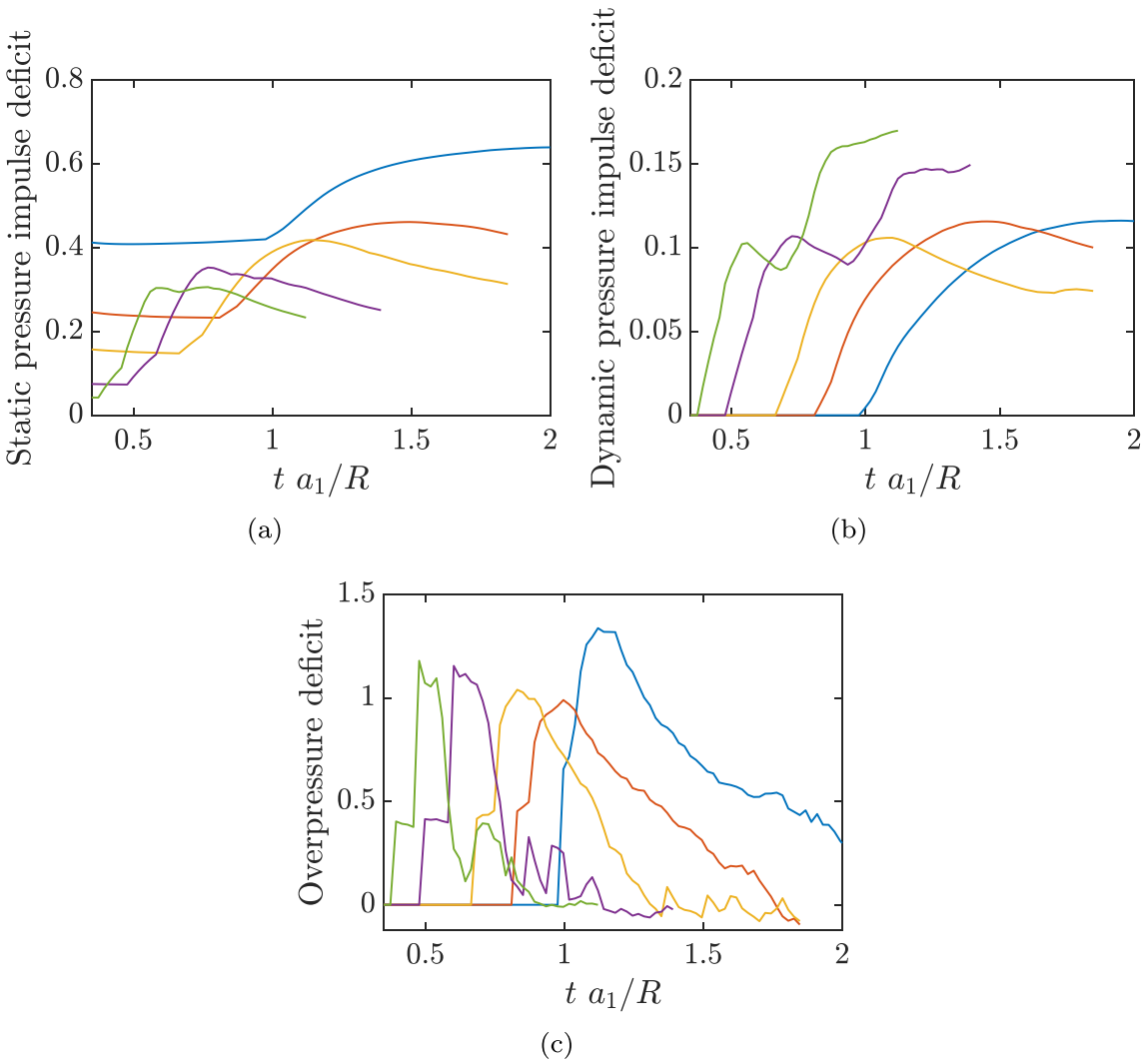

Fig. 13. Time history of (a): static pressure impulse deficit (b): dynamic pressure impulse deficit and (c): overpressure deficit, for different M_s at P_2 (– $M_s = 1.6$, – $M_s = 2.0$, – $M_s = 2.5$, – $M_s = 3.5$, – $M_s = 4.5$).

Table 2
Error estimates.

Allowable error (%)	Grid resolution	Physical time simulated (μs)	Number of time steps	Accumulated error	Allowable number of time steps	Reliability $R_s = \eta_{max}/\eta$
5	1793 × 1025	294	4311	9.48×10^{-16}	2.78×10^{27}	6.45×10^{23}
5	2817 × 1793	294	7854	5.84×10^{-17}	7.33×10^{29}	9.33×10^{25}
5	3841 × 2305	294	10307	1.8×10^{-17}	7.71×10^{30}	7.48×10^{26}
5	5633 × 3073	294	14061	6.94×10^{-18}	5.19×10^{31}	3.69×10^{27}
5	7681 × 3585	294	18728	7.14×10^{-19}	4.87×10^{33}	2.61×10^{29}

strong decrease. At the last stage of the diffraction, we can see a succession of peaks due to the passage of the shocklets and the emergence of flow instabilities in this zone. These peaks are visible only for high Mach numbers ($M_s = 4.5$, $M_s = 3.5$), for which the turbulent region is highly perturbed. It is worth noticing that for high M_s the flow relaxes until it reaches negative overpressure values, because of the strong vortex suction acting on this highly perturbed turbulent zone.

In order to investigate the effect of the first concave surface on the shock strength, the deficit of various parameters mentioned above is calculated. This deficit is defined as the ratio of the impulses and overpressure calculated at the two points: $I_p(P_2)/I_p(P_1)$, $I_{pd}(P_2)/I_{pd}(P_1)$, $\mathscr{P}(P_2)/\mathscr{P}(P_1)$. For static pressure impulse, we can see that the deficit is more important for the high Mach numbers because of the highly turbulent region generated behind the strong shock wave and the intense vortex suction exerted on the flow (see Fig. 13(a)). By comparing the static and dynamic pressure impulses deficit (Fig. 13(a) and (b), respectively) we can see that the deficit in dynamic pressure impulse is more important because of the decrease of density and the square of velocity together. For the overpressure deficit (Fig. 13(c)), the peaks are exceeding unit, which means that the overpressure in P_2 is greater than in P_1 and this is mainly caused by the passage of the reflected shock which induces the formation of shocklets (small shocks embedded into turbulent region).

5. Accumulation of numerical errors

Estimating accuracy and errors accumulation is necessary in CFD, especially when dealing with high-fidelity numerical simulations.

Depending on the spatial resolution and on the numerical scheme, a definite error occurs due to numerical integration at each time step [21]. According to Smirnov et al. [21], the relative integration error for one-dimensional problem is:

$$S_1 = \left(\frac{h}{L_1}\right)^{k+1} \tag{13}$$

where h is the cell size, L_1 is the domain length and k the order of accuracy of the numerical scheme. For multi-dimensional problem, the integration errors can be summed up as:

$$S_{err} = \sum_{i=1}^{3} S_i \tag{14}$$

The maximal allowable number of time steps for solving a given problem could be determined by the following formula:

$$\eta_{max} = (S^{max}/S_{err})^2 \tag{15}$$

where S^{max} is the allowable value of the total error, which is presumed to be between 1% and 5%. Smirnov et al. [21] have introduced another important measurement of numerical errors suitable for high-performance computing, which is the ratio of the maximal allowable number of time steps η_{max} to the actual number of time steps used to obtain the results η:

$$R_s = \eta_{max}/\eta \tag{16}$$

According to Smirnov et al. [21], the parameter R_s can characterize the reliability of the numerical results, i.e. how far below the limit, the simulations were finalized. Indirectly, this parameter characterizes the accumulated error. The higher is the value of R_s, the lower is the error. On tending R_s to unity, the error tends to a maximal allowable value.

Table 2 summarizes the results of different grid resolutions and physical time in our simulations. As it can be seen, a quite high level of reliability is achieved in our case.

6. Conclusions

In this paper, shock-wave diffraction over double cylindrical wedges have been numerically investigated by means of two-dimensional high-fidelity numerical simulation. The objective was to study the flow structure and the vorticity formation with regards to the incident-shock-wave Mach number. Different grid resolutions were used in order to investigate the mesh sensitivity of the results. It was found that although the upstream flow topology (shape of the eddies) changes with the grid resolution, the vorticity production and the shock diffraction process are quite independent from the grid resolution. In terms of rate of vorticity production and circulation, it is shown that the shock strength enhances the vorticity production and the rate of vorticity production increases as the incident shock strength increases and remains virtually constant after an elapsed time. For the vorticity transport equation, it was found that the stretching of vorticity due to flow compressibility plays an important role in the vorticity dynamics, for low-Mach numbers regimes ($Ms \leq 2.5$). The diffusion of the vorticity due to the viscous effects is seen to be quite important compared to the baroclinic term, while this trends is inverted for higher Mach numbers regimes ($Ms \geq 3.5$). In terms of shock strength, it was found that the effect of the first concave surface is effective in decreasing sufficiently the dynamic pressure impulse (up to 90% for $M_s = 2.5$) as well as the static pressure impulse (up to 75% for $M_s = 4.5$). However for the overpressure deficit, the peaks are accentuated by the passage of the reflected shock and the formation of shocklets that tend to reduce the overall overpressure deficit.

Acknowledgments

The first author gratefully acknowledges support from the Algerian Government through a Ph.D Fellowship. Computational facilities from 'Centre Régional Informatique et d'Applications Numériques de Normandie (CRIANN)', Rouen, France under allocation 1998022, are acknowledged.

References

[1] B. Skews, The perturbed region behind a diffracting shock wave, J. Fluid Mech. 29 (4) (1967) 705.
[2] L. Howard, D. Matthews, On the vortices produced in shock diffraction, J. Appl. Phys. 27 (3) (1956).
[3] T.V. Bazhenova, L.G. Gvosdeva, Y.V. Zhilin, Change in the shape of the diffracting shock wave at a convex corner, Acta Astronaut. 6 (1951) (1979) 401–412.
[4] F. Gnani, K.H. Lo, H. Zare-Behtash, K. Kontis, Experimental investigation on shock wave diffraction over sharp and curved splitters, Acta Astronaut. 99 (1) (2014) 143–152.
[5] M. Sun, K. Takayama, Vorticity production in shock diffraction, J. Fluid Mech. 478 (2003) 237–256.
[6] T. Tseng, R. Yang, Numerical simulation of vorticity production in shock diffraction, AIAA J. 44 (5) (2006) 1040–1047.
[7] A. Chaudhuri, G.B. Jacobs, Dynamics of shock wave diffraction over sharp splitter geometry using entropy-based artificial viscosity method, Shock Waves (2017) 1–15.
[8] M. Sun, K. Takayama, The formation of a secondary shock wave behind a shock wave diffracting at a convex corner, Shock Waves 7 (5) (1997) 287–295.
[9] M.K. Quinn, K. Kontis, A Combined Study on Shock Diffraction, 5th Symposium on Integrating CFD and Experiments in Aerodynamics, 2012, pp. 3–5.
[10] J. Cai, J. Zhou, S. Liu, Z. Lin, Effects of dynamic backpressure on shock train motions in straight isolator, Acta Astronaut. 141 (2017) 237–247.
[11] J. Reeves, B. Skews, Unsteady three-dimensional compressible vortex flows generated during shock wave diffraction, Shock Waves 22 (2) (2012) 161–172.
[12] G. Abate, W. Shyy, Dynamic structure of confined shocks undergoing sudden expansion, Prog. Aero. Sci. 38 (1) (2002) 23–42.
[13] J. Zhao, R. Li, H. Wu, Investigate the shock focusing under a single vortex disturbance using 2D Saint-Venant equations with a shock-capturing scheme, Acta Astronaut. 143 (2018) 337–352.
[14] A. Chaudhuri, A. Hadjadj, O. Sadot, E. Glazer, Computational study of shock-wave interaction with solid obstacles using immersed boundary methods, Int. J. Numer. Methods Eng. 8 (89) (2012) 975–990.
[15] V. Soni, A. Hadjadj, A. Chaudhuri, G. Ben-Dor, Shock-wave reflections over double-concave cylindrical reflectors, J. Fluid Mech. 813 (2017) 70–84.
[16] V. Soni, A. Hadjadj, O. Roussel, On the use of adaptive multiresolution method with time-varying tolerance for compressible fluid flows, Shock Waves (2017) 1–14.
[17] V. Soni, A. Hadjadj, O. Roussel, G. Moebs, Parallel multi-core and multi-processor methods on point-value multiresolution algorithms for hyperbolic conservation laws, J. Parallel Distr. Comput. 123 (2019) 192–203.
[18] A. Chaudhuri, A. Hadjadj, A. Chinnayya, On the use of immersed boundary methods for shock/obstacle interactions, J. Comput. Phys. 230 (5) (2011) 1731–1748.
[19] A. Chaudhuri, A. Hadjadj, A. Chinnayya, S. Palerm, Numerical study of compressible mixing layers using high-order WENO schemes, J. Sci. Comput. 47 (2) (2011) 170–197.
[20] N. Brahmi, A. Hadjadj, V. Soni, A. Chaudhuri, Analysis of shock-wave diffraction over double concave cylindrical wedges, Part I: Shock Dynamics, Acta Astronautica (2020), https://doi.org/10.1016/j.actaastro.2020.01.025.
[21] N.N. Smirnov, V.B. Betelin, V.F. Nikitin, L.I. Stamov, D.I. Altoukhov, Accumulation of errors in numerical simulations of chemically reacting gas dynamics, Acta Astronaut. 117 (2015) 338–355.

5

Velocity scaling of a shock wave diffracting over double concave cylindrical surfaces

Submitted to: *Shock waves journal*

Highlights

- Shock propagation over double cylindrical wedges in different working gases is studied.
- A new scaling of shock velocity propagation is proposed for different specific heat ratios.

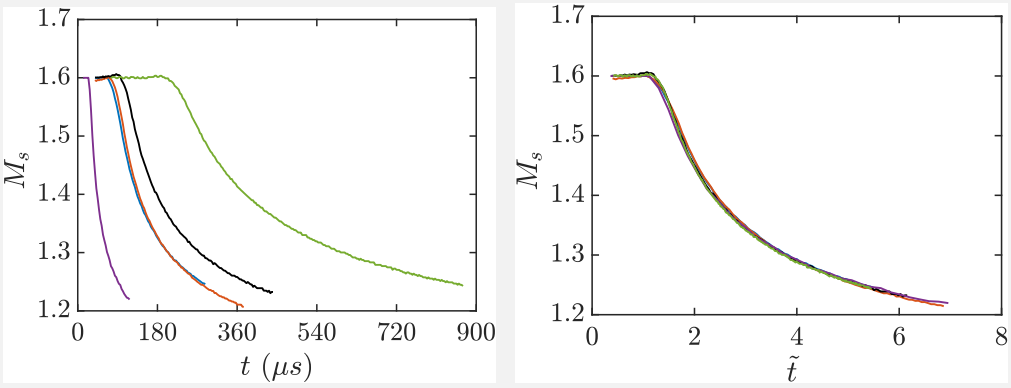

(a) (b)

Figure 5.1: (a): shock-wave Mach number, (d): shock-wave Mach number *vs.* normalized time, for different gases (– air, – Argon, – Helium, – SF_6, – CO_2).

abstract

This paper deals with a numerical study of shock-wave propagation over double concave cylindrical surfaces. The incident shock-wave Mach number is kept constant such as $M_s = 1.6$. Four gases ,with different molecular weights, specific heat ratios, and acoustic impedances in addition to the air, are used as working gases, namely, He, Ar, CO_2 and SF_6. The shock wave velocity propagating in the heavy gases is always less than that propagating in the light ones. An approximate universal relation is proposed, which predicts the incident-shock trajectory and velocity as a function of the incident-shock Mach number, the radius of the cylinder, and the gas properties. This relation is tested for five different working gases. The shock position and velocity are proportional to the shock initial velocity reduced by a scaling function that depending on the incident shock-wave Mach number, the heat capacity ratio and the concave surface radius.

keyword

Shock waves, Shock velocity, Numerical simulation, scaling function

5.1 Introduction

Significant attention was given to shock wave (in air) interaction with liquid bubble(s) and/or to the interaction of shock waves propagating in water with air bubbles. These phenomena attracted attention due to their usage in applying shock and acoustic waves in medicine. While less attention has been given to the interaction between shock and blast waves propagating in air with bubbles containing a different gas or shock and blast waves propagating in a gas other than air. The work of Haas & Sturtevant (1987) is one of the typical publications appearing in the past century. They investigated experimentally the interaction of a plane weak shock wave with a single gas bubble containing either helium or R22. The wave configurations were predicted by geometrical acoustics, including the effects of refraction, reflection, and diffraction, and were compared to the recorded observations. Also, the pressure field on the axis of symmetry downstream of the bubble was recorded. Falcovitz et al. (2012) considered a classical shock tube with Helium-filled driver section, and a driven section filled with a He-Ar gaseous mixture of continuously varying composition where the density either increases, or decreases, continuously. Their study reveals that in the decreasing density case, a negative pressure gradient evolved behind the shock front, accelerating the post-shock flow velocity to levels well above that obtained in any of the single-species shock tube cases. In the increasing density

case, the evolving flow pattern is reminiscent of the system of transmitted and reflected-shock, in that a reflected smooth compression wave is formed instantly behind the shock front. Siefert (2007) presented experimental study on the propagation of shock waves into weakly ionized nitrogen, air, and argon glow discharges. They concluded that the main mechanism for increasing shock velocity in weakly ionized gases is thermal heating of the neutral gas species via elastic collisions with electrons. Luo et al. (2015) investigated the interaction of a planar shock wave with different SF_6 polygons shapes inhomogeneity surrounded by air. Their study showed that the velocities and the trajectories of the triple points are self-similar or pseudo-stationary. Si et al. (2012) experimentally investigated the phenomena of a spherical helium or SF_6 interface interacting with a planar shock wave and the reshock in a shock tube environment. The shock waves velocities were estimated and compared with those calculated from one-dimensional gas dynamics model. A discrepancy is observed between the estimated velocities and the calculated ones. According to them, the reasons of this discrepancy lie in two insights. On one hand, the gas contaminations inside and outside the SF_6 interface can change the shock velocities. In general, the shock velocity in a heavy (light) gas will increase (decrease) when the heavy (light) gas is contaminated by a light (heavy) gas according to the one-dimensional gas dynamics model. On the other hand, the convergence (divergence) of the refracted shock inside the SF_6 (helium) bubble which is absent in the one-dimensional model may increase (decrease) its velocity. Igra & Igra (2018) studied numerically the interaction between a planar shock wave and different bubbles shapes containing either SF_6, He, Ar, or CO_2. They showed that the difference in the physical properties between the ambient air and the gas contained inside the investigated bubbles has a significant effect on the evolved wave pattern and pressure distribution inside the bubbles during the interaction process. They noticed that in the case of heavy gases, the velocity of the shock wave propagating along the bubble inner surface is always less than that of the incident shock wave and higher than that of the transmitted one. However, in the case of the light gas (He), the fastest one is the transmitted shock wave and the slowest one is the incident shock wave. Glazer et al. (2011) conducted experimental and numerical studies of a planar shock wave interaction with circular cylinders where they investigated the effects of different initial conditions such as, shock-wave strength, cylinder diameter and working gas on the reflected shock path. In this study an approximate universal relation is proposed, which predicts the reflected-shock trajectory as a function of the incident-shock Mach number, the diameter of the cylinder, and the gas properties. According to them, the velocity is proportional to the reflected-shock velocity from a planar rigid wall reduced by a factor that depends on the incident shock-wave Mach number and the specific heat ratio. The proposed relation is limited to weak shock waves ($M_s < 1.4$). Accordingly, in

a recent numerical study, Brahmi et al. (2020*a*) investigated shock-wave diffraction over double concave cylindrical surfaces and proposed a scaling function which predicts the incident-shock trajectory and velocity as a function of the incident-shock Mach number and the cylinder radius. The proposed relation in Brahmi et al. (2020*a*) was tested in the range of M_s ($1.6 < M_s < 4.5$) but limited to air as working gas which has heat ratio of 1.4. Accordingly, the main objective of the present study is to verify and generalize the scaling function proposed in Brahmi et al. (2020*a*) to different working gases other than air using the same geometry. The paper is organized as follows: Sect. 5.2 describes the numerical methodology along with the problem setup. Results and discussion are presented in Sect. 5.3, while concluding remarks with perspectives are given in Sect. 5.4.

5.2 Numerical methodology and problem setup

The numerical simulations carried out in this study are based on the use of an *in-house* parallel compressible solver, called CHOC-WAVES. The code is equipped with an adaptive multi-resolution method for mesh refinement (Soni et al. 2017, 2019, 2017), along with an immersed boundary method (IBM) to handle fluid-solid interaction problems Chaudhuri et al. (2011). The solid body, identified using a ray-tracing technique, is embedded into a Cartesian grid. Two-dimensional fully compressible Navier-Stokes equations are solved assuming the gas as ideal and the viscosity obeying to Sutherland's law. Inviscid and viscous fluxes are computed using a fifth-order weighted essentially non-oscillatory (WENO5) scheme and a fourth-order central difference formula, respectively. The time is advanced using a third-order Runge-Kutta method Chaudhuri et al. (2011). The code is validated through a variant of test problems including shock/shock, shock/turbulence and shock/obstacles interactions (Soni et al. 2017, 2019, 2017).

As for the problem setup, a schematic illustration of the studied configurations is depicted in Figure 5.2, where a planar shock travels at $M_s = 1.6$ through a double-concave cylindrical surfaces. The geometry of the cavity flow configuration is taken similar to that presented in the numerical study of Brahmi et al. (2020*a*) and Brahmi et al. (2020*b*). As for the computational specifications, the boundary conditions were set to inlet and outlet at the left and the right side of the computational domain, respectively, while the top boundary and the bottom-right part of the domain are treated as symmetry plane, and the solid surface is considered with a no-slip boundary condition. In all the simulations, the geometric parameters such; $R_1 = R_2 = R = 50\,mm$ and $\omega_1 = \omega_2 = 75^\circ$ are kept constant. Initially, the shock is located at $x = 5$ mm for all gases. Rankine-Hugoniot relations are used to set the initial conditions for the left (shocked state) and the right (stagnant state) states associated with the chosen M_s. The different considered working gases and their

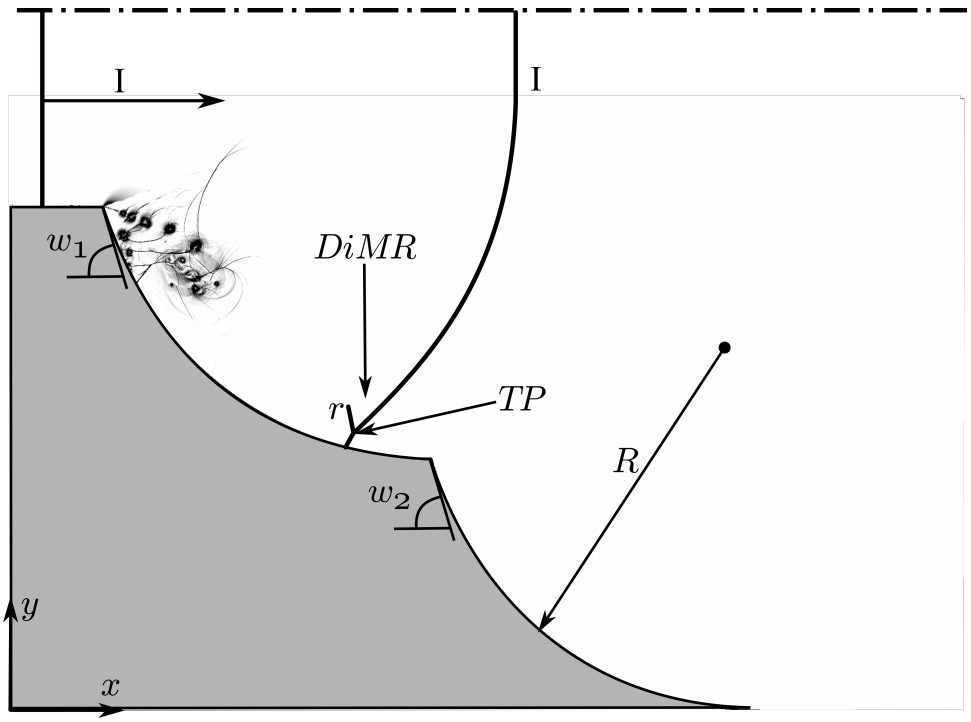

Figure 5.2: Schematic representation of a double-concave cylindrical surfaces. I: incident shock, r: reflected shock, $DiMR$: direct-Mach reflection, TP: triple point, R: cylinder surfaces radius, $w_1 = w_2 = 75°$: first and second diffraction angles.

physical properties are presented in Table D.1. The initial stagnant state is assigned with temperature $T_0 = 300\ K$ and pressure $p_0 = 101.3\ kPa$, and the flow is initialized as uniform flow.

Gas	Density ($kg\,m^{-3}$)	Specific heat ratio	Sound speed ($m\,s^{-1}$)	Molecular weight ($g\,mol^{-1}$)
Air	1.27	1.4	346	29
SF_6	6.03	1.1	135	146
Argon	1.75	1.67	323	40
Helium	0.17	1.66	1003	4
CO_2	1.93	1.3	268	44

Table 5.1: Physical properties of the considered working gases.

5.3 Results and discussions

Trajectories of incident-shock waves computed for the five different working gases (air, SF_6, Ar, CO_2, and He) are shown in Figure 5.3(a). It is clear from this figure that the fastest wave is witnessed in the He case, while the slowest one is seen in the SF_6 case. In the Ar case, due to the similarity in the acoustic impedance between air and Ar, both waves propagate with almost the same velocity. Based on these results, the velocities of

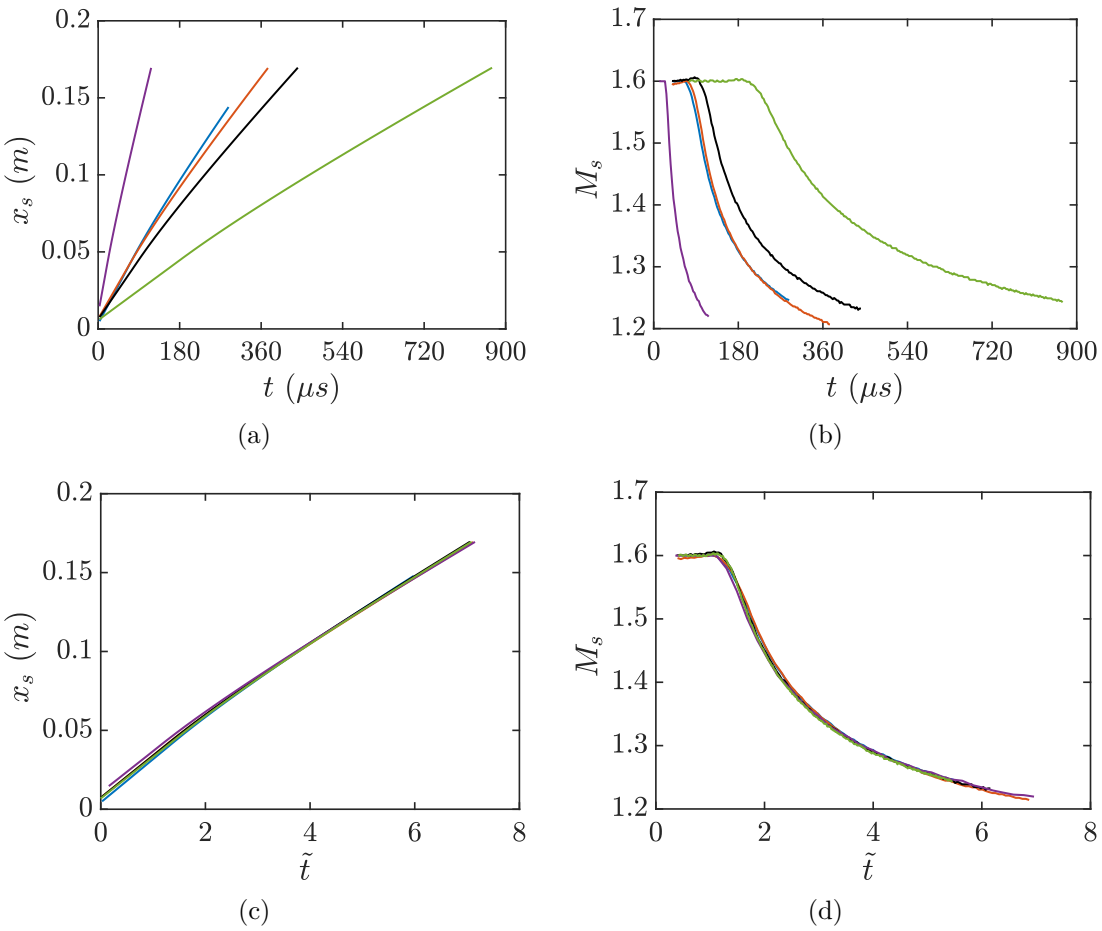

Figure 5.3: (a): shock-wave position; (b): shock-wave Mach number; (c): shock-wave position *vs.* normalized time and (d): shock-wave Mach number *vs.* normalized time, for different gases (– air, – Argon, – Helium, – SF_6, – CO_2).

these shock waves can be obtained. The results are shown in Figure 5.3(b), for all gases, the speed of the incident shock wave starts with a constant value (equal to the initial velocity) then reduces dramatically in time. Furthermore, its rate of change is at first very large, but becomes smaller as it propagates through the double concave surfaces, and as we can see in Figure 5.3(b), the incident shock-wave Mach number starts to decrease earlier for light gases (highest acoustic impedance) and this result is expected because the shock waves in the case of light gases reach the diffracting edge of the double concave first.

With regard to the scaling law, the objective is to construct a simple expression based on the obtained data to normalize the incident-shock waves trajectories and velocities. The incident-shock waves trajectories and velocities are plotted using dimensionless coordinates. By finding the appropriate dimensionless time, it was possible to show the data from different simulations with different working gases collapse into a single curve. From the data analysis, the following relationship is found:

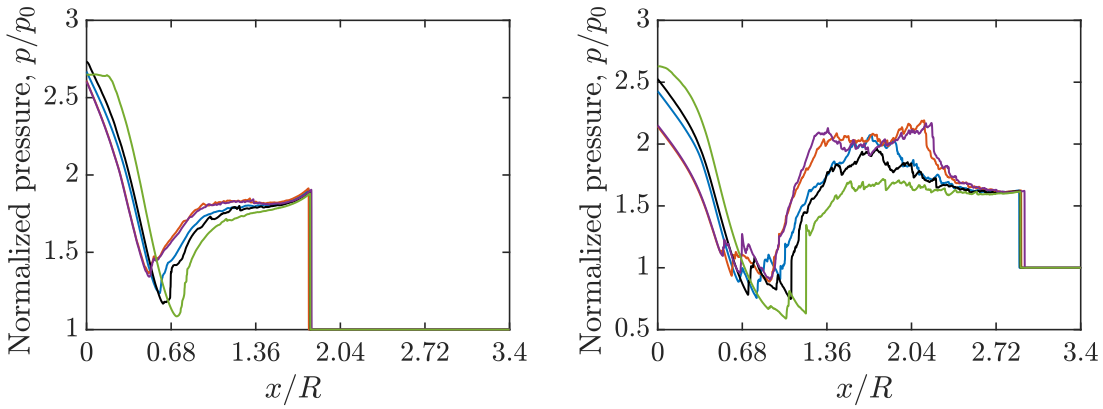

(a) $\tilde{t} \approx 3.3$ (b) $\tilde{t} \approx 5.26$

Figure 5.4: Normalized pressure profiles at $y/R = 1.8$ and (a): $\tilde{t} \approx 3.3$, (b): $\tilde{t} \approx 5.26$ for different gases (– air, – Argon, – Helium, – SF_6, – CO_2).

$$\tilde{t} = \frac{W_s^i}{R}\,\varphi(\gamma, M_s)\,t \tag{5.1}$$

The scaling function $\varphi(\gamma, M_s)$ is defined as:

$$\varphi(\gamma, M_s) = \frac{(M_s+1)}{\gamma}\left(ln(M_s+1) - (\gamma-1)(M_s-1)\right) \tag{5.2}$$

Where, W_s^i: is the initial incident-shock wave velocity depending on the working gas and R: is the cylindrical concave surfaces radius.

By applying this normalization (Equation(5.1) and (5.2)), all results (shock position and velocity for different working gases) collapse together into single curve and the results are presented in Figures 5.3(c) and 5.3(d) respectively.

Normalized pressure variations are shown in Figure 5.4 for different gases, at two different normalized times, $\tilde{t}$. At $\tilde{t} \approx 3.3$, the normalized pressure is decreasing dramatically for all the gases until reaching a minimum value at around $x/R = 0.68$. This minimum value depends on the working gas, so that the gas with the lowest specific heat ratio reaches the lowest value (SF_6, CO_2, air, Helium and Ar, from the lowest specific heat ratio to the highest). After this decreasing part, compression or secondary shocks appear (as we will see later) in order to increase the pressure ratio to reach its value behind the transmitted shock wave. It is important to mention that, at this stage of evolution, the pressure ratio profiles evolve almost similarly for Ar and Helium since they have almost the same specific heat ratio. The observed pressure state behind the propagating shock wave is fairly uniform, during the investigated time shown in Figure 5.4(a) for all the gases.

At $\tilde{t} \approx 5.26$, shown in Figure 5.4(b), the pressure ratio behavior, in general, is almost

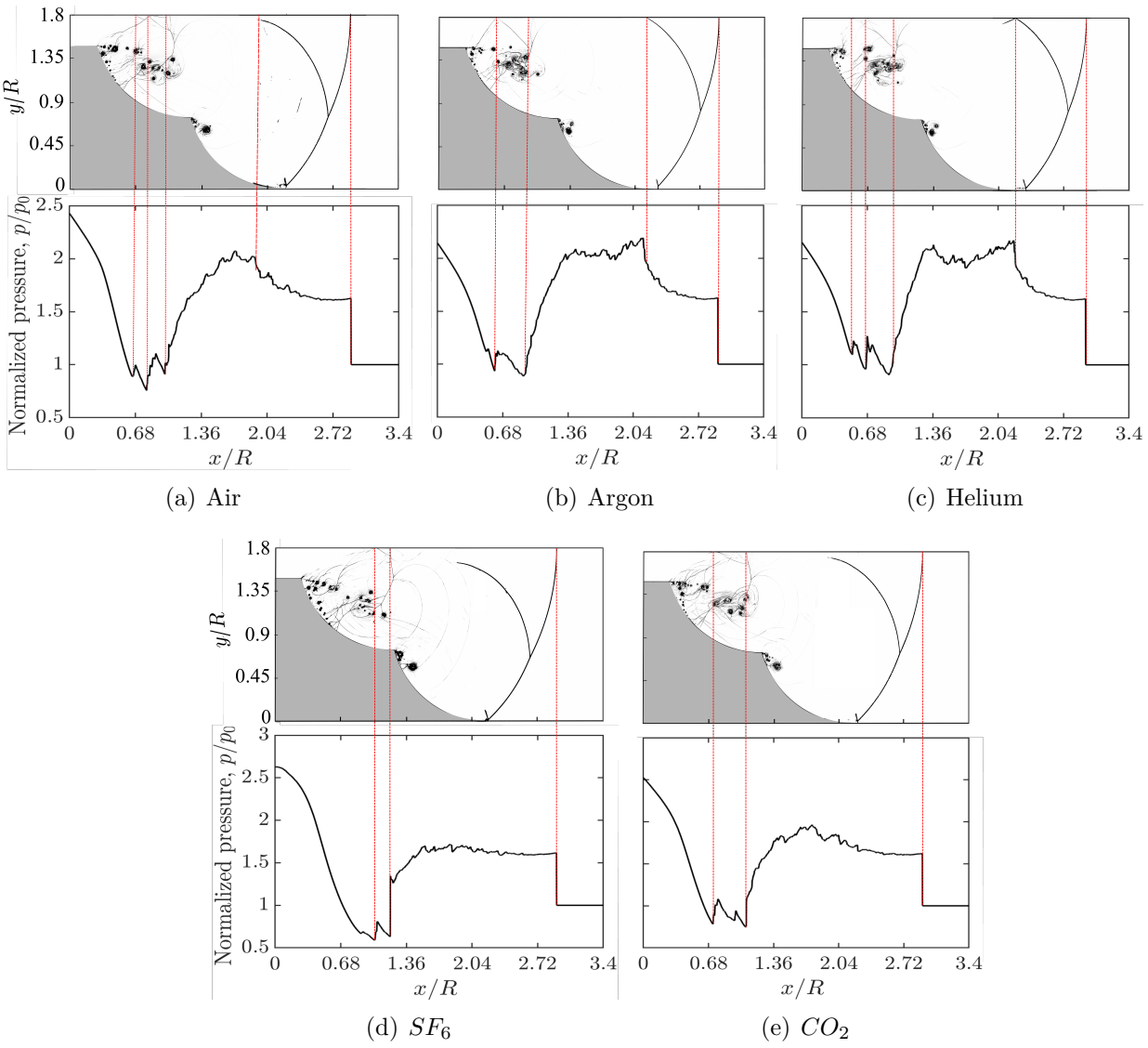

(a) Air (b) Argon (c) Helium

(d) SF_6 (e) CO_2

Figure 5.5: Spatial distribution of Normalized pressure at $y/R = 1.8$ along with numerical schlieren pictures for different gases at $\tilde{t} \approx 5.26$, p_0 is the pressure of the gas at rest taken as $p_0 = 101.3\ kPa$.

the same as the previous one. For, approximately, $x/R < 0.68$ the pressure level is important for gases with a lower specific heat ratio, this behavior is reversed for the second part of the graph, $x/R > 0.68$, where, this time, the pressure level is important for gases with a higher specific heat ratio.

Intending to shed more light on the pressure ratio distribution, spatial evolutions of the normalized pressures at $y/R = 1.8$ along with numerical schlieren pictures for different gases at $\tilde{t} \approx 5.26$ are presented in Figure 5.5. As it can be seen, several secondary shocks with different intensities appear in the range of $0.68 < (x/R) < 1.36$ for all gases. These secondary shocks are formed because of the existence of a locally supersonic flow behind the diffracting shock wave. Behind the diffracting shock wave, the subsonic flow is

accelerated and eventually becomes locally supersonic Brouillette et al. (1995). A direct Mach reflection (DiMR) is formed at the end of the first concave surface, inducing to the formation of a reflected shock, r, (see Figure5.2). The reflected shock, r, hits the upper boundary and this phenomenon is observed through the pressures jumps for air, Argon and Helium at $x/R \approx 2.04$. For the two remaining gases, SF_6 and CO_2, the observed pressure state behind the propagating shock wave is fairly uniform.

5.4 Concluding remarks and perspectives

In this study, the propagation of planar shock wave over double-concave cylindrical surfaces is numerically investigated. The incident shock-wave Mach number is kept constant such as $M_s = 1.6$. Five gases, with different physical properties, are used as working gases, namely, air, He, Ar, CO_2 and SF_6. As expected, the fastest transmitted shock wave is found in the He case, while the slowest one is seen in the SF_6 case. In the Ar case, due to the similarity in the acoustic impedance between air and Ar, both waves propagate with almost the same velocity.

It has been found that the incident-shock wave trajectory and velocity can be approximated by a simple universal relation. The shock position and velocity are proportional to the initial shock velocity reduced by a scaling function that depending on the incident shock-wave Mach number, the specific heat ratio and the concave surface radius. The proposed scaling was tested in five different specific heat ratios and concave surface radius of 50 mm and diffraction angles of $w_1 = w_2 = 75°$.

Based on the present numerical results, and in order to make the scaling function, proposed in this study and the previous one Brahmi et al. (2020a), universal, the effect of the geometrical parameters, such as concave surfaces radius and diffraction angles, can be investigated.

6

Achieving an optimal shock-wave mitigation inside open channels with cavities for weak shock waves: A computational study

Published in: *Theoretical and Applied Mechanics Letters*

Highlights

- A shock-wave propagation and its attenuation in channel flows with cylindrical cavities is studied.
- An optimal arrangement of channel position/height and a cavity depth is numerically retrieved.
- About 57% of pressure attenuation is achieved.

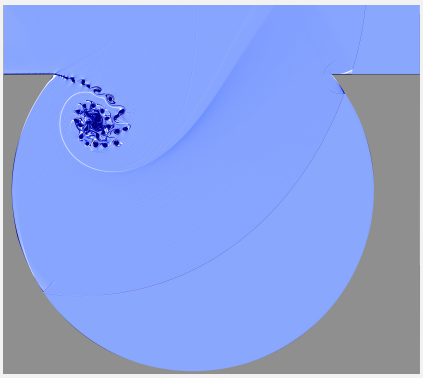

Numerical shleiren picture of a shock-wave diffraction over cylindrical cavity with initial diffraction angle $\theta_w = 140°$.

Theoretical & Applied Mechanics Letters 10 (2020) 354-365

Contents lists available at ScienceDirect

Theoretical & Applied Mechanics Letters

journal homepage: www.elsevier.com/locate/taml

Letter

Achieving an optimal shock-wave mitigation inside open channels with cavities for weak shock waves: A computational study

N. Brahmi*, A. Hadjadj

Normandie University, Institut National des Sciences Appliquées of Rouen, CNRS, CORIA, 76000 Rouen, France

HIGHLIGHTS

- A shock-wave propagation and its attenuation in channel flows is studied.
- A best cavity depth and diffraction angle is found.
- An optimal arrangement of channel position/height and a cavity depth is found.
- A pressure attenuation by a factor of 57% is achieved.

ARTICLE INFO

Article history:
Received 7 March 2020
Received in revised form 27 May 2020
Accepted 1 June 2020
Available online 12 June 2020
This article belongs to the Fluid Mechanics.

Keywords:
Shock diffraction
Shock reflection
Shock attenuation
Vortex generation

ABSTRACT

This paper deals with a numerical study of weak shock-waves propagation and their attenuation in channel flow having different heights and exhibiting a hollow circular cavities with different depths and diffraction angles inside. The effect of initial diffraction angle and cavity depth on the shock mitigation is investigated. A better shock attenuation is achieved with diffraction angle $\theta_w = 90°$ by a factor of approximately 17% in terms of shock-Mach number and 38% in terms of total energy. The obtained results show also, in addition to the initial diffraction angle and cavity depth, the importance of reducing the channel heights as well as the position of the reduced section in achieving an optimal shock-wave attenuation. The presence of a cavity inside the channel helps to attenuate faster the shock wave. The underlying physics relies on the shock diffraction phenomenon that generates large amount of vortical structures capable of dissipating part of the shock energy by inducing a pressure loss behind it. A subtle arrangement of channel position/height and a cavity location leads to an efficient pressure attenuation by approximately a factor of 57% for $M_s = 1.6$ and 16% for $M_s = 1.1$.

The propagation of planar shock waves inside channels, mines of underground bunkers can create serious human injury and installations damage due to several wave reflections that can locally generate zones of dangerous high-pressure amplification. Thus, the knowledge of shock-wave propagation in confined media is essential for engineering applications dealing with safety, blast wave and explosion attenuation. This is why many studies regarding ways to attenuate oncoming shock or blast waves were conducted in the past. Shock-wave attenuation can be achieved by various means, e.g. foams [1–3], porous materials, granular filters, metallic grids, perforated plates, branched/bend duct [4–6], duct with rough walls, etc. Other possibilities consist of using obstacles with appropriate geometries to attenuate shocks [7–9]. From a numerical point of view, attenuating a shock wave in a two-dimensional channel floor with rigid obstacles has been investigated by Chaudhuri et al. [10]. Obstacles of different shapes, i.e., cylindrical, square and triangular were placed in either staggered or non-staggered matrix forms. The pressure evolutions upstream and downstream of the matrices were monitored as to evaluate the attenuation effect. Results showed that the staggered matrix of reversed triangular

* Corresponding author.
E-mail address: nassim.brahmi@insa-rouen.fr (N. Brahmi).

http://dx.doi.org/10.1016/j.taml.2020.01.046

prisms is the most efficient combination in mitigating shock waves. For the same purpose, Wan et al. [11] have studied the possibility of attenuating shock waves by using a water spray obstacles. According to their study, water drops have the potential to efficiently attenuate shock waves given the important amount of heat that could be absorbed by water when mitigating the blast wave. In their study, shock attenuation effects of the water spray have been compared to solid obstacles devices using the same geometrical setup. Results showed that water like cylinders have a better capability to absorb the shock energy compared to solid obstacles of the same blockage area. Britan et al. [12] investigated the attenuation of an incident shock by porous barriers having different geometries and porosities. Using a one-dimensional modeling approach, it was found that the overpressure acting on an end-wall protected by a barrier decreases almost linearly with increasing distance between the end-wall and the barrier. Berger et al. [13] investigated experimentally the effects of different types of obstacles on the load developed by a shock wave. They identified the most influential parameters, noting that the geometry is the second most significant parameter in attenuating/amplifying the shock wave loads. It turns out that understanding the complex wave dynamics and the flow patterns is crucial for designing shock attenuators or shock amplifiers. Mortazawy et al. [14] presented both experimental and numerical investigations of normal shock with different strengths propagating inside ducts with surfaces roughness added in the form of grooves. Their results showed the effectiveness of roughness in terms of grooves in attenuating shock waves. The case of a planar shock-wave propagation through a double-bend duct was investigated numerically by Chaudhuri [15]. Contrary to the shock-shear layer and shock-boundary layer dynamics, the principal shock wave patterns are seen to be less dependent on the flow Reynolds number. As for the overpressure attenuation, a factor of about 0.51 was found for shock wave Mach-number M_s = 1.53. Shi et al. [16] investigated the influence of high temperature effects on the protrusion of Mach stem in strong shock reflection over a wedge. The protrusion degree depends on the thermal energy buffer capacity of the testing gas that escalates the protrusion effect. In a recent numerical study, Brahmi et al. [17] investigated shock-wave diffraction over double concave cylindrical surfaces. This study reveals that the shock velocity deficit increases by increasing the shock-Mach number. In a second study [18], the authors showed that the first concave surface is effective in decreasing sufficiently the dynamic as well as the static pressure impulses. The results showed also the effect of the reflected and the secondary shocks in increasing the overall overpressure.

For attenuating shock/blast waves propagating inside channels, Igra et al. [19] summarized existing experimental and numerical studies related to geometrical aspects. Examples include abrupt changes in the channel geometry, and introduction of rigid barriers along the shock wave path.

Based on the above discussion, it is clear that the attenuating shock/blast waves propagating inside channels is still an active research topic where much effort is still needed to better understand the physical mechanism of the shock mitigation in confined areas. Intending to shed more light on this complex fluid problem, numerical simulations, solving two-dimensional compressible Navier–Stokes equations, are used to study the shock waves propagation inside channels. The main objective of the present study is to better understand the physical aspects of shock propagation and its attenuation in confined areas with embedded cavities inside. The optimization of the channel geometry and dimensions for better shock wave attenuation is one of the main scope of the present contribution.

The numerical simulations carried out in this study are based on the use of an *in-house* parallel compressible solver, called CHOC-WAVES. The code is equipped with an adaptive multi-resolution method for mesh refinement [20–22], along with an immersed boundary method (IBM) to handle fluid-solid interaction problems [23]. The solid bodies, identified using a ray-tracing technique, are embedded into a Cartesian grid. Two-dimensional fully compressible Navier–Stokes equations are solved assuming the gas as ideal and the viscosity obeying to Sutherland's law. Inviscid and viscous fluxes are computed using a fifth-order weighted essentially non-oscillatory (WENO) scheme and a fourth-order central difference formula, respectively. The time is advanced using a third-order Runge–Kutta method [24]. The code is validated through a variant of test problems including shock/shock, shock/turbulence and shock/obstacles interactions [20–22].

As for the computational specifications, the boundary conditions are set to inlet and outlet at the left and the right sides of the computational domain, respectively. The solid boundaries (top and bottom) are treated as no-slip walls (see Fig. 1).

The problem setup of the simulations is shown in Fig. 1. In all the considered simulations, the cavity radius, R, is kept constant as R = 50 mm. Since R is kept constant and the cavity depth, d, is varied, the initial cavity angle, θ_w, must necessarily vary in order to keep the circular shape of the cavity. In this study we chose three different values of 60°, 90° and 140°. Two shock wave Mach-numbers are used namely, M_s = 1.6 and 1.1. The moving normal shock wave is initiated by imposing the Rankine–Hugoniot relations across an initial discontinuity. The simulations are carried out using a structured mesh with more than 80 million points with 28 processors. A single simulation took on average 200 hours which makes 5600 CPU hours.

Figure 2 shows a schematic illustration of the shock diffraction process past cylindrical cavities. Shortly after the penetration of the shock into the cavity, the expanded flow evolves into a complicated system of distorted and secondary shocks with separation regions (depending on the diffraction angle) and an end-wall corner vortex is formed with a rolling-up of eddies that are convected quasi-linearly away from the cavity entrance as the diffraction process evolves. In addition to this important primary vortex, a secondary instabilities appear along the cavity wall for $\theta_w \leq 90°$.

Here, we present the effect of different cavity depths and diffraction angles on the shock-wave patterns by comparing them to the case without cavity (a straight tube).

Figure 3a shows the space-time evolution of the shock wave. One can see that the transmitted shock reaches the channel exit earlier for the straight tube then for θ_w = 60° and later for 140° and 90°, respectively. These results are also highlighted through the variation of the shock-wave speed, presented in Fig. 3b in terms of M_s and total energy presented in Fig. 3c. For all cases, we first notice a constant shock wave Mach-number and energy. After the diffraction process starts, an end-wall corner vortex is formed with a rolling-up of eddies. The formation of these vortices leads to a shock velocity and energy drop, except for the

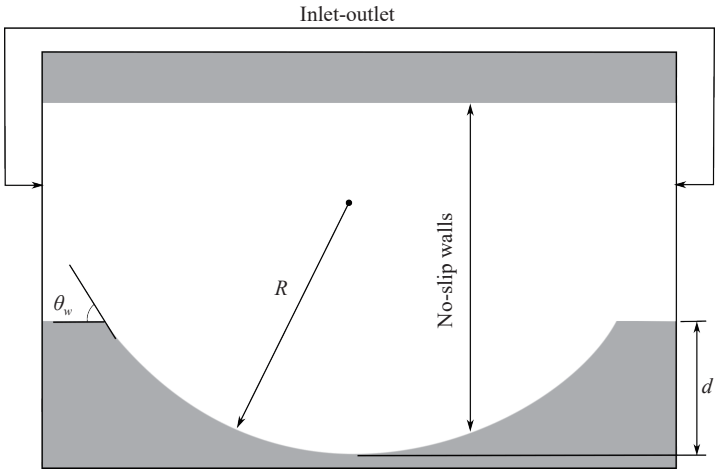

Fig. 1. Schematic representation of the problem setup. θ_w: initial cavity angle, R: cavity radius, d: cavity depth.

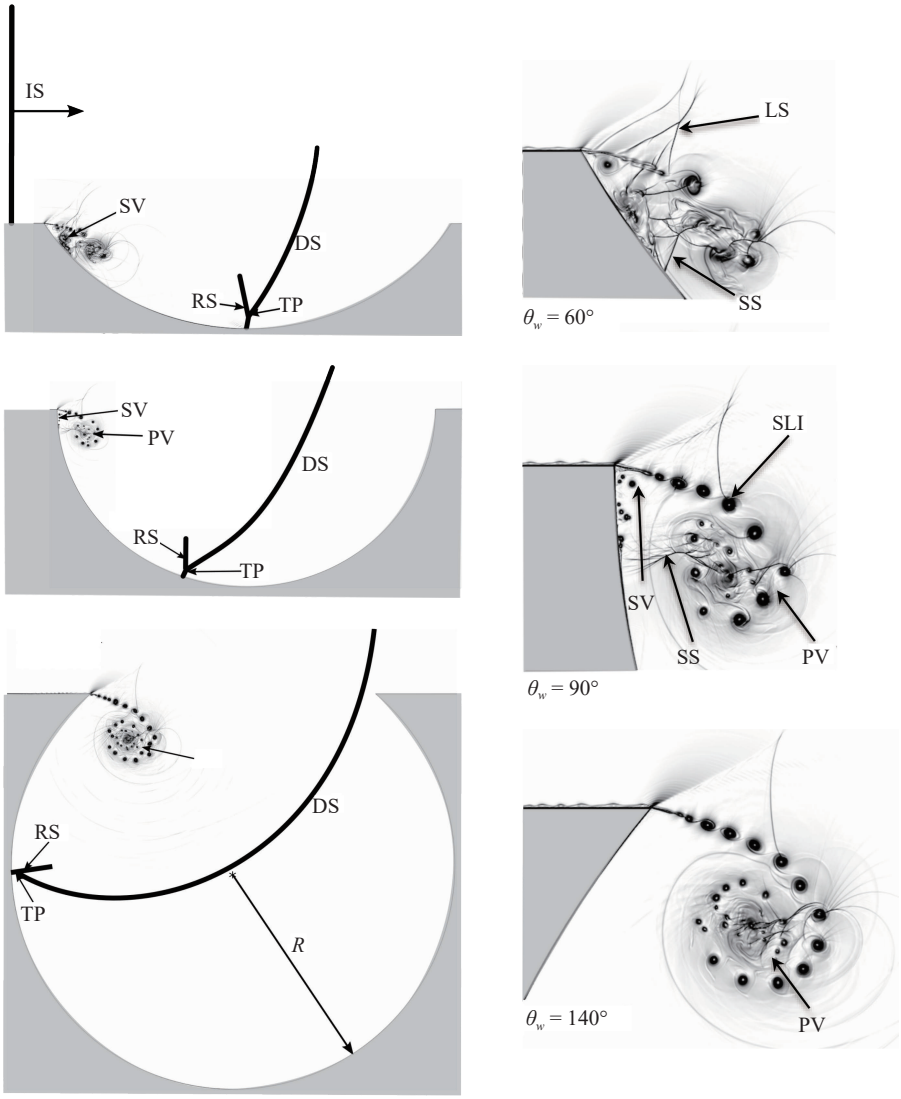

Fig. 2. Shock diffraction for different initial cavity angles and depths. IS: incident shock; RS: reflected shock; DS: diffracted shock; TP: triple point; PV: primary vortex; SV: secondary vortex; LS: lambda shock; SLI: shear-layer instabilities; SS: secondary shock. The images on the right side are the enlargement of the portions on the left side.

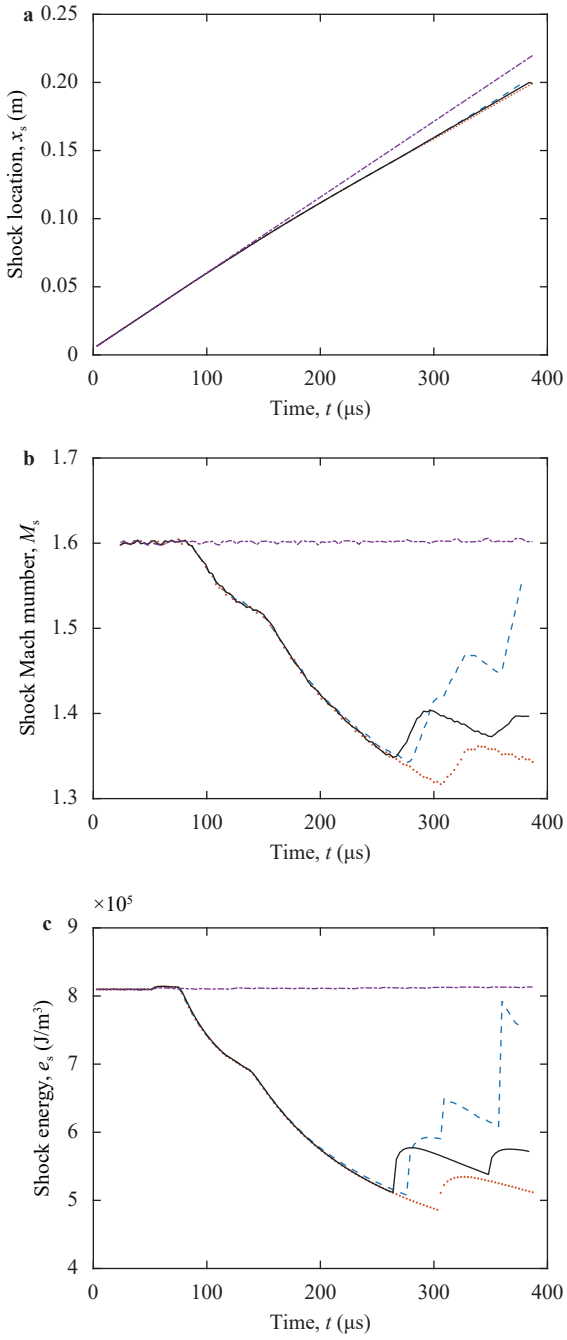

Fig. 3. Time history of **a** shock position, **b** shock Mach number, and **c** shock energy for different diffraction angles (blue dash line: θ_w = 60°, red dot line: θ_w = 90°, black line: θ_w = 140°, dash-dot line: straight tube).

straight tube for which the shock velocity and energy remain quasi-constant. As this process evolves in time, the shock patterns differ from one case to another depending on the cavity geometry.

For θ_w = 60°, we notice a drop in the shock velocity and energy until three successive peaks appear at $t \approx$ 280, 305, and 360 μs, respectively. In order to understand the origin of these peaks we will discuss the shock reflection phenomenon in the second half of the cavity (depicted in Fig. 4). Roughly in the middle of the cavity, an inverse-Mach reflection (InMR) configuration appears. A bit further, in the second half of the cavity (rising part), the InMR terminates to a transitioned regular reflection (TRR), with two additional shocks, r' and d' (as shown in Fig. 4b). The additional shock, d', catches the incident shock (I) at the exit of the cavity and merge together into a single shock (see Fig. 4c). This process increases the shock velocity and energy and forms a new transmitted shock, I', hence the first velocity and energy jumps of the graphs. Note that r' will catch the new transmitted shock (I'), and increases the velocity and the energy behind by forming a new transmitted shock, I''. This phenomenon is observed through the second velocity and energy jumps of the plots. The additional shocks, r' and d', from the TRR configuration, will successively be reflected from the upper boundary forming new reflected shocks, r'' and d'', which will merge together into a more intense shock, d^*. The new shock, d^*, catches the incident shock, I'', and merge together into a single stronger shock, I^*, at the exit of the channel (see Fig. 4(d, e)). The speed and the energy of the resulting shock are enhanced. This phenomenon is observed through the third velocity and energy jumps.

For θ_w = 90°, we notice a drop in the shock velocity and energy towards a lower value. A peak appears at $t \approx$ 310 μs. At $t \approx$ 216 μs, the incident shock, hits the upper right corner of the cavity giving birth to a direct-Mach reflection (DiMR) inducing to the formation of a reflected shock r_1. r_1 catches the incident shock at the channel exit and merge into a single shock. This process increases the shock velocity and energy and forms I', hence the velocity and energy jumps of the graphs. The reflection process is highlighted in Fig. 5.

For θ_w = 140°, two successive peaks appear at $t \approx$ 260 and 350 μs, respectively. As for θ_w = 90°, the incident shock, hits the upper right corner of the cavity leading to the formation of a DiMR inducing to the formation of a reflected shock r_1. r_1 catches the incident shock I and merge together into a single shock (see Fig. 6(a, b)) increasing the shock velocity and energy by the formation of I', hence the first velocity and energy jumps. The reflected shock r_1 is again reflected by the upper boundary. The new reflected shock, r'_1 catches the transmitted shock, I', hence the second velocity and energy jumps. The reflection process is highlighted in Fig. 6.

Figure 7 represents spatial distribution, at y/R = 2, of energy along with numerical schlieren pictures for different configurations at t = 378 μs. For θ_w = 60°, presented in Fig. 7a, the energy is decreasing until a series of peaks appears. These peaks are due to the formation of secondary and reflected shocks. The most intense peak is located at $x/R \approx$ 0.6, which is caused by the merger of the secondary shock, SS, and the reflected shock, r^*.

As for θ_w = 60°, for θ_w = 90°, presented in Fig. 7b, the energy is decreasing until a secondary shock appears to increase the energy level. A bit further, at $x/R \approx$ 1.6 , an intense peak appears due the reflected shock r thus increasing the energy level to a higher value. After this important peak, a series of less intense peaks appears due to the reflected shocks from the upper and the lower boundaries. It is important to mention that the transmitted shock energy for θ_w = 90° at the channel exit is reduced by 32% compared to that of θ_w = 60°.

For the last configuration, θ_w = 140°, presented in Fig. 7c, the energy decreases towards the lower value of the three configura-

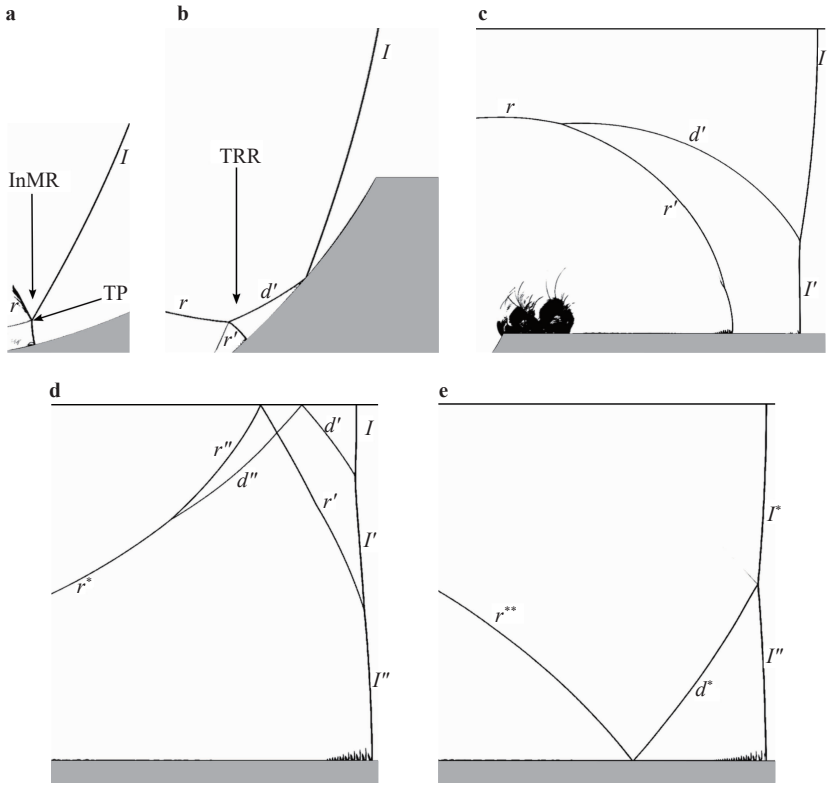

Fig. 4. Numerical schlieren pictures for $\theta_w = 60°$. I: incident shock; r: reflected shock; TP: triple point; InMR: inverse-Mach reflection; TRR: transitioned regular reflection; r' and d': additional shocks created from TRR state; I': new incident shock resulting from the merger of I and d'; d'' and r'' and r^*: reflected shocks from the upper boundary; I'': new incident shock resulting from the merger of r' and I'; r^{**}: reflected shock from the lower boundary; d^*: new shock resulting from the merger of r'' and d''; I^*: new incident shock resulting from the merger of d^* and I''.

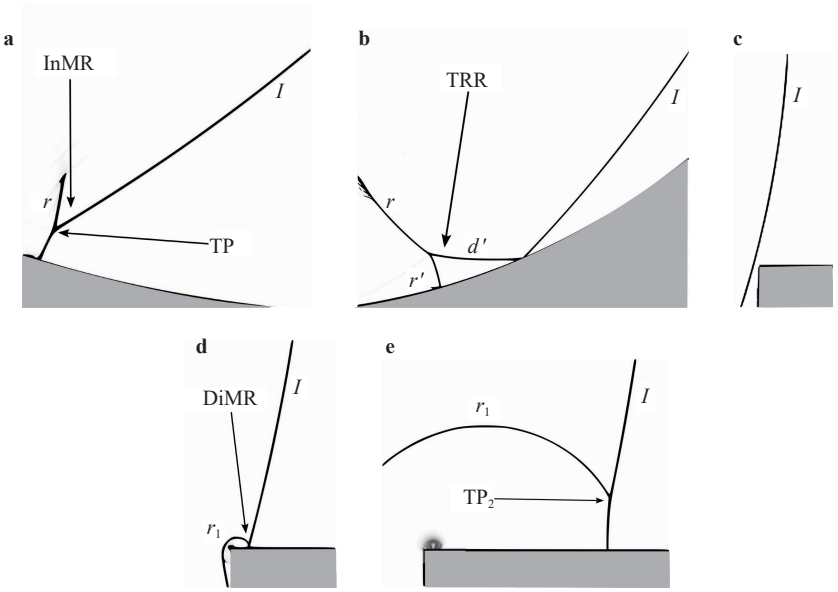

Fig. 5. Numerical schlieren pictures for $\theta_w = 90°$. I: incident shock; r: reflected shock; InMR: inverse-Mach reflection; TP: triple point; TRR: transitioned regular reflection; r' and d': additional shocks created from TRR state; DiMR: direct-Mach reflection, r_1: reflected shock; TP_2: second triple point.

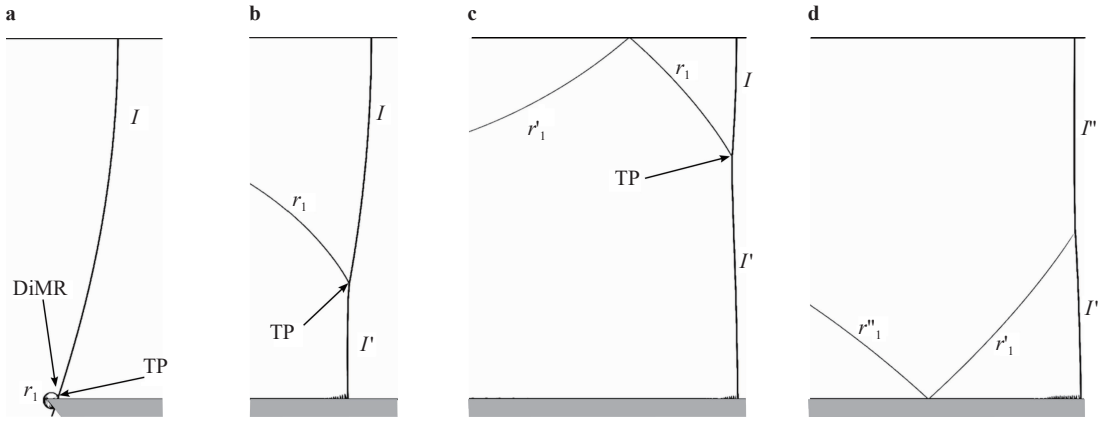

Fig. 6. Numerical schlieren pictures for $\theta_w = 140°$. *I*: incident shock; r_1: reflected shock; TP : triple point; DiMR: direct-Mach reflection; r'_1: reflected shock from the upper boundary; r'': reflected shock from the lower boundary.

tions. At $x/R \approx 1.2$, secondary shocks appear and increase the energy level to a quasi-constant value. No more considerable peaks are seen in the channel.

Although the energy level reaches its minimum for $\theta_w = 140°$ in the cavity zone, a better shock attenuation, in the channel exit, is achieved for the second configuration, $\theta_w = 90°$, by a factor of approximately 38%, and this is due, as explained above, to the different reflection phenomena from one case to another, specially at the cavity exit.

In the first part of this study, we were interested in the effect of the cavity depth (d) and the initial diffraction angle (θ_w) while keeping the tunnel height (h) constant. In this second part we kept d and θ_w constant while varying h, for that we have defined: $\zeta = h/d$, and we took two different values of the latter, namely: 0.25 and 2.36. Six different cases are considered where basically the inlet and the outlet volumes have been varied to cover the most relevant situations. The problem setup is shown in Fig. 8. According to the results obtained in the first part, we chose to use the case with $\theta_w = 90°$ and $d = 50$ mm,.

Figure 9 presents numerical schlieren pictures for different configurations at $t = 288$ µs. The incident shock wave starts to diffract over the top left corner of the cavity resulting in the formation of an end-wall corner vortex with a rolling-up of coherent structures. Roughly in the middle of the cavity, an InMR appears, whose termination leads to the formation of a TRR. More details are shown in Figs.5(a, b). At approximately $t = 216$ µs the incident shock wave I hits the upper right corner of the cavity giving birth to a DiMR inducing to the formation of a reflected shock. More details are shown in Fig. 5(c–e). After the passage of the shock, vortices are formed at the upper right corner of the cavity, and at the lower right end of the upper wall for C3 and C4 configurations. When the transmitted shock propagates further away from the cavity and approaching the channel exit, the developed flow field can be divided into two separated zones. In the first one, noted Zone A, the compressed gas expands over the cavity and forms a series of vortices that dominate the flow features in this region. The second region, named Zone B, is mostly characterized by a quasi-uniform flow, followed by a series of wave reflections arising from both InMR and TRR. Transverse waves are then created due to the reflection of the shock on upper and lower channel walls, for C2 and C4. These observations confirm the earlier findings of Berger et al. [25].

Here, we present the effect of the channel height and the position of the expanding area on the shock wave patterns. Figure 10a shows the space-time evolution of the shock wave. One can see that the transmitted shock reaches the channel exit earlier for C1, C5, C4, C6 and later for C2 and C3, respectively. These results are also highlighted through the variation of the shock-wave speed, presented in Fig. 10b in terms of shock Mach-number M_s. For all cases, we first notice a constant shock speed and then a decrease just after the beginning of the diffraction process. As this process evolves in time, the shock dynamics differ from one case to another depending on the channel geometry. Thus, in order to understand the shock behavior, some important physical parameters are discussed, such as the variation of the pressure ratio, p_s/p_1 (p_s being the pressure behind the shock wave and p_1 the initial pressure in the shocked gas taken as, $p_s = 285.7$ kPa). The results are presented in Fig. 11.

For case C1, depicted in Fig. 11a, the flow structures can be divided into three main parts. The first one (part I), identical for all cases, highlights the shock dynamics before the startup of the diffraction process which is represented by a short horizontal line corresponding to the initialization values of the shock. After the diffraction process starts (part II), an end-wall corner vortex is formed with a rolling-up of eddies. The formation of these vortices leads to a pressure decrease and the more this disturbed region spreads over the diffraction volume, the more the pressure decreases (see cases C2 and C3). At approximately $t \approx 216$ µs the incident shock wave (I) hits the upper right corner of the cavity giving birth to a DiMR inducing to the formation of a reflected shock, r_1. The later catches up the incident shock (I) and merge into a single shock, the phenomenon is depicted in Fig. 12(a–c). This process increases the pressure ratio, hence the first pressure jump for the third phase (part III) of the graph. After that, the observed pressure state behind the propagating shock wave is fairly uniform.

As for the first case, the pressure ratio evolution for the second one C2 can be divided into three parts (see Fig. 11b). Part I is identical to that of case C1. For part II, we notice a drop in the pressure ratio towards a lower value. By reducing the channel height to $h_1/d = 0.25$, the formed vortex at the upper left corner of the cavity occupies a much larger volume, thus lowering fur-

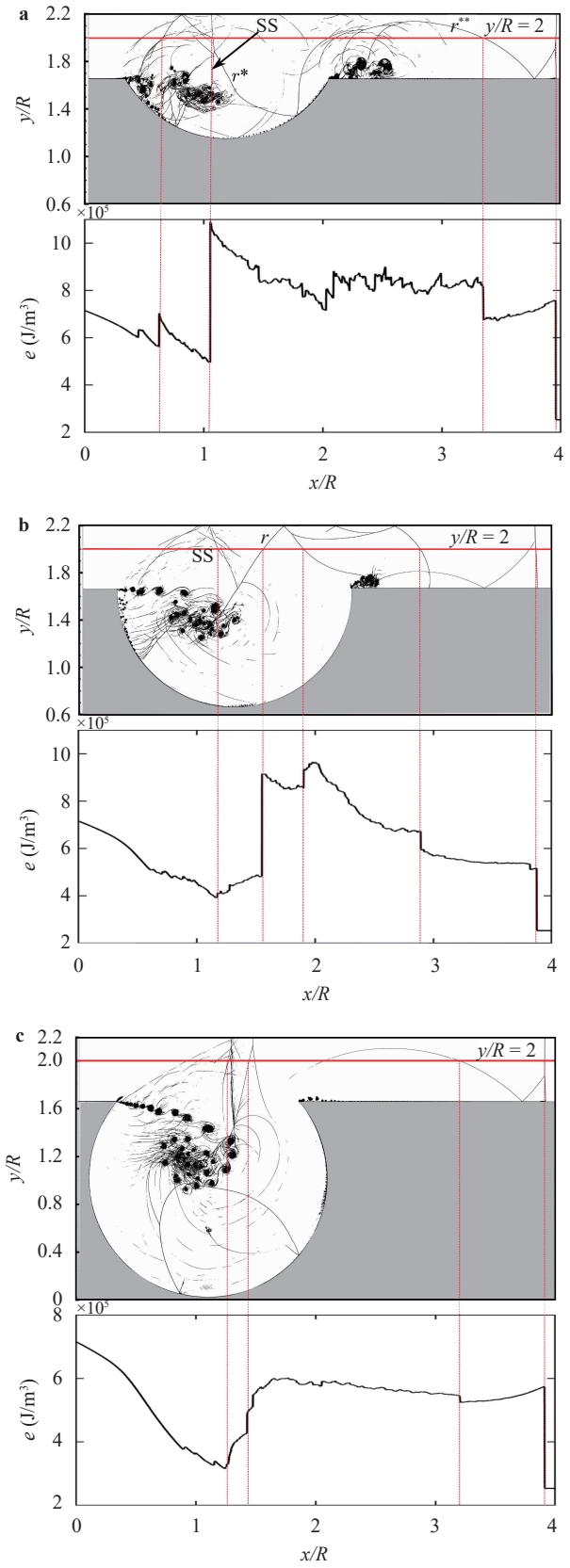

Fig. 7. Spatial distribution of energy along with numerical schlieren pictures for different configurations at $t = 378$ µs.

ther the pressure level in the cavity and behind the shock as well. For part III, we observe a presence of a series of successive three pressure jumps. The first pressure jump is caused by the DiMR, phenomenon as mentioned before. The two following pressure peaks are essentially due to the multiple shock reflections arising from the upper and the lower channel walls. These reflected shocks successively catch the transmitted shock and merge all together into a single stronger shock, the phenomenon is depicted in Fig. 12(d–f). The pressure as well as the speed of the resulting shock are bit enhanced.

As depicted in Fig. 1c, stages I and II of C3 are similar to that of C2. Indeed in stage III, we notice an additional decrease in the pressure ratio due to the formation of two vortices. The first one is initiated at the lower-right corner of the top wall and the second one takes place at the top-right corner of the cavity. The decrease of the pressure is followed by a small jump, at the start of the fourth phase IV, which is due, as explained above, to the reflected shock resulting from the DiMR configuration (r_1). After this jump, the pressure ratio decreases quasi-linearly and reaches a value of approximately 0.43 at the channel exit.

Phases I and II in the fourth case, C4, presented in Fig. 11d, which in terms of geometry, is the inverse of the third case (C3), are similar to those in case C1. Phase III is similar to that of case C3. For part IV, we notice the presence of a series of successive pressure jumps. As reported previously, the first peak is caused by the reflected shock resulting from the DiMR configuration (r_1). The other peaks are due to the multiple wave reflections as explained for C2.

In order to to shed more light on the effect of the cavity, we realized a case similar to C3 but without cavity. The results for this case, C5, are presented in Fig. 11e. As we can see, the pressure ratio evolution for this case is divided into two parts. The first one, I, is similar to the previous cases, the second one, II, is characterized by a drop in the pressure ratio. This pressure drop is caused by the shock-wave diffraction and the formation of vortex at the lower right corner of the upper boundary. The effect of the cavity is clearly visible by comparing the two cases where the best pressure attenuation is achieved with the cavity for C3. Note that the only difference between C3 and C5 is the absence of the cavity, all the other geometrical dimensions are kept the same.

The effect of another geometrical parameter has been investigated, namely the length of the tunnel at the inlet. The results for this case, C6, are presented in Fig. 11f. Compared to the previous case, the pressure ratio for this case starts decreasing earlier because of the early shock-wave diffraction and the formation of vortex at the lower right corner of the upper boundary. Although the pressure started decreasing earlier for C6, at the exit of the tunnel it reaches a value almost equal to that of C5. This configuration confirms the role played by the cavity in the pressure attenuation.

Table 1 shows the time variation of the pressure, defined as $\mathrm{d}p/\mathrm{d}t = (p_e - p_{\min})/(t_e - t_{p_{\min}})$. Here, p_e is the pressure behind the transmitted shock at the exit of the channel, $p_{\min}$ is the minimum pressure behind the shock, t_e is the instant when the shock arrives at the end of the channel and $t_{p_{\min}}$ is the instant when the pressure behind the shock reaches its minimum value. As shown in Table 1, the only configuration where a pressure reduction is achieved is C3. The most critical case is the one related to configuration C1, where an increase, of approximately 426 MPa/s, is obtained. Table 1 shows also the shock attenu-

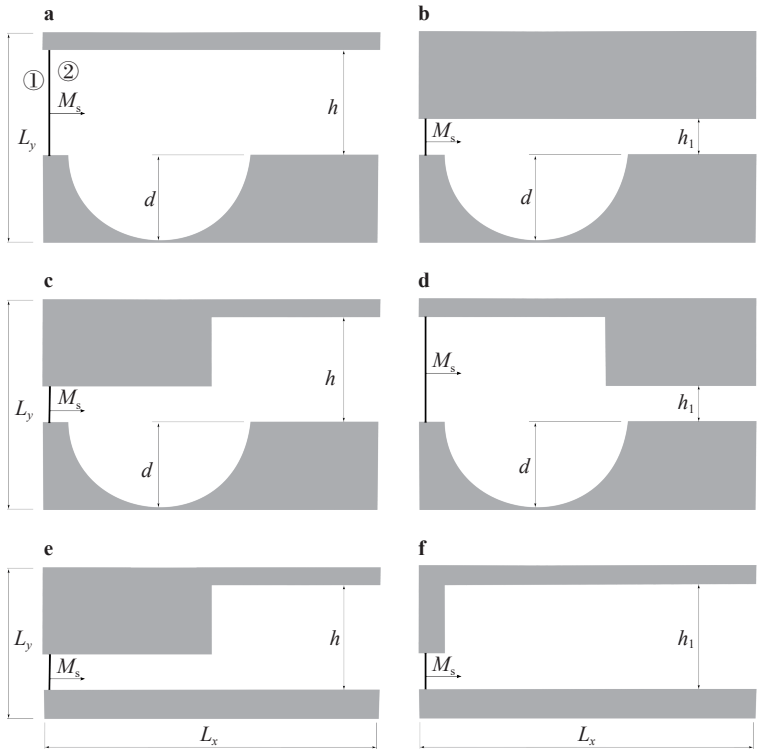

Fig. 8. Schematic illustration of the geometrical setups, **a** C1, **b** C2, **c** C3, **d** C4, **e** C5, and **f** C6. d = 50 mm: cavity depth, h: height of the first channel, h_1: height of the second channel (L_x = 200 mm, L_y = 171 mm). The dimensions of the computation domain in x and y directions, respectively. ① shocked gas, ② gas at rest.

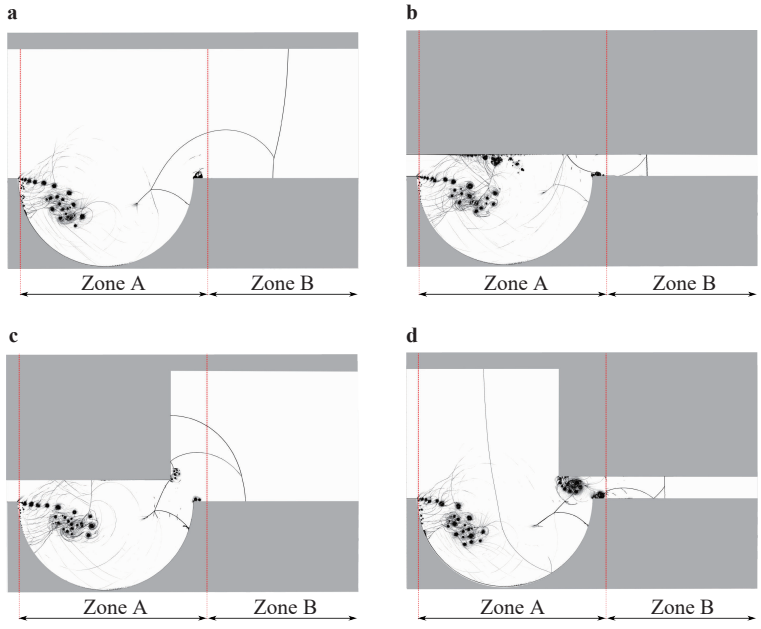

Fig. 9. Numerical schlieren pictures for different flow configurations C1, C2, C3, and C4 at t = 288 μs.

ation factor $\mathcal{A}$ defined as the ratio of the relative pressure behind the transmitted shock (at the exit of the channel) to the initial shocked gas pressure such as, $\mathcal{A} = (p_1 - p_s)/p_1$, where p_1 = 285.7 kPa and p_s is the exit pressure. Comparison between all configurations indicates that the height and the expanded area position of the channel significantly affect the shock wave attenuation. The results show that a better attenuation factor is obtained for C3 (about 57%). However, for case C1 the attenuation effects are minor, about 3%.

The effect of different configurations on shock strength is

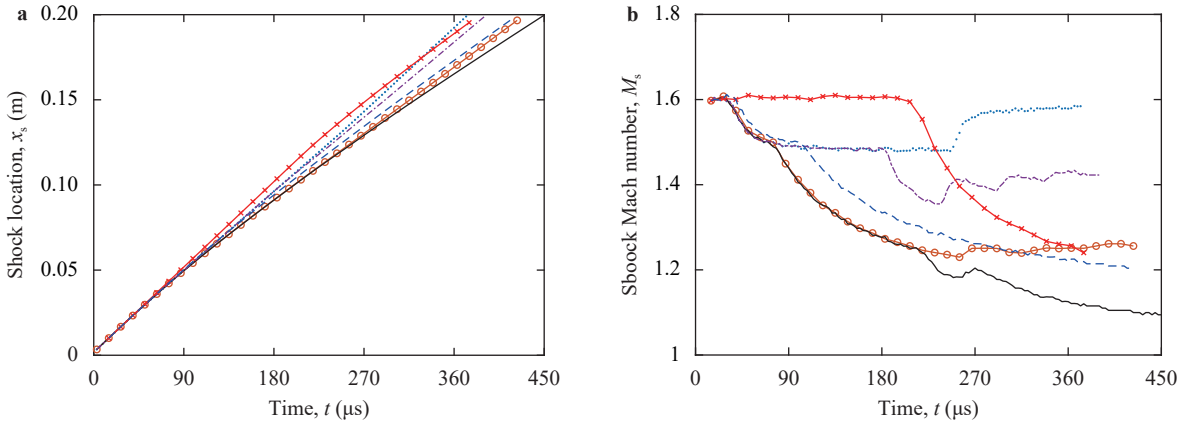

Fig. 10. Time variation of **a** shock location and **b** shock Mach number for blue dot line: C1, red "o" line: C2, black line: C3, black dash-dot line: C4, red "×" line: C5, blue dash line: C6.

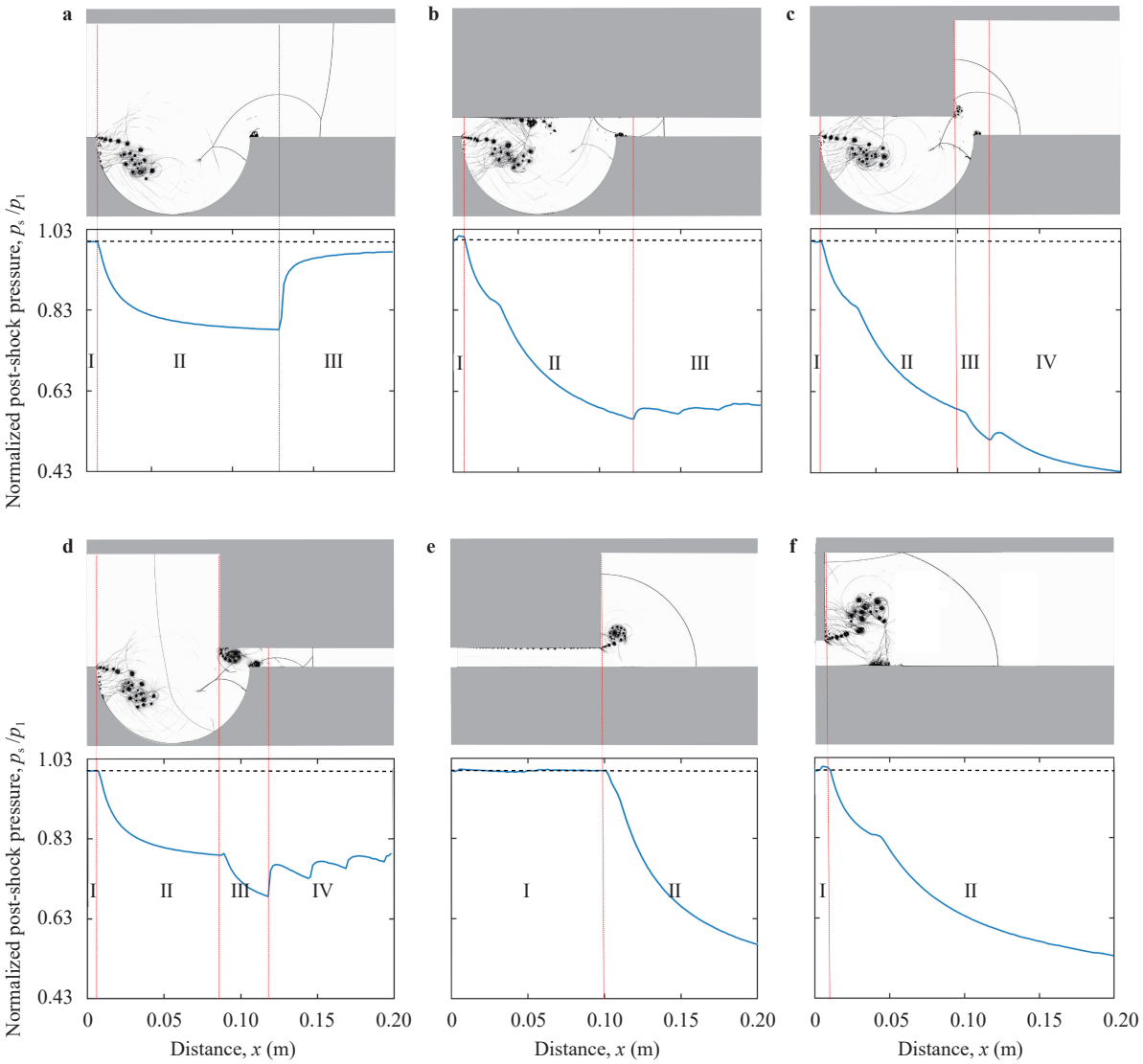

Fig. 11. Spatial distribution of the normalized shock pressure along with numerical schlieren pictures for different flow configurations at $t = 288$ μs. p_1 is the initial pressure taken as $p_1 = 285.7$ kPa and p_s is the pressure behind the shock.

Table 1 Pressure variation $\mathrm{d}p/\mathrm{d}t$ and attenuation factor $\mathcal{A}$ for M_s = 1.6.

	C1	C2	C3	C4	C5	C6
$\mathrm{d}p/\mathrm{d}t$ (MPa/s)	426	55	-111	197	-	-
$\mathcal{A}$ (%)	3	40	57	21	42	46

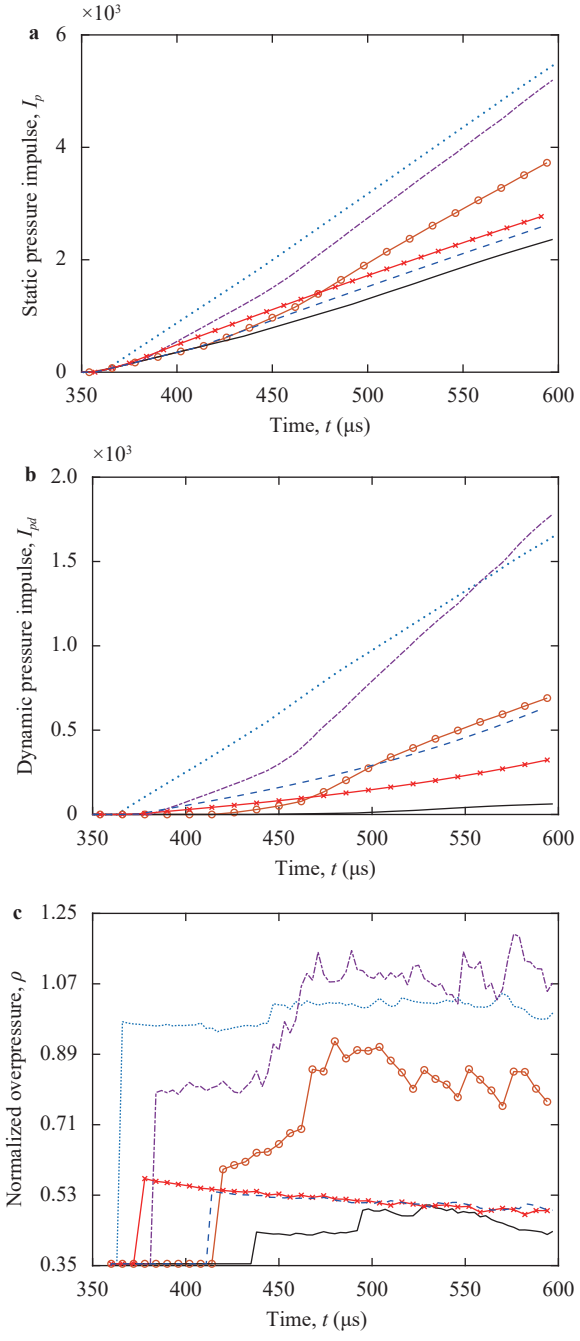

Fig. 13. Time evolution of **a** static impulses, **b** dynamic impulses, and **c** normalized overpressures at $y/d = 1.28$ and $x/d = 4$ for blue dot line: C1, red "o" line: C2, black line: C3, black dash-dot line: C4, red "×" line: C5, blue dash line: C6.

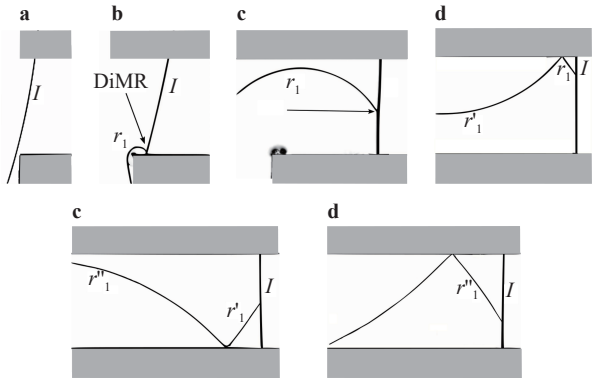

Fig. 12. Numerical schlieren pictures for $\theta_w = 90°$ and $\zeta = 0.25$.

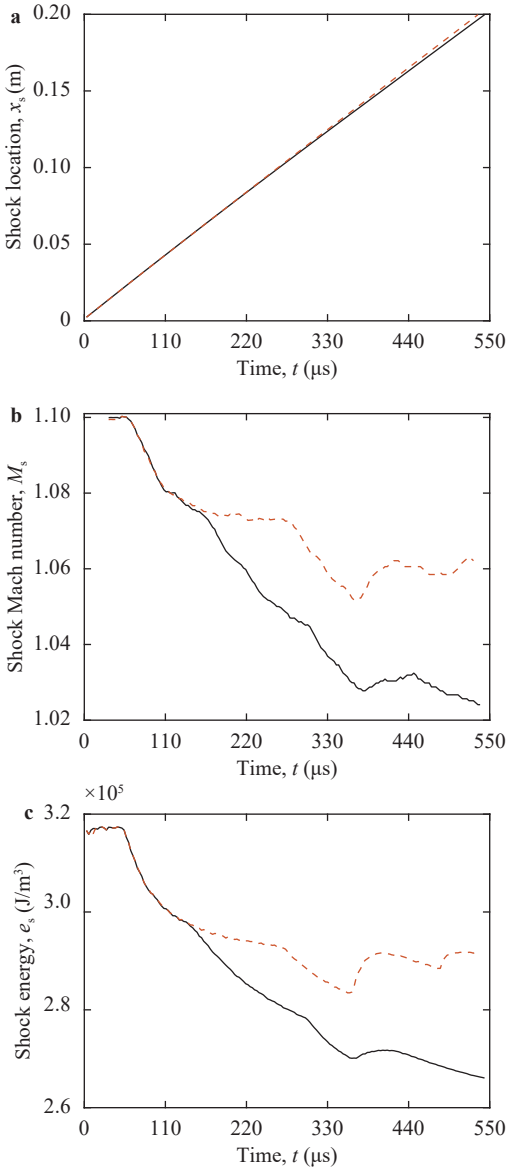

Fig. 14. Time history of **a** shock position, **b** shock Mach-number, and **c** shock energy for different diffraction cases. Black line: C3, red dash line: C4 for M_s = 1.1.

also investigated by computing the static, I_p, as well the dynamic, I_{pd}, pressure impulses along with the normalized over pressure, $\mathcal{P}$. These three parameters are defined as,

$$I_p = \int_{t_0}^{t_f} p\,\mathrm{d}t, \quad I_{pd} = \int_{t_0}^{t_f} \frac{1}{2}\rho v^2\,\mathrm{d}t, \quad \mathcal{P} = p/p_1,$$

where p, ρ and v are the pressure, density and velocity in the shocked region, respectively. The initial time t_0 is picked when the transmitted shock wave reaches the channel exit (x/d = 4) and t_f is the final time of the simulations. The obtained pressure impulses are presented in Fig. 13(a, b). The general trends show that these quantities increase quasi-linearly after the passage of the shock. The exit of the channel is mostly comprised by a quasi-uniform gas, hence the quasi-linear behavior of static and dynamic impulses. As expected from previous results, the minimum value for both static and dynamic pressure impulses is obtained for C3. As for the normalized overpressure, Fig. 13c shows a sudden jump due to the passage of the incident shock, which remains almost constant later for C1, C5, and C6. For C2, C3, and C4, a successive peaks can be seen, these peaks are due to the reflection phenomena at the cavity exit as explained before. The intensity of the normalized overpressure at t_f varies between a maximum value for C4 and a minimum value for C3. Note that, except the shock delay, no remarkable differences are seen between the normalized overpressure of C5 and C6.

Then we investigated the effect of the incident-shock Mach number by setting M_s = 1.1 for C3 and C4. Figure 14a shows the space-time evolution of the shock wave. One can see that the transmitted shock reaches the end of the channel earlier for C4 and later for C3. These results are also highlighted through the variation of the shock-wave speed, presented in Fig. 14b in terms of shock-wave Mach number, M_s. For the two cases, we first notice a constant shock speed and then a decrease just after the beginning of the diffraction process. As this process evolves in time, the shock dynamics differ from one case to another depending on the channel geometry and the shock reflection phenomena at the cavity exit. Thus, in order to understand the shock behavior, some important physical parameters are discussed, such as the variation of the pressure ratio, p_s/p_1 (p_s being the pressure behind the shock wave and p_1 the initial pressure in the shocked gas taken as p_1 = 126.15 kPa) along with schlieren pictures. The results are presented in Fig. 15. As we can see in this figure, no significant effect of reducing the shock Mach number. Among the remarkable effects, the reduction in the number of peaks for phase IV of C4. This reduction is mainly linked to the reduction of the speed of the shock wave as well as those of the reflected waves and their intensities as shown in Fig. 16c and 16d. The reduction of the shock Mach number does not affect the reflection process in the upper right corner of the cavity where a direct-Mach reflection takes place as seen for M_s = 1.6, the reflection process is depicted in Fig. 16.

Table 2 shows the time variation of the pressure. As for M_s = 1.6 a pressure reduction is achieved with C3 and a pressure increase is obtained with C4. As for the attenuation factor, $\mathcal{A}$, a shock mitigation is achieved with both cases. The results show that, as for M_s = 1.6, a better attenuation factor is obtained for C3.

In summary, this paper reports new computational results on weak shock-waves propagation and their attenuation in channel flows with different heights. A circular section cavities with different depths and diffraction angles are added to the channel as to induce shock diffraction and to generate vortices responsible for the pressure drop behind the shock. A better shock mitigation is achieved with diffraction angle θ_w = 90°, where, the total shock energy is reduced by approximately 38%. A careful analysis of the flow structures reveals that in addition to the variation of the channel height, the position of these modifications play an important role in the shock mitigation. A subtle arrangement of channel position/height and cavity is found, leading to a significant attenuation factor of about 57% for M_s = 1.6 and 16% for M_s =

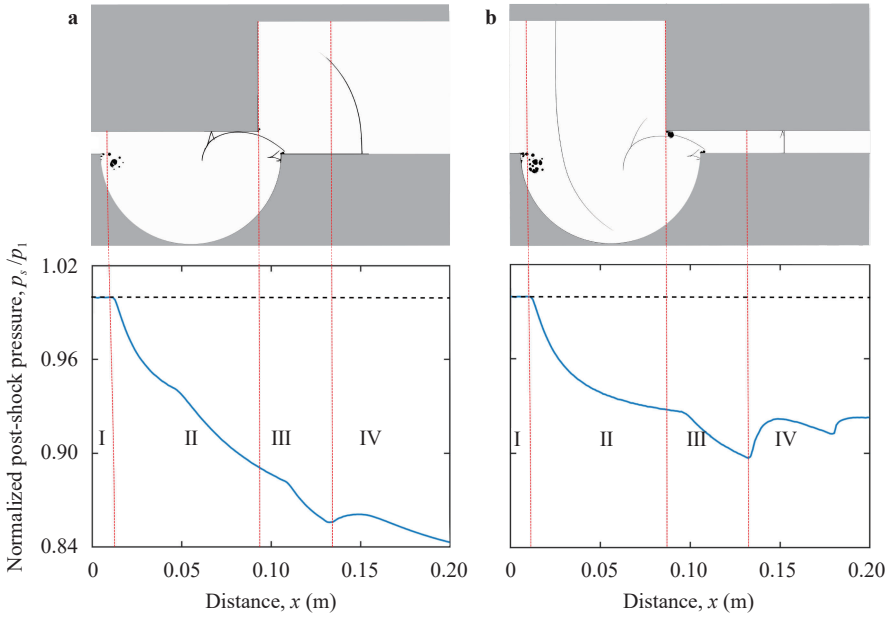

Fig. 15. Spatial distribution of the normalized shock pressure along with numerical schlieren pictures for different flow configurations at t = 408 μs for M_s = 1.1. p_1 is the initial pressure taken as p_1 = 126.15 kPa and p_s is the pressure behind the shock.

Table 2 Pressure variation $\mathrm{d}p/\mathrm{d}t$ and attenuation factor $\mathcal{A}$ for M_s = 1.1.

	C3	C4
$\mathrm{d}p/\mathrm{d}t$ (MPa/s)	-9	18
$\mathcal{A}$ (%)	16	8

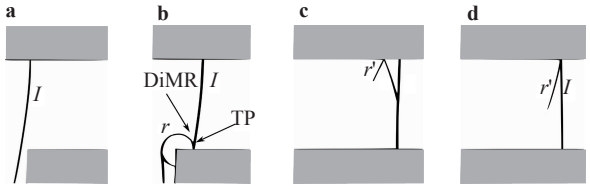

Fig. 16. Numerical schlieren pictures for θ_w = 90° and M_s = 1.1, for C4.

1.1. In summary, the shock wave attenuation in an open channel with a cavity inside can be associated to the following mechanisms: (1) shock diffraction over the cavity that results in the formation of an end-wall corner vortex, leading to a large dissipative region responsible for the pressure decrease behind the shock, (2) appearance of an InMR due to the shock reflection which result in the formation of a TRR over the cavity, (3) appearance of a DiMR due to the shock reflection from the upper right corner of the cavity, and (4) formation of multiple transverse waves due to shock reflections from top and bottom channel walls owing to the confinement effect.

Based on the present numerical results, other forms of cavity can be proposed to further attenuate shocks in channel flows. The idea is to avoid the formation of the DiMR. This can be achieved by suppressing the rising part of the cavity.

Acknowledgement

The first author gratefully acknowledges support from the Algerian Government through a Ph.D Fellowship. Computational facilities from 'Centre Régional Informatique et d'Applications Numériques de Normandie (CRIANN), Rouen, France (Grant 1998022) are acknowledged.

References

[1] K. Kitagawa, K. Takayama, M. Yasuhara, Attenuation of shock waves propagating in polyurethane foams, Shock Waves 15 (2006) 437–445.
[2] A. Britan, M. Liverts, H. Shapiro, et al., Macro-mechanical modeling of blast-wave mitigation in foams. Part I: Review of available experiments and models, Shock Waves 23 (2013) 5–23.
[3] A. Britan, M. Liverts, H. Shapiro, et al., Macro-mechanical modeling of blast-wave mitigation in foams. Part II: Reliability of pressure measure- ments, Shock Waves 23 (2013) 25–38.
[4] O. Igra, X. Wu, J. Falcovitz, et al., Experimental and theoretical study of shock wave propagation through double-bend ducts, J. Fluid Mech. 437 (2001) 255–282.
[5] P. Kosinski, On shock wave propagation in a branched channel with particles, Shock Waves 15 (2006) 13–20.
[6] Z. Jiang, K. Takayama, H. Babinsky, et al., Transient shock wave flows in tubes with a sudden change in cross section, Shock Waves 7 (1997) 151–162.
[7] I. Sochet, S. Eveillard, J.Y. Vinçont, et al., Influence of the geometry of protective barriers on the propagation of shock waves, Shock Waves 27 (2017) 209–219.
[8] S. Sha, Z. Chen, X. Jiang, Influences of obstacle geometries on shock wave attenuation, Shock Waves 27 (2014) 573–582.
[9] A. Marty, E. Daniel, J. Massoni, et al., Experimental and numerical investigations of shock wave propagation through a bifurcation, Shock Waves 29 (2019) 321–326.
[10] A. Chaudhuri, A. Hadjadj, O. Sadot, et al., Numerical study of shock-wave mitigation through matrices of solid obstacles, Shock Waves 23 (2013) 91–101.
[11] Q. Wan, R. Deiterding, V. Eliasson, Numerical investigation of shock wave attenuation in channels using water obstacles, multiscale and multidisci plinary modeling, Experiments and Design 2 (2019) 159–173.
[12] A. Britan, O. Igra, G. Ben-Dor, et al., Shock wave attenuation by grids and orifice plates, Shock Waves 16 (2006) 1–15.
[13] S. Berger, O. Sadot, G. Ben-Dor, Experimental investigation on the shock-wave load attenuation by geometrical means, Shock Waves 20 (2010) 29–40.
[14] S.M. Mortazawy, K. Kontis, J. Ekaterinaris, Normal shock wave attenuation during propagation in ducts with grooves, Shock Waves 30 (2020) 91–113.
[15] A. Chaudhuri, On shock propagation through double-bend ducts by entropy-generation-based artificial viscosity method, Entropy 21 (2019) 1–14.
[16] X. Shi, Y. Zhu, X. Luo, et al., High temperature effects in moving shock reflection with protruding Mach stem, Theoretical & Applied Mechanics Letters 6 (2016) 222–225.
[17] N. Brahmi, A. Hadjadj, V. Soni, et al., Analysis of shock-wave diffraction over double concave cylindrical wedges. Part I: Shock dynamics, Acta Astronautica (2020) 134–139.
[18] N. Brahmi, A. Hadjadj, V. Soni, Analysis of shock-wave diffraction over double cylindrical wedges. Part II: Vorticity generation, Acta Astronautica 172 (2020) 140–150.
[19] O. Igra, J. Falcovitz, L. Houas, et al., Review of methods to attenuate shock/blast waves, Progress in Aerospace Sciences 58 (2013) 1–35.
[20] V. Soni, A. Hadjadj, O. Roussel, On the use of adaptive multiresolution method with time-varying tolerance for compressible fluid flows, Shock Waves 29 (2019) 37–50.
[21] V. Soni, A. Hadjadj, O. Roussel, et al., Parallel multi-core and multi-processor methods on point-value multiresolution algorithms for hyperbolic conservation laws, J. Parallel Distrib. Comput. 123 (2019) 192–203.
[22] V. Soni, O. Roussel, A. Hadjadj, On the accuracy and efficiency of point-value multiresolution algorithms for solving scalar wave and Euler equations, J. Computational & Applied Mathematics 323 (2017) 159–175.
[23] A. Chaudhuri, A. Hadjadj, A. Chinnayya, On the use of immersed boundary methods for shock/obstacle interactions, J. Comput. Phys. 230 (2011) 1731–1748.
[24] A. Chaudhuri, A. Hadjadj, A. Chinnayya, et al., Numerical study of compressible mixing layers using high-order WENO schemes, J. Sci. Comput. 47 (2011) 170–197.
[25] S. Berger, G. Ben-Dor, O. Sadot, Experimental and numerical investigations of shock-wave attenuation by geometrical means: A single barrier configuration, European Journal of Mechanics, B/Fluids 50 (2015) 60–70.

7

Conclusions and perspectives

The main purpose of this thesis is to use high resolution numerical simulations to further clarify the flow physics related to shock-wave propagation and attenuation in confined areas. Particular emphasis is put in the study of different complex geometries.

The outcomes of the present study can be summarized as follows:

- **Shock-wave diffraction over double concave cylindrical surfaces**

The shock-wave diffraction over double concave cylindrical surfaces is first investigated at different flow regimes by varying the incident-shock-wave Mach number from $M_s = 1.6$ (transonic regime) to $M_s = 4.5$ (supersonic regime). The shock-wave dynamics are deeply analyzed, the evaluation of the transition angle, θ^{tr}, from a regular reflection to a Mach reflection (RR $\rightarrow$ MR) has shown that θ^{tr} increases with the Mach number. The analysis revealed also that θ^{tr} is almost the same for both surfaces for weak Mach numbers, up to $M_s = 2.5$, and to be relatively larger on the second surface for high Mach numbers, $M_s = 3.5$ and 4.5. The tracking of the triple point trajectory showed different shock-wave behaviors, especially at the second half of the second surface. Depending on the shock-wave Mach number, different shock patterns are observed:

- For $M_s \leq 2.5$: appearance of a single triple point configuration, known as a STP (single triple point).

- For $M_s = 3.5$: after the appearance of the first triple point, a second one is formed, provoking a transition from STP to DTP configurations (STP $\rightarrow$ DTP transition).

- For $M_s = 4.5$: after the formation of the first and the second triple points, the two configurations merge together and give birth again to a STP configuration, leading to STP $\rightarrow$ DTP $\rightarrow$ STP transition.

Further analysis concerns the study of the vorticity generated by the shock-wave diffraction over double concave cylindrical surfaces. It was shown that the shock strength

enhances the vorticity production as found by Sun & Takayama (2003*b*). The vorticity production has been further investigated by evaluating the evolution of the instantaneous vorticity transport equation. It was found that the stretching of vorticity due to the flow compressibility plays an important role in the vorticity dynamics. The results show also that the diffusion of the vorticity due to the viscous effects is quite important compared to the baroclinic term for low Mach numbers regimes, $M_s \leq 2.5$, while this trend is inverted for higher Mach numbers regimes, $M_s \geq 3.5$. To the best of the author's knowledge, this result has not been reported so far. In terms of shock strength, the effect of the first concave surface was found to be effective in decreasing sufficiently the dynamic as well as the static pressure impulses. In terms of shock velocity, the shock deceleration was found to be increasing with the shock-wave Mach number. Quantitative comparisons between the numerical results for different initial conditions (shock-wave strengths, gas properties) are made to find the physical parameters affecting the incident shock path and velocity. An approximate universal relation is derived, which predicts the incident-shock-wave trajectory and velocity as a function of the incident-shock-wave Mach number. The proposed relation was tested in the range of M_s ($1.6 \leq M_s \leq 4.5$) and different working gases, having different molecular weights, specific heat ratios, and acoustic impedances, mainly: air, He, Ar, CO_2 and SF_6. By finding the appropriate dimensionless time, it was possible to show the data from different simulations with different initial conditions collapsing into a single curve.

- **Shock-wave propagation inside channel with cylindrical cavities**

In a second part, the dynamics of the complex unsteady flows inside channel with cylindrical cavities of different depths and diffraction angles are investigated in a second part. As the diffraction process evolves, the end-wall corner vortices are formed with a rolling-up of eddies that are convected quasi-linearly away from the cavity entrance. These corner instabilities are characterized by the formation of a primary vortex that is followed by a secondary one for cavities having a diffraction angle $\theta_w \leq 90°$. The key mechanisms behind the appearance of this secondary near-wall instability are the large enough advection velocity generated by the cavity boundary layer. It is found that the interaction of this secondary instability with the primary vortex core in the upstream part of the cavity is one of the main sources of excitations and possible transition to turbulence. Configurations with no secondary instabilities were also present, mainly for diffraction angles higher than 90°, where the advection velocity is not sufficient to destabilize the wall-boundary layer. Also the results highlight the effect of the diffraction angles on the evolution and the trajectory of the main vortex in which the secondary instabilities play an important role. The total vorticity production has been quantified. The effect of initial

diffraction angles on the vorticity production is investigated and is found to be negligible at least in the earlier stage of the diffraction process. Furthermore, the contribution of the shock wave in vorticity production has been evaluated using a shock indicator based on Ducros sensor, and the contribution was found to be negligible ($\sim$ 10% of the total vorticity).

In terms of shock mitigation, a better shock attenuation is achieved with a diffraction angle of $\theta_w = 90°$, where the total shock energy is reduced by approximately 38%. The effect of the tunnel height on the shock mitigation for two diffraction angles was examined. A careful analysis of the flow structures revealed that in addition to the variation of the channel height, the position of these modifications play an important role in the shock mitigation. A subtle arrangement of channel position/height and cavity depth was found, leading to a significant attenuation factor of about 57% at the channel exit.

For $\theta_w = 60°$, an arbitrary arrangement may have a dramatic consequences on the amplification of the shock wave by a factor of approximately 30% at the end of the channel which is undesirable from safety and risk prevention management point of view.

In summary, the shock wave attenuation in a half-open channel with a cavity inside can be associated to the following mechanisms:

- Shock diffraction over the cavity that results in the formation of an end-wall corner vortex, leading to a large dissipative region responsible for the pressure decrease behind the shock.

- Appearance of an inverse-Mach reflection (InMR) due to the shock reflection which results in the formation of a transitioned regular reflection (TRR) over the cavity that leads to additional shocks.

- Appearance of a Direct-Mach reflection (DiMR) due to the shock reflection from the upper right corner of the cavity.

- Formation of multiple transverse waves due to shock reflections from the top and the bottom channel walls owing to the confinement effect.

- Perspectives

This section provides future work that can be conducted to further strengthen the present study. Hence the following items can be considered:

- Further assessment of the validity of the scaling low proposed in this study for the prediction of both shock-wave position and velocity for different geometries and shapes of the two concave surfaces.

- Other cavity depths, diffraction angles and forms like triangular, elliptical, square. etc. could be proposed in order to investigate their effects on the shock-wave mitigation/amplification.

- As an improvement, a better shock-wave mitigation in tunnels with circular cavity, would be achieved by: i) adding grooves to the channel walls, ii) avoiding the formation of the Direct-Mach reflection (DiMR) and the transitioned regular reflection (TRR) by suppressing the rising part of the cavity.

- Investigation of the effect of the dynamic and/or the thermal boundary layer upstream of the incident shock on the vorticity generation and the shock attenuation. This leads to the study of the Reynolds number on the shock-wave propagation.

- Extension of the study for spherical and semi-spherical shock waves in order to verify the effectiveness of the geometries proposed in the attenuation of shock waves from real explosions.

Appendix A

Numerical method

A.1 Inviscid flux computations

A.1.1 WENO5

The space discretization is achieved through higher–order finite differences. The fluxes are discretized using a fifth-order WENO scheme (Liu et al. 1994, Jiang & Shu 1996). The underlying principle of the WENO scheme is to superpose of many sub–stencils with adaptive coefficients to get a high-order approximate solution, preventing oscillations across discontinuities and retaining a high-order of accuracy throughout the smooth solutions. For the sake of clarity, we present here the WENO scheme for the one-dimensional scalar equation. It can be straightforwardly extended to higher dimensions. For the fifth-order WENO scheme, let us consider third-order polynomial reconstructions on three different stencils

$$\begin{aligned} u^{(0)}_{i+\frac{1}{2}} &= \frac{1}{3}u_i + \frac{5}{6}u_{i+1} - \frac{1}{6}u_{i+2} \\ u^{(1)}_{i+\frac{1}{2}} &= -\frac{1}{6}u_{i-1} + \frac{5}{6}u_i + \frac{1}{3}u_{i+1} \\ u^{(2)}_{i+\frac{1}{2}} &= \frac{1}{3}u_{i-2} - \frac{7}{6}u_{i-1} + \frac{11}{6}u_i \end{aligned} \tag{A.1}$$

The convex combination of the fifth-order WENO flux corresponds to

$$u_{i+\frac{1}{2}} = \sum_{j=0}^{2} w_j u^{(j)}_{i+\frac{1}{2}} \tag{A.2}$$

where the *nonlinear weights* w_j are given by

$$w_j = \frac{\alpha_j}{\alpha_0 + \alpha_1 + \alpha_2}, \text{ with } \alpha_j = \frac{\gamma_j}{(\beta_j + \epsilon)^2} \ . \tag{A.3}$$

Here, ϵ is a constant set to 10^{-6} in order to prevent the denominator from becoming zero. The *smoothness indicators* of the function u are defined by the coefficients β_j, $j \in \{0,1,2\}$, as

$$\begin{aligned}
\beta_0 &= \frac{13}{12}(u_i - 2u_{i+1} + u_{i+2})^2 + \frac{1}{4}(3u_i - 4u_{i+1} + u_{i+2})^2 \\
\beta_1 &= \frac{13}{12}(u_{i-1} - 2u_i + u_{i+1})^2 + \frac{1}{4}(u_{i-1} - u_{i+1})^2 \\
\beta_2 &= \frac{13}{12}(u_{i-2} - 2u_{i-1} + u_i)^2 + \frac{1}{4}(u_{i-2} - 4u_{i-1} + 3u_i)^2
\end{aligned} \tag{A.4}$$

The *linear weights* γ_j, $j \in \{0,1,2\}$ of the fifth-order WENO scheme are provided as

$$\gamma_0 = \frac{3}{10}\ ,\ \gamma_1 = \frac{3}{5}\ ,\ \gamma_2 = \frac{1}{10}. \tag{A.5}$$

To compute the numerical flux for $u_{i-\frac{1}{2}}$, the procedure is simply the mirror symmetry of the one mentioned above.

A.1.2 Roe flux differencing scheme

In this section, an overview of the Roe approximate (Roe 1981) Riemann solver is given in continuation with the WENO scheme. Applying the chain rule to Eq. 2.2 for one-dimensional case

$$\frac{\partial \mathbf{U}}{\partial t} + \underbrace{\frac{\partial \mathbf{F}}{\partial U}}_{A} \cdot \frac{\partial \mathbf{U}}{\partial x} = 0 \tag{A.6}$$

where A in the above equation forms a Jacobian matrix, which together with Eq. 2.12, can be written as,

$$A = \begin{bmatrix} 0 & 1 & 0 \\ \frac{1}{2}(\gamma-3)u^2 & (3-\gamma)u & \gamma-1 \\ \left(\frac{1}{2}(\gamma-1)u^2 - h\right)u & h-(\gamma-1)u^2 & \gamma u \end{bmatrix} \tag{A.7}$$

where

$$h = e + \frac{p}{\rho} = \frac{c^2}{\gamma-1} + \frac{1}{2}u^2 \tag{A.8}$$

denotes the total enthalpy per unit of mass, and c is the speed of sound. Now, since the Jacobian matrix can be diagonalized, it can be written as,

$$A = R\Lambda L \tag{A.9}$$

where R and $L(=R^{-1})$ are the right and left eigenvector matrices, and Λ is the eigenvalue matrix. These matrices are given by,

$$\Lambda = \begin{bmatrix} u & 0 & 0 \\ 0 & u+c & 0 \\ 0 & 0 & u-c \end{bmatrix} \tag{A.10}$$

$$R = \begin{bmatrix} 1 & 1 & 1 \\ u & u+c & u-c \\ \frac{u^2}{2} & h+uc & h-uc \end{bmatrix} \tag{A.11}$$

$$L = \begin{bmatrix} 1-\frac{u^2}{2h'} & \frac{u}{h'} & -\frac{1}{h'} \\ \frac{u^2}{4h'}-\frac{u}{2c} & \frac{1}{2c}-\frac{u}{2h'} & \frac{1}{2h'} \\ \frac{u^2}{4h'}+\frac{u}{2c} & -\frac{1}{2c}-\frac{u}{2h'} & \frac{1}{2h'} \end{bmatrix} \tag{A.12}$$

where h' denotes the internal enthalpy given by

$$h' = h - \frac{u^2}{2} = \frac{c^2}{\gamma-1} \tag{A.13}$$

Roe averaging

The Roe averaging method is a type of Godunov scheme; and its formulation for the point–based finite difference scheme on the uniform grids reduces to the same form of the cell averaged one. The Roe averaging for the density, velocity and enthalpy can be written as

$$\rho_{i+\frac{1}{2}} = \sqrt{\rho_L \rho_R} \qquad u_{i+\frac{1}{2}} = \frac{\sqrt{\rho_L}u_L + \sqrt{\rho_R}u_R}{\sqrt{\rho_R}+\sqrt{\rho_L}} \qquad h_{i+\frac{1}{2}} = \frac{\sqrt{\rho_L}h_L + \sqrt{\rho_R}h_R}{\sqrt{\rho_R}+\sqrt{\rho_L}} \tag{A.14}$$

where, the left and right states are derived from Eq. A.2 of WENO computation. Now, using these averaged form of equations and applying them in Eq. A.10, A.11 and A.12, the Jacobian matrix can be found as

$$\left|A_{i+\frac{1}{2}}\right| = R_{i+\frac{1}{2}} \left|\Lambda_{i+\frac{1}{2}}\right| L_{i+\frac{1}{2}} \tag{A.15}$$

This makes the flux computation equation as

$$F^{L/R}_{i+\frac{1}{2}} = \frac{1}{2}\left(F^{L}_{i+\frac{1}{2}} + F^{R}_{i+\frac{1}{2}} - \left|A_{i+\frac{1}{2}}\right|(U_R - U_L)\right) \tag{A.16}$$

A.2 Viscous flux computations

The viscous fluxes given in Eq. 2.9 are computed using a fourth–order compact central differential scheme. The classical form of a fourth–order scheme is depicted in one dimension as

$$\frac{\partial F}{\partial x} = \frac{-F_{i+2} + 8F_{i+1} - 8F_{i-1} + F_{i-2}}{12\Delta x} \tag{A.17}$$

The derivatives of the elements of F_v vector are computed using a five point stencils as follow

$$\begin{aligned}
\left(\frac{\partial f}{\partial x}\right)_{i-2} &= \frac{-25f_{i-2} + 48f_{i-1} - 36f_i + 16f_{i+1} - 3f_{i+2}}{12\Delta x} + \mathcal{O}(\Delta x^4) \\
\left(\frac{\partial f}{\partial x}\right)_{i-1} &= \frac{-3f_{i-2} - 10f_{i-1} + 18f_i - 6f_{i+1} + f_{i+2}}{12\Delta x} + \mathcal{O}(\Delta x^4) \\
\left(\frac{\partial f}{\partial x}\right)_{i+1} &= \frac{-f_{i-2} + 6f_{i-1} - 18f_i + 10f_{i+1} + 3f_{i+2}}{12\Delta x} + \mathcal{O}(\Delta x^4) \\
\left(\frac{\partial f}{\partial x}\right)_{i+2} &= \frac{3f_{i-2} - 16f_{i-1} + 36f_i - 48f_{i+1} + 25f_{i+2}}{12\Delta x} + \mathcal{O}(\Delta x^4)
\end{aligned} \tag{A.18}$$

As can be seen, the primary advantage of using a compact numerical scheme is that it works with a very narrow interval of points. Since the current solver uses ghost points near the edges and corners, this numerical scheme delivers a fourth–order accurate solution without requiring additional memory.

A.3 Time integration

The explicit third-order TVD Runge-Kutta (RK3) (Butcher 2008) scheme is used for the time integration. The system (2.1) - (2.2) can be reduced to the following ODE:

$$\partial_t \mathbf{U} = \mathcal{D}(\mathbf{U}) \ , \tag{A.19}$$

where $\mathcal{D}$ is the divergence operator. Using the RK3 scheme, the temporal discretization of the above equation is given bellow, with Δt denotes the time step.

$$\mathbf{U}^* = \mathbf{U}^n + \Delta t\, \mathcal{D}(\mathbf{U}^n)$$

$$\mathbf{U}^{**} = \frac{1}{4}\left[3\,\mathbf{U}^n + \mathbf{U}^* + \Delta t\, \mathcal{D}(\mathbf{U}^*)\right] \tag{A.20}$$

$$\mathbf{U}^{n+1} = \frac{1}{3}\left[\mathbf{U}^n + 2\,\mathbf{U}^{**} + 2\,\Delta t\, \mathcal{D}(\mathbf{U}^{**})\right] \tag{A.21}$$

Appendix B

Wavelet theory and coefficients of the prediction operator

B.1 Wavelet theory and multiresolution analysis

The concept of wavelet has found its applications in many disciplines such as image processing, signal analysis, statistics, numerical analysis, etc. The readers are advised to refer to Mallat (1989), Daubechies (1992), Cohen (2003), Müller (2003) for detailed explanation on the multiresolution analysis and wavelet theory.

A set of functions, $\{\phi_{r,s}(x)\}$ lying in the square integrable real space, $\mathcal{L}^2(\mathbb{R})$ can be written as,

$$\phi_{r,s}(x) = 2^{r/2}\phi(2^r x - s) \ , \quad r, s \in \mathbb{Z} \tag{B.1}$$

where ϕ, r and s denote the *scaling function*, scaling parameter and the shifting parameter, respectively. Let us consider a subspace associated with the set of scaling functions $V_0 : \{\phi_{0,s}(x)\}$. Now, if the scaling parameter is increased by a unity, it represents the subspace $V_1 : \{\phi_{1,s}(x)\}$ such that it becomes the superset of the subspace V_0. This can be interpreted as whatever is analyzed using the set of functions $\{\phi_{0,s}(x)\}$ can also be analyzed using $\{\phi_{1,s}(x)\}$, as the latter encompasses the former. This can be illustrated pictorially as in Fig. B.1. Since the only variation between each set of scaling function is the scaling parameter, it can be understood from Eq. B.1 that the amplitude is the only change found from one scale to another scale of the scaling functions for given shift parameter s. Hence, it can be implied that each scaling function in this case is covered by the next higher scaling function. This can be written is the form of nested subspaces as,

$$V_{-\infty} \subset \ldots \subset V_{-1} \subset V_0 \subset V_1 \subset \ldots \subset V_{\infty} \tag{B.2}$$

Since the scaling function in V_0 can be approximated from the different weighted summation of the shifted versions of the next higher scaling function, it can written in the form of the scaling function series as,

$$\phi(x) = \sum_s h_\phi(s)\sqrt{2}\ \phi(2x - s) \tag{B.3}$$

where h_ϕ is called the scaling coefficient. Now, if a function spans in the V_1 but not in the V_0 subspace, the subspace forms with the difference between the V_1 and V_0 subspaces can be called W_0 (see Fig. B.1). In this case,

$$V_1 = V_0 \oplus W_0 \qquad V_2 = V_1 \oplus W_1 = V_0 \oplus W_0 \oplus W_1 \tag{B.4}$$

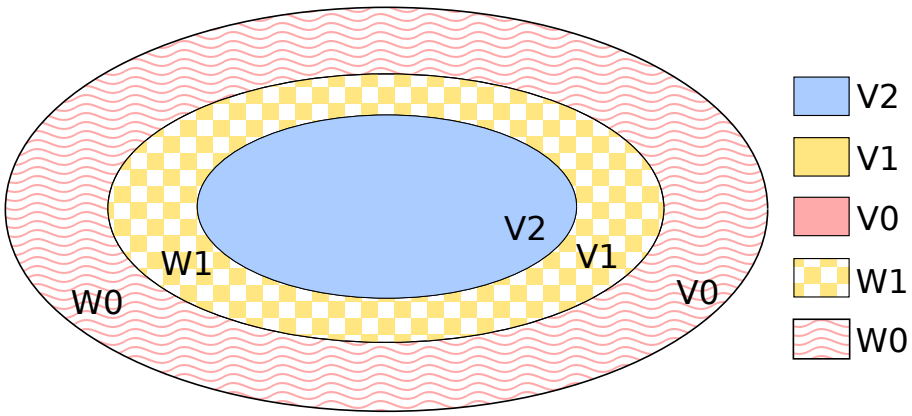

Figure B.1: Schematic representation of the subspaces associated with the scaling (color) and wavelet (pattern) functions.

where the symbol $\oplus$ represents the union of subspaces.

The class of functions which cover the difference subspaces are called the wavelet functions; and they are given similar to Eq. B.1 by,

$$\psi_{r,s}(x) = 2^{r/2}\psi(2^r x - s)\ , \quad r, s \in \mathbb{Z} \tag{B.5}$$

These functions hold the following properties: 1) the shifted versions of these functions should be orthogonal to each other, and 2.) the oscillatory nature of these functions should have zero area under them. Now, the relationship between the wavelet and scaling functions can be established as $W_0 \subset V_1$ by,

$$\psi(x) = \sum_s h_\psi(s)\sqrt{2}\ \phi(2x - s) \tag{B.6}$$

Suppose given a set of scaling functions $\{\phi_{r_0,s}\}$ and a set of wavelet functions $\{\psi_{r,s}\}$, where $r \geq r_0$, a continuous function $f(x) \in \mathcal{L}^2$ can be approximated by,

$$f(x) = \sum_s a_{r_0,s}\phi_{r_0,s}(x) + \sum_{r=r_0}^{\infty}\sum_s b_{r,s}\psi_{r,s}(x) \ , \quad r,s \in \mathbb{Z} \tag{B.7}$$

As the set of $\{\phi_{r_0,s}\}$ is orthogonal for a fixed value of r_0 and the set of $\{\psi_{r,s}\}$ is orthogonal itself from its property, the coefficients $a_{r_0,s}$ and $b_{r,s}$ can be derived as

$$a_{r_0,s} = \int f(x)\phi_{r_0,s}(x)dx$$
$$b_{r,s} = \int f(x)\psi_{r,s}(x)dx$$

B.2 Coefficients of the prediction operator

Multiresolution prediction operators are given in one, two and three dimensional form.

B.2.1 One–dimensional case

The polynomial of degree $(r-1)$ used for the interpolation of the prediction operator in one dimension writes

$$\begin{aligned} \hat{u}_{l+1,2i+1} &= \textstyle\sum_{n=1}^{r/2}\phi_n\left(u_{l,i-n+1} + u_{l,i+n}\right) && (odd\ index) \\ \hat{u}_{l+1,2i} &= u_{l,i} && (even\ index) \end{aligned} \tag{B.8}$$

B.2.2 Two–dimensional case

The prediction operator for two dimensions writes

$$\begin{aligned} \hat{u}_{l+1,2i+\zeta,2j+\eta} = \sum_{n=\zeta}^{\zeta r/2}\phi_n \sum_{m=\eta}^{\eta r/2}\phi_m \Big(& c_1 u_{l,i-n+1,j-m+1} + c_2 u_{l,i+n,j-m+1} \\ & + c_3 u_{l,i-n+1,j+m} + c_4 u_{l,i+n,j+m}\Big) \end{aligned} \tag{B.9}$$

In Eq. (B.9), the coefficients change with the index of x and y coordinates, where $\zeta, \eta \in \{0,1\}$. The different terms are

$$\text{if}(\zeta = 1, \eta = 1) \quad \text{then} \quad c_1 = c_2 = c_3 = c_4 = 1$$

$$\text{if}(\zeta = 1, \eta = 0) \quad \text{then} \quad c_3 = c_4 = 1;\ c_1 = c_2 = 0$$

$$\text{if}(\zeta = 0, \eta = 1) \quad \text{then} \quad c_2 = c_4 = 1;\ c_1 = c_3 = 0$$

$$\text{if}(\zeta = 0, \eta = 0) \quad \text{then} \quad \hat{u}_{l+1,2i,2j} = u_{l,i,j}$$

B.2.3 Three–dimensional case

The prediction operator in 3D can be written in the following way

$$\begin{aligned}\hat{u}_{l+1,2i+\zeta,2j+\eta,2k+\kappa} = \sum_{n=\zeta}^{\zeta r/2} \phi_n \sum_{m=\eta}^{\eta r/2} \phi_m \sum_{p=\kappa}^{\kappa r/2} \phi_p \Big(& c_1 u_{l,i-n+1,j-m+1,k-p+1} \\ & + c_2 u_{l,i+n,j-m+1,k-p+1} + c_3 u_{l,i-n+1,j+m,k-p+1} \\ & + c_4 u_{l,i+n,j+m,k-p+1} + c_5 u_{l,i-n+1,j-m+1,k+p} \\ & + c_6 u_{l,i+n,j-m+1,k+p} + c_7 u_{l,i-n+1,j+m,k+p} \\ & + c_8 u_{l,i+n,j+m,k+p} \Big)\end{aligned} \tag{B.10}$$

Eq. (B.10) is a generalized form of the prediction operator. It varies with the index of each dimension depending on $\zeta, \eta, \kappa \in \{0, 1\}$. Following are the details associated with the prediction operator:

$$\text{if}(\zeta=1,\eta=1,\kappa=1) \quad \text{then} \quad c_1=c_2=\ldots=c_8=1$$

$$\text{if}(\zeta=1,\eta=0,\kappa=0) \quad \text{then} \quad c_7=c_8=1;\ c_1=c_2=\ldots=c_6=0$$

$$\text{if}(\zeta=0,\eta=1,\kappa=0) \quad \text{then} \quad c_6=c_8=1;\ c_1=\ldots=c_5=c_7=0$$

$$\text{if}(\zeta=0,\eta=0,\kappa=1) \quad \text{then} \quad c_4=c_8=1;\ c_1=c_2=c_3=c_5=c_6=c_7=0$$

$$\text{if}(\zeta=1,\eta=1,\kappa=0) \quad \text{then} \quad c_5=\ldots=c_8=1;\ c_1=\ldots=c_4=0$$

$$\text{if}(\zeta=0,\eta=1,\kappa=1) \quad \text{then} \quad c_3=c_4=c_7=c_8=1;\ c_1=c_2=c_5=c_6=0$$

$$\text{if}(\zeta=1,\eta=0,\kappa=1) \quad \text{then} \quad c_2=c_4=c_6=c_8=1;\ c_1=c_3=c_5=c_7=0$$

$$\text{if}(\zeta=0,\eta=0,\kappa=0) \quad \text{then} \quad \hat{u}_{l+1,2i,2j,2k}=u_{l,i,j,k}$$

The interpolation coefficient ϕ for second-, fourth- and sixth-order polynomial interpolations used in Eqs. (B.8), (B.9) and (B.10) write (see Harten (1995))

$$\begin{cases} r=2 \ \Rightarrow \ \phi_0=1, \ \ \phi_1=1/2 \\ r=4 \ \Rightarrow \ \phi_0=1, \ \ \phi_1=9/16, \ \ \ \phi_2=-1/16 \\ r=6 \ \Rightarrow \ \phi_0=1, \ \ \phi_1=150/256, \ \ \phi_2=-25/256, \ \ \phi_3=3/256 \end{cases} \tag{B.11}$$

Appendix C

Vorticity production in shock-waves diffraction over circular cavities

Abstract The dynamics of complex unsteady flows inside channel with cylindrical cavities at incident-shock Mach number $M_s = 1.6$ are numerically investigated. As the diffraction process evolves, end-wall corner vortices are formed with a rolling-up of eddies that are convected quasi-linearly away from the cavity entrance. These corner instabilities are characterized by the formation of a primary vortex that is followed by a secondary one for cavities having a diffraction angle $\theta_w \leq 90°$. The key mechanism behind the appearance of this secondary near-wall instability are a large enough advection velocity generated by the cavity boundary layer. It is found that the interaction of this secondary instability with the primary vortex core in the upstream part of the cavity is one of the main sources of excitations and possible transition to turbulence. Configurations with no secondary instabilities are also present, mainly for diffraction angles higher than 90°, where the advection velocity is not sufficient to destabilize the wall-boundary layer. In order to investigate the effect of initial diffraction angle on the vorticity field, the total vorticity production is first evaluated by integrating the local vorticity ω over the entire domain. The spatio-temporal evolution of the vorticity is further analyzed through the balance of the vorticity transport equation. The results show that the diffusion of vorticity due to viscous effects is dominated by the other mechanisms (stretching of vorticity due to flow compressibility and baroclinic term), while the stretching of the vorticity due to the compressibility effects and the convection term play a major role in the vorticity dynamics. A shock sensor is used to evaluate the contribution of shocks in vorticity production, which is found to be negligible.

C.1 Primary vortex evolution

Initially, the shock is located at $x/R = 0,06$. Shortly after the penetration of the shock into the cavity, the expanded flow evolves into a complicated system of distorted and secondary shocks with separation regions (depending on the diffraction angle). An end-wall corner vortex is formed with a rolling-up of eddies that are convected quasi-linearly away from the cavity entrance as the diffraction process evolves. In addition to this important primary vortex, a secondary instability appears along the cavity wall for $\theta_w \leq 90°$.

Figure C.1 shows the trajectory of the primary vortex centroid. The vortex emerges not at the time the diffraction begins but after the gas velocity at a certain point on the surface has vanished. Up to certain time t, the vortex trajectory is almost linear, and then its motion becomes oscillatory for the three diffraction angles. After this time, for $\theta_w \leq 90°$, the position of the primary vortex centroid is difficult to detect. As the diffraction process evolves, a laminar boundary layer takes place in the reversing flow near the cavity wall. This boundary layer interacts with the secondary shocks giving a transition to a highly perturbed one with large scale coherent vortices, thus making detection of the primary vortex centroid complicated. Figure C.1(d) shows the evolution of the angle between the vortex centroid trajectory and the horizontal, θ_v, as a function of the diffraction angle, θ_w. The θ_v is increasing with θ_w, this shows the effect of the diffraction angle on the primary vortex evolution and trajectory.

C.2 Vorticity production

The circulation Γ is defined as the summation of vorticity ω in the domain S,

$$\Gamma = \int_s \omega \, ds = \int_L u \, dl \tag{C.1}$$

The integral contour or path L is taken along the boundary that exactly encloses the perturbed region behind the shock wave. The vorticity production in shock-wave diffraction can also be characterized by the time history of the ratio of circulation rate, Γ/t.

The numerical calculation of the circulation is directly obtained from summing the vorticity over each individual surface area. In general, the circulation calculation is performed only in the perturbed region behind the diffracted shock. However, in this study the circulations are calculated over the complete computational domain because the unperturbed flow regions (uniform regions) provides no contribution to the circulation effect (Brahmi et al. (2020*b*)). Note that in all the present study, the circulation is presented by its absolute value.

Figure C.2 represents the space vorticity distribution for different diffraction angles

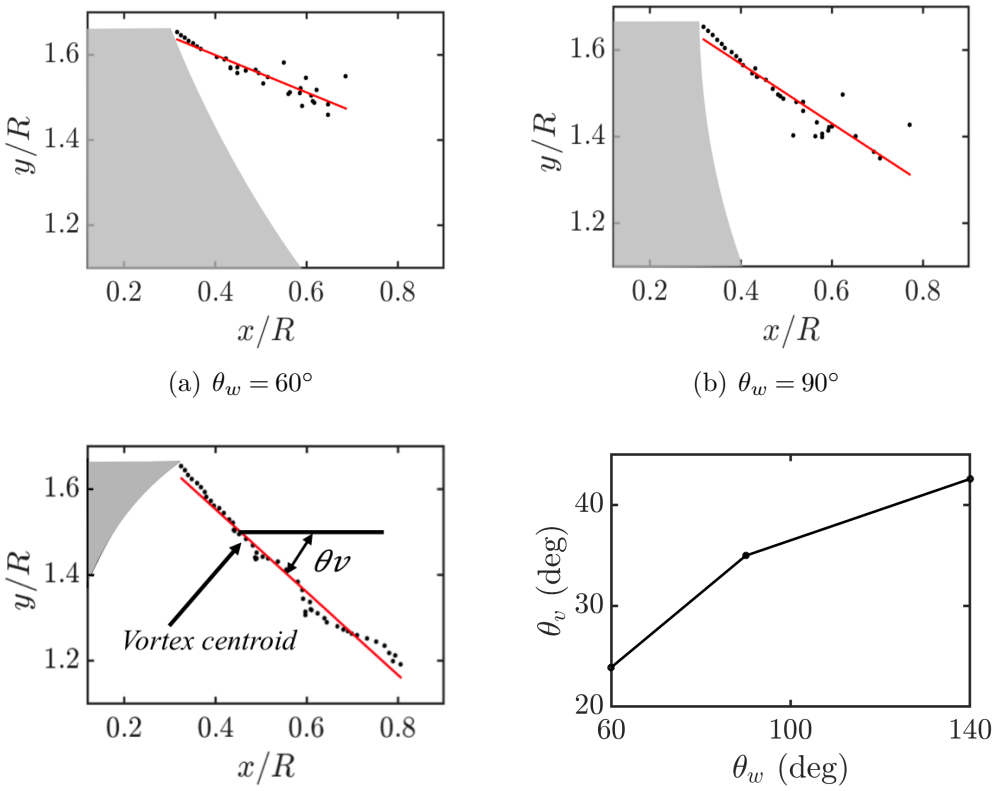

(a) $\theta_w = 60°$ (b) $\theta_w = 90°$

(c) $\theta_w = 140°$ (d) θ_v

Figure C.1: Trajectory of the primary vortex centroid for different diffraction angles, θ_w. The red line represents an averaged linear regression.

in two different instants ($t = 123\ \mu s$ and $t = 228\ \mu s$). As it can be seen, the main vortex and the shear layer split due to the interaction with the secondary shocks resulting in small vortices. The main production of vorticity remains concentrated in the shear layer region, the vortex cores, the secondary shocks and the secondary vortices formed near the cavity wall (for $\theta_w \leq 90°$). Depending on the flow direction of rotation, the vorticity is negative in the primary vortex region and positive near the cavity wall where the secondary vortices are formed.

The effect of the initial diffraction angle on the vorticity production is investigated. Figure C.3(a) represents the time history of circulation, Γ, for different initial diffraction angles. The vorticity production occurs before the shock diffraction begins as a result of the boundary layer that develops behind the incident shock on the solid wall. This demonstrates the role played by viscous effects in forming the shock-wave diffraction structures as mentioned by Tseng & Yang (2006). As it can be seen, the vorticity production is monotonically increasing with more or less a steep slope, until the shock leaves the computational domain, at $t \approx 250\ \mu s$, thus inducing a decrease in the vorticity production. The decrease in the vorticity production is more important for $\theta_w = 60°$.

Figure C.3(b) shows the rate of circulation production, Γ/t. The three curves reach the same constant value of approximately 1.8. Sun & Takayama (1997) noticed the similar behavior and they called this as invariant of the Euler equations in shock-wave diffraction. At $t \approx 250\ \mu s$, the shock leaves the computational domain and this causes a decrease in the rate of circulation production. The decrease in the rate of circulation production is more important for $\theta_w = 60°$. As we can see in Figure C.2, vorticity is composed of two components; negative and positive vorticity. The time history of these two components is presented in Figure C.4 and as we can see, the negative vorticity, mainly concentrated in the primary vortex region, is the dominant component for all diffraction angle.

C.2.1 Ducros sensor

In order to evaluate the shocks contribution in vorticity production, the Ducros sensor Ducros et al. (1999) is used as:

$$\Theta = \frac{(\nabla \cdot u)^2}{(\nabla \cdot u)^2 + (\nabla \times u)^2 + \epsilon}, \qquad 0 \leq \Theta \leq 1 \tag{C.2}$$

The values of this sensor vary between 0 for weakly compressible regions to about 1 in shock regions. Ducros et al. (1999), took $\epsilon = 10^{-30}$ as a positive real number chosen to avoid numerical divergence when both $(\nabla \times u)$ and $(\nabla \cdot u)$ are null. Pirozzoli (2011), noted that the Ducros sensor in its original formulation does not perform properly outside of the wall layer, where $\nabla \times u \approx 0$, due to excessive sensitivity to dilatational fluctuations. The sensor can be conveniently adapted to this case by setting $\epsilon = (u_1/\delta_0)^2$. Where δ_0 denotes the incoming boundary layer thickness and u_1 the uniform velocity of the shocked gas.

The performance of shock sensors in practical computations can be seen in Figure C.5, which illustrates results of the application of the Ducros sensor mentioned above to the instantaneous flow field obtained from simulation of shock-wave diffracting over cylindrical cavities. The results presented in Figure C.5 suggest that Ducros sensor is capable of selectively isolating shocks.

Ducros sensor is applied to the instantaneous vorticity field in order to estimate the shocks contribution in the vorticity production. The results are presented in Figure C.6 as time evolution of circulation Γ, and in Figure C.7 as vorticity distribution. Figures C.6(a), C.6(b) and C.6(c) represent time evolution of circulation Γ for different diffraction angles, with and without Ducros sensor. For the first stage of diffraction process, the two curves are almost superposed for all diffraction angles which means that the shocks contribution on vorticity production is quasi-null for this stage. The effect of shocks on vorticity production appears after the diffraction of the incident shock and development

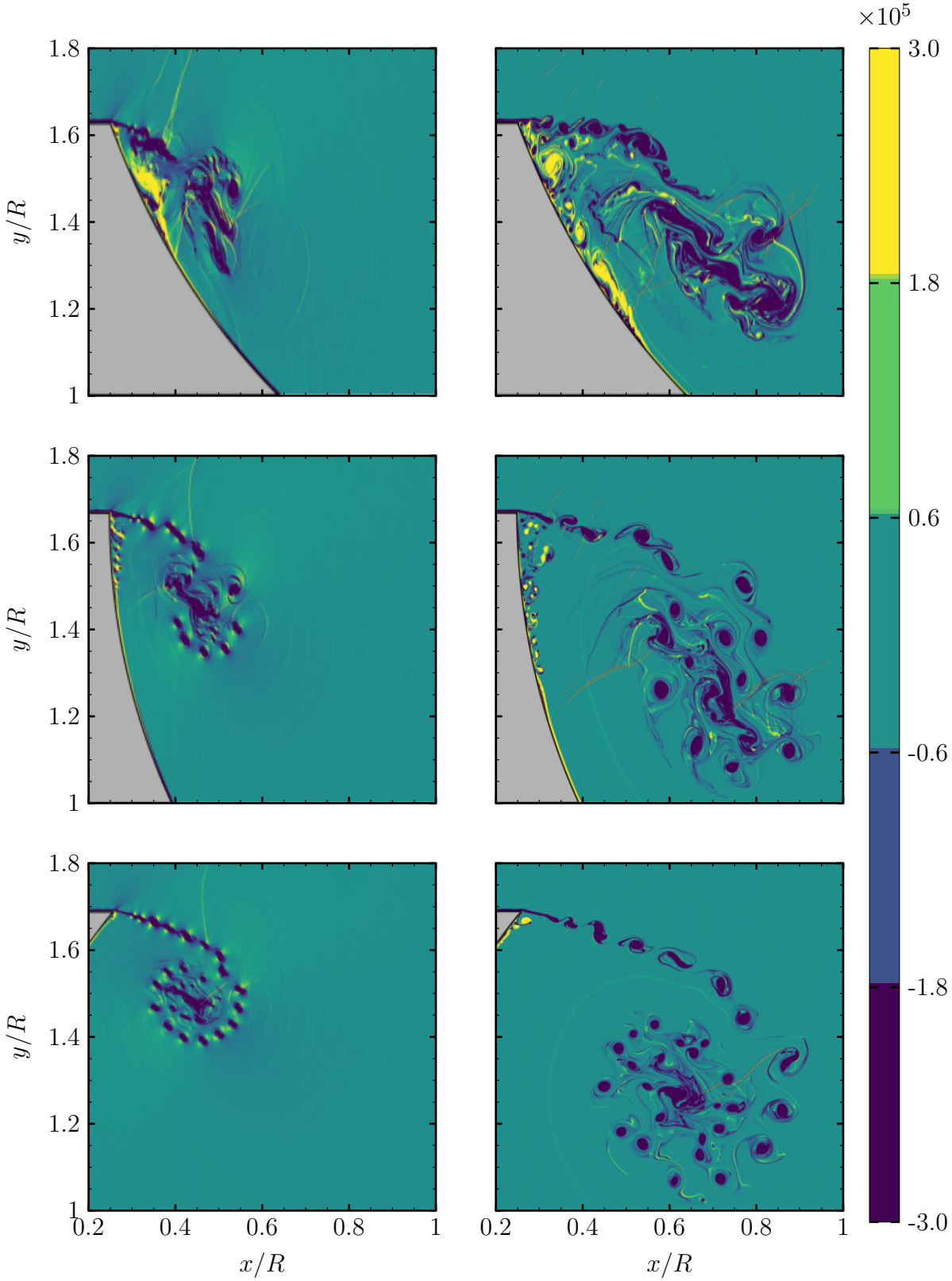

Figure C.2: Instantaneous vorticity contours for different diffraction angles. Column-wise (left-to-right): $t = 123\ \mu s$ and $t = 228\ \mu s$. Row-wise (top-to-bottom): $\theta_w = 60°$, $\theta_w = 90°$, $\theta_w = 140°$.

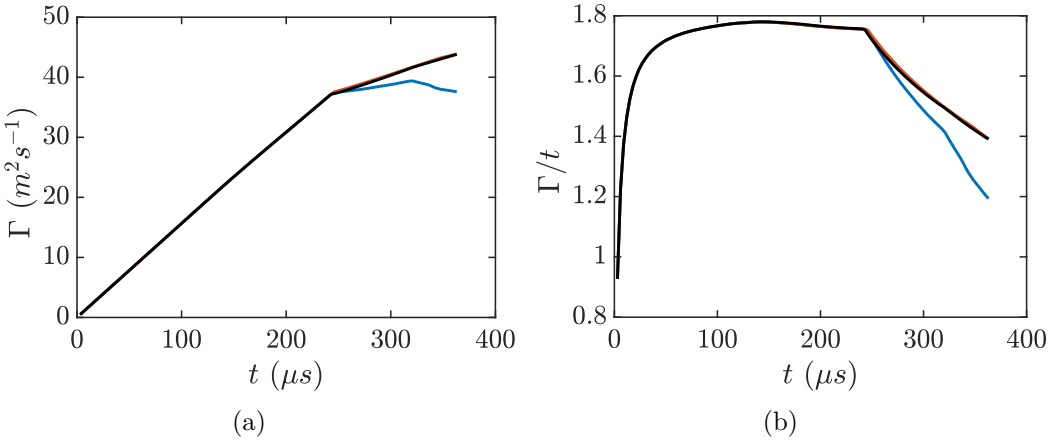

Figure C.3: Time history of (a): circulation Γ and (b): rate of circulation production (Γ/t) for different diffraction angles, (– $\theta_w = 60°$, – $\theta_w = 90°$, – $\theta_w = 140°$).

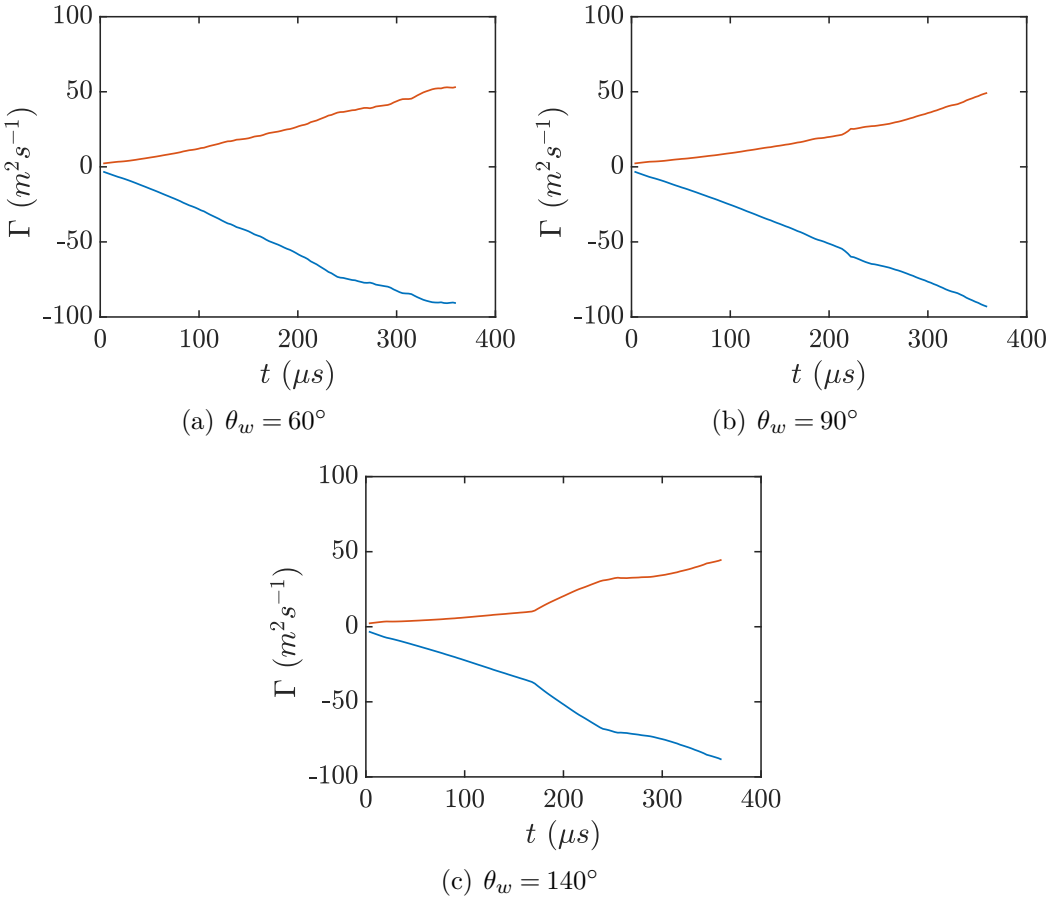

Figure C.4: Time history of: – negative circulation, – positive circulation, for different diffraction angles.

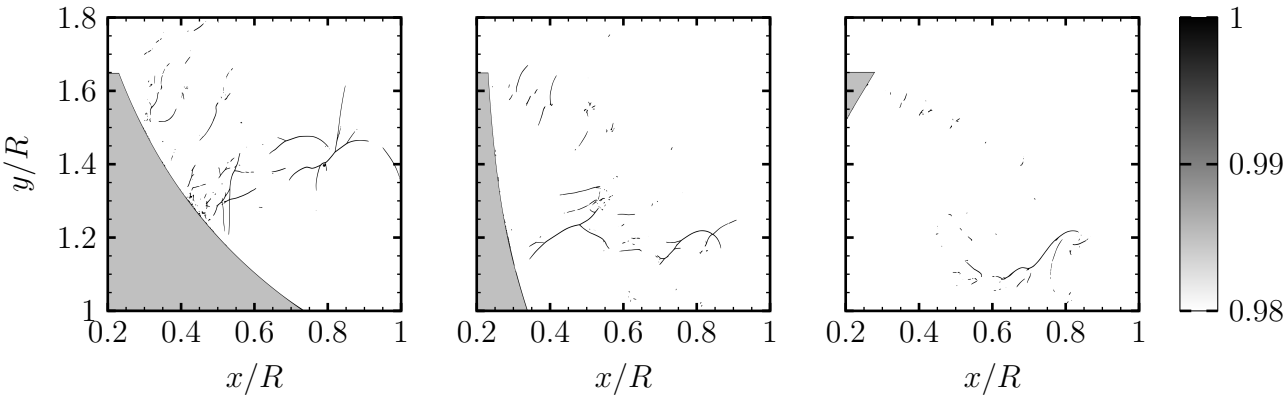

Figure C.5: Shock sensor at $t = 228\ \mu s$. Column-wise (left-to-right): $\theta_w = 60°$, $\theta_w = 90°$, $\theta_w = 140°$.

of the flow behind it, but the shocks contribution on vorticity production still negligible. Note that the maximum of this contribution is around 10% as shown in Figure C.6(d). Figure C.7 shows vorticity distribution in the field, in row-wise, for all diffraction angles, and in column-wise, with and without Ducros sensor at $t = 228\ \mu s$. As opposed to the left column, where the Ducros sensor is deactivated, the vorticity on shocks region in the right column, where the Ducros sensor is activated, is null.

C.2.2 Vorticity transport equation

A vorticity transport equation is developed to describe the space and time evolution of the vorticity as follows:

$$\frac{D\omega}{Dt} = \underbrace{(\omega \cdot \nabla)\, u}_{\text{VSG}} - \underbrace{\omega\,(\nabla \cdot u)}_{\text{VSC}} + \underbrace{\frac{1}{\rho^2}\,(\nabla\rho \times \nabla p)}_{\text{BAR}} + \underbrace{\nabla \times \left(\frac{\nabla \cdot \tau}{\rho}\right)}_{\text{DFV}} \tag{C.3}$$

where $\frac{D\omega}{Dt}$: is the material derivative of the vorticity vector. It describes the rate of change of vorticity of the moving fluid particle. This change can be attributed to unsteadiness in the flow, $\omega_t = \frac{\partial \omega}{\partial t}$, or to the convection, $\omega_c = u \cdot (\nabla \omega)$. VSG: stretching or tilting of vorticity due to the flow velocity gradients (VSG = 0 in two-dimensional flows). VSC: is the stretching of vorticity due to flow compressibility. BAR: is the baroclinic term. It accounts for the changes in the vorticity due to the intersection of density and pressure surfaces. DFV: is the diffusion of vorticity due to the viscous effects.

Eq. C.3 provides further details on the dynamics of the vorticity generation. Time evolution of different normalized terms of vorticity transport equation is presented in Figure C.8. The stretching of vorticity due to flow compressibility (VSC) term, represents the effects of expansion on the vorticity field and plays a major role in the vorticity

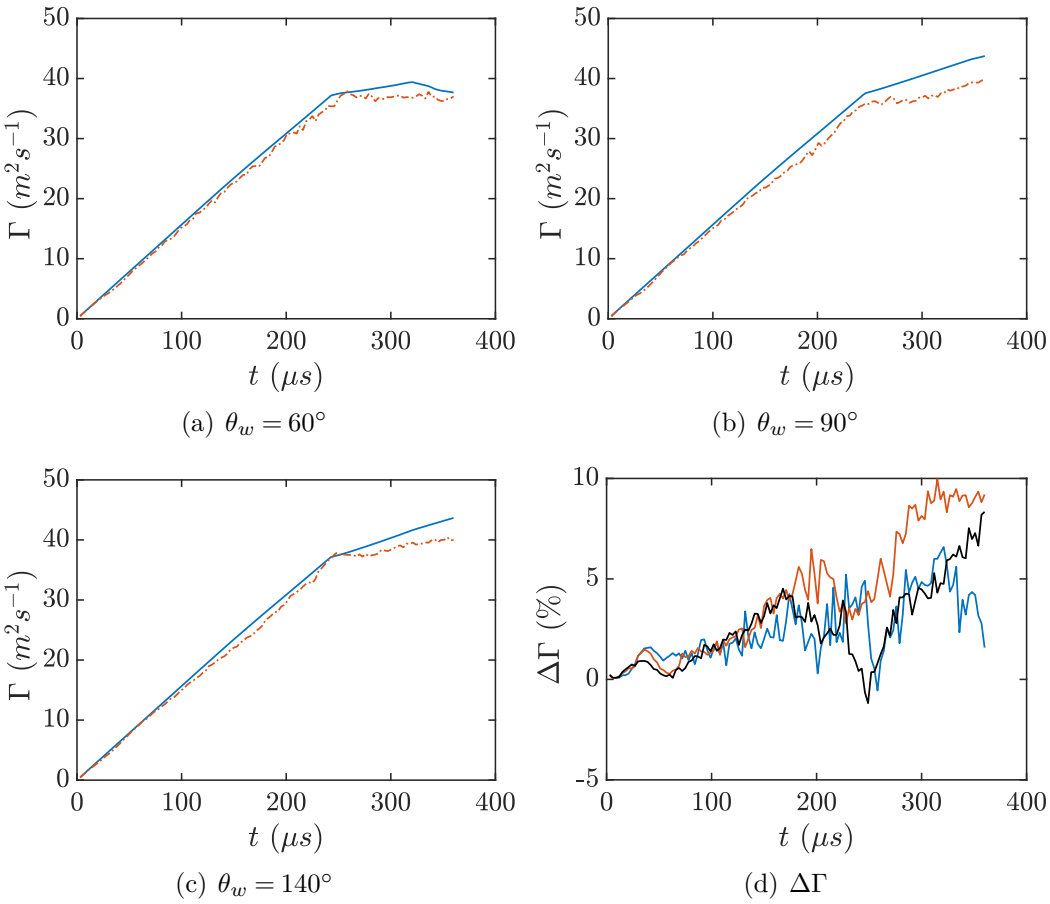

(a) $\theta_w = 60°$ (b) $\theta_w = 90°$

(c) $\theta_w = 140°$ (d) $\Delta\Gamma$

Figure C.6: Time history of circulation Γ for different diffraction angles, θ_w. For (a), (b) and (c); – Ducros sensor deactivated, -· Ducros sensor activated, for (d); – $\theta_w = 60°$, – $\theta_w = 90°$, – $\theta_w = 140°$.

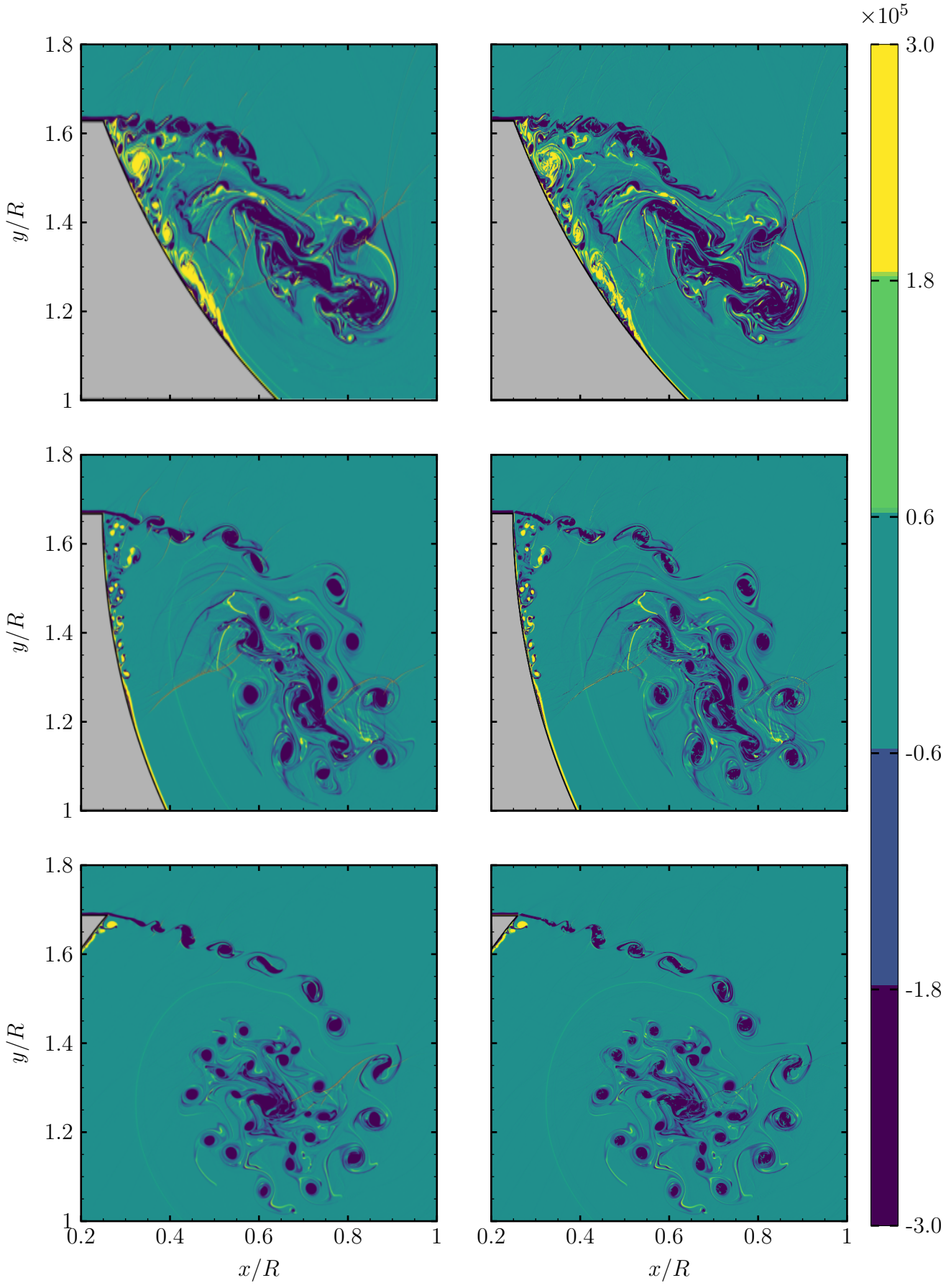

Figure C.7: Vorticity contours at $t = 228\ \mu s$. Column-wise (left-to-right): Ducros sensor deactivated and Ducros sensor activated. Row-wise (top-to-bottom): $\theta_w = 60°$, $\theta_w = 90°$, $\theta_w = 140°$

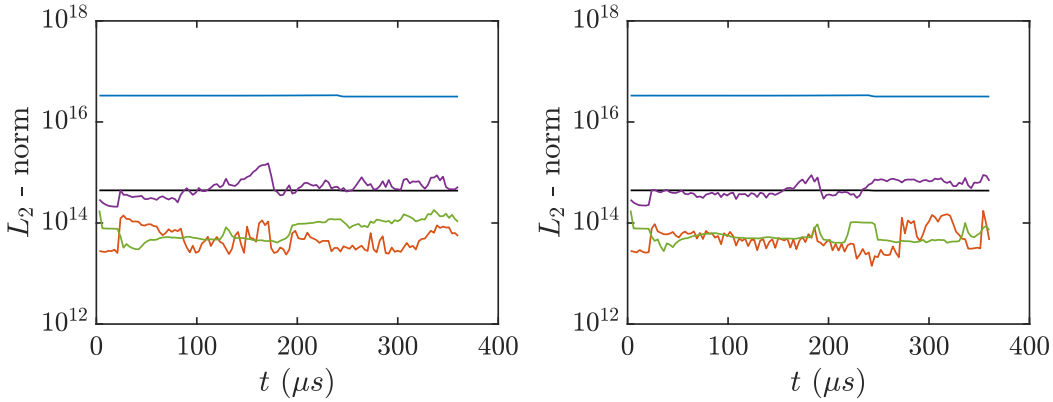

(a) $\theta_w = 60°$ (b) $\theta_w = 90°$

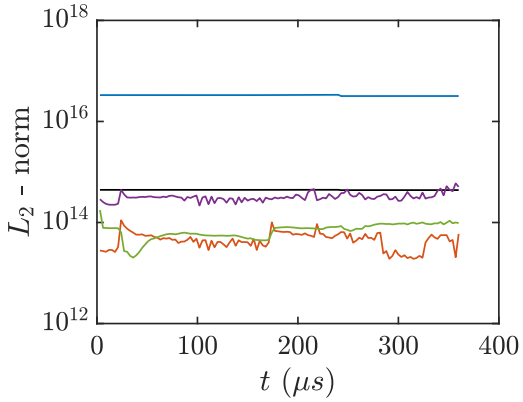

(c) $\theta_w = 140°$

Figure C.8: Time history of VTE terms, (a): $\theta_w = 60°$, (b): $\theta_w = 90°$, (c) $\theta_w = 140°$ (– VSC, – BAR, – DFV, – ω_c, – ω_t).

dynamics. The baroclinic term (BAR) results in a generation of vorticity from unequal acceleration as a result of nonaligned density and pressure gradients. The lighter density fluid will be accelerated faster than the high density fluid, resulting in a shear layer, thus the generation of vorticity. Diffusion of vorticity due to the viscous effects (DFV) highlights the effects of viscous diffusion on the vorticity distribution. Due to viscosity, the vorticity formed in the flow tends to diffuse in space and time. The diffusion of vorticity due to viscous effects (DFV) is dominated by the other mechanisms (VSC, BAR) in the vorticity transport equation because of the high Reynolds number (which is of order of 10^6). The effects of viscosity on the large-scale vortex structures in a turbulent flow are generally small.

The different terms of vorticity transport equation are shown in Figure C.9(b) (in Row-wise), for different diffraction angles (in Column-wise) by contours pictures at $t = 228\ \mu s$. As one can see, the dominant term is the stretching of vorticity due to flow compressibility (VSC). The figure also clearly shows the existence of the evolving vortices and their interaction with multiple secondary shock-waves resulting in split vortices for $\theta_w \leq 90°$. From the VSC contour, it is clear that there are locally stretched structures in the core vortex region due to compressibility effect arising from local regions of compression/expansion. Figure C.9(a) represents contours pictures of ω_c and ω_t (in Row-wise, ω_c and ω_t, top-to-bottom respectively), for different diffraction angles (in Column-wise) at $t = 228\ \mu s$. As we can see, the convection term is concentrated in the turbulent region, shear layer, shocks and viscous vortices formed near the wall (for $\theta_w \leq 90°$). This term represents the change of vorticity of the moving fluid particle due to its motion as it moves from one point to another and plays a major role in the vorticity dynamics. The unsteady term (ω_t) represents the change of vorticity of the moving fluid particle attributed to unsteadiness in the flow.

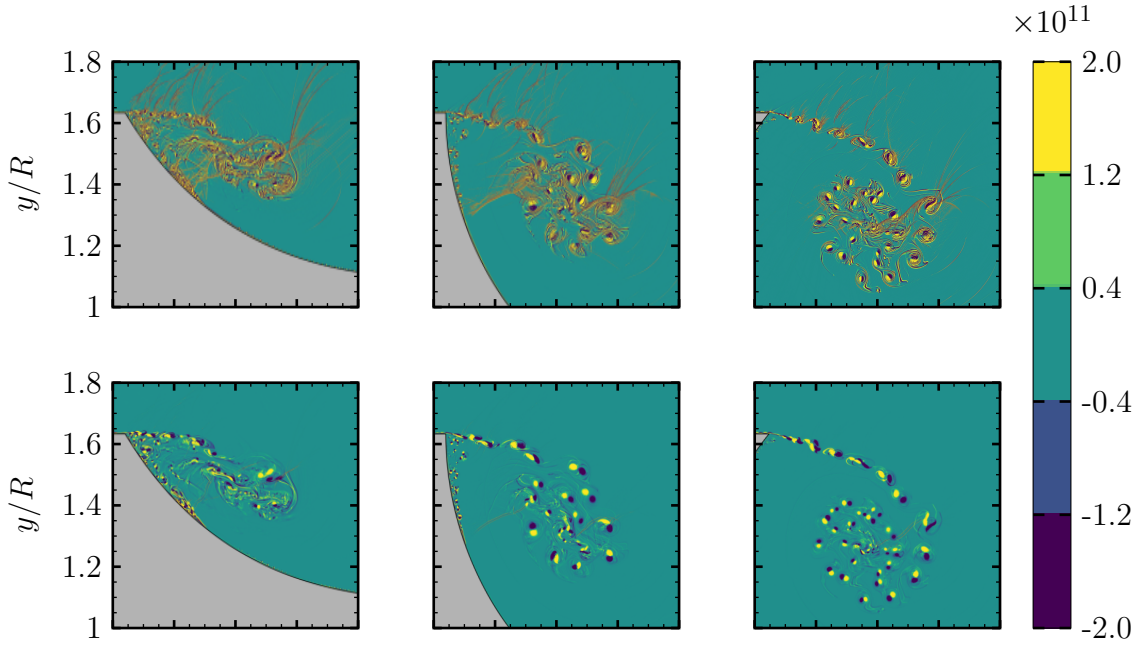

(a)

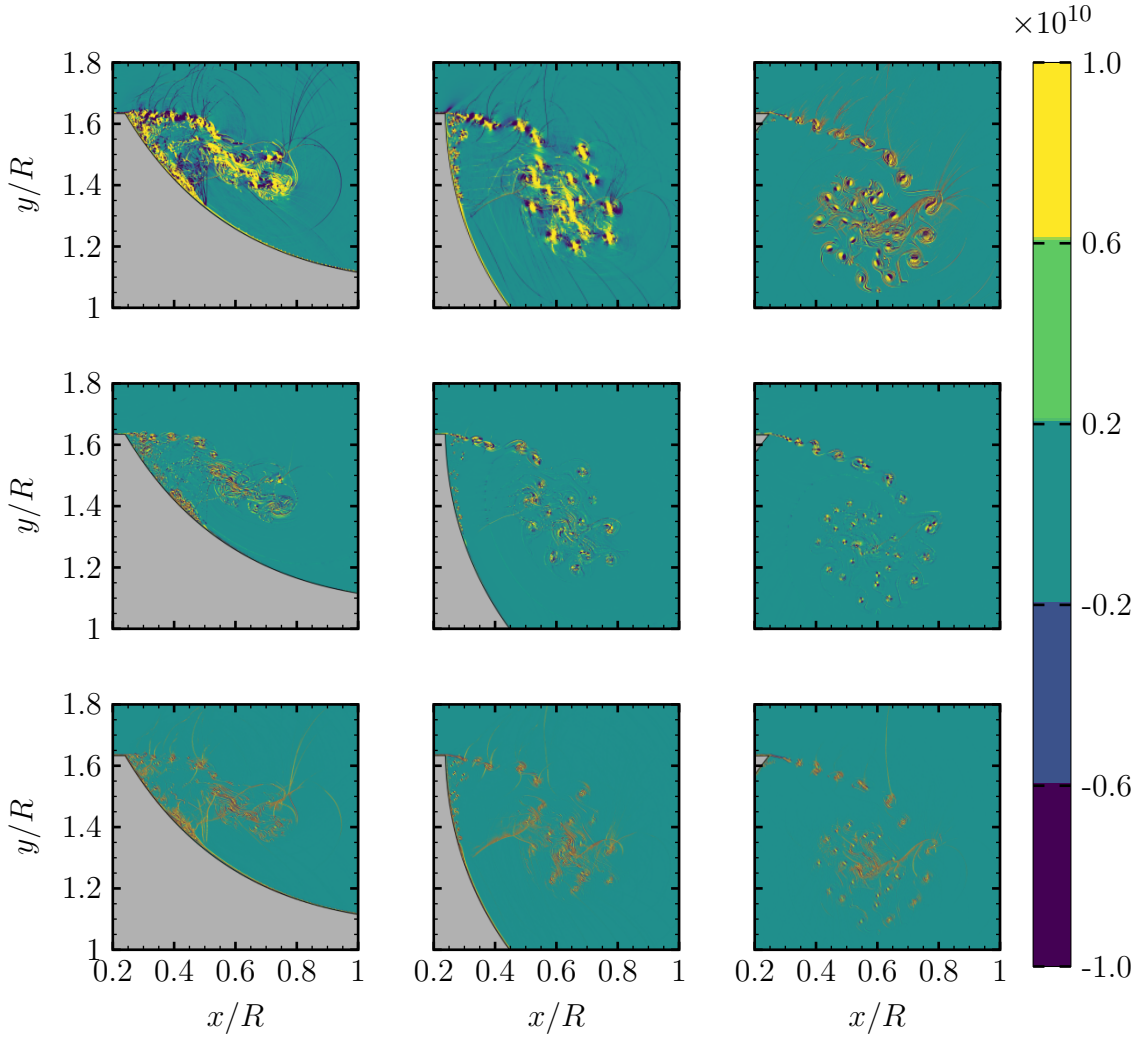

(b)

Figure C.9: VTE budget at $t = 228\ \mu s$. Row-wise (top-to-bottom): (a): ω_c and ω_t terms, (b): VSC, BAR and DFV terms. Column-wise (left-to-right): $\theta_w = 60°$, $\theta_w = 90°$, $\theta_w = 140°$.

C.3 Conclusion

In this part, a shock-wave, at incident-shock Mach number $M_s = 1.6$, propagation over cylindrical cavities was numerically investigated. The objective was to study the vortex formation with regards to the initial diffraction angle. An end-wall corner vortex is seen to be formed with a rolling-up of eddies that are convected quasi-linearly away from the cavity entrance as the diffraction process evolves. In addition to this important primary vortex, a secondary instability appear along the cavity wall for $\theta_w \leq 90°$. The trajectory of the center of the primary vortex is captured and found to be quasi-linear, with some oscillatory behavior that is more or less pronounced depending on the diffraction angle, θ_w. For $\theta_w > 90°$, the position of the center of the primary vortex is easy to detect.

The total amount of vorticity expressed in terms of circulation produced by shock diffraction has been quantified. The effect of initial diffraction angle on the vorticity production is investigated and found to be negligible at least in the earlier stage of the diffraction process. A shock indicator based on Ducros sensor showed that the contribution of shocks in vorticity production is negligible. A detailed analysis of the vorticity transport equation showed that the stretching of vorticity due to flow compressibility (VSC) and the convection term (ω_c) play the most important role in the vorticity dynamics.

Appendix D

Shock mitigation/amplification inside channels with circular cavity with diffraction angle, $\theta_w = 60°$

Abstract This appendix discusses about shock-wave propagation and its attenuation/amplification in tunnels having different heights and circular cavity with diffraction angle of $\theta_w = 60°$ inside. A schematic illustration of the studied configurations is depicted in Figure D.1, where a planar shock travels at $M_s = 1.6$ inside a channel. The later has different inlet and exit heights. A cylindrical cavity with a given depth d is placed at the bottom of the channel as to increase the volume of discharge. Four different cases are considered where basically the inlet and the outlet volumes have been varied to cover the most relevant situations. In all considered cases, the cavity depth is kept constant ($d = 25\,mm$) along with the initial diffraction angle, $\theta_w = 60°$, while varying the height of the tunnel (h), for that we have defined $\zeta = h/d$ and we took two different values of the latter, namely: 0.5 and 5.36. In the precedent chapter 6 the effect of the containment was investigated for the cavity with $\theta_w = 90°$ and $d = 50\,mm$ where an optimal arrangement was found and a shock-wave mitigation is achieved by approximately a factor of 57%.

D.1 Primary vortex evolution

First, we investigated the effect of ζ on the primary vortex centroid trajectory. The results are presented in Figure D.2. At the early stages of the diffraction process, the vortex trajectory is almost linear and easy to detect. As the diffraction process evolves, the vortex trajectory becomes more difficult to detect, specially for low ζ values. The channel height is reduced, so the shock waves are quickly reflected by the upper boundary and interacts with the main vortex resulting in highly perturbed region with large scale

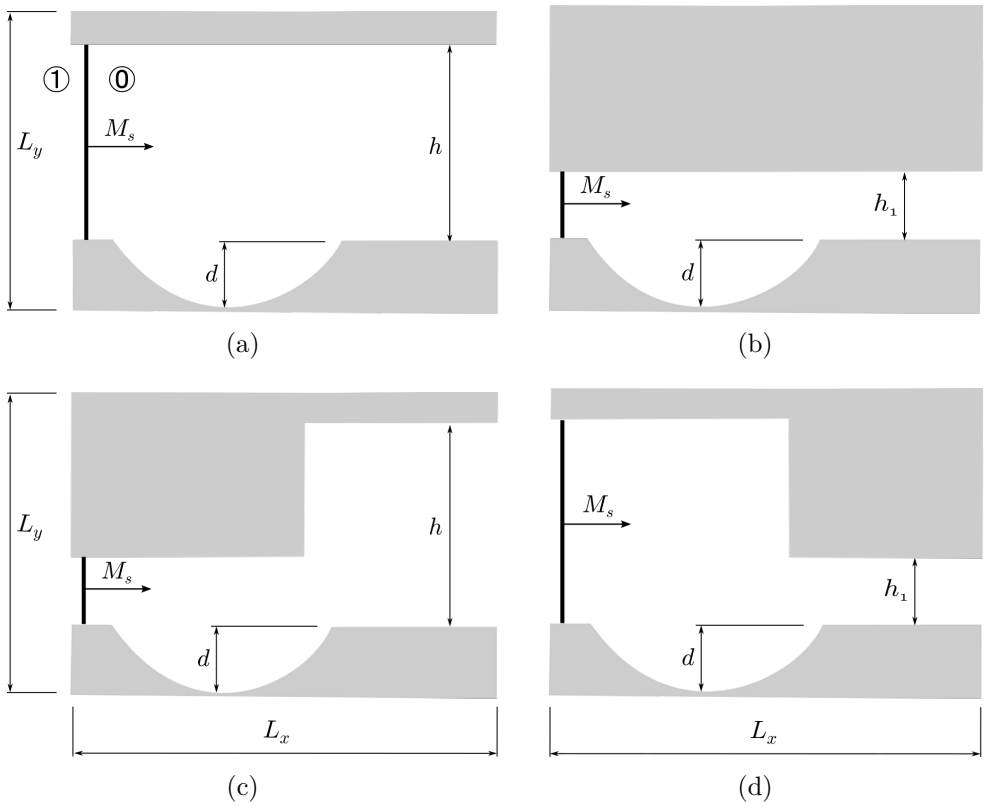

Figure D.1: Schematic illustration of the geometrical setups, (a): $C1$, (b): $C2$, (c): $C3$ and (d): $C4$, M_s: Incident shock Mach, $d = 25\ mm$: cavity depth, h: height of the first channel, h_1: height of the second channel, ($L_x = 200\ mm$, $L_y = 165\ mm$): the dimensions of the computation domain in x and y directions, respectively, ①: shocked gas, ⓪: gas at rest.

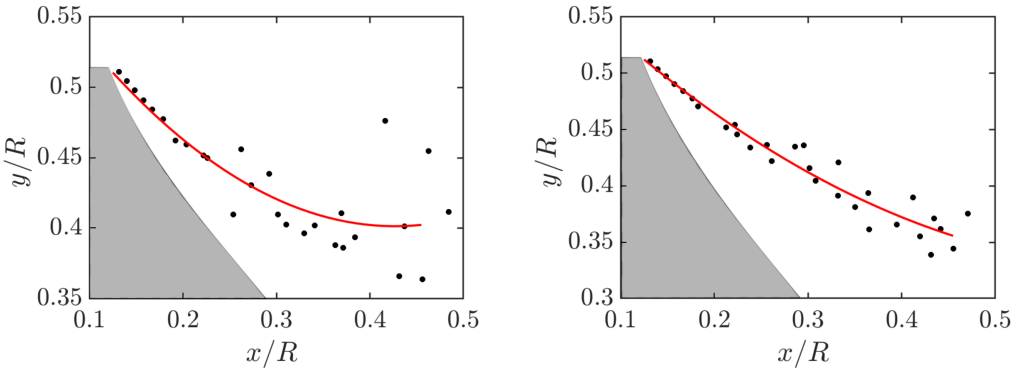

Figure D.2: Trajectory of the primary vortex centroid for different ζ; (a): $\zeta = 0.5$, (b): $\zeta = 5.3$. The red line represents an averaged linear regression.

coherent vortices, thus making detection of the primary vortex centroid complicated.

D.2 General flow evolution

Figure D.3 presents numerical schlieren pictures for different configurations at $t = 273\ \mu s$. The incident shock wave starts to diffract over the top left corner of the cavity resulting in the formation of an end-wall corner vortex with a rolling-up of coherent structures. Roughly in the middle of the cavity, an inverse-Mach reflection (InMR) appears, whose termination leads to the formation of a transitioned regular reflection (TRR). More details are shown in Figures D.7(b) and D.7(c). After the passage of the shock, vortices are formed at the upper right corner of the cavity, and at the lower right end of the upper wall for $C3$ and $C4$ configurations. When the transmitted shock propagates further away from the cavity and approaching the channel exit, the developed flow field can be divided into two separated zones. In the first one, noted Zone A, the compressed gas expands over the cavity and forms a series of vortices that dominate the flow features in this region. The second region, named Zone B, is mostly characterized by a quasi-uniform flow, followed by a series of wave reflections arising from both inverse-Mach reflection (InMR) and transitioned regular reflection (TRR). Transverse waves are then created due to the reflection of the shock on upper and lower channel walls, for $C2$ and $C4$. These observations confirm the earlier findings of Berger et al. (2015).

D.3 Shock-wave characteristics

Here, we present the effect of the channel height and the position of the expanding area on the shock wave patterns. Figure D.4(a) shows the space-time evolution of the shock wave.

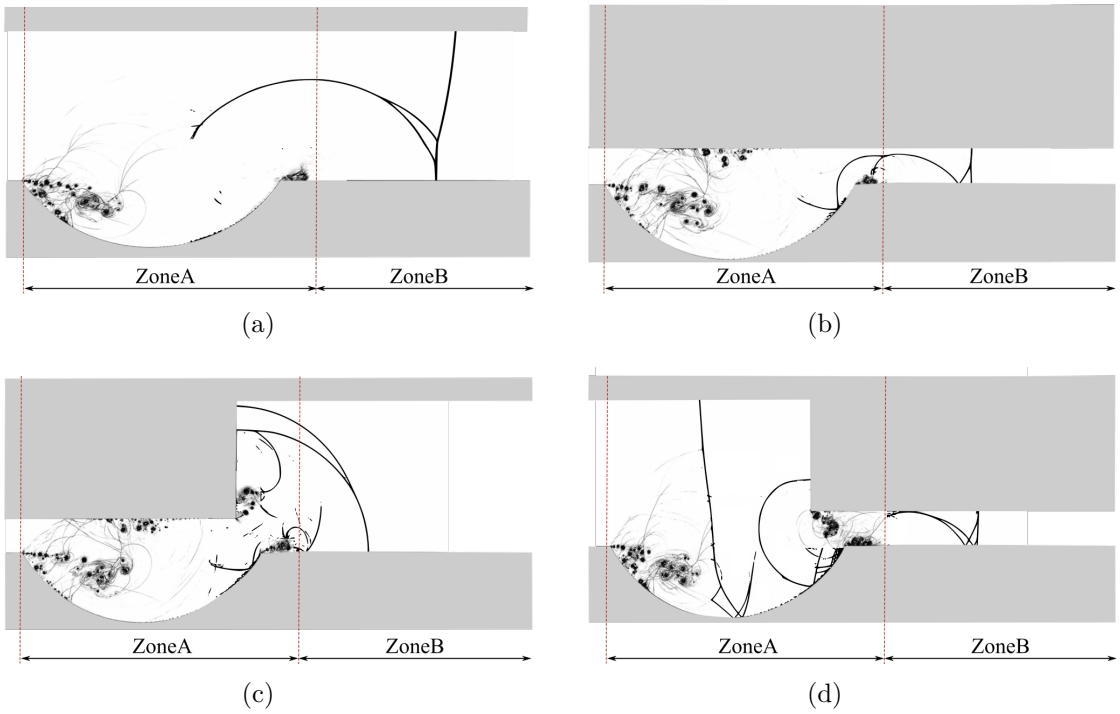

Figure D.3: Numerical schlieren pictures for different flow configurations $C1$, $C2$, $C3$ and $C4$ at $t = 273\ \mu s$.

One can see that the transmitted shock reaches the end of the channel earlier for $C1$ and $C4$ and later for $C2$ and $C3$, respectively. These results are also highlighted through the variation of the shock-wave speed, presented in Figure D.4(b) in terms of Mach number M_s. For all cases, we first notice a constant shock speed and then a decrease just after the beginning of the diffraction process. As this process evolves in time, the shock dynamics differ from one case to another depending on the channel geometry. Thus, in order to understand the shock behavior, some important physical parameters are discussed, such as the variation of the pressure ratio, p_s/p_1 (p_s being the pressure behind the shock wave and p_1 the initial pressure in the shocked gas taken as, $p_1 = 285.7$ kPa). The results are presented in Figure D.5.

For case $C1$, depicted in Figure D.5(a), the flow structures can be divided into three main parts. The first one (I), identical for all cases, highlights the shock dynamics before the startup of the diffraction process which is represented by a short horizontal line corresponding to the initialization values of the shock. After the diffraction process starts (part II), an end-wall corner vortex is formed with a rolling-up of eddies. The formation of these vortices leads to a pressure decrease and the more this disturbed region spreads over the diffraction volume, the more the pressure decreases (see cases $C2$ and $C3$). Roughly in the middle of the cavity, an InMR configuration appears, which induces the formation of a reflected shock (r) as depicted in Figure D.7(a). A bit further, in the

second half of the cavity (rising part), the triple point (TP) of the inverse-Mach reflection (InMR) collides with the reflecting surface. The termination of the InMR configuration leads to the formation of a transitioned regular reflection (TRR), with two additional shocks, r' and d' (as shown in Figure D.7(b)). The additional shock, d', catches up the incident shock (I) at the exit of the cavity and merge into a single shock (see Figure D.7(c)). This process increases the pressure ratio and forms a new transmitted shock (I'), hence the first pressure jump for the third phase (III) of the graph. Note that r' will catch the new transmitted shock (I'), and increases the pressure behind by forming a new transmitted shock (I''). This phenomenon is also observed through the second pressure jump in the third phase (III) of the plot.

As for the first case, the pressure ratio evolution for the second one $C2$ can be divided into three parts (see Figure D.5(b)). Part (I) is identical to that of case $C1$. For part (II), we notice a drop in the pressure ratio towards a lower value. By reducing the channel height to $h_1/d = 0.5$, the formed vortex at the upper left corner of the cavity occupies a much larger volume, thus lowering further the pressure level in the cavity and behind the shock as well. For part (III), we observe a presence of a series of successive pressure jumps that increase the pressure ratio from a minimum value, at the exit of the cavity, up to a value approximately equal to the initial one at the exit of the channel. The first two pressure jumps are caused by the inverse-Mach reflection (InMR) phenomenon and the associated transitioned regular reflection (TRR) as mentioned before. The following pressure peaks are essentially due to the multiple shock reflections resulting from the Mach reflection (r) and the TRR (r' and d') arising from the upper and the lower channel walls. These reflected shocks successively catch the transmitted shock and merge all together into a single stronger shock (see Figure D.7). The pressure as well as the speed of the resulting shock are enhanced.

As depicted in Figure D.5(c), stages I and II of $C3$ are similar to that of $C2$. Indeed in stage (III), we notice an additional decrease in the pressure ratio due to the formation of two vortices. The first one is initiated at the lower-right corner of the top wall and the second one takes place at the top-right corner of the cavity. The decrease of the pressure is followed by two successive jumps, at the start of the fourth phase (IV), which are due, as explained above, to the additional shocks resulting from the TRR configuration (r' and d'). After these jumps, the pressure ratio decreases quasi-linearly and reaches a value of approximately 0.5 at the exit of the channel.

Phases I and II in the last case, $C4$, presented in Figure D.5(d), which, in terms of geometry, is the inverse of the third case ($C3$), are similar to those in case $C1$. Phase III is similar to that of case $C3$. For part IV, we notice the presence of a series of successive pressure jumps that increase the pressure ratio from a minimum value, at the cavity exit,

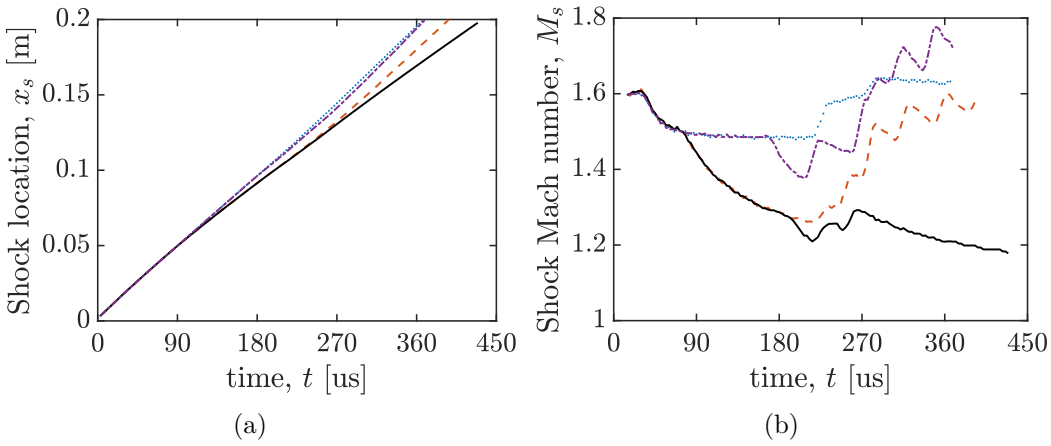

Figure D.4: Time variation of (a): Shock location; (b): Shock Mach number at $y/d = 1.28$ for: ···· $C1$, – – – $C2$, — $C3$, -·-·- $C4$.

up to a value of approximately 1.18 at the end of the channel. As reported previously, the first two peaks are caused by the inverse-Mach reflection (InMR) and the transitioned regular reflection (TRR). The other peaks are due to the multiple wave reflections as explained for $C2$.

Table D.1 shows the time variation of the pressure, defined as $dp/dt = (p_e - p_{min})/(t_e - t_{p_{min}})$. Here, p_e is the pressure behind the transmitted shock at the exit of the channel, p_{min} is the minimum pressure behind the shock, t_e is the instant when the shock arrives at the end of the channel and $t_{p_{min}}$ is the instant when the pressure behind the shock reaches its minimum value. As shown in Table D.1, the only configuration where a pressure reduction is achieved is $C3$. The most critical case is the one related to configuration $C4$, where an increase, of approximately 798 MPa/s, is obtained. Table D.1 shows also the shock attenuation (positive) or amplification (negative) factor $\mathcal{A}$ defined as the ratio of the relative pressure behind the transmitted shock (at the exit of the channel) to the initial shocked gas pressure such as, $\mathcal{A} = (p_s - p_1)/p_1$, where $p_1 = 285.7$ kPa and p_s is the exit pressure. Comparison between all configurations indicates that the height and the expanded area position of the channel significantly affect the shock wave attenuation (or amplification). The results show that a better attenuation factor is obtained for $C3$ (50%) and an amplification factor is attained for $C4$ (−31%). However, for cases $C1$ and $C2$ the attenuation/amplification effects are minor, about −3% for $C1$ and 4% for $C2$, respectively.

The effect of different configurations on shock strength is also investigated by computing the static, I_p, as well the dynamic, I_{pd}, pressure impulses along with the normalized over pressure, $\mathcal{P}$. These three parameters are defined as, $I_p = \int_{t_0}^{t_f} p\,dt$, $I_{pd} = \int_{t_0}^{t_f} \frac{1}{2}\rho \mathbf{v}^2\,dt$, $\mathcal{P} = p/p_1$, where p, ρ and $\mathbf{v}$ are the pressure, density and velocity in the shocked region,

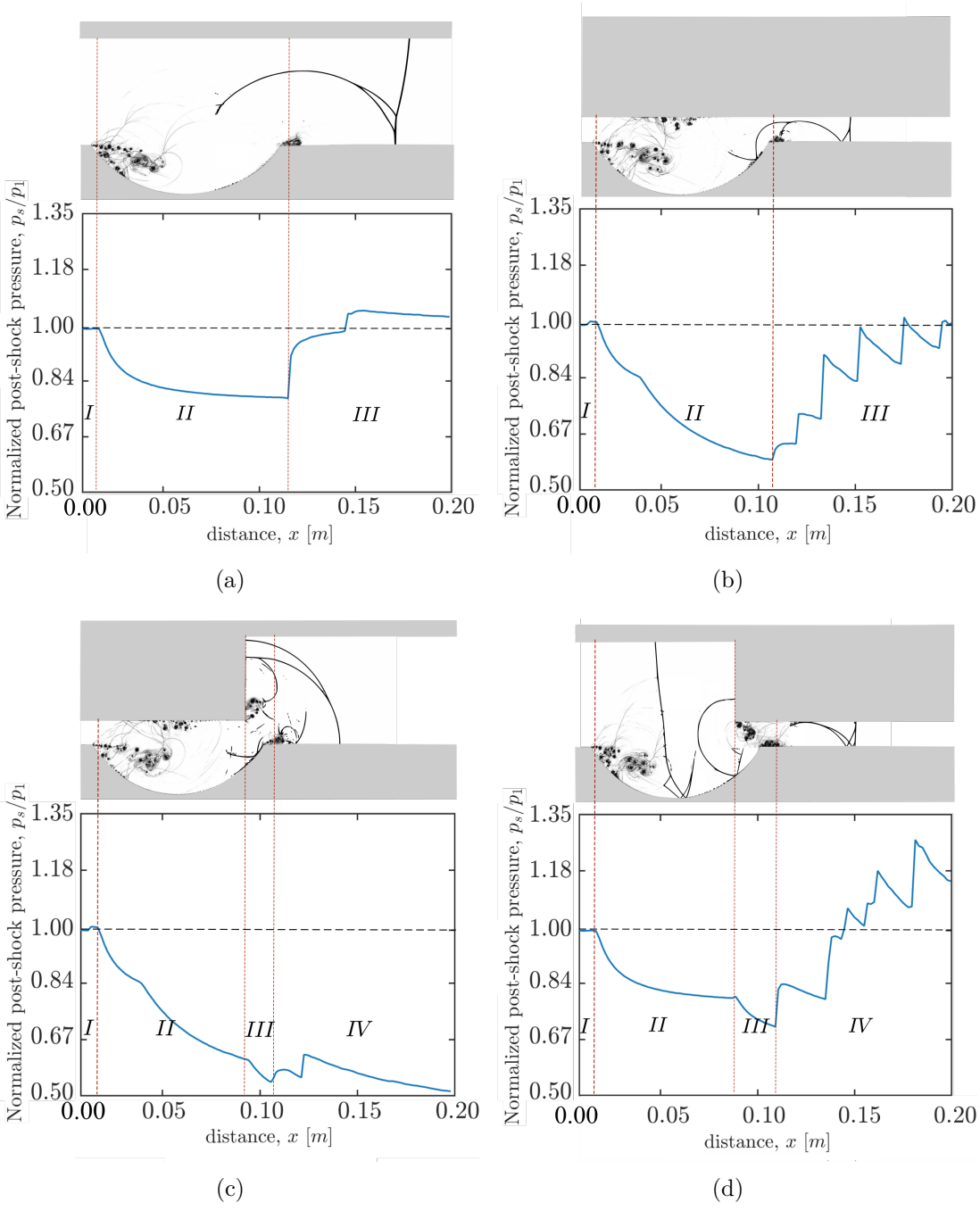

Figure D.5: Spatial distribution of the normalized shock pressure along with numerical schlieren pictures for different flow configurations at $t = 273$ μs. p_1 is the initial pressure taken as p_1=285.7 kPa and p_s is the pressure behind the shock.

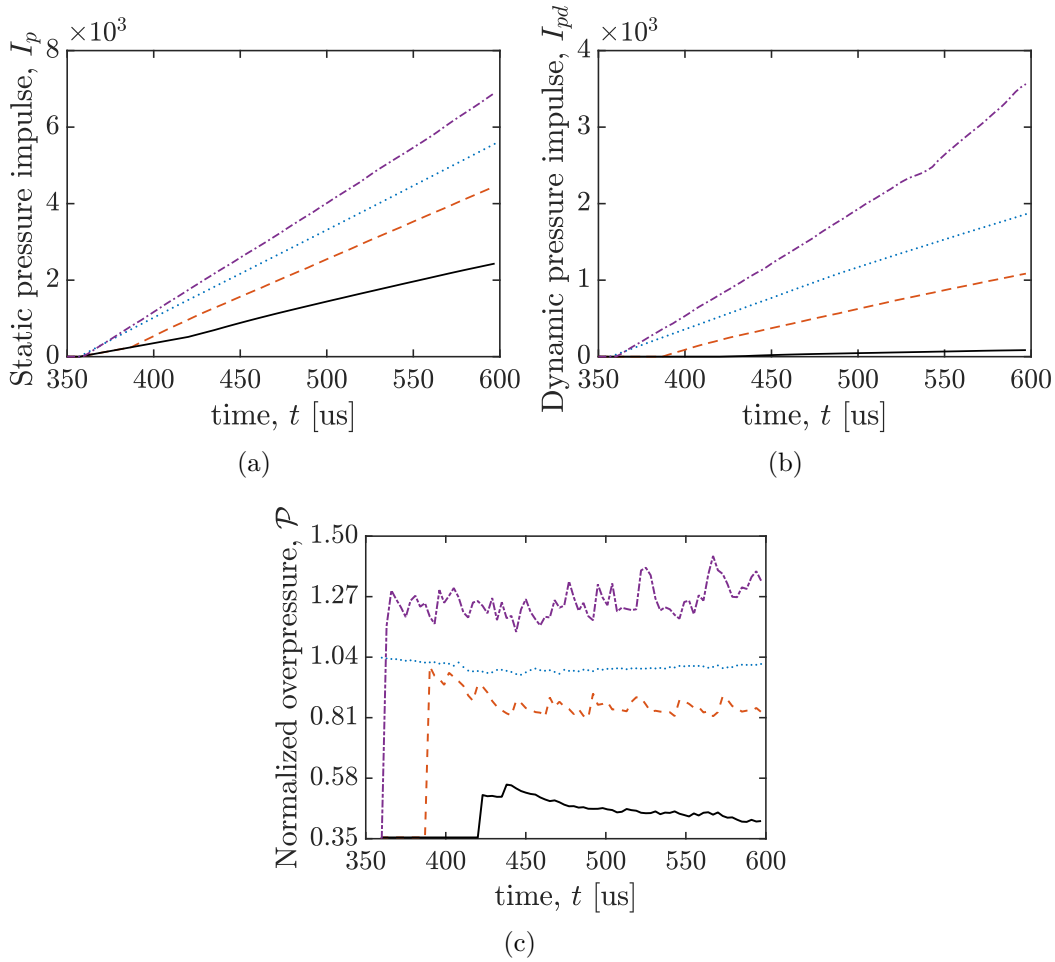

Figure D.6: Time evolution of (a): Static impulses (b): Dynamic impulses (c): Normalized overpressures at $y/d = 1.28$ and $x/d = 7.8$ for: ··· $C1$, – – – $C2$, — $C3$, -·-·- $C4$.

	$C1$	$C2$	$C3$	$C4$
$dp/dt\ [MPa/s]$	337	655	-37	798
$\mathcal{A}$	-3%	4%	50%	-31%

Table D.1: dp/dt: pressure variation, $\mathcal{A}$: attenuation (positive) /amplification (negative) factor, for $\theta_w = 60°$.

respectively. The initial time t_0 is picked when the transmitted shock wave reaches the channel exit ($x/d = 7.8$) and t_f is the final time of the simulations. The obtained pressure impulses are presented in Figures D.6(a) and D.6(b). The general trends show that these quantities increase quasi-linearly after the passage of the shock. The exit of the channel is mostly comprised by a quasi-uniform gas, hence the quasi-linear behavior of static and dynamic impulses. As expected from previous results, the minimum value for both static and dynamic pressure impulses is obtained for $C3$, while the maximum is reached for $C4$. As for the normalized overpressure, Figure D.6(c) shows a sudden jump due to the passage of the incident shock, which remains almost constant later. The peak intensity of the normalized overpressure varies between a maximum value for $C4$ and a minimum value for $C3$.

Further analysis of the pressure signals at $y/d = 1.28$ highlights the attenuation aspect in different configurations. For instance, the effect of the additional shocks resulting from the InMR and the TRR shock patterns (r, r' and d', respectively) is clearly visible in Figure D.8 at t= 213 μs, 228 μs, and 243 μs. Peaks with different intensities appear for different configurations. Once the shock leaves the cavity and propagates over the second half of the channel, the effect of reducing the height of the channel appears. For cases $C2$ and $C4$, this part is characterized by the emergence of additional peaks visible for $t > 243\ \mu s$ and $x > 0.13\ m$ due to multiple shock reflections (see Figures D.8(b) and D.8(d)). The normalized pressure profiles are in accordance with the results presented above, where we can see that the case $C3$ attenuates the shock with a peak of $p/p_1 \approx 0.5$ at the exit, while case $C4$ amplifies it up to $p/p_1 \approx 1.3$. Finally, a shock retardation is also noticed as a result of the pressure drop.

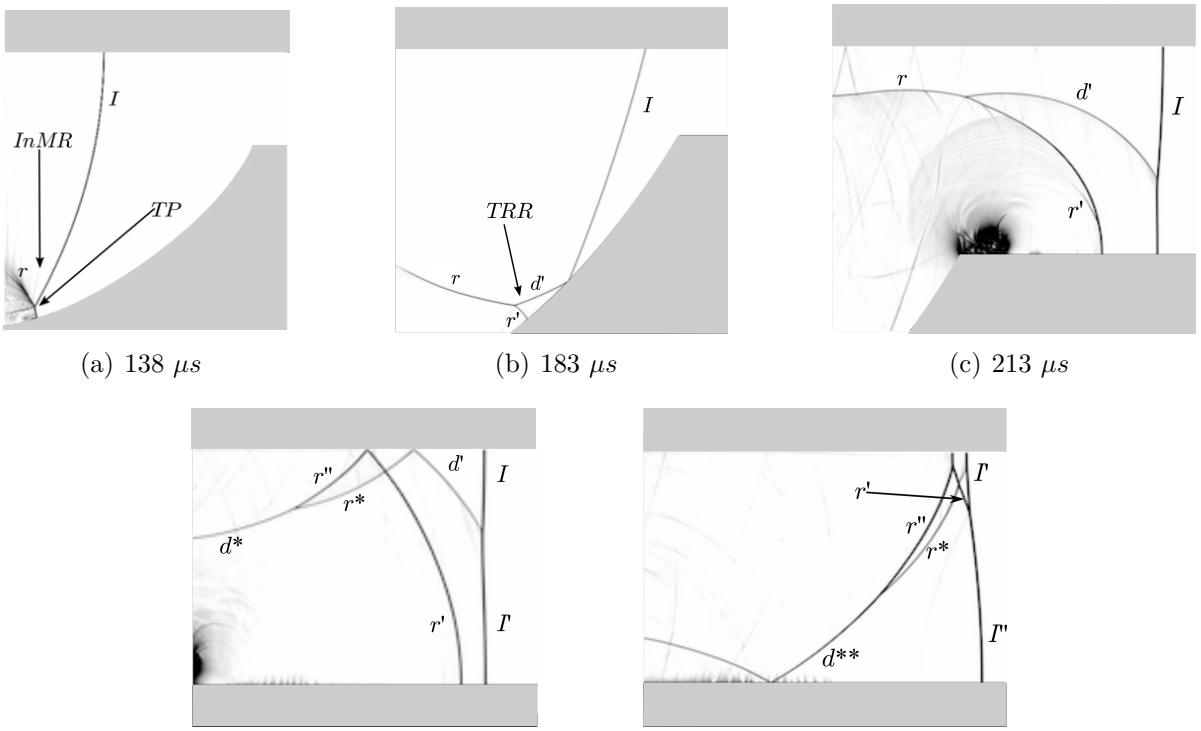

(a) 138 μs (b) 183 μs (c) 213 μs

(d) 231 μs (e) 255 μs

Figure D.7: Numerical schlieren pictures at different time intervals for $C2$. I: incident shock, r: reflected shock, TP: triple point, $InMR$: inverse-Mach reflection, TRR: transitioned regular reflection, r' and d': additional shocks created from TRR state, $d*$ and $r*$ and r'': reflected shocks from the upper boundary, I': new incident shock resulting from the merger of d' and I, I'': new incident shock resulting from the merger of r' and I'.

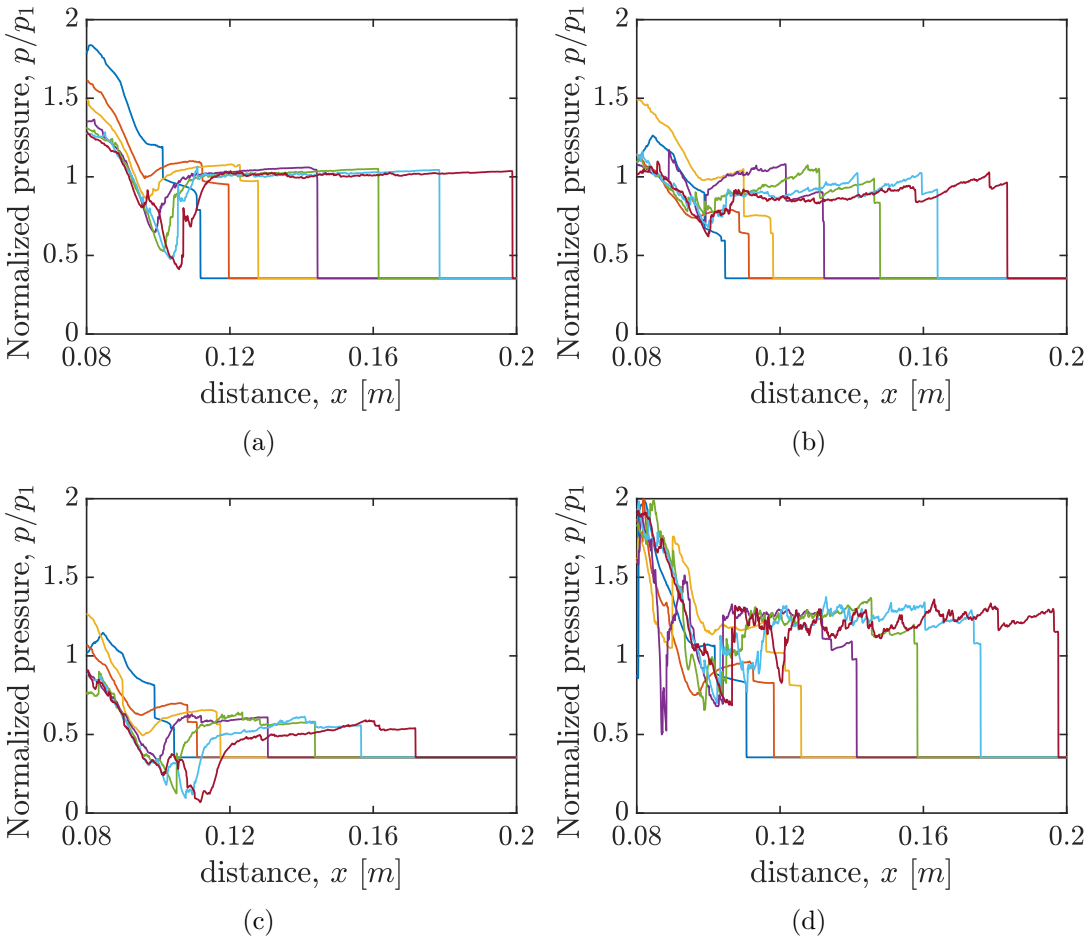

Figure D.8: Normalized pressure profiles at $y/d = 1.28$ for; (a): $C1$; (b): $C2$; (c): $C3$ and (d): $C4$, at different time intervals: –t= 213 μs, –t = 228 μs, –t = 243 μs, –t = 273 μs, –t=303 μs, –t = 333 μs, –t=369 μs.

D.4 Effect of the diffraction angle and the cavity depth on the shock wave attenuation/amplification

In this section and in order to further clarify the effect of the diffraction angle and the depth of the cavity on the attenuation/amplification of the shock waves we present a comparison between two different cavities, namely: $\theta_w = 60°$ and $\theta_w = 90°$. The results are presented in Figures D.9 for shock position and D.10 for shock Mach number. As we can see in the Figures, the curves collapse during the early stages of the propagation process. At the exit of the cavities, the curves behave differently. For the four studied cases, we note that the shock wave propagating over the cavity with the diffraction angle $\theta_w = 60°$ arrives at the exit of the tunnel first. This result is also noticed by the variation of the shock Mach numbers. The shock wave propagating over the cavity with the diffraction angle $\theta_w = 60°$, propagates faster in the second half of the domain. This difference is due to the dynamics of the shock at the exit of the cavity that depends on the right angle of the cavity. The shock dynamics for the both angles are depicted in Figure D.11. For $\theta_w = 60°$, the TRR configuration leads to the formation of two additional shocks, r' and d'. These shocks and their successive reflections from the upper and lower walls of the tunnel (depending on the geometry), as shown in Figure D.11(a), contribute to significantly increase the shock Mach number as well as the strength of the transmitted wave. For $\theta_w = 90°$, the incident shock, I, hits the upper right cavity corner leading to the formation of a direct Mach reflection with a single reflected shock, r_1. This wave and its successive reflections from the upper and lower walls of the tunnel (depending on the geometry), as shown in Figure D.11(b), increase slightly the shock Mach number as well as the strength of the transmitted shock. Unlike $\theta_w = 60°$, the shock wave propagating through the cavity with the diffraction angle of $\theta_w = 90°$ is always attenuated at the exit of the tunnel, the level of attenuation varies from one case to another. The best shock attenuation is achieved with C_3 and $\theta_w = 90°$, while a shock amplification is achieved with C_4 and $\theta_w = 60°$.

Table D.2 confirms the previous results. The attenuation factor for $\theta_w = 90°$ varies between a minimum value for C_4, of 3%, and a maximum value, of 57%, for C_3. Whereas for $\theta_w = 60°$ an amplification of the shock wave is obtained with two cases; C_4 and C_1.

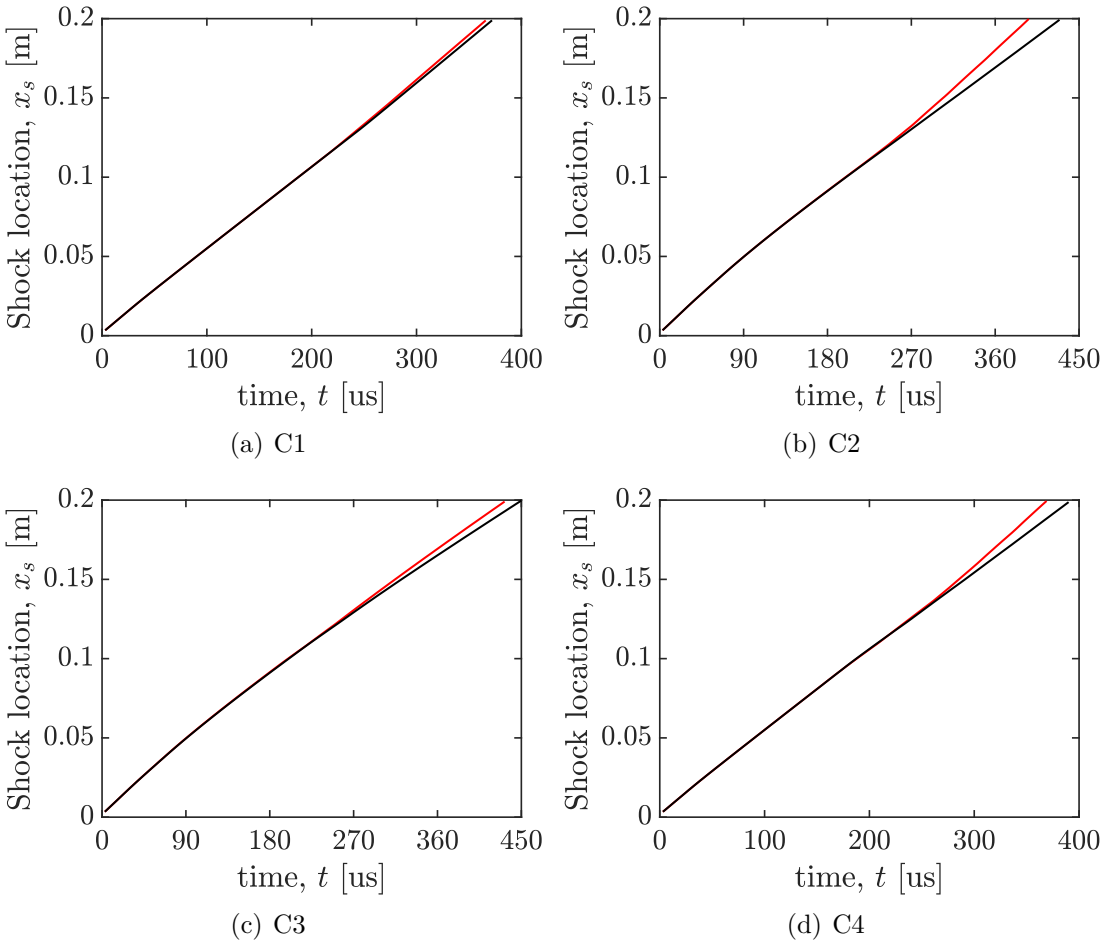

(a) C1 (b) C2

(c) C3 (d) C4

Figure D.9: Time variation of shock location at $y/d = 1.28$ for: (a): $C1$, (b): $C2$, (c): $C3$, (d): $C4$. With, – $\theta_w = 60°$ and – $\theta_w = 90°$.

D.5 Conclusion

An optimal arrangement of channel position/height for cavity with diffraction angle of $\theta_w = 60°$ is found, leading to a significant attenuation factor of about 50%. On the other hand, the results showed that an arbitrary arrangement may have a dramatic consequence on the amplification of the shock by a factor of approximately 30% at the end of the channel.

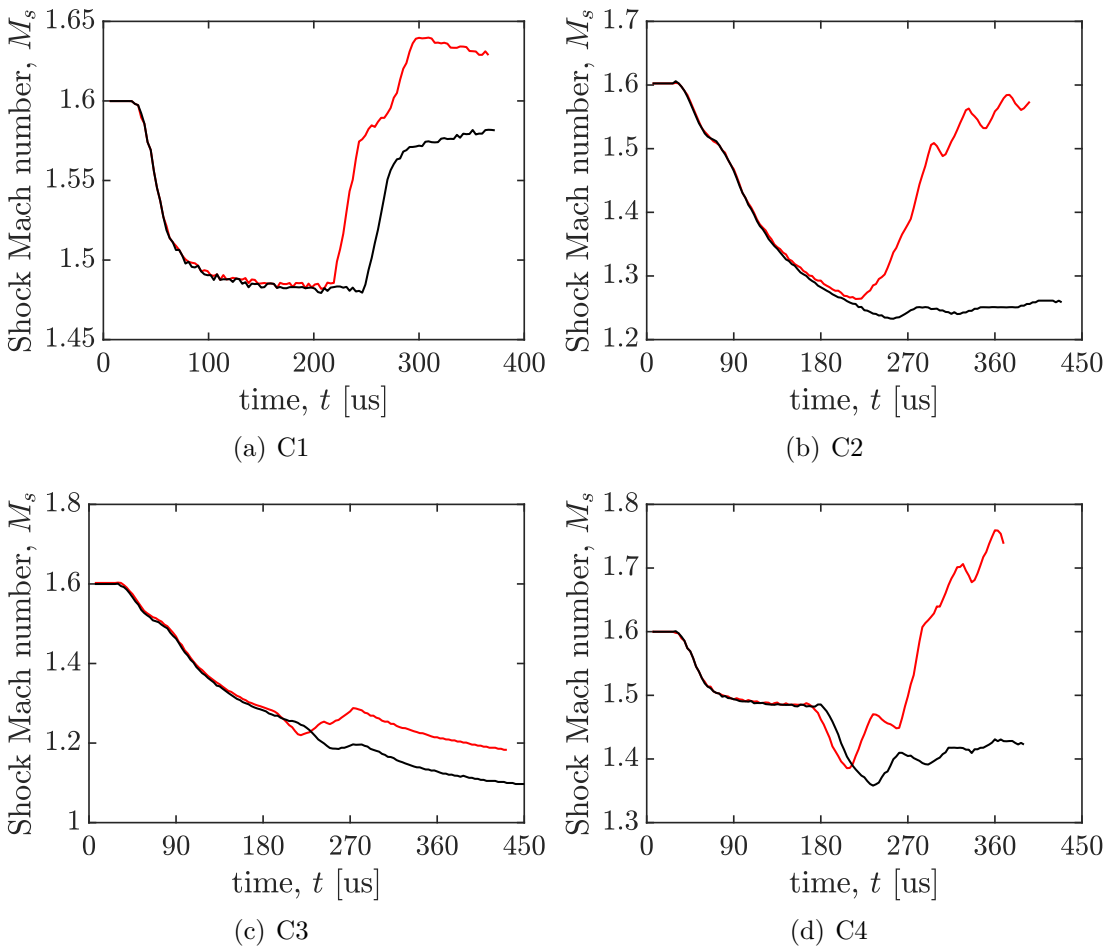

Figure D.10: Time variation of shock-Mach number at $y/d = 1.28$ for: (a): $C1$, (b): $C2$, (c): $C3$, (d): $C4$. With, – $\theta_w = 60°$ and – $\theta_w = 90°$.

	θ_w	$C1$	$C2$	$C3$	$C4$
dp/dt $[MPa/s]$	60°	337	655	−37	798
	90°	426	55	−111	197
$\mathcal{A}$	60°	−3%	4%	50%	−31%
	90°	3%	40%	57%	21%

Table D.2: dp/dt: pressure variation, $\mathcal{A}$: attenuation (positive)/amplification (negative) factor.

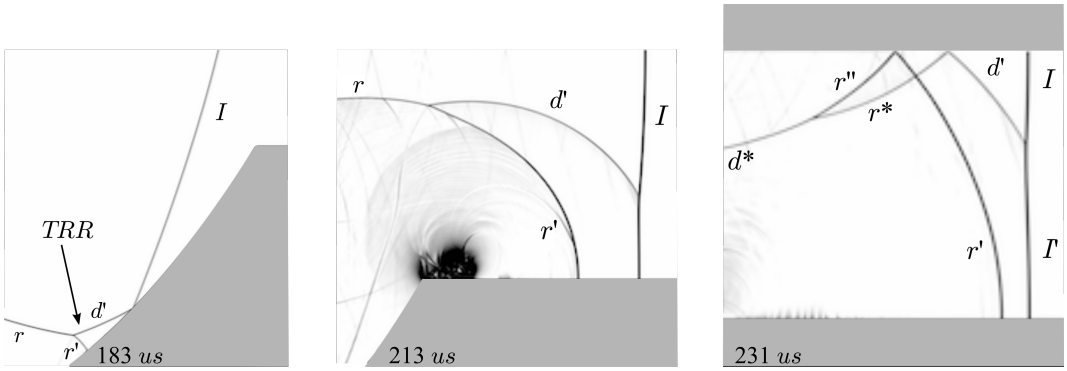

(a) $\theta_w = 60°$

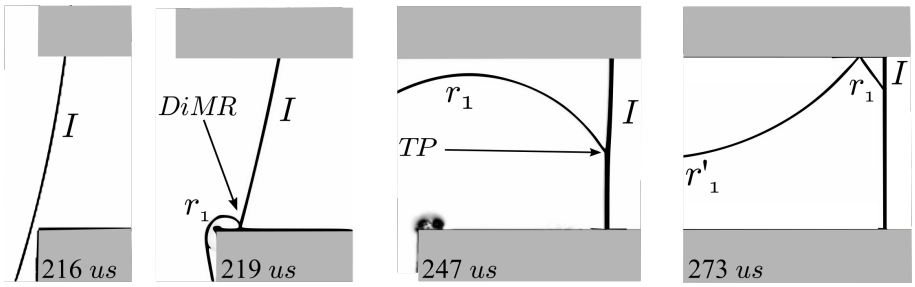

(b) $\theta_w = 90°$

Figure D.11: Numerical schlieren pictures at different time intervals for $C2$. (a): $\theta_w = 60°$, (b): $\theta_w = 90°$. I: incident shock, r: reflected shock, TP: triple point, $DiMR$: direct-Mach reflection, TRR: transitioned regular reflection, r' and d': additional shocks created from TRR state, d^* and $r*$ and r'': reflected shocks from the upper boundary, I': new incident shock resulting from the merger of d' and I, r_1: reflected shock from the $DiMR$ r'_1: reflected shocks from the upper boundary.

Appendix E

Turbulent structures of shock-wave diffraction over 90° convex corner

Turbulent structures of shock-wave diffraction over 90° convex corner

Cite as: Phys. Fluids **31**, 086103 (2019); https://doi.org/10.1063/1.5113976
Submitted: 10 June 2019 . Accepted: 11 July 2019 . Published Online: 12 August 2019

V. Soni, A. Chaudhuri, N. Brahmi, and A. Hadjadj

Physics of Fluids ARTICLE scitation.org/journal/phf

Turbulent structures of shock-wave diffraction over 90° convex corner

Cite as: Phys. Fluids 31 , 0861 03 (201 9); doi: 1 0.1 063/1 .511 3976
Submitted: 1 0 June 201 9 • Accepted: 11 July 201 9 •
Published Online: 1 2 August 201 9

V. Soni,[1] A. Chaudhuri,[2,a)] N. Brahmi,[1] and A. Hadjadj[1]

AFFILIATIONS

[1] Normandie University, INSA of Rouen, CNRS, CORIA, 76000 Rouen, France
[2] Department of Civil Engineering and Energy Technology OsloMet— Oslo Metropolitan University, Pilestredet 35, PB 4, St. Olavs Plass, 0130 Oslo, Norway

[a)] Electronic mail: arnab.chaudhuri@oslomet.no

ABSTRACT

The turbulent structures and long-time flow dynamics of shock diffraction over 90° convex corner associated with an incident shock Mach number $M_s = 1.5$ are investigated by large eddy simulation (LES). The average evolution of the core of the primary vortex is in agreement with the previous two dimensional studies. The Type-N wall shock structure is found to be in excellent agreement with the previous experimental data. The turbulent structures are well resolved and resemble those observed in the experimental findings. Subgrid scale dissipation and subgrid scale activity parameter are quantified to demonstrate the effectiveness of the LES. An analysis based on turbulent-nonturbulent interface reveals that locally incompressible regions exhibit the universal teardrop shape of the joint probability density function of the second and third invariants of the velocity gradient tensor. Stable focus stretching (SFS) structures dominate throughout the evolution in these regions. Stable node/saddle/saddle structures are found to be predominant at the early stage in locally compressed regions, and the flow structures evolve to more SFS structures at later stages. On the other hand, the locally expanded regions show a mostly unstable nature. From the turbulent kinetic energy, we found that the pressure dilatation remains important at the early stage, while turbulent diffusion becomes important at the later stage. Furthermore, the analysis of the resolved vorticity transport equation reveals that the stretching of vorticity due to compressibility and stretching of vorticity due to velocity gradients plays an important role compared to diffusion of vorticity due to viscosity as well as the baroclinic term.

NOMENCLATURE

General description and validation

I	incident shock wave
DS	diffraction shock wave
EW	expansion shock wave
CS	contact surface
SL	shear layer
KHI	Kelvin-Helmholtz instabilities
V	vortex core
VV	viscous vortex
VS	vortex shock
LS	lambda shock

Local flow topology

$\boldsymbol{P}$	first invariant of the velocity gradient tensor
$\boldsymbol{Q}$	second invariant of the velocity gradient tensor
$\boldsymbol{R}$	third invariant of the velocity gradient tensor
$\boldsymbol{Q_w}$	second invariant of the rotation-rate tensor
UFC	unstable focus compressing
UN/S/S	unstable node/saddle/saddle
SN/S/S	stable node/saddle/saddle
SFS	stable focus stretching
SFC	stable focus compressing
UFS	unstable focus stretching

Vorticity transport equation (VTE)

VSC ($\mathcal{V}_c$)	stretching of vorticity due to compressibility
VSG ($\mathcal{V}_g$)	stretching/tilting of vorticity due to velocity gradients
$\mathcal{B}$	Baroclinic torque
DFV ($\mathcal{D}_v$)	diffusion of vorticity due to viscosity
$\mathcal{E}$	enstrophy

I. INTRODUCTION

Study of shock diffraction over various geometries has been an active research field for several decades. For example, Griffith and Bleakney[1] addressed the complexity involved in unsteady shock dynamics related to such shock-wave diffraction phenomenon in early 50's. Understanding shock diffraction is important for internal/external compressible flows involving the propagation of shock waves over solid surfaces, e.g., applications like mitigating shock/blast wave with designing effective shock resistant structures. The flow dynamics of these applications involves complex coupled interactions such as shock-shock, shock-vortex, vortex-vortex, and shock-turbulence interactions. Along with experimental approaches, with the advent of numerical techniques, numerical studies gained popularity for addressing intricate issues associated with such complex flow dynamics. Two-dimensional (2D) inviscid simulations[2–5] are capable of resolving the general features associated with shock-wave diffraction. Most of the studies in the literature relied upon the inviscid predictions to establish the basic wave characteristics. Among these, Baum *et al.*[4] presented a 2D numerical study of complex geometry canisters using an adaptive finite element based shock capturing scheme. Subsequently, several qualitative studies addressed the shock wave interaction with the compressible vortex associated with shock diffraction[6–10] problems. Viscous effects are important to resolve the long-time evolution of shock-vortex dynamics and shock-boundary layer/shock-shear layer interactions. High-order scheme based numerical solvers equipped with robust shock capturing capabilities are essential to resolve the shock dynamics as well as the wide range of length/time scales of the turbulence. In this regard, several studies utilized high-order Weighed Essentially Non Oscillatory (WENO) based schemes[11–17] or Discontinuous spectral element method (DSEM) with artificial viscosity[18–20] to address complex flow features associated with shock diffraction, shock propagation, shock focusing, shock obstacle interaction, etc. Unsteady three-dimensional (3D) studies of shock diffraction are not abundant in the literature. Reeves and Skews[21] studied the evolution of spiral vortex for 3D edges ("V," "inverted-V," "parabolic," and "inverted parabolic" types). A general and preliminary three-dimensional study of the merging of vortices resulting from shock diffraction and vortex shedding off a discontinuous edge is presented by Cooppan and Skews.[22] Also, Skews and Bentley[23] addressed a 3D analysis of the merging of two diffracting shocks.

In a recent study,[19] the authors revisited the shock diffraction over 90° convex corner and addressed some intricate features of resolving the viscous and turbulent flow features. The main issues related to the 2D numerical predictions of this flow dynamics are to address the experimentally observed (i) secondary viscous vortex associated with the wall shock interaction with the boundary layer and (ii) the shear layer behavior (see, e.g., Refs. 24 and 6 for detail of this canonical benchmark case). These are addressed with a high-order numerical scheme based predictions by Chaudhuri and Jacobs.[19] It can be realized from the relatively recent experiments (e.g., Refs. 25 and 26) that the shear layer structures associated with the long-time evolution exhibit fine turbulent flow structures.

It is evident that 3D simulations and analysis are required to shed light into the turbulent structures and shear layer instabilities observed in these experiments. To the best of our knowledge, analysis of 3D flow features associated with shock diffraction over sharp corners has never been reported before. The objective of this work is to perform large eddy simulation (LES) to explore the 3D turbulent flow structures and analyze the long-time behavior of the shock diffraction over 90° convex corner with incident shock Mach number $M_s = 1.5$. The paper is organized as follows. In Sec. III, a brief description of the methodology is described. The numerical setup is presented in Sec. II followed by the results and discussions in Sec. IV. Finally, conclusions are drawn in Sec. V.

II. PROBLEM SETUP

Moving shock wave of shock Mach number $M_s = 1.5$ is allowed to pass through a 90° convex corner having a rectangular cross section of 35 mm × 25 mm. The step height h is taken as 140 mm, and the step length is set to 25 mm. The problem setup of the simulation is shown in Fig. 1. The mesh resolution of the computational domain of 200 mm × 175 mm × 35 mm (length-height-width) is summarized in Table I. The initial location of the moving shock is positioned at 75% of the step length. Rankine-Hugoniot relations are used to set the initial conditions for left (shocked state) and right (stagnant state) states associated with the chosen M_s. Air is considered as working fluid, and the initial stagnant state is assigned with temperature $T = 288$ K and pressure $p = 101\,325$ Pa. The spanwise (z-direction) direction is considered as the homogeneous direction, and periodic boundary conditions are applied at these boundaries. The left and right boundaries (x-direction) are kept as the initial conditions, and simulations are executed avoiding any reflections from these boundaries. We apply the symmetry condition at the top boundary, and adiabatic no-slip boundary conditions are set for the remaining solid walls. To assign realistic velocity fluctuations, homogeneous isotropic turbulent velocity fluctuations are superimposed with the initial velocity field in the shocked gas region.

III. METHODOLOGY

We solve the filtered compressible Navier Stokes system of equations to simulate the diffraction of the moving shock, over a convex corner. The definition of any filtered quantity with a filtered function G_Δ and filter width $\Delta = (\Delta_x \times \Delta_y \times \Delta_z)^{1/3}$ is given by $\bar{\phi}(\vec{x},t) = \int_{R^3} \phi(\vec{\eta},t) G_\Delta(\vec{x}-\vec{\eta}) d\vec{\eta}$. Favre averaged quantities $\tilde{\phi} = \overline{\rho\phi}/\bar{\rho}$ are used to reduce subgrid scale (SGS) terms. The in-house parallel compressible flow solver equipped with the immersed boundary method is used for this purpose. The fifth-order WENO scheme is used for inviscid fluxes, and the sixth-order central difference scheme is used for viscous fluxes. A third-order explicit Runge-Kutta method is used to advance in time. The SGS stress and SGS heat flux terms are closed by the wall adapting the local eddy viscosity (WALE) model. For brevity, the filtered governing equations, LES model, and the immersed boundary methodology are not presented here, and the details are available in our previous works.[12,27–29] The immersed boundary method (we use trilinear interpolation; see Ref. 29) in 3D simulations and LES model constants are essentially similar to those mentioned in these references. The flow solver is validated with relevant standard benchmark problems and is reported in our previous works. It is to be noted that only resolved quantities are used for the analysis and discussions

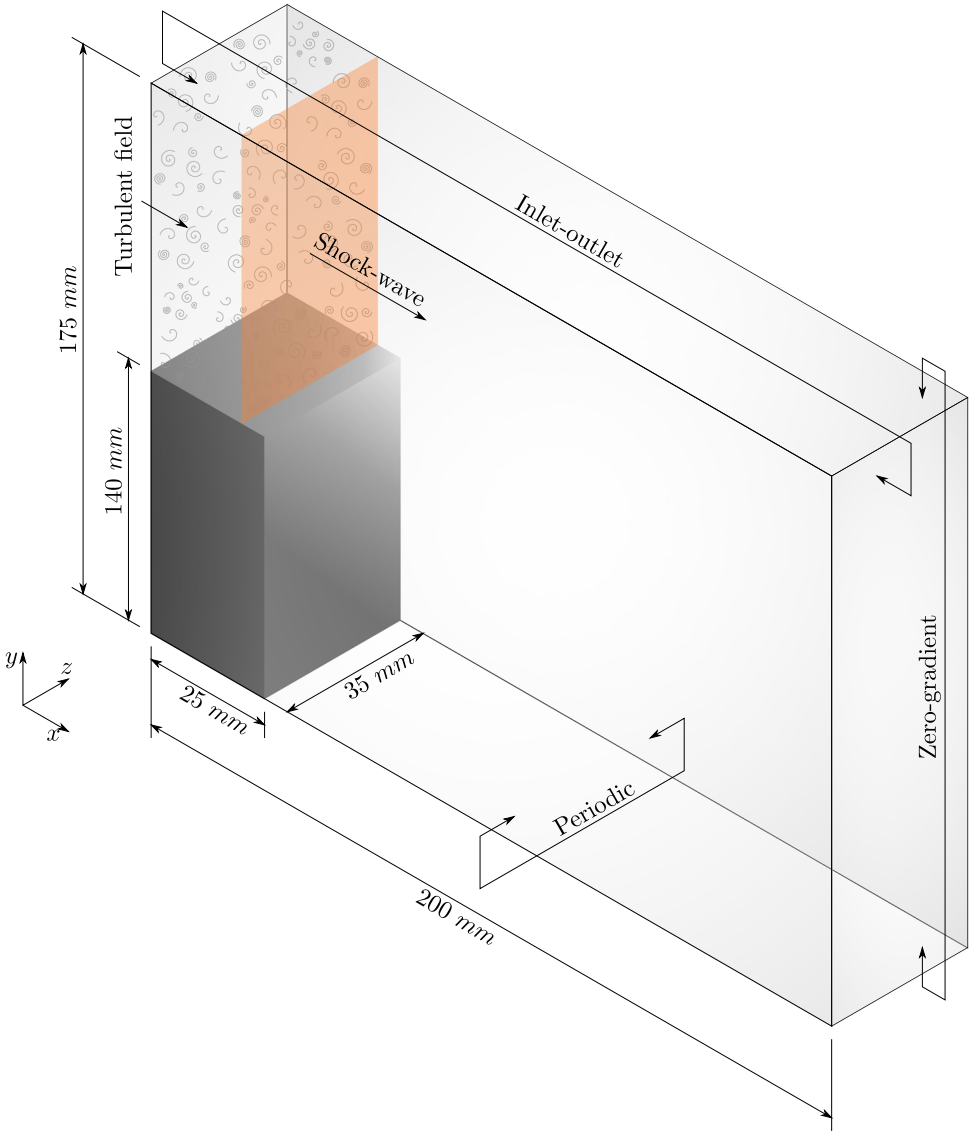

FIG. 1. Schematic diagram of the problem setup.

below. The resolved fluctuating component of any parameter is obtained by subtracting the spatially averaged (along the homogeneous z-direction) resolved quantity from the corresponding instantaneous resolved parameter as defined as $\phi'' = \widetilde{\phi} - \langle\widetilde{\phi}(x,y,t)\rangle$, where $\langle\widetilde{\phi}(x,y,t)\rangle = \frac{1}{L_z}\int_{L_z}\widetilde{\phi}\,dz$.

To reduce the complexity of the notation, the resolved quantities are expressed without overbar $\overline{(\cdot)}$ or tilde $\widetilde{(\cdot)}$ notation in most of the discussions below. This means $\widetilde{\phi}_i \equiv \phi_i$. To have better clarity, only the notations for the turbulent kinetic energy budget equation are presented with actual notations.

TABLE I. Simulation parameters.

Total no. of meshes	Δx (μm)	Δy (μm)	Δz (μm)	Final time t (μs)
3.3×10^9	52.6	51.4	136.7	757.75

IV. RESULTS AND DISCUSSIONS

A. General description and validation

The shock diffraction over 90° diffraction corner is associated with complex coupled interactions like shock-vortex, shock-boundary layer, vortex-vortex, and shock-shock interactions. Studies in the literature show that, 2D Euler predictions sufficiently agree with the early stage of the general shock dynamics but suffers from inability to resolve secondary vortex formation due to boundary layer interactions with the wall shock. Nevertheless, high-resolution 2D Navier-Stokes simulations with consideration of viscous/turbulent effects can predict these behaviors well.[19,29] This

canonical benchmark problem of diffraction is being studied in the literature by several authors, but no 3D numerical studies are available to account for the long-time behavior of turbulent flow structures. Experimental observations show existence of these 3D structures (see Refs. 25 and 26). The LES performed in this study demonstrates these structures. The early and later stages shock dynamics and the complex interactions are presented in Fig. 2 and compared favorably with the experimental results. Especially, the present LES resolved the intricate turbulent structures illustrated by the numerical schlieren pictures. A detailed analysis of turbulent flow features is presented in Secs. IV B–IV E.

The convective Mach number $\left(M_c = \frac{U_1 - U_c}{a_1} = \frac{U_c - U_2}{a_2}\right)$ at various locations at $t = 757.75\ \mu s$ is found to be 0.53 at A*, 0.43 at B*, 0.29 at C*, and 0.16 at D* (see Fig. 3 for the locations of the measurements of M_c). Here, $U_c = \frac{a_1 U_2 + a_2 U_1}{a_1 + a_2}$. Also, U_1 and U_2 are the free stream velocities across the shear layer, and a_1 and a_2 are the respective speeds of the sound. The shear layer behavior shows prominent compressibility effects near the diffraction corner (A*) and progressively shifts toward near incompressible regime around D*.

We analyze the sufficiency of the domain length in the homogeneous direction via two-point autocorrelation function given by

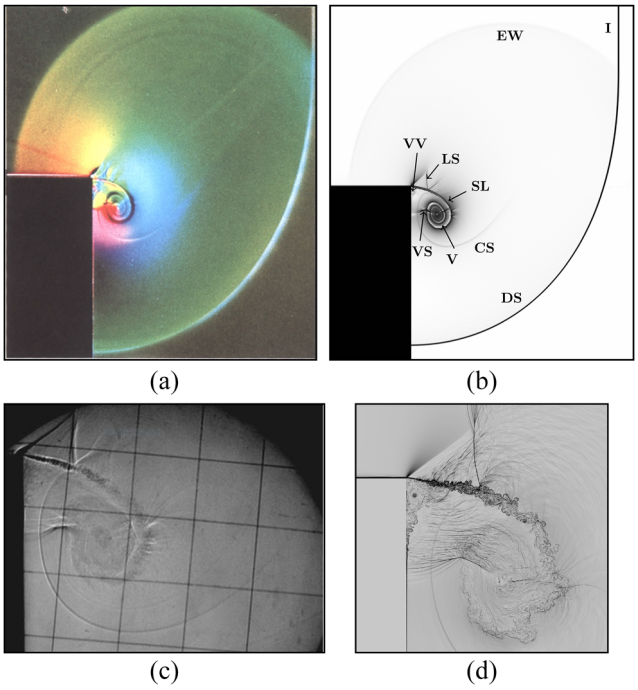

FIG. 2. Comparison of the flow features of the shock wave diffraction: top row: at early stage and bottom row: at later stage. See nomenclature. Figure (a) experiment, Takayama and Inoue.[24] [Reproduced with permission from K. Takayama and O. Inoue, "Shock wave diffraction over a 90 degree sharp corner–posters presented at 18th ISSW," Shock Waves **1**, 301–312 (1991). Copyright 1991 Springer-Verlag.] (b) Schlieren: present LES. Figure (c) experiment, Skews *et al.*[25] [Reproduced with permission from Skews *et al.*, "Shear layer behavior resulting from shock wave diffraction," Exp. Fluids **52**, 417–424 (2012). Copyright 2012 Springer-Verlag.] (d) Schlieren: present LES.

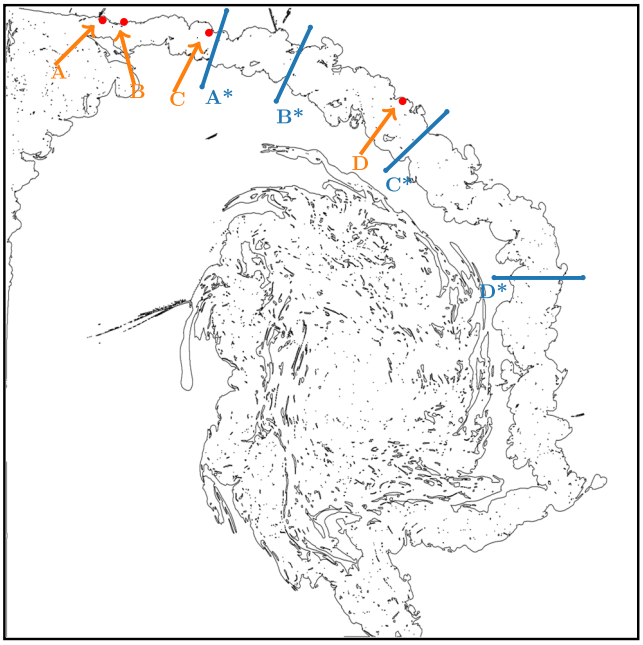

FIG. 3. Locations of probes/segments over a turbulent-nonturbulent interface (TNTI) contour for the computation of convective Mach number, two-point correlation, and normalized energy spectra.

$$R_{\phi\phi}(r_z) = \sum_{n=1}^{N_z} \phi''_n \phi''_{n+n_r}, \qquad n_r = 0, \ldots, N_z - 1;\ r_z = n_r \Delta z. \tag{1}$$

Figure 4 shows the autocorrelation distributions for velocity fluctuations at different probe locations A to D (see Fig. 3). The curves degenerate to near zero values within the half of the domain length in the homogeneous direction. The domain size is thus sufficient enough so that the periodic boundary condition does not inhibit the turbulence in the spanwise z-direction.

The accuracy of the LES is further checked by computing the normalized energy spectra of the fluctuating velocity components. These are shown in Fig. 5 together with the −5/3 law. These spectra show similar behavior of the peak values and exhibit drop off of about two decades. The large turbulent scales of the flow features are well resolved by the current LES, and SGS dissipation takes into account the dissipation effects of very fine scales. The effectiveness of the WALE model and SGS activity are illustrated in Subsection IV B.

Figure 6 shows the locus of the vortex centroid and the comparison with the previous 2D numerical results of Sun and Takayama.[6] The wall shock for the present case is of Type-N as classified in the work of Matsuo *et al.*[3] Note that an excellent agreement of the shape of the wall shock with the experimental results of Skews[30] is predicted by the present simulation. The circulation, $\Gamma = \int_s \omega\ d\boldsymbol{s}$, is computed over the 3D interaction region and is illustrated in Fig. 7. The circulation rate is nondimensionalized with the property of the air at the stagnant state, $RT = 287 \times 288\ \mathrm{m}^2/\mathrm{s}^2$. The nondimensional circulation is found to be attaining a saturation value of ≈1.2. However, Sun and Takayama[7] reported a circulation rate of 1.36 based on their 2D study.

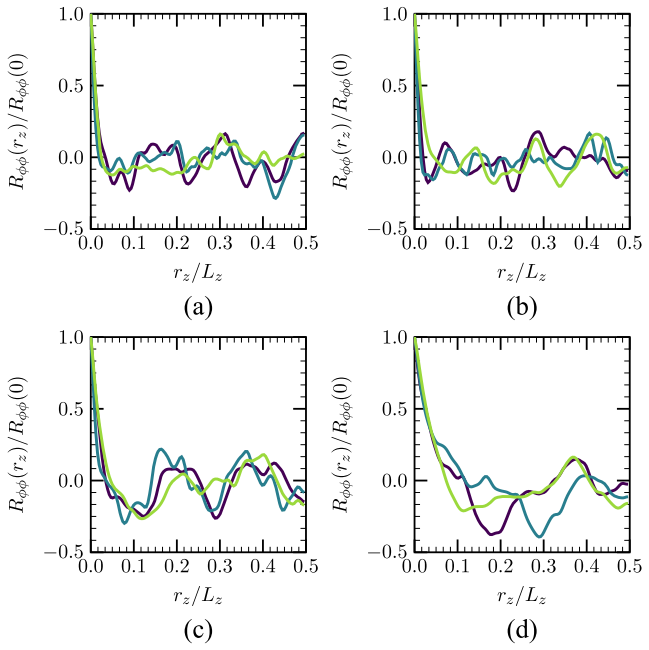

FIG. 4. Two-point correlation evaluation at $t = 757.75\ \mu s$: (a) location A, (b) location B, (c) location C, and (d) location D. Violet solid curve: u, dark green solid curve: v, and light green solid curve: w.

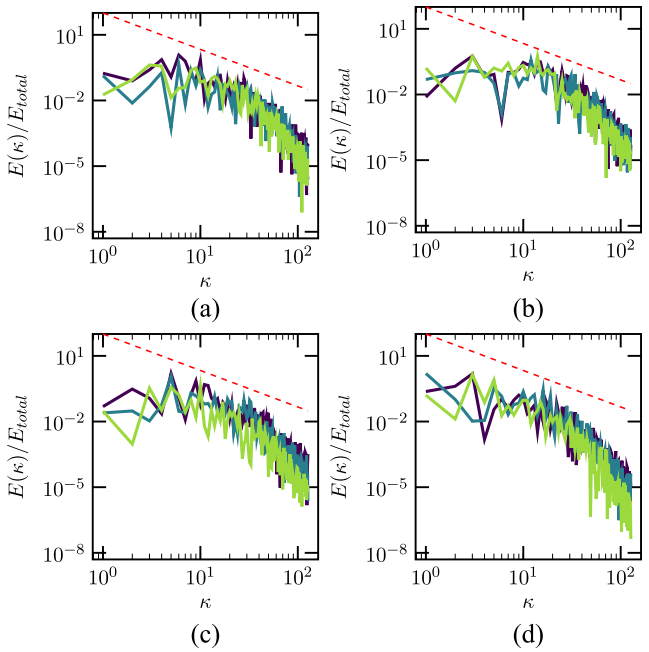

FIG. 5. Normalized energy spectra with wavenumber κ, at $t = 757.75\ \mu s$ in the homogeneous direction: (a) location A, (b) location B, (c) location C, and (d) location D. Violet solid curve: u, dark green solid curve: v, light green solid curve: w, and red short-dashed curve: $-5/3$ law.

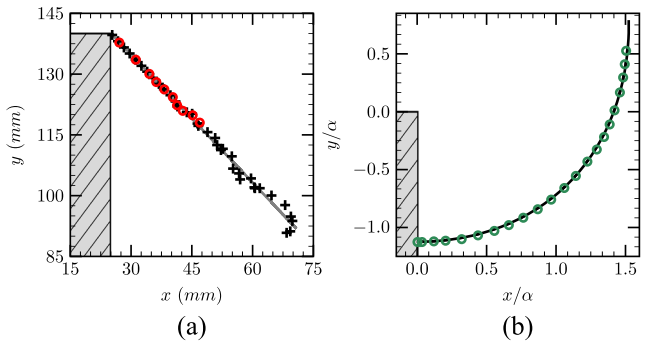

FIG. 6. (a) Location of the vortex centroid. Black plus sign: centroid path (simulation), gray solid curve: mean path, and red open circle: numerical data.[6] (b) Diffracted shock wave location (here, $\alpha = a_0 t$, where a_0 is the speed of sound at the stagnant state). Black solid curve: simulation data and green open circle: experimental data.[30]

The turbulent and nonturbulent regions for different turbulent flows are separated by a distinct boundary having several interesting characteristics like entrainment, abrupt changes in turbulence properties and intermittency. The shape of this interface is influenced by all scales of turbulence, in general. Vorticity norm or passive scalar concentration or concentration field can be used to define this turbulent-nonturbulent interface (TNTI).[31–36] To do this, we use the mean magnitude of the vorticity at each x-y plane. The 30% of it is then set as the threshold value to define a TNTI parameter as $\mathrm{TNTI}_z = 0.3\overline{|\omega|}_z,\ z = 1, \ldots, N_z$. A location is considered inside the turbulent region if the magnitude of its local vorticity is higher than the TNTI_z in that x-y plane. Figure 3 depicts the inner turbulent region covered by the TNTI surface at $t = 757.75\ \mu s$. The choice of the threshold value is intuitive, and these contours effectively identify the vortex dominated turbulent regions for further analysis. The irrotational engulfed pockets are also visible in this figure. Rotational dominated regions of the flow field can be illustrated from the normalized Q-criteria,[37,38] $\Lambda = \frac{W_{ij}W_{ij} - S_{ij}S_{ij}}{W_{ij}W_{ij} + S_{ij}S_{ij}}$, where $S_{ij} = 1/2(\partial u_i/\partial x_j + \partial u_j/\partial x_i)$ is the strain-rate tensor and $W_{ij} = 1/2(\partial u_i/\partial x_j - \partial u_j/\partial x_i)$ is the rotation-rate tensor. The positive isosurfaces of Λ shown in Fig. 8 illustrate the vortex tubes and 3D turbulent flow features.

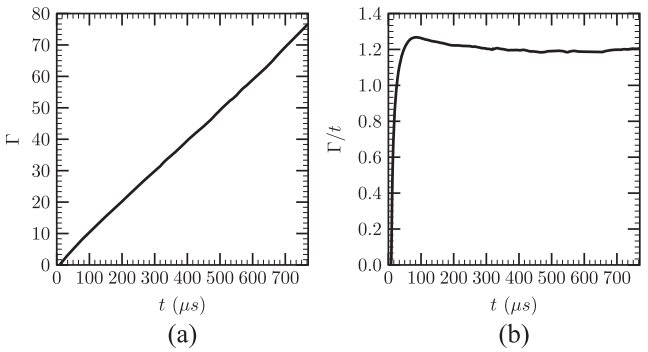

FIG. 7. Time evolution of (a) circulation (Γ) and (b) circulation rate (Γ/t).

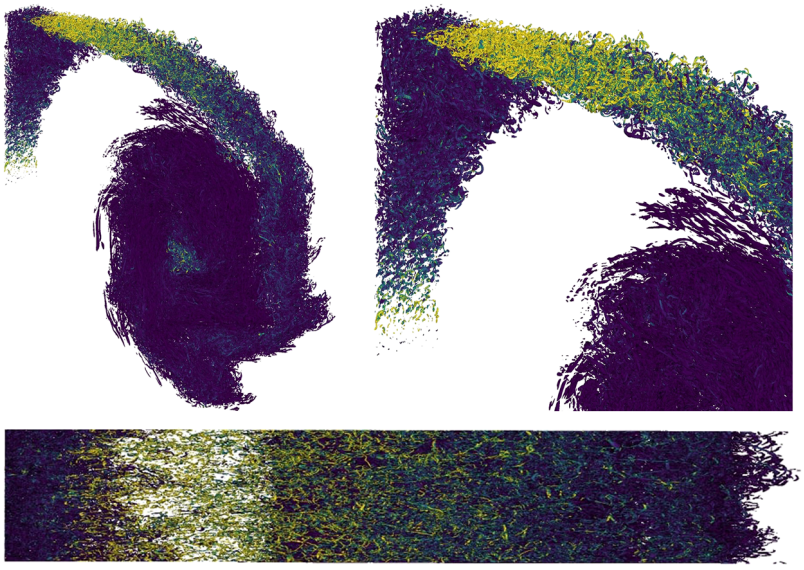

FIG. 8. Isosurfaces of $\Lambda = 0.5$ at $t = 757.75$ μs colored with the enstrophy.

B. SGS model assessment

In this section, we present the relative contribution of SGS dissipation and assess the effectiveness of the WALE model. The ratio of μ_{sgs}/μ is the measure of effectiveness of the LES model. Figure 9 shows the time evolution of the spatially averaged contours of μ_{sgs}/μ (averaged in the homogeneous z-direction) in the interaction zone. The ratio, $\mu_{sgs}/\mu \leq 5$, indicates that the grid resolution and the contribution of SGS viscosity are in the acceptable range for well resolved LES. The SGS modeled dissipation ε_{sgs} can be defined as[28] the summation of contribution of fluctuating flow-field to SGS dissipation and the contribution of mean flow-field to SGS dissipation as

$$\varepsilon_{sgs} = \varepsilon''_{sgs} + \varepsilon_{\langle sgs\rangle}. \tag{2}$$

The contribution of fluctuating flow-field to SGS dissipation approximated as

$$\varepsilon''_{sgs} \approx -2\langle \mu_{sgs} S''^{*}_{ij} S''_{ij}\rangle, \tag{3}$$

where $S''_{ij} = \frac{1}{2}\left(\frac{\partial u''_i}{\partial x_j} + \frac{\partial u''_j}{\partial x_i}\right)$ and $S''^{*}_{ij} = S''_{ij} - \frac{1}{3}S''_{kk}\delta_{ij}$.

The contribution of mean flow-field to SGS dissipation can be expressed as

$$\varepsilon_{\langle sgs\rangle} \approx -2\langle \mu_{sgs}\rangle\langle S^{*}_{ij}\rangle\langle S_{ij}\rangle, \tag{4}$$

where $\langle S_{ij}\rangle = \frac{1}{2}\left(\frac{\partial\langle u_i\rangle}{\partial x_j} + \frac{\partial\langle u_j\rangle}{\partial x_i}\right)$ and $\langle S^{*}_{ij}\rangle = \langle S_{ij}\rangle - \frac{1}{3}\langle S_{kk}\rangle\delta_{ij}$.

The details of these approximations can be found in the work of Ben-Nasr *et al.*[28] and Davidson.[39]

Figure 10 shows the different SGS dissipation parameters (averaged in the homogeneous z-direction) in the interaction zone at different time instants. It can be seen from this figure that ε''_{sgs} contributes more toward ε_{sgs} compared to $\varepsilon_{\langle sgs\rangle}$. The contours of $\frac{\varepsilon_{sgs}}{\varepsilon}$ show a similar range of values of μ_{sgs}/μ as mentioned before. This corroborates the fact that the mesh resolution in the shear layer region is sufficient for this LES study. The modeling effectivity of a LES can also be quantified with the SGS activity parameter as defined by

$$\zeta = \frac{\varepsilon_{sgs}}{\varepsilon_{sgs} + \varepsilon}, \tag{5}$$

where the resolved molecular dissipation $\varepsilon = \left\langle \tau'_{ij}\frac{\partial u'_i}{\partial x_j}\right\rangle$. Evidently, $0 \leq \zeta < 1$, and the lower the value of ζ the more resolved is the LES. It could be noted that the vortex core region is very well resolved by the current LES. These are in accordance with the 3D flow

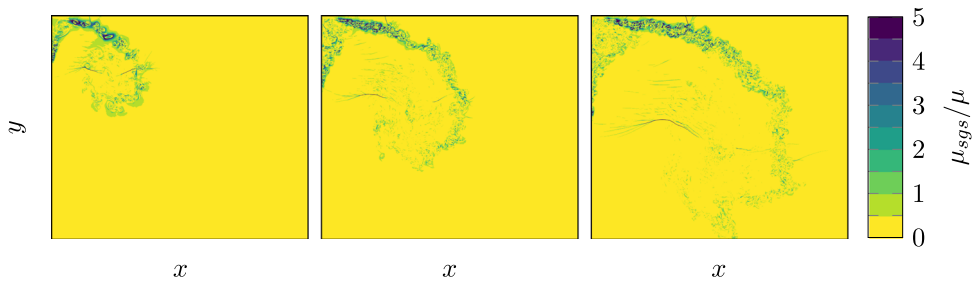

FIG. 9. μ_{sgs}/μ of a slice at $t = 339.75$, 537.75, and 757.75 μs column-wise, respectively.

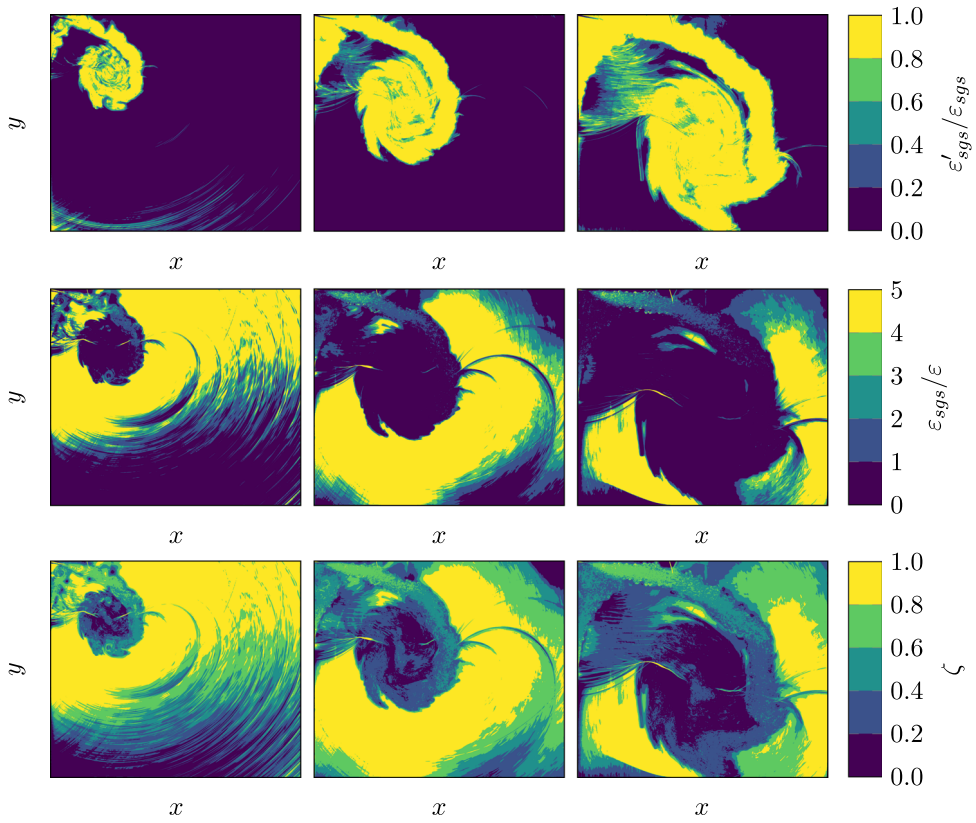

FIG. 10. Different subgrid-scale dissipation terms at t = 339.75, 537.75, and 757.75 μs column-wise, respectively.

visualization of resolved flow structures illustrated with the isosurfaces of $\Lambda = 0.5$ in Fig. 8.

C. Analysis on the local flow topology

The flow topology analysis based on the turbulent/nonturbulent interface (TNTI) which separates the inner core of the turbulent region from the neighborhood of the irrotational regions is much revealing and enriching to characterize the zonal turbulent flow structures. The literature shows that the locally compressed regions in a turbulent flow field are dominated by stable topological structures, while the locally expanded regions are mainly unstable in nature and more dissipative. In this section, we present the flow topology associated with the dynamics of the shear layer at the 90° diffraction corner. The invariants of the velocity (resolved) gradient tensor (P, Q, and R) are given by

$$\boldsymbol{P} = -S_{ii}, \tag{6}$$

$$\boldsymbol{Q} = \frac{1}{2}(\boldsymbol{P}^2 - S_{ij}S_{ji} - W_{ij}W_{ji}), \tag{7}$$

$$\boldsymbol{R} = \frac{1}{3}(-\boldsymbol{P}^3 + 3\boldsymbol{P}\boldsymbol{Q} - S_{ij}S_{jk}S_{ki} - 3W_{ij}W_{jk}S_{ki}), \tag{8}$$

where S_{ij} and W_{ij} are strain-rate tensor and rotation-rate tensor as defined before.

It is well known that the $P - Q - R$ space is divided into several regions.[40–45] The discriminant surface $\mathscr{L}_1$, of the characteristic equation of the eigenvalues of the velocity gradient tensor, separates the region of real and complex eigenvalues. This can be further split into $\mathscr{L}_{1a}$ and $\mathscr{L}_{1b}$. All eigenvalues are real and equal at a location where these surfaces form a cusp. On the other hand, purely imaginary eigenvalues lie on the surface $\mathscr{L}_2$ [see Eq. (13)].

The second invariant of W_{ij} is given by

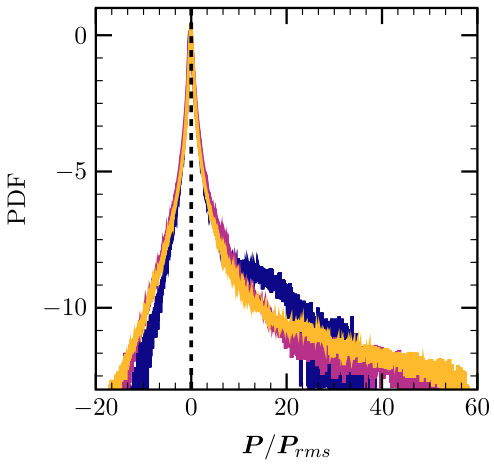

FIG. 11. PDF plot of the normalized first invariant of velocity gradient tensor in the entire turbulent region at t = 251.75 (violet solid curve), 449.75 (pink solid curve), and 757.75 (yellow solid curve) μs.

TABLE II. Quantification of the flow topology enclosed by TNTI as a percentage of their sample size.

Dilatation	Time (μs)	Quantity (% of TNTI)	Sample ($\times 10^6$)	UFC	UN/S/S	SN/S/S	SFS	SFC	UFS
	251.75	10.4	2.7	5.0	6.3	7.8	80.7	...	...
$P = 0 \pm 0.05$	449.75	9.8	8.5	3.2	3.7	2.2	90.9	...	...
	757.75	14	33.4	1.1	1.6	1.6	95.6	...	...
	251.75	0.2	0.05	11.6	7.1	48.1	21.8	9.8	...
$P = 3 \pm 0.25$	449.75	0.3	0.2	12.3	10.4	24.8	44.5	6.9	...
	757.75	0.2	0.4	10.8	10.2	17.2	55.9	5.8	...
	251.75	0.1	0.03	18.7	25.1	4.7	24.8	...	23.9
$P = -3 \pm 0.25$	449.75	0.2	0.2	17.7	30.8	2.6	30.7	...	16.9
	757.75	0.1	0.3	16.9	34.1	3.3	31.1	...	12.9

$$\boldsymbol{Q_w} = -\frac{1}{2} W_{ij} W_{ji}. \tag{9}$$

The surfaces dividing the $P - Q - R$ space are

$$\mathscr{L}_1 = 27\boldsymbol{R}^2 + (4\boldsymbol{P}^3 - 18\boldsymbol{PQ})\boldsymbol{R} + (4\boldsymbol{Q}^3 - \boldsymbol{P}^2\boldsymbol{Q}^2) = 0, \tag{10}$$

$$\mathscr{L}_{1a} = \frac{1}{3}\boldsymbol{P}\left(\boldsymbol{Q} - \frac{2}{9}\boldsymbol{P}^2\right) - \frac{2}{27}\left(-3\boldsymbol{Q} + \boldsymbol{P}^2\right)^{3/2} - \boldsymbol{R} = 0, \tag{11}$$

$$\mathscr{L}_{1b} = \frac{1}{3}\boldsymbol{P}\left(\boldsymbol{Q} - \frac{2}{9}\boldsymbol{P}^2\right) + \frac{2}{27}\left(-3\boldsymbol{Q} + \boldsymbol{P}^2\right)^{3/2} - \boldsymbol{R} = 0, \tag{12}$$

$$\mathscr{L}_2 = \boldsymbol{PQ} - \boldsymbol{R} = 0. \tag{13}$$

We summarize the nomenclature of the invariants and various 3D critical points in the nomenclature section.

The evolution of the probability density function (PDF) of the first invariant of the velocity gradient tensor is shown in Fig. 11. A self-similar behavior with highly peaked distribution has been found. A large positive skewness of the distributions clearly depicts the similar behavior observed in the compressible isotropic turbulence and compressible mixing layer turbulence of the literature.[42] The JPDFs of the $Q - R$ are shown for constant P planes. Three representative values of P are chosen to distinguish the features of locally incompressible, compressed, and expanded regions in the flow-field. Here, Q and R are normalized with Q_w and $Q_w^{3/2}$ in these figures. Table II summarizes all the quantities of the local flow topology for different dilatation levels at different time instants. Evidently, the sample size is large at a later time instant. Note that the percentage of TNTI is large for $P = 0$ compared to locally compressed and expansion regions. This corroborates with highly peaked distribution of PDF of P mentioned before. For incompressible turbulent flows ($P = 0$), the JPDF of second and third invariants (Q and R) of

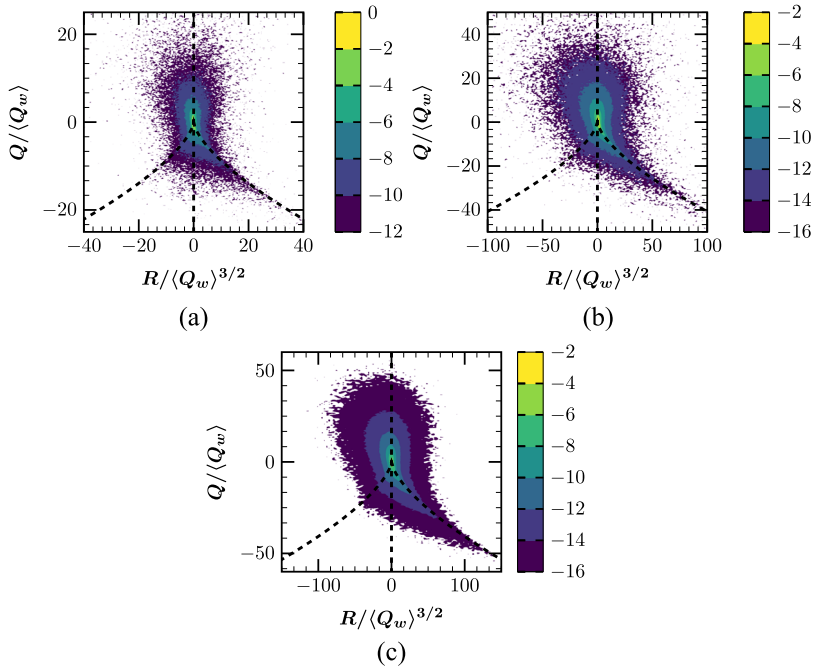

FIG. 12. JPDF plot of the normalized second and third invariants of velocity gradient tensor in the entire turbulent (TNTI) region at t = 251.75, 449.75, and 757.75 μs for $\boldsymbol{P} = 0 \pm 0.05$.

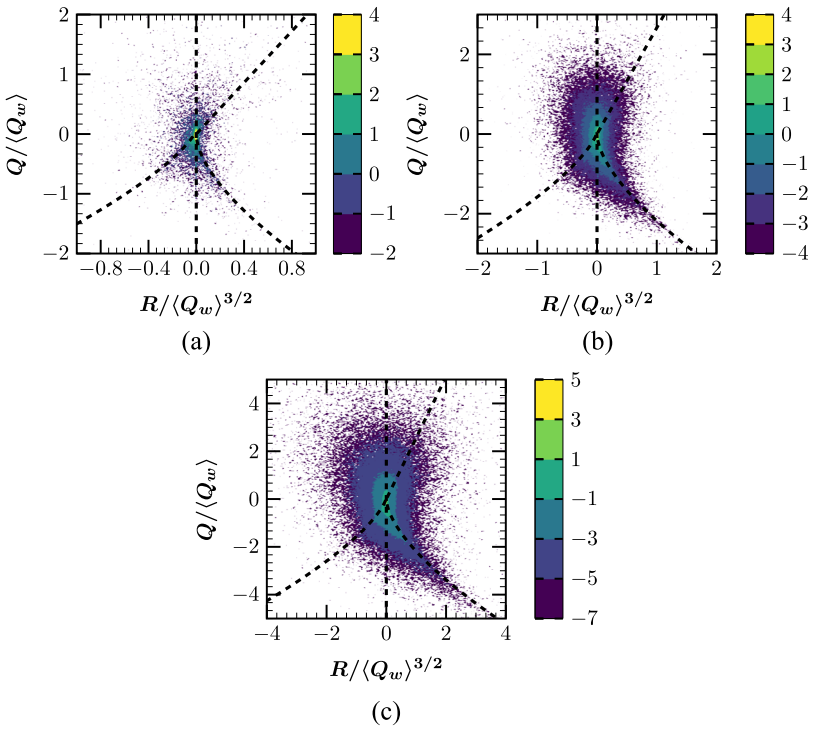

FIG. 13. JPDF plot of the normalized second and third invariants of velocity gradient tensor in the entire turbulent (TNTI) region at t = 251.75, 449.75, and 757.75 μs for P = 3 ± 0.25.

the velocity gradient tensor exhibits a typical tear drop shape (see Fig. 12). This signifies the universal small-scale structures of turbulence. The similar universal tear drop shape is also being found for compressible flows when the JPDF of second and third invariants of the anisotropic part of the deformation rate tensor is analyzed. This is similar to the characteristics of incompressible turbulence, compressible isotropic turbulence, compressible turbulent boundary layer, and compressible mixing layer turbulence. Clearly, the SFS

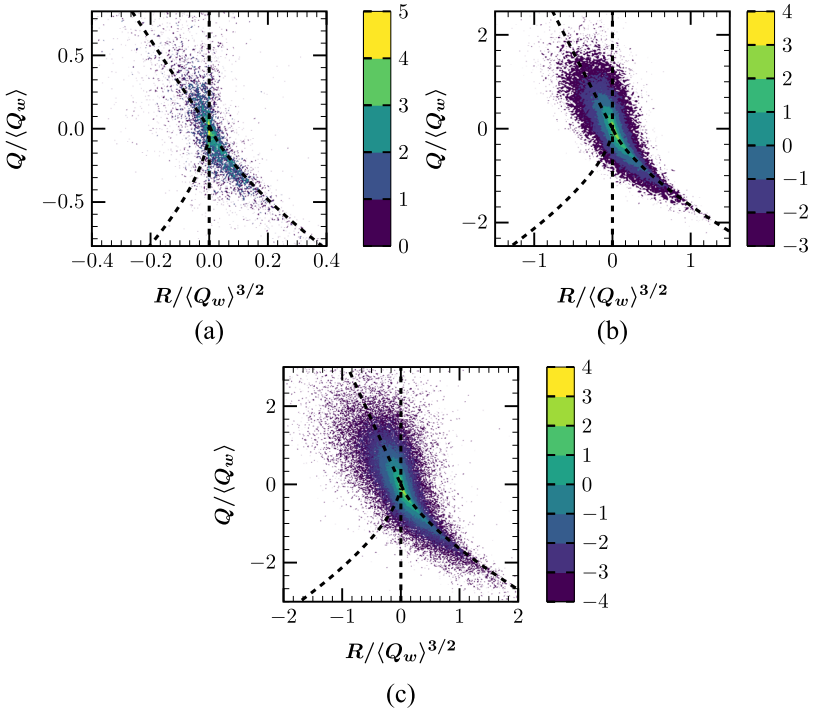

FIG. 14. JPDF plot of the normalized second and third invariants of velocity gradient tensor in the entire turbulent (TNTI) region at t = 251.75, 449.75, and 757.75 μs for P = −3 ± 0.05.

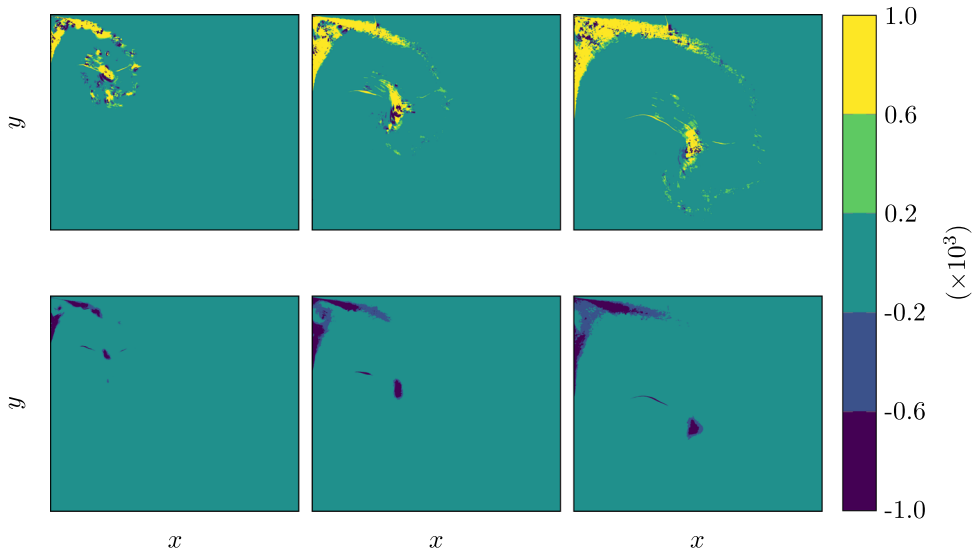

FIG. 15. TKE budget. Row-wise (top-to-bottom): production and dissipation terms. Column-wise (left-to-right): t = 339.75, 537.75, and 757.75 μs.

structure dominates throughout the evolution with an increasing trend of the SFS structure with time (95.5% at 757.75 μs).

Figure 13 depicts JPDFs of $Q - R$ for locally compressed regions. The shape of these distributions evolves to nearly tear drop shape. However, it can be seen from Table II, that a dramatic distribution of the topologies is existent. Initially, we observe dominant nonfocal stable structures (48.1% of SN/S/S). Most of the structures remain stable for compressed regions. Nevertheless, the unstable structures are also found to be present. The initial SN/S/S structures shifts toward SFS structures. Although, there exist some more unstable structures compared to locally incompressible regions, the stable structures are predominant in locally compressed regions.

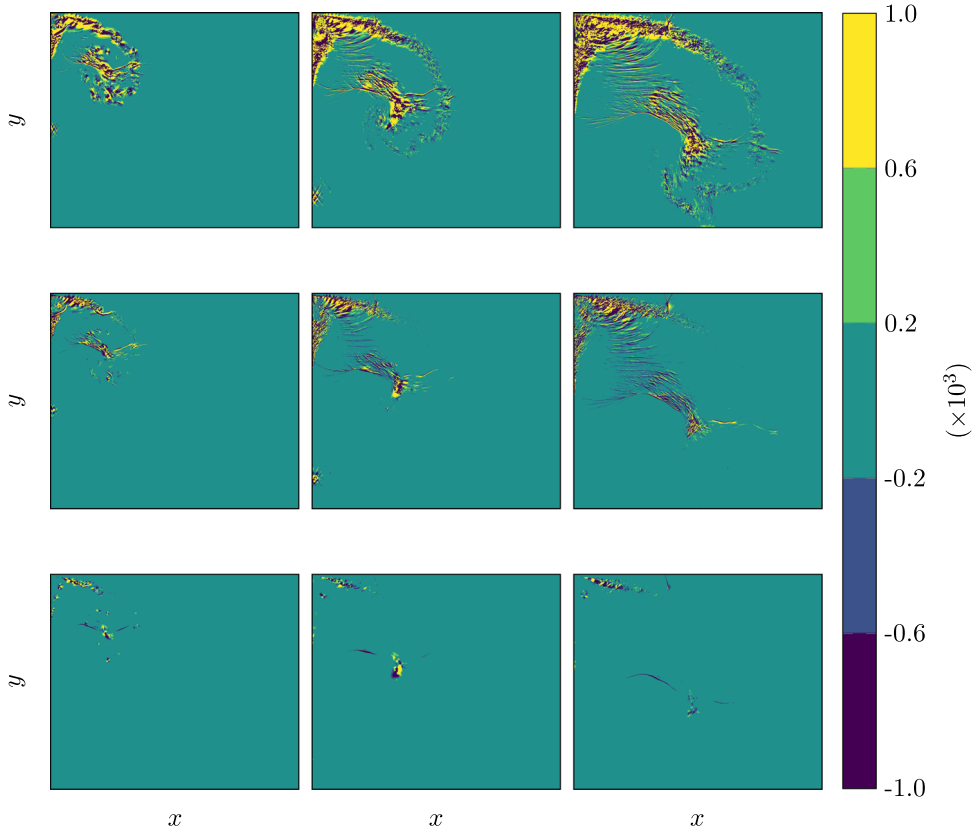

FIG. 16. TKE budget. Row-wise (top-to-bottom): diffusion, pressure-dilatation, and pressure-work terms. Column-wise (left-to-right): t = 339.75, 537.75, and 757.75 μs.

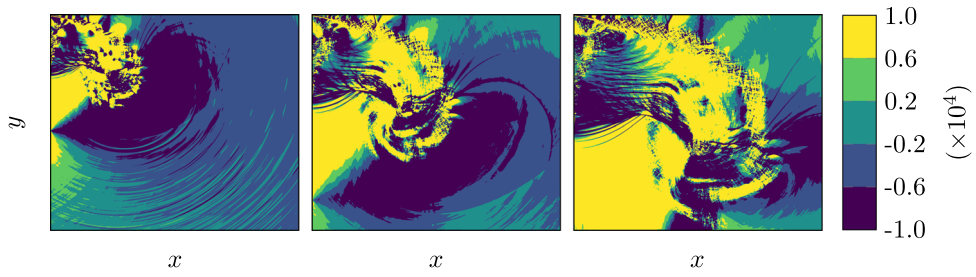

FIG. 17. TKE budget—advection term. Column-wise (left-to-right): t = 339.75, 537.75, and 757.75 μs.

Figure 14 shows the JPDFs for locally expanded regions. The distributions are found to be skewed toward the surface $\mathscr{L}_2$, and most of the flow structures show unstable nature. The present analysis reveals the absence of UFS for the locally compressed region and the absence of SFC for locally expanded regions. UN/S/S structures eventually become predominant in these regions. The unstable structures indeed become significant for locally expanded regions. It can be realized that the local streamlines in stable topologies are convergent toward critical points, and for unstable topologies, the local streamlines are divergent from the critical points.

D. Analysis of the turbulent kinetic energy

The Favre averaged transport equation of turbulent kinetic energy (TKE) is given by

$$\underbrace{\frac{\partial \bar{\rho} k}{\partial t} + \frac{\partial \bar{\rho}\tilde{u}_j k}{\partial x_j}}_{\mathcal{A}} = \underbrace{-\langle \rho u_i'' u_j'' \rangle \frac{\partial \tilde{u}_i}{\partial x_j}}_{\mathcal{P}} \underbrace{-\left\langle \tau_{ji} \frac{\partial u_i''}{\partial x_j} \right\rangle}_{\mathcal{D}} + \underbrace{\frac{\partial}{\partial x_j}\left(\langle \tau_{ji} u_i'' \rangle - \left\langle \rho u_j'' \frac{1}{2} u_i'' u_i'' \right\rangle - \langle p' u_j'' \rangle \right)}_{\mathcal{D}_f} \underbrace{-\langle u_i'' \rangle \frac{\partial \bar{p}}{\partial x_i}}_{\mathcal{P}_w} \underbrace{+\left\langle p' \frac{\partial u_i''}{\partial x_i} \right\rangle}_{\mathcal{P}_d}, \tag{14}$$

where $\mathcal{P}$ is the production term, $\mathcal{D}$ is the dissipation term, $\mathcal{D}_f$ is the diffusion term, $\mathcal{P}_w$ is the pressure-work term, $\mathcal{P}_d$ is the pressure-dilatation term, and $\mathcal{A}$ is the advection term. Note that we kept the overbar $\overline{(\cdot)}$ or tilde $\widetilde{(\cdot)}$ notation here for better clarity.

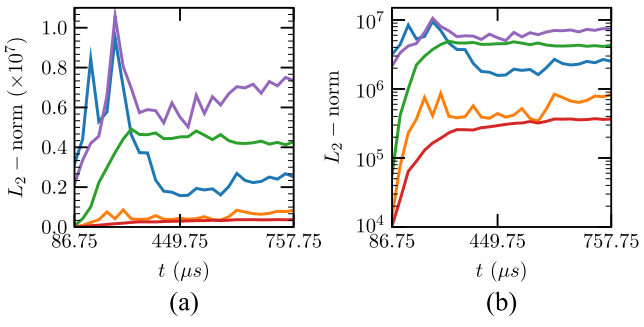

FIG. 18. Norm of TKE budget terms as a function of time (a) linear-scale and (b) logarithmic-scale. Blue solid curve: pressure-dilatation, orange solid curve: pressure-work, green solid curve: production, red solid curve: dissipation, and violet solid curve: diffusion.

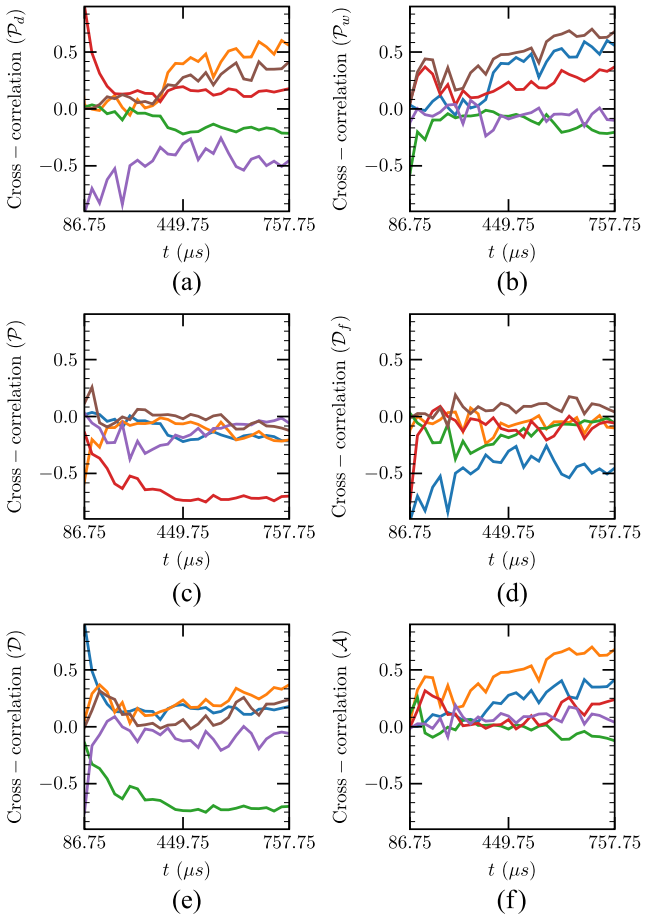

FIG. 19. Spatial cross-correlation of (a) pressure-dilatation ($\mathcal{P}_d$), (b) pressure-work ($\mathcal{P}_w$), (c) production ($\mathcal{P}$), (d) diffusion ($\mathcal{D}_f$), (e) dissipation ($\mathcal{D}$), and (f) advection ($\mathcal{A}$) terms of TKE budget with each other in time. Blue solid curve: pressure-dilatation, orange solid curve: pressure-work, green solid curve: production, red solid curve: dissipation, violet solid curve: diffusion, and brown solid curve: advection.

The spatially averaged contours of these resolved terms are shown in Figs. 15–17. The behavior of the TKE budget terms of the shear layer region is found to be typically similar to the compressible mixing layers (see Ref. 38). These contours also show the out of equilibrium behavior of the turbulent flow linked with the transient flow evolution. The pressure dilatation and pressure work terms are associated with the regions of the shear layer near the diffraction corners (having high convective Mach numbers) as well as regions where the interactions of the shocklets and the core of the vortex are significant. It can be seen that sporadic patches of negative production of turbulent kinetic energy are also predicted. These are associated with the regions with shear layer/vortex interactions with local compressions/expansions.[27,46,47] We analyze the time evolution of the magnitude of these terms and their cross-correlations within the spatially averaged two dimensional turbulent region bounded by the TNTI. These are shown in Figs. 18 and 19. At the early stage, the pressure dilatation term remains important, and the diffusion term plays a major role in the later stage. Diffusion, production, and pressure dilatation terms are found to be nearly one order of magnitude higher than pressure work and dissipation. Note that the pressure dilatation is more correlated with dissipation term at the beginning and evolves to a state with more correlated with pressure work at the later stage. The overall anticorrelation is evident between production and dissipation terms. Pressure dilatation and pressure work remain linked with dissipation. Noticeably, the diffusion term is found to be anticorrelated with the pressure dilatation term throughout the evolution. It can be realized that the diffusion terms interact with the outer regions of the shear layer through the edges of the shear layer. The advection term is found to be predominantly linked with pressure work apart from the other terms.

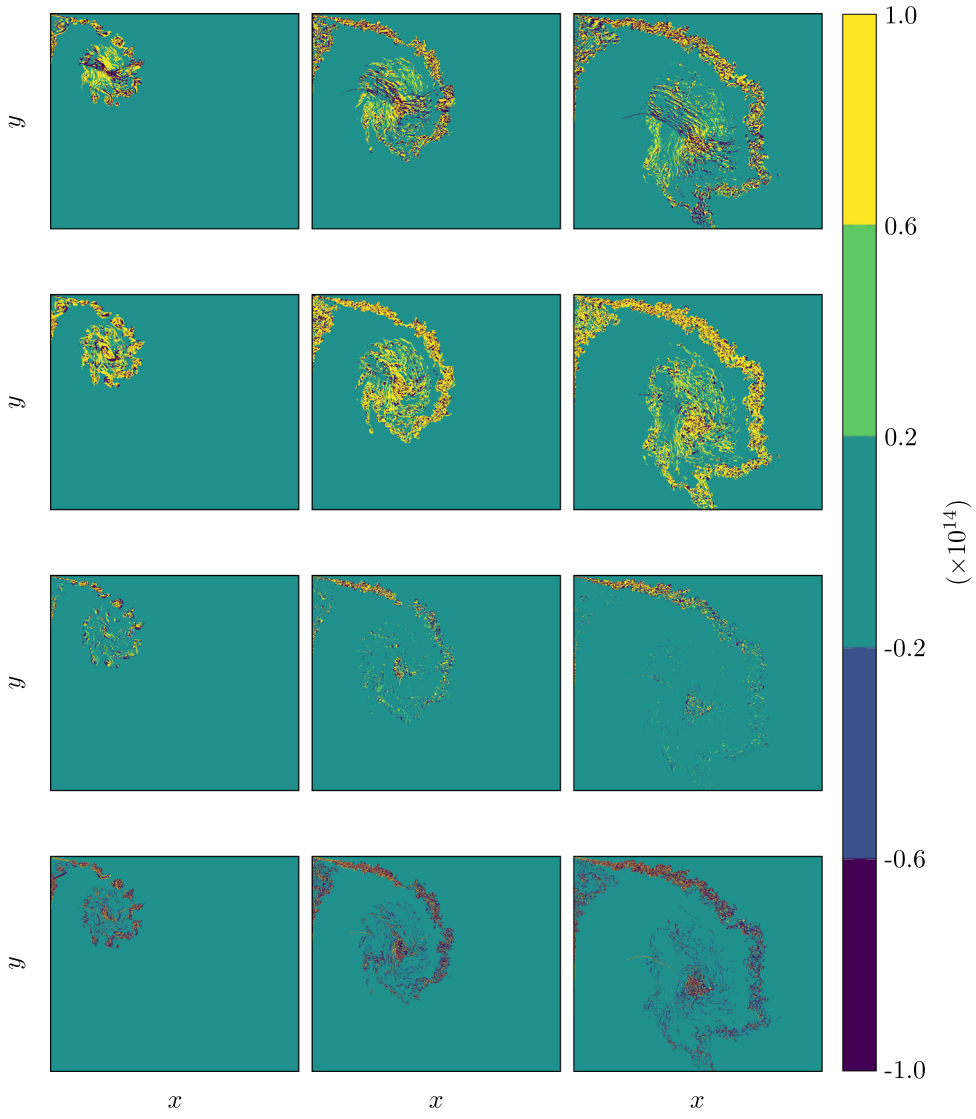

FIG. 20. VTE budget. Row-wise (top-to-bottom): VSC, VSG, baroclinic, and DFV terms. Column-wise (left-to-right): t = 339.75, 537.75, and 757.75 μs.

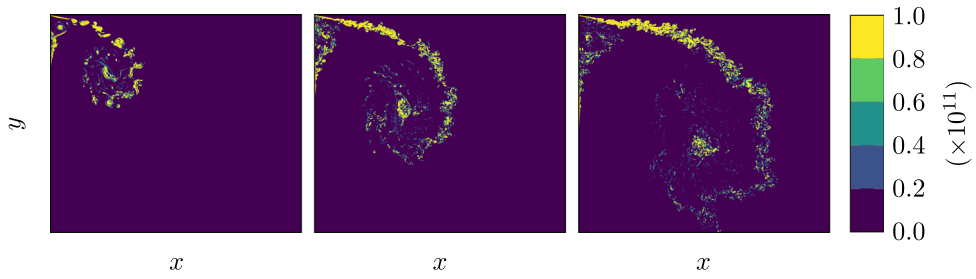

FIG. 21. Enstrophy contour. Column-wise (left-to-right): t = 339.75, 537.75, and 757.75 μs.

E. Analysis of the vorticity transport equation

We further analyze the budget terms of the mean vorticity transport equation [Eq. (15)] to shed light into the large scale structures and the mechanism of the complex flow evolution associated with the shock diffraction phenomena. The contribution of SGS terms can be assumed to be negligible for the mutual interactions among the relatively large vortical structures. The nomenclature of the different terms of the transport equation is summarized in the nomenclature section,

$$\frac{\partial \boldsymbol{\omega}}{\partial t} + (\boldsymbol{u}\cdot\nabla)\boldsymbol{\omega} = \underbrace{(\boldsymbol{\omega}\cdot\nabla)\boldsymbol{u}}_{\mathcal{V}_g} - \underbrace{\boldsymbol{\omega}(\nabla\cdot\boldsymbol{u})}_{\mathcal{V}_c} + \underbrace{\frac{1}{\rho^2}\nabla\rho\times\nabla p}_{\mathcal{B}} + \underbrace{\nabla\times\left(\frac{\nabla\cdot\tau}{\rho}\right)}_{\mathcal{D}_v}. \tag{15}$$

The evolution of the contours of these terms is shown in Fig. 20. VSC, VSG, DFV, and baroclinic terms interplay during the evolution process. From the VSC contour, it is clear that there are locally stretched structures in the core region of the vortex due to compressibility effect arising from local regions of compression/expansion. The evolution of enstrophy is illustrated in Fig. 21. This corroborates to saturation of the magnitude of the enstrophy. The time evolution of the magnitude of these terms and their cross-correlations within the 3D turbulent region bounded by the TNTI are analyzed further. Note that the magnitude of the VSG term and VSC term is nearly one order of magnitude higher compared to the baroclinic term and DFV term (see Fig. 22). Indeed, VSG plays a major role transferring the turbulent energy from large scales to small scales in flows at high Reynolds number as found in the work of Cottet *et al.*[48]

Positive correlation of VSG and VSC is observed (see Fig. 23). However, enstrophy is found to be predominantly correlated with VSG compared to VSC. Furthermore, viscous effects via DFV term are anticorrelated with enstrophy. DFV is also found to be anticorrelated with VSG, which is in accordance with the contours shown in Fig. 20.

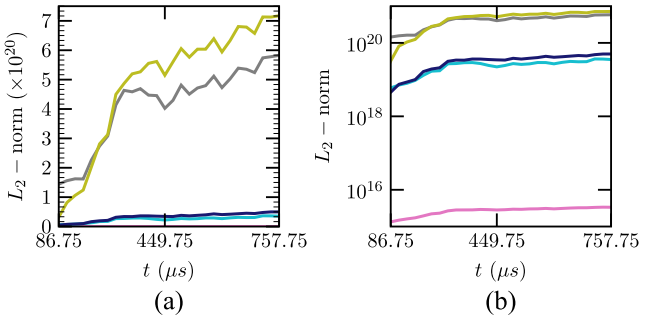

FIG. 22. Norm of VTE budget terms as a function of time (a) linear-scale and (b) logarithmic-scale. Pink solid curve: enstrophy, gray solid curve: VSC, light green solid curve: VSG, sky blue solid curve: baroclinic, and blue solid curve: DFV.

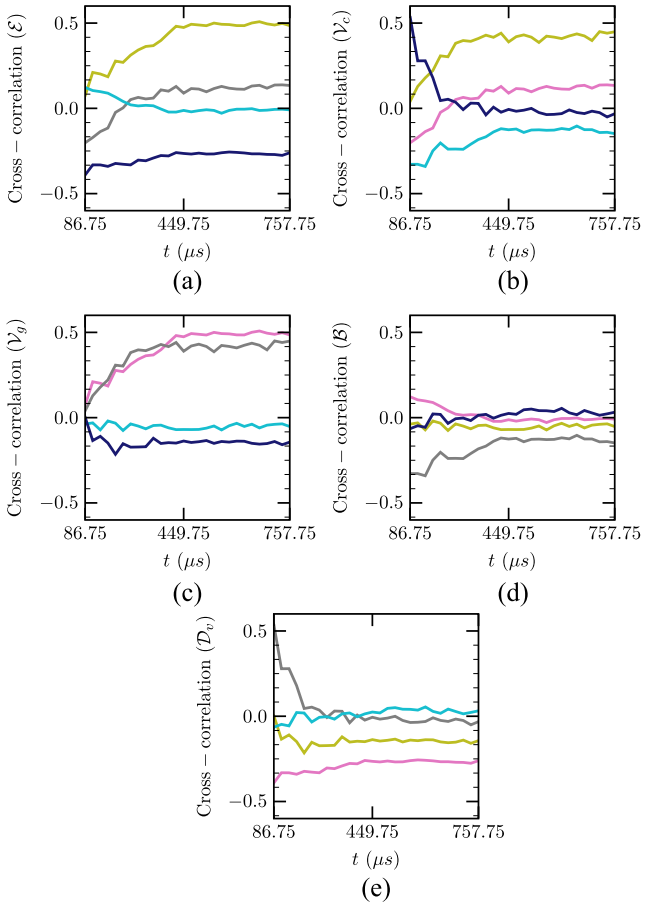

FIG. 23. Spatial cross-correlation of (a) enstrophy ($\mathcal{E}$), (b) VSC ($\mathcal{V}_c$), (c) VSG ($\mathcal{V}_g$), (d) baroclinic ($\mathcal{B}$), and (e) DFV ($\mathcal{D}_v$) terms of VTE budget with each other in time. Pink solid curve: enstrophy, gray solid curve: VSC, light green solid curve: VSG, sky blue solid curve: baroclinic, and blue solid curve: DFV.

V. CONCLUSION

In this work, we presented a 3D analysis of turbulent flow features originating from a shock wave diffraction over 90° convex corner that has never been attempted before. The intricate features of the viscous effects, shock boundary layer interactions, and shock shear layer interactions are well addressed by this analysis. LES with the WALE model together with high-order numerical schemes (fifth order WENO for inviscid, sixth order central differencing for viscous fluxes, and third order explicit Runge-Kutta scheme for the time advancement) is chosen to resolve the complex flow scales. The in-house parallel solver used 3.3×10^9 cells to resolve the flow structures. The general dynamics of vortex core and shape of the Type-N wall shock has been compared with the literature data[30] favorably. The chosen domain size in the spanwise direction is demonstrated to be sufficient enough through the behavior of autocorrelation functions. The effectiveness of the LES model and the mesh resolution characteristics are quantified by SGS viscosity and SGS dissipation. The 3D flow visualization with rotation dominated regions by normalized Q criteria shows the quality of the current well resolved LES. The 3D instantaneous field resembles the turbulent scale structures observed in the experimental findings.[25] We performed a flow topology analysis based on TNTI. The JPDFs of the second and third invariants (Q and R) of the velocity gradient tensor are used for constant (first invariant) P planes for this purpose. Locally, incompressible regions exhibit the teardrop shape of the PDF of Q and R indicating the universal nature of the resolved smaller scales of the turbulence. We found that SFS structures are dominating throughout the flow transients in these regions. SN/S/S structures remain predominant at the early stage in locally compressed regions, and at the later stage, the flow structures evolve to more SFS structures. Although unstable structures are found to be present relatively more compared to locally incompressible regions. On the other hand, we found mostly unstable structures at the locally expanded regions. The present analysis also reveals the absence of UFS for locally compressed region and the absence of SFC for locally expanded regions. Neglecting the SGS contributions, the turbulent kinetic energy budget terms are analyzed with only resolved parameters. This reveals that the pressure dilatation is important at the early stage, while turbulent diffusion becomes important at later stages and the diffusion term exhibits anticorrelation with the pressure dilatation term throughout the flow evolution. Furthermore, the relative contribution of the constituent terms of the resolved mean vorticity transport equation is analyzed. The VSC and VSG plays an important role compared to DFV, and baroclinic term and enstrophy are predominantly correlated with VSG compared to VSC.

The 2D viscous simulations of shock-wave diffraction over 90° sharp corner with a high resolution numerical scheme can predict the basic shock diffraction wave pattern, main vortex, secondary viscous vortex associated with the wall shock interaction with the boundary layer, shear layer, and lambda shocks observed in the experiments specially at the early stage of the evolution. However, 2D simulations are limited to resolve the inherent 3D nature of the turbulent flow features and together with the small-scale dissipation. The present 3D LES captures the 3D turbulent scales, embedded shocks/shocklets within the main vortex and the shear layer behavior and boundary layer interactions in the viscous vortex region. The spatio-temporal growth of the shear layer is strongly influenced by the lambda shock as well as by the counterclockwise rotating viscous vortex near the diffraction corner. Apparently, the lambda-shock-shear-layer interaction at the upper side of the shear layer is more intense than that of the interaction of the contact surface at the bottom side of the shear layer. Note that the foot of the lambda shock more effectively perturbs the shear layer and increases its growth. This aspect is clearly resolved in the present LES. The shape and large-scale structures of the turbulent envelop at the wall viscous vortex region is also satisfactorily predicted by the LES. A further investigation regarding the mechanism and possible influence (upstream and downstream) of the contact surface at the underside of the shear layer could be addressed in future work.

Future works will be undertaken to address the performance of different LES models resolving this complex flow dynamics. A detailed analysis of the local entrainment across the TNTI can be explored for the compressible turbulent shear layer. The present LES is performed with 3×10^9 mesh points and can be considered as well resolved; however, further ensemble averaging could be attempted[27] with phase-incohorence in the initial isotropic turbulence to make stable flow statistics and detailed analysis toward the local mechanisms of the complex evolution. From the large-scale tests of Skews *et al.*,[25] it appears that several lambda shocks could play an important role toward large-scale KH instabilities at the later stage of the shear layer development. Also, the onset of the decay of the turbulence in the viscous vortex zone due to viscous dissipation is evident from the experimental findings. These long-time flow features could be investigated further to enhance the understanding of the complex flow dynamics.

ACKNOWLEDGMENTS

This study was supported by the BIOENGINE project, which is funded by the European Regional Development Fund (ERDF) and the Regional Council of Normandie under Contract No. HN-0002484. This work was performed using computing resources from Centre Régional Informatique et d'Applications Numériques de Normandie (CRIANN), Rouen, France.

REFERENCES

[1] W. C. Griffith and W. Bleakney, "Shock waves in gases," Am. J. Phys. **22**, 597–612 (1954).
[2] I. I. Glass, J. Kaca, D. L. Zhang, H. M. Glaz, J. B. Bell, J. A. Trangenstein, and J. P. Collins, "Diffraction of planar shock waves over half-diamond and semicircular cylinders: An experimental and numerical comparison," AIP Conf. Proc. **208**, 246–251 (1990).
[3] K. Matsuo, T. Aoki, and H. Kashimura, "Diffraction of a shock wave around a convex corner," AIP Conf. Proc. **208**, 252–257 (1990).
[4] J. D. Baum, E. Loth, and R. Löhner, "Numerical simulation of shock interaction with complex geometry canisters," AIP Conf. Proc. **208**, 909–914 (1990).
[5] S. Sivier, E. Loth, J. Baum, and R. Löhner, "Vorticity produced by shock wave diffraction," Shock Waves **2**, 31–41 (1992).
[6] M. Sun and K. Takayama, "A note on numerical simulation of vortical structures in shock diffraction," Shock Waves **13**, 25–32 (2003).
[7] M. Sun and K. Takayama, "Vorticity production in shock diffraction," J. Fluid Mech. **478**, 237–256 (2003).
[8] P. Halder, S. De, K. Sinhamahapatra, and N. Singh, "Numerical simulation of shock–vortex interaction in Schardin's problem," Shock Waves **23**, 495–504 (2013).
[9] R. Ripley, F.-S. Lien, and M. Yovanovich, "Numerical simulation of shock diffraction on unstructured meshes," Comput. Fluids **35**, 1420–1431 (2006).

[10]G. Abate and W. Shyy, "Dynamic structure of confined shocks undergoing sudden expansion," Prog. Aerosp. Sci. **38**, 23–42 (2002).
[11] A. Chaudhuri, A. Hadjadj, O. Sadot, and G. Ben-Dor, "Numerical study of shock-wave mitigation through matrices of solid obstacles," Shock Waves **23**, 91–101 (2013).
[12]A. Chaudhuri, A. Hadjadj, O. Sadot, and E. Glazer, "Computational study of shock-wave interaction with solid obstacles using immersed boundary methods," Int. J. Numer. Methods Eng. **89**, 975–990 (2012).
[13]A. Chaudhuri, A. Hadjadj, O. Sadot, and G. Ben-Dor, "Study of shock-wave mitigation through solid obstacles," in *28th International Symposium on Shock Waves*, edited by K. Kontis (Springer Berlin Heidelberg, Berlin, Heidelberg, 2012), pp. 493–498.
[14]A. Chaudhuri, A. Hadjadj, and A. Chinnayya, "On the use of immersed boundary methods for shock/obstacle interactions," J. Comput. Phys. **230**, 1731–1748 (2011).
[15]E. Glazer, O. Sadot, A. Hadjadj, and A. Chaudhuri, "Velocity scaling of a shock wave reflected off a circular cylinder," Phys. Rev. E **83**, 066317 (2011).
[16]M. Shadloo, A. Hadjadj, and A. Chaudhuri, "On the onset of postshock flow instabilities over concave surfaces," Phys. Fluids **26**, 076101 (2014).
[17]V. Soni, A. Hadjadj, A. Chaudhuri, and G. Ben-Dor, "Shock-wave reflections over double-concave cylindrical reflectors," J. Fluid Mech. **813**, 70–84 (2017).
[18]A. Chaudhuri, G. Jacobs, W. Don, H. Abbassi, and F. Mashayek, "Explicit discontinuous spectral element method with entropy generation based artificial viscosity for shocked viscous flows," J. Comput. Phys. **332**, 99–117 (2017).
[19]A. Chaudhuri and G. B. Jacobs, "Dynamics of shock wave diffraction over sharp splitter geometry using entropy-based artificial viscosity method," Shock Waves **29**, 101–115 (2019).
[20]A. Chaudhuri, "Shock propagation and diffraction through cavity," in *Proceedings of the 59th Conference on Simulation and Modelling (SIMS 59), 26–28 September 2018, Oslo Metropolitan University, Norway* (Linköping University Electronic Press, Linköpings Universitet, 2018), Vol. 153, pp. 111–117.
[21] J. O. Reeves and B. Skews, "Unsteady three-dimensional compressible vortex flows generated during shock wave diffraction," Shock Waves **22**, 161–172 (2012).
[22]S. Cooppan and B. Skews, "Three-dimensional shock wave diffraction off a discontinuous edge," Shock Waves **27**, 131–142 (2017).
[23]B. W. Skews and J. J. Bentley, "Merging of two independent diffracting shock waves," Shock Waves **26**, 327–331 (2016).
[24]K. Takayama and O. Inoue, "Shock wave diffraction over a 90 degree sharp corner–posters presented at 18th ISSW," Shock Waves **1**, 301–312 (1991).
[25]B. Skews, C. Law, A. Muritala, and S. Bode, "Shear layer behavior resulting from shock wave diffraction," Exp. Fluids **52**, 417–424 (2012).
[26]C. Law, A. Muritala, and B. Skews, "Unsteady flow with separation behind a shock wave diffracting over curved walls," Shock Waves **24**, 283–294 (2014).
[27]A. Chaudhuri and A. Hadjadj, "Numerical investigations of transient nozzle flow separation," Aerosp. Sci. Technol. **53**, 10–21 (2016).
[28]O. Ben-Nasr, A. Hadjadj, A. Chaudhuri, and M. S. Shadloo, "Assessment of subgrid-scale modeling for large-eddy simulation of a spatially-evolving compressible turbulent boundary layer," Comput. Fluids **151**, 144–158 (2017).
[29]V. Soni, A. Hadjadj, and O. Roussel, "On the use of adaptive multiresolution method with time-varying tolerance for compressible fluid flows," Shock Waves **29**, 37–50 (2019).
[30]B. W. Skews, "The shape of a diffracting shock wave," J. Fluid Mech. **29**, 297–304 (1967).
[31] C. B. da Silva and J. C. F. Pereira, "Invariants of the velocity-gradient, rate-of-strain, and rate-of-rotation tensors across the turbulent/nonturbulent interface in jets," Phys. Fluids **20**, 055101 (2008).
[32]M. Gampert, J. Boschung, F. Hennig, M. Gauding, and N. Peters, "The vorticity versus the scalar criterion for the detection of the turbulent/non-turbulent interface," J. Fluid Mech. **750**, 578–596 (2014).
[33]T. Watanabe, Y. Sakai, K. Nagata, Y. Ito, and T. Hayase, "Turbulent mixing of passive scalar near turbulent and non-turbulent interface in mixing layers," Phys. Fluids **27**, 085109 (2015).
[34]R. Jahanbakhshi, N. S. Vaghefi, and C. K. Madnia, "Baroclinic vorticity generation near the turbulent/non-turbulent interface in a compressible shear layer," Phys. Fluids **27**, 105105 (2015).
[35]G. Borrell and J. Jiménez, "Properties of the turbulent/non-turbulent interface in boundary layers," J. Fluid Mech. **801**, 554–596 (2016).
[36]R. Jahanbakhshi and C. K. Madnia, "Entrainment in a compressible turbulent shear layer," J. Fluid Mech. **797**, 564–603 (2016).
[37]P. Davidson, *Turbulence: An Introduction for Scientists and Engineers* (Oxford University Press, 2015).
[38]A. Chaudhuri, A. Hadjadj, A. Chinnayya, and S. Palerm, "Numerical study of compressible mixing layers using high-order WENO schemes," J. Sci. Comput. **47**, 170–197 (2011).
[39]L. Davidson, "Transport equations in incompressible URANS and LES," in Publication 2006/01, Chalmers University of Technology, 2006.
[40]M. S. Chong, A. E. Perry, and B. J. Cantwell, "A general classification of three-dimensional flow fields," Phys. Fluids A **2**, 765–777 (1990).
[41] S. Pirozzoli and F. Grasso, "Direct numerical simulations of isotropic compressible turbulence: Influence of compressibility on dynamics and structures," Phys. Fluids **16**, 4386–4407 (2004).
[42]N. S. Vaghefi and C. K. Madnia, "Local flow topology and velocity gradient invariants in compressible turbulent mixing layer," J. Fluid Mech. **774**, 67–94 (2015).
[43]J. Wang, Y. Shi, L.-P. Wang, Z. Xiao, X. T. He, and S. Chen, "Effect of compressibility on the small-scale structures in isotropic turbulence," J. Fluid Mech. **713**, 588–631 (2012).
[44]S. Suman and S. S. Girimaji, "Velocity gradient invariants and local flow-field topology in compressible turbulence," J. Turbul. **11**, N2 (2010).
[45]K. Kumari, S. Mahapatra, S. Ghosh, and J. Mathew, "Invariants of velocity gradient tensor in supersonic turbulent pipe, nozzle, and diffuser flows," Phys. Fluids **30**, 015104 (2018).
[46]J. Gaviglio, J. Dussauge, J. Debieve, and A. Favre, "Behavior of a turbulent flow, strongly out of equilibrium, at supersonic speeds," Phys. Fluids **20**, S179–S192 (1977).
[47]J. P. Dussauge, J. Gaviglio, and A. Favre, "Density changes and turbulence production in the expansion or compression of a turbulent flow at supersonic speed," in *Structure and Mechanisms of Turbulence II*, edited by H. Fiedler (Springer Berlin Heidelberg, Berlin, Heidelberg, 1978), pp. 385–395.
[48]G.-H. Cottet, D. Jiroveanu, and B. Michaux, "Vorticity dynamics and turbulence models for large-eddy simulations," ESAIM: Math. Modell. Numer. Anal. **37**, 187–207 (2003).

List of Figures

List of Tables

List of Algorithms

Bibliography

Abate, G. & Shyy, W. (2002), 'Dynamic structure of confined shocks undergoing sudden expansion', Prog. Aerosp. Sci **38**, 23–42. (Cited on page 9).

Abe, A. & Takayama, K. (2001), 'Study of attenuation of shock waves propagating over arrayed spheres', Proceedings of the 24th International Congress on High-Speed Photography and Photonics-SPIE 2001 **4183**, 581–589. (Cited on page 27).

Abe, A., Utsunomiya, G., Lee, J. H. & Takayama, K. (2003), 'Shock wave interaction with rigid porous baffle plates', 25th International Congress on High-Speed Photography and Photonics **4948**, 689. (Cited on pages 20 & 25).

Acton, M., Sutton, P. & Wickens, M. J. (1990), 'An investigation of mitigation of gas cloud explosions by water sprays', Piper Alpha. Lessons for Life Cycle Safety Management, Symposium Series No. 122, IChemE, Rugby, UK . (Cited on page 32).

Allain, L. (1994), 'Barricade influence on blast wave propagation', SNPE / Division Defense and Space, private communication . (Cited on pages 21, 33, 34 & 169).

Baird, J. P. & Stollery, L. J. (1987), 'Supersonic vortex rings', Proc Roy Soc Lond A 409 **7**, 59–65. (Cited on page 5).

Bazhenova, T. V., Gvozdeva, L. G., Komarov, V. S. & Sukhov, B. G. (1973), 'Diffraction of strong shock waves by convex corners', Fluid Dynamics **8**, 611–619. (Cited on page 5).

Bazhenova, T. V., Gvozdeva, L. G., Lagutov, P. Y. & Rayevsky, D. K. (1990), 'Non stationary interaction of a shock wave with shallow cavity', In Current Topics in Shock Waves (ed. Y. W. Kim). AIP Conf. Proc. 208 American Institute of Physics . (Cited on page 13).

Bazhenova, T. V., Gvozdeva, L. G. & Nettleton, M. A. (1984), 'Unsteady interactions of shock waves', Progress in Aerospace Sciences. **21**, 249–331. (Cited on pages 3 & 5).

Ben-Dor, G. (1980), 'Analytical solution of double-mach reflection', *AIAA J.* **18**, 1036–1043. (Cited on page 1).

Ben-Dor, G. (2007), *Shock Wave Reflection Phenomena*. (Cited on pages 4, 25 & 167).

Ben-Dor, G. & Glass, I. I. (1979), 'Domains and boundaries of non-stationary oblique shock-wave reflexions. 1. diatomic gas', Journal of Fluid Mechanics. **92**, 459–496. (Cited on page 1).

Ben-Dor, G., Takayama, K. & Kawauchi, T. (1980), 'The transition from regular to mach reflexion and from mach to regular reflexion in truly non-stationary flows', Journal of Fluid Mechanics. **100**, 147–160. (Cited on page 1).

Berger, S., Ben-Dor, G. & Sadot, O. (2015), 'Experimental and numerical investigations of shock-wave attenuation by geometrical means: A single barrier configuration', *European Journal of Mechanics, B/Fluids* **50**, 60–70. (Cited on page 135).

Berger, S., Sadot, O. & Ben-Dor, G. (2010), 'Experimental investigation on the shock-wave load attenuation by geometrical means', *Shock Waves* **20**(1), 29–40. (Cited on pages 19 & 168).

Besset, C. & Blanc, E. (1994), 'Propagation of vertical shock waves in the atmosphere', *Journal of the Acoustical Society of America* **95**(4), 1830–1839. (Cited on page 39).

Best, J. P. (1991), 'A generalisation of the theory of geometrical shock dynamics', *Shock Waves* **1**(4), 251–273. (Cited on page 39).

Biamino, L., Jourdan, G., Igra, O., Mariani, C., Tosello, R., Leriche, D. & Houas, L. (2014), 'Experimental investigation of shock wave propagation in a 90° branched duct', Shock Waves **24**, 307–315. (Cited on page 14).

Bjerkelvedt, D. & Bjarkhaug, M. (1991), 'Experimental investigation: Effect of water spray on gas explosions', Report prepared by the Christian Michelsen Institute, Bergen, Norway, for the UK Department of Energy, OTH 90 316, HMSO . (Cited on page 32).

Bond, C., Hill, D. J., Meiron, D. I. & Dimotakis, P. E. (2009), 'Shock focusing in a planar convergent geometry: experiment and simulation', Journal of Fluid Mechanics **641**, 297–333. (Cited on page 37).

Borgers, J. (2010), 'Blast walls reviewed', 21st Military Aspect of Blast and Shock (MABS), Jerusalem . (Cited on pages 21, 33, 34 & 169).

Borisov, A. A., Gelfand, B. E. & Skatchkov, G. I. (1988), 'Ignition of gaseous combustible mixtures in focused shock waves', Sov. J. Chimicheskaya Phys **7**, 1387. (Cited on page 37).

Brahmi, N., Hadjadj, A., Soni, V. & Chaudhuri, A. (2020*a*), 'Analysis of shock-wave diffraction over double concave cylindrical wedges. Part I: Shock dynamics', *Acta Astronautica* **172**, 134–139. (Cited on pages 43, 84 & 89).

Brahmi, N., Hadjadj, A., Soni, V. & Chaudhuri, A. (2020*b*), 'Analysis of shock-wave diffraction over double cylindrical wedges. Part II: Vorticity generation', *Acta Astronautica.* **172**, 140–150. (Cited on pages 43, 84 & 120).

Broadbent, E. G. & Moore, D. W. (1987), 'The interaction of a vortex ring and a coaxial supersonic jet', Proc Roy Soc Lond A 409 **7**, 47–57. (Cited on page 6).

Brouillette, M., Tardif, J. & Gauthier, E. (1995), 'Experimental study of shock-generated vortex ring', Proc 19th ISSW, Marseille pp. 361–366. (Cited on pages 6 & 89).

Butcher, J. C. (2008), Chapter 3: Runge–Kutta Methods, *in* 'Numerical Methods for Ordinary Differential Equations', 2nd Ed. John Wiley & Sons, Ltd, pp. 137–316. (Cited on page 112).

Catherasoo, C. J. & SturteVant, B. (1983), 'Shock dynamics in non-uniform media', *Journal of Fluid Mechanics* **127**, 539–561. (Cited on page 39).

Catlin, C. A., Gregory, W., Johnson, D. M. & Walker, D. G. (1993), 'Explosion mitigation in offshore modules by general area deluge', Trans IChmE **71**, 101–111. (Cited on page 32).

Chan, C. K., Lau, D., Thibault, P. A. & Penrose, J. D. (1989), 'Ignition and detonation initiation by shock focussing', AIP Conference Proceedings pp. 161–166. (Cited on page 38).

Chang, S. & Chang, K. (2000), 'On the shock-vortex interaction in Schardin's problem', *Shock Waves* **10**(5), 333–343. (Cited on pages 59 & 169).

Chaudhuri, A. (2019), 'On shock propagation through double-bend ducts by entropy-generation-based artificial viscosity method', Entropy **21**, 837. (Cited on pages 18, 24, 167 & 168).

Chaudhuri, A., Hadjadj, A. & Chinnayya, A. (2011), 'On the use of immersed boundary methods for shock/obstacle interactions', *J. Comput. Phys.* **230**(5), 1731–1748. (Cited on pages 54 & 84).

Chaudhuri, A., Hadjadj, A., Chinnayya, A. & Palerm, S. (2011), 'Numerical Study of Compressible Mixing Layers Using High-Order WENO Schemes', *J. Sci. Comput* **47**, 170–197. (Cited on page 84).

Chaudhuri, A., Hadjadj, A., Sadot, O. & Ben-Dor, G. (2013), 'Numerical study of shock-wave mitigation through matrices of solid obstacles', Shock Waves **23**, 91–101. (Cited on pages 19, 28, 29, 30 & 168).

Chaudhuri, A., Hadjadj, A., Sadot, O. & Glazer, E. (2012), 'Computational study of shock-wave interaction with solid obstacles using immersed boundary methods', International Journal For Numerical Methods In Engineering **89**, 975–990. (Cited on pages 19, 27, 28, 29 & 168).

Chaudhuri, A. & Jacobs, G. B. (2017), 'Dynamics of shock wave diffraction over sharp splitter geometry using entropy-based artificial viscosity method', Shock Waves **1**, 1–15. (Cited on pages 6 & 10).

Chauvin, A., Jourdan, G., Daniel, E., Houas, L. & Tosello, R. (2011), 'Experimental investigation of the propagation of a planar shock wave through a two-phase gas-liquid medium', Physics of Fluids **23**, 1–14. (Cited on pages 19, 31, 32, 33 & 168).

Chester, W. (1953), 'The propagation of shock waves in a channel of non-uniform width', Quarterly Journal of Mechanics and Applied Mathematics **6**, 440–452. (Cited on pages 18 & 22).

Chisnell, R. F. (1955), 'The normal motion of a shock wave through a non-uniform one-dimensional medium', Proceedings of the Royal Society of London. Series A. Mathematical and Physical Sciences **232**, 350–370. (Cited on pages 18 & 22).

Cohen, A. (2003), *Numerical analysis of wavelet methods*, Vol. 32, Elsevier Science B. V. (Cited on page 113).

Cohen, A., Kaber, S. M., Müller, S. & Postel, M. (2003), 'Fully adaptive multiresolution finite volume schemes for conservation laws', *Math. Comp.* **72**, 183–225. (Cited on page 52).

Dadone, A. & Grossman, B. (2004), 'Ghost-cell method for inviscid two-dimensional flows on Cartesian grids', *AIAA J.* **42**(12), 2499–2507. (Cited on page 54).

Daubechies, I. (1992), *Ten lectures on wavelets*, SIAM. (Cited on page 113).

Dosanjh, D. S. (1956), 'Interaction of grids with traveling shock waves', NACA Technical Note 3680, Johns Hopkins University, Washington, DC, USA . (Cited on pages 19 & 27).

Ducros, F., Ferrand, V., Nicoud, F., Weber, C. & Darracq, D. (1999), 'Large-eddy simulation of the shock/turbulence interaction', *Journal of Computational Physics* **152**(2), 517–549. (Cited on page 122).

Fadlun, E., Verzicco, R., Orlandi, P. & Mohd-Yusof, J. (2000), 'Combined immersed-boundary finite-difference methods for three-dimensional complex flow simulations', *J. Comput. Phys.* **161**(1), 35–60. (Cited on page 54).

Falcovitz, J., Igra, O. & Igra, D. (2012), 'Shock wave propagation in non-uniform gas mixtures', *Proceedings of the Institution of Mechanical Engineers, Part G: Journal of Aerospace Engineering* **226**(2), 123–130. (Cited on page 82).

Gao, T., Tseng, Y.-H. & Lu, X.-Y. (2007), 'An improved hybrid Cartesian/immersed boundary method for fluid–solid flow', *Int. J. Numer. Meth. Fl.* **55**, 1189–1211. (Cited on page 54).

Gelfand, B. E., Khomik, S. V., Bartenev, A. M., Medvedev, S. P., Grönig, H. & Olivier, H. (2000), 'Detonation and deflagration initiation at the focusing of shock waves in combustible gaseous mixture', Shock Waves **10**, 197–204. (Cited on page 38).

Geva, M., Ram, O. & Sadot, O. (2013), 'The non-stationary hysteresis phenomenon in shock wave reflections', Journal of Fluid Mechanics. **732**. (Cited on page 1).

Ghias, R., Mittal, R. & Dong, H. (2007), 'A sharp interface immersed boundary method for compressible viscous flows', *J. Comput. Phys.* **225**(1), 528–553. (Cited on page 54).

Glazer, E., Sadot, O., Hadjadj, A. & Chaudhuri, A. (2011), 'Velocity scaling of a shock wave reflected off a circular cylinder', *Physical Review* **83**(6), 1–9. (Cited on page 83).

Gnani, F., Lo, K. H., Zare-Behtash, H. & Kontis, K. (2014), 'Experimental investigation on shock wave diffraction over sharp and curved splitters', Acta Astronautica **99**, 143–152. (Cited on page 9).

Gongora-Orozco, N. (2010), Experimental studies on internal shock wave phenomena and interactions, PhD thesis, University of Manchester. (Cited on pages 20, 26 & 168).

Gongora-Orozco, N., Zare-Behtash, H. & Kontis, K. (2009), 'Experimental studies on shock wave propagating through junction with grooves', *47th AIAA Aerospace Sciences Meeting including the New Horizons Forum and Aerospace Exposition* . (Cited on page 20).

Guderley, G. (1942), 'Starke kugelige und zylindrische verdichtungstösse in dernähe des kugelmittelpunktes bzw der zylinderachse', *Luftfahrt forschung* **302**. (Cited on page 37).

Guildenbecher, D. R., López-Rivera, C. & Sojka, P. E. (2009), 'Secondary atomization', Experiments in Fluids **46**, 371–402. (Cited on page 31).

Gvozdeva, L. G., Lagutov, P. Y., Rayevsky, D. K., Kharitovnov, A. E. & Sharov, Y. L. (1988), 'Investigation of non stationary flows with separation over cavities', Izv. Mekh. Zidk. Gaza **3**, 185–191. (Cited on page 13).

Gvozdeva, L. G., Lagutov, Y. P. & Fokeev, V. P. (1982), 'Transition from mach reflection to regular reflection when strong shock waves interact with cylindrical surfaces', Fluid Dyn. **17**, 273–278. (Cited on page 1).

Haas, J. F. & Sturtevant, B. (1987), 'Interaction of weak shock waves with cylindrical and spherical gas inhomogeneities', *Journal of Fluid Mechanics* **181**, 41–76. (Cited on page 82).

Hadjadj, A. & Sadot, O. (2013), 'Shock and blast waves mitigation', *Shock Waves* **23**(1), 1–4. (Cited on pages 19 & 168).

Harten, A. (1993), 'Discrete multi-resolution analysis and generalized wavelets', *J. Appl. Num. Math.* **12**, 153–193. (Cited on page 47).

Harten, A. (1995), 'Multiresolution algorithms for the numerical solution of hyperbolic conservation laws', *Comm. Pure Appl. Math.* **48**, 1305–1342. (Cited on pages 47, 51, 52 & 117).

Heilig, W. (1975), 'Propagation of shock waves in various branched ducts', Modern Developments in Shock Tube Research, Shock Tube Research Society, Japan pp. 273–283. (Cited on page 13).

Heilig, W. H. (1969), 'Diffraction of a shock wave by a cylinder', Phys. Fluids. **12**, 1036–1043. (Cited on page 1).

Hillier, R. (1991), 'Computation of shock wave diffraction at a ninety degrees corner', Shock Waves **1**, 89–98. (Cited on page 6).

Howard, L. N. & Matthews, J. (1956), 'On the vortices produced in shock diffraction', J. Appl. Phys **27**, 223–231. (Cited on page 9).

Iaccarino, G. & Verzicco, R. (2003), 'Immersed boundary technique for turbulent flow simulations', *Appl. Mech. Rev.* **56**(3), 331–347. (Cited on page 54).

Igra, D. & Igra, O. (2012), 'Simulation of shock wave propagation in a duct with a side branch', 20th International Shock Interaction Symposium Stockholm . (Cited on page 13).

Igra, D. & Igra, O. (2016*a*), 'Planar shock-wave diffraction into a square cavity filled with different gases', AIAA Journal **54**, 1798–1802. (Cited on pages 14, 18 & 167).

Igra, D. & Igra, O. (2016*b*), 'Shock wave mitigation by different combination of plate barriers; A numerical investigation', *European Journal of Mechanics, B/Fluids* **59**, 115–123. (Cited on pages 19 & 168).

Igra, D. & Igra, O. (2018), 'Numerical investigation of the interaction between a planar shock wave with square and triangular bubbles containing different gases', *Physics of Fluids* **30**(5). (Cited on page 83).

Igra, D. & Takayama, K. (2003), 'Experimental investigation of two cylindrical water columns subjected to planar shock wave loading', J Fluids Eng **125**, 325–331. (Cited on pages 19 & 33).

Igra, O., Falcovitz, J., Houas, L. & Jourdan, G. (2013), 'Review of methods to attenuate shock/blast waves', Progress in Aerospace Sciences **58**, 1–35. (Cited on page 35).

Igra, O., Falcovitz, J., Reichenbach, H. & Heilig, W. (1996), 'Experimental and numerical study of the interaction between a planar shock wave and a square cavity', Journal of Fluid Mechanics **313**, 105–130. (Cited on pages 13, 14, 15, 16, 23 & 167).

Igra, O., Wang, L., Falcovitz, J. & Heilig, W. (1998), 'Shock wave propagation in a branched duct', Shock Waves **8**, 375–381. (Cited on pages 13, 18 & 23).

Igra, O., Wu, X., Falcovitz, J., Meguro, T., Takayama, K. & Heilig, W. (2001), 'Experimental and theoretical study of shock wave propagation through double-bend ducts', Journal of Fluid Mechanics **437**, 255–282. (Cited on pages 18, 20, 22, 23, 24, 25 & 168).

Inoue, O., Imuta, G., Milton, B. E. & Takayama, K. (1995), 'Computational study of shock wave focusing in a log-spiral duct', Shock Waves **5**, 183–188. (Cited on page 37).

Itoh, S., Okazaki, N. & Itaya, M. (1981), 'On the transition between regular and mach reflection in truly non-stationary flows', Journal of Fluid Mechanics. **108**, 383–400. (Cited on page 1).

Izumi, K., Aso, S. & Nishida, M. (1994), 'Experimental and computational studies focusing processes of shock waves reflected from parabolic reflectors', Shock Waves **3**, 213–222. (Cited on page 37).

Jiang, G. S. & Shu, C. W. (1996), 'Efficient implementation of weighted ENO schemes', *J. Comput. Phys.* **12**, 202–228. (Cited on page 109).

Jiang, S., Sha, Z. & Chen, X. (2014), 'Influences of obstacle geometries on shock wave attenuation', *Shock Waves* pp. 573–582. (Cited on pages 20, 21 & 168).

Jourdan, G., Biamino, L., Mariani, C., Blanchot, C., Daniel, E., Massoni, J., Houas, L., Tosello, R. & Praguine, D. (2010), 'Attenuation of a shock wave passing through a cloud of water droplets', Shock Waves **20**, 285–296. (Cited on pages 19 & 32).

Kailasanath, K., Tatem, P. & Mawhinney, J. (2002), 'Blast mitigation using water a status report', Technical report, NRL/MR/6400-02-8606 . (Cited on page 31).

Kang, S., Iaccarino, G., Ham, F. & Moin, P. (2009), 'Prediction of wall-pressure fluctuation in turbulent flows with an immersed boundary method', *J. Comput. Phys.* **228**(18), 6753–6772. (Cited on page 54).

Kim, H. D., Kweon, Y. H. & Setoguchi, T. (2004), 'A study of the weak shock wave propagating through an engine exhaust silencer system', *Journal of Sound and Vibration* **275**(3-5), 893–915. (Cited on pages 18 & 167).

Kleine, H., Kallweit, S., Michaux, F., Havermann, M. & Olivier, H. (2016), 'Piv measurement of shock wave diffraction', 18th International Symposium on the Application of Laser and Imaging Techniques to Fluid Mechanics, LISBON-PORTUGAL . (Cited on page 6).

LeVeque, R. J. (1992), *Numerical Methods for Conservation Laws*, 2nd Ed. Birkhäuser Verlag. (Cited on page 46).

Liu, X., Osher, S. & Chan, T. (1994), 'Weighted essentially non-oscillatory schemes', *J. Comput. Phys.* **115**(1), 200–212. (Cited on page 109).

Luo, X., Wang, M. & T. Si, Z. Z. (2015), 'On the interaction of a planar shock with an SF_6 polygon', *Journal of Fluid Mechanics* **773**, 366–394. (Cited on page 83).

Mach, E. (1878), 'Über den verlauf von funkenwellen in der ebene und im räume', Sitzungsbr. Akad. Wiss. Wien. **78**, 819–838. (Cited on page 1).

MacLucas, D., Skews, B. & Kleine, H. (2020), 'Shock wave interactions within concave cavities', Experiments in Fluids **61**, 1–27. (Cited on page 37).

Mallat, S. (1989), 'Multiresolution approximation and wavelet orthonormal bases of $L^2(R)$', *Trans. Amer. Math. Soc.* **315**, 69–88. (Cited on pages 47 & 113).

Marty, A., Daniel, E., Massoni, J., Biamino, L., Houas, L., Leriche, D. & Jourdan, G. (2019), 'Experimental and numerical investigations of shock wave propagation through a bifurcation', Shock Waves **29**, 321–326. (Cited on pages 18, 24 & 167).

Mittal, R. & Iaccarino, G. (2005), 'Immersed Boundary Methods', *Annu. Rev. Fluid Mech.* **37**(1), 239–261. (Cited on page 54).

Mortazawy, S. M., Kontis, K. & Ekaterinaris, J. (2019), 'Normal shock wave attenuation during propagation in ducts with grooves', Shock Waves **4948**, 689. (Cited on pages 20, 26 & 168).

Müller, S. (2003), *Adaptive Multiscale Schemes for Conservation Laws*, Springer-Verlag. (Cited on page 113).

Nettleton, M. A. (1973), 'Shock attenuation in a gradual area expansion', Journal of Fluid Mechanics **60**, 209–223. (Cited on pages 18 & 22).

O'Rourke, J. (1998), *Computational Geometry In C*, 2nd Ed. Cambridge University Press. (Cited on page 56).

Oshima, K. (1965), 'Propagation of spacially non-uniform shock waves', *ISAS Rep* **30**(6), 195. (Cited on page 41).

Oshima, K., Sugaya, K., Yamamoto, M. & Totoki, T. (1965*a*), 'Diffraction of a plane shock wave around a corner', ISAS report **30**, 51–82. (Cited on page 5).

Oshima, K., Sugaya, K., Yamamoto, M. & Totoki, T. (1965*b*), 'Diffraction of a plane shockwave around a corner', *ISAS Rep* **30**(2), 51,Äì82. (Cited on page 41).

Pandey, M. & Sharma, V. (2009), 'Kinematics of a shock wave of arbitrary strength in a non-ideal gas', *Quarterly of Applied Mathematics* **67**(3), 305–322. (Cited on page 40).

Perry, R. W. & Kantrowitz, A. (1951), 'The production and stability of converging shock waves', Journal of Applied Physics **22**, 878–886. (Cited on page 37).

Peskin, C. S. (1972), Flow patterns around heart valves: A digital computer method for solving the equations of motion, Ph.D. Thesis, Yeshiva University. (Cited on page 53).

Pirozzoli, S. (2011), 'Numerical Methods for High-Speed Flows', *Annual Review of Fluid Mechanics* **43**(1), 163–194. (Cited on page 122).

Reeves, J. O. & Skews, B. W. (2012), 'Unsteady three-dimensional compressible vortex flows generated during shock wave diffraction', Shock Waves **22**, 161–172. (Cited on page 9).

Ridoux, J. (2017), Contribution au développement d'une méthode de calcul rapide de propagation des ondes de souffle en présence d'obstacles, Ph.D. Thesis, Pierre et Marie Curie University. (Cited on pages 41 & 42).

Ridoux, J., Lardjane, N., Monasse, L. & Coulouvrat, F. (2019), 'Beyond the limitation of geometrical shock dynamics for diffraction over wedges', *Shock Waves* **29**(6), 833–855. (Cited on pages 39, 40, 41 & 169).

Roe, P. L. (1981), 'Approximate Riemann solvers, parameter vectors, and difference schemes', *J. Comput. Phys.* **43**, 357–372. (Cited on page 110).

Rosciszewski, J. (1960), 'Propagation of waves of finite amplitude along a duct of non-uniform cross-section', Journal of Fluid Mechanics **8**, 625–633. (Cited on page 5).

Russel, D. A. (1986), 'Shock dynamic of noninvasive fracturing of kidney stones', In: Bershader D, Hanson R (eds) 15th lnt Syrup Shock Waves and Tubes. Stanford, USA pp. 57–64. (Cited on page 37).

Sasoh, A., Matsuoka, K., Nakashio, K., Timofeev, E., Takayama, K., Voinovich, P., Saito, T., Hirano, S., Ono, S. & Makino, Y. (1998), 'Attenuation of weak shock waves along pseudo-perforated walls', *Shock Waves* **8**(3), 149–159. (Cited on page 20).

Sasoh, A., Onodera, O. & Takayama, K. (1994), 'Scaled train tunnel simulator for weak shock wave generation experiment', Review Scientific Instrumentation **65**, 3000–3004. (Cited on pages 20, 22 & 25).

Schardin, H. (1957), 'High frequency cinematography in the shock tube', *J. Photo Sci.* **5**(2), 19–26. (Cited on page 58).

Schneider, K. (2015), 'Immersed boundary methods for numerical simulation of confined fluid and plasma turbulence in complex geometries: a review', *J. Plasma Phys.* **81**(06), 1–21. (Cited on page 54).

Schwendeman, D. W. (2002), 'On converging shock waves of spherical and polyhedral form', *Journal of Fluid Mechanics* **454**, 365–386. (Cited on page 39).

Schwendeman, D. W. & Whitham, G. B. (1987), 'on Converging Shock Waves.', *Proceedings of The Royal Society of London, Series A: Mathematical and Physical Sciences* **413**(1845), 297–311. (Cited on page 39).

Sebastien, E. (2013), Propagation d'une onde de choc en presence d'une Barréire De Protection, PhD thesis, UNIVERSITÉ D'ORLÉANS. (Cited on pages 21, 33, 34, 168 & 169).

Shadloo, M. S., Hadjadj, A. & Chaudhuri, A. (2014), 'On the onset of postshock flow instabilities over concave surfaces', Phys. Fluids. **26**. (Cited on pages 1, 37, 38, 58 & 169).

Sharma, V. & Radha, C. (1995), 'Three dimensional shock wave propagation in an ideal gas', *International Journal of Non-Linear Mechanics* **30**(3), 305–322. (Cited on page 40).

Si, T., Zhai, Z., Yang, J. & Luo, X. (2012), 'Experimental investigation of reshocked spherical gas interfaces', *Physics of Fluids* **24**(5). (Cited on page 83).

Siefert, N. S. (2007), 'Shock velocity in weakly ionized nitrogen, air, and argon', *Physics of Fluids* **19**(3), 1–8. (Cited on page 83).

Skews, B. (2005), 'Shock wave interaction with porous plates', Experiments in Fluids **39**, 875–884. (Cited on pages 20, 25 & 168).

Skews, B. W. (1967*a*), 'The perturbed region behind a diffracting shock wave', Journal of Fluid Mechanics **29**, 705–722. (Cited on pages 5, 7, 8, 9 & 167).

Skews, B. W. (1967*b*), 'The shape of a diffracting shock wave', Journal of Fluid Mechanics **29**, 297–304. (Cited on pages 5 & 39).

Skews, B. W., Draxl, M. A., Felthun, L. & Seitz, M. W. (1998), 'Shock wave trapping', Shock Waves **8**, 23–28. (Cited on pages 19, 27, 28 & 168).

Skews, B. W. & Kleine, H. (2007), 'Flow features resulting from shock wave impact on a cylindrical cavity', Journal of Fluid Mechanics. **580**, 481–493. (Cited on page 1).

Skews, B. W., Law, C., Muritala, A. & Bode, S. (2012), 'Shear layer behavior resulting from shock wave diffraction', Experiments in Fluids **52**, 417–424. (Cited on pages 5 & 9).

Smith, L. G. (1945), 'Photographic investigation of the reflection of plane shocks in air', Tech. Rep. OSRD Rep. 6271. Off. Sci. Res. Dev., Washington DC, USA. . (Cited on page 1).

Sochet, I., Eveillard, S., Piserchia, P. & Vinçont, J. (2013), 'Dimensioning physical protection barricades against the propagation of pressure waves following a detonation', *in: 13th Interdisciplinary Workshop on Global Security* . (Cited on pages 21, 36 & 169).

Sochet, I., Eveillard, S., Vincont, J. Y., Piserchia, P. F. & Rocourt, X. (2017), 'Influence of the geometry of protective barriers on the propagation of shock waves', Shock Waves **27**, 209–219. (Cited on pages 21, 34 & 168).

Soni, V. (2016), Parallel Adaptive Multiscale Numerical Methods for Complex Compressible Flows, Ph.D. Thesis, INSA de Rouen, France. (Cited on pages 58, 59, 60, 169 & 170).

Soni, V., Chaudhuri, A., Brahmi, N. & Hadjadj, A. (2019), 'Turbulent structures of shock-wave diffraction over 90° convex corner', Physics of Fluids **31**. (Cited on pages 7, 10 & 58).

Soni, V., Hadjadj, A., Chaudhuri, A. & Ben-Dor, G. (2017), 'Shock-wave reflections over double-concave cylindrical reflectors', Journal of Fluid Mechanics. **813**, 70–84. (Cited on pages 1, 4 & 58).

Soni, V., Hadjadj, A. & Roussel, O. (2017), 'On the use of adaptive multiresolution method with time-varying tolerance for compressible fluid flows', Shock Waves pp. 1–14. (Cited on pages 8, 58, 84 & 167).

Soni, V., Hadjadj, A., Roussel, O. & Moebs, G. (2019), 'Parallel multi-core and multi-processor methods on point-value multiresolution algorithms for hyperbolic conservation laws', *J. Parallel Distrib. Comput* **123**, 192–203. (Cited on page 84).

Soni, V., Roussel, O. & Hadjadj, A. (2017), 'On the accuracy and efficiency of point-value multiresolution algorithms for solving scalar wave and Euler equations', *J. Computational & Applied Mathematics* **323**, 159–175. (Cited on page 84).

Sturtevant, B. (1989), 'The physics of shock focusing in the context of eswl. in: Proceedings of the international workshop on shock wave focusing', ed. K. Takayama, Shock Wave Research Center, Institute of Fluid Science, Tohoku University, Sendai, Japan pp. 39–64. (Cited on page 37).

Sturtevant, B. & Kulkarny, V. A. (1976), 'The focusing of weak shock waves', Journal of Fluid Mechanics **76**, 651–671. (Cited on page 37).

Sun, M. & Takayama, K. (1997), 'The formation of a secondary wave behind a shock wave diffracting at a convex corner', Shock Waves **7**, 287–295. (Cited on pages 5, 6 & 122).

Sun, M. & Takayama, K. (2003*a*), 'A note on numerical simulation of vortical structures in shock diffraction', Shock Waves **13**, 25–32. (Cited on page 9).

Sun, M. & Takayama, K. (2003*b*), 'Vorticity production in shock diffraction', Journal of Fluid Mechanics **478**, 237–256. (Cited on pages 9, 11, 12, 106 & 167).

Szwumoski, A. (1971), 'Attenuation of a shock wave along a perforated tube', Shock Tube Research, 8th International Shock Tube Symposium, Imperial Coll. Sci. Technol **14**, 1–10. (Cited on pages 20 & 25).

T. V. Bazhenova, L. G. G. & Zhilin, Y. V. (1979), 'Change in the shape of the diffracting shock wave at a convex cornert', *Acta Astronautica* **6**(1951), 401–412. (Cited on page 39).

Takayama, K., Sasoh, A., Onodera, O., Kaneko, R. & Matsui, Y. (1995), 'Experimental investigation on tunnel sonic boom', Shock Waves **5**, 127–138. (Cited on pages 20, 22 & 25).

Thomas, G. & Brenton, J. (1993), 'A study of turbulent flame acceleration in water sprays', Paper presented at the 14th International Colloquium on the Dynamics of Explosions and Reactive systems, Coimbra, Portugal . (Cited on page 32).

Tseng, T. I. & Yang, R. J. (2006), 'Numerical simulation of vorticity production in shock diffraction', AIAA Journal **44**, 1040–1047. (Cited on pages 9, 12, 13, 121 & 167).

Tseng, Y.-H. & Ferziger, J. H. (2003), 'A ghost-cell immersed boundary method for flow in complex geometry', *J. Comput. Phys.* **192**(2), 593–623. (Cited on page 54).

von Neumann, J. (1943*a*), 'Oblique reflection of shocks', John von Neumann Collected Works. **6**, 238–299. (Cited on page 3).

von Neumann, J. (1943*b*), 'Reflection, intersection and reflection of shock waves', NAVORD Rep 203-45, Navy Dept, Bureau of Ordinance, Washington, DC, USA. . (Cited on page 3).

von Neumann, J. (1963), 'Collected works of john von neumann', 2nd Ed. Pergamon Press. . (Cited on page 1).

Wan, Q., Deiterding, R. & Eliasson, V. (2019), 'Numerical investigation of shock wave attenuation in channels using water obstacles', Multi-scale and Multidisciplinary Modeling, Experiments and Design **2**, 159–173. (Cited on pages 19, 33 & 168).

Wan, Q. & Eliasson, V. (2015), 'Numerical study of shock wave attenuation in two-dimensional ducts using solid obstacles: How to utilize shock focusing techniques to attenuate shock waves', Aerospace **2**, 203–221. (Cited on pages 19, 30 & 168).

Wang, B. Y., Wu, Q. S., Wang, C., Igra, O. & Falcovitz, J. (2001), 'Shock wave diffraction by a square cavity filled with dusty gas', Shock Waves **11**, 7–14. (Cited on page 13).

White, D. R. (1951), 'An experimental survey of the mach reflection of shock waves', Tech. Rep. II-10. Department of Physics, Princeton University, Princeton, USA. . (Cited on page 1).

Whitham, G. B. (1957), 'A new approach to problems of shock dynamics part i two-dimensional problems', Journal of Fluid Mechanics **2**, 145–171. (Cited on pages 5 & 38).

Whitham, G. B. (1958), 'On the propagation of shock waves through regions of non-uniform area or flow', Journal of Fluid Mechanics **4**, 337–360. (Cited on pages 18 & 22).

Whitham, G. B. (1959), 'A new approach to problems of shock dynamics part ii three-dimensional problems', Journal of Fluid Mechanics **5**, 369–386. (Cited on pages 5 & 38).

Wingerden, K. V., Wilkins, B. A., Bakken, J. & Pedersen, G. H. (1995), 'The influence of waterspray on gas explosions. part 2: Mitigation', J. Loss Prev. Process Ind . (Cited on page 32).

Wright, T. W. (1976), 'An intrinsic description of unsteady shock waves', *Quarterly Journal of Mechanics and Applied Mathematics* **29**(3), 311–324. (Cited on page 40).

Yasuhara, K., Kitagawa, K. & Takayama, M. (2006), 'Attenuation of shock waves propagating in polyurethane foams', *Shock Waves* pp. 437–445. (Cited on page 19).

Zhou, X. Q. & Hao, H. (2008), 'Prediction of airblast loads on structures behind a protective barrier', *International Journal of Impact Engineering* **35**(5), 363–375. (Cited on page 21).

Zhu, Y., Gao, L. & Yang, Z. (2020), 'Sulfur hexafluoride bubble evolution in shock accelerated flow with a transverse density gradient', Physics of Fluids **32**, 161–172. (Cited on page 10).